Author's Declaration

The work described in this thesis was carried out in the Department of Chemistry at the University of Sheffield. The work presented here is based on the original work done by me under the guidance of Prof. dr. Anthony J. H. M. Meijer, FRAS FRSC. This work has not been included in any other thesis previously.

Rasha W. M. Al-saedi

December 2018

Theoretical Studies of Heterogeneous Catalysis using Particles with a High Surface to Volume Ratio

By:

Rasha Wali Mohi Al-Saedi

Supervised by: Prof. dr. Anthony J. H. M. Meijer

A thesis submitted in partial fulfilment of the requirements for the degree of Doctor of Philosophy

The University of Sheffield

Department of Chemistry

December 2018

Acknowledgment

In the name of God, most Gracious, most Merciful.

This thesis would not be possible without the assistance and encouragement of several people. I would like to express my sincere appreciation to all of them.

Foremost, I would like to thank my academic advisor Prof. Anthony J. H. M. Meijer, for his patience, guidance, constant feedback and excellent environment he has provided me with throughout the entire research.

I am so grateful to the University of Sheffield for giving me this opportunity. Special thanks goes to the Graduate Research Centre for providing me with all facilities and support.

I owe a great debt of gratitude to the financial support of Higher Committee of Education of Iraq since otherwise, I would not have been able to pursue my dreams. I am indebted to them for their support.

I also appreciate all the people who contributed to the work described in this thesis. A very special thanks going to Brammer's group (Eliott and Rebecca) and Dr. Jonathan Foster for sharing their experimental data, knowledge and their invaluable contribution to my research.

I would like to express my gratitude to my colleagues in the office for a great help on many occasions, special thanks to dr.Theo Keane, for his invaluable input on the numerous questions that came up throughout the project. He always willing to help and give his best suggestions.

I am also in debated to all my friends for providing me support in all things of life beyond doing a PhD.

My words cannot express how grateful I am to my family for their unconditional care and love. I am owing my eternal gratitude to my hard-working mom, who sacrificed her life for myself and my brothers. Your prayers for me was what sustained me thus far. My heartfelt thanks goes to my brothers (Muhanned, Ali and Mokhld) for believing in me which gives me extra strength and motivation to get the thing done. Special thanks to Ali, my Attorney-in-fact, who's managed all my affairs in home.

Last but not least, I am thankful to all people whose names I may have forgotten to mention.

Dedicated to my father's soul, Wali Mohi.

List of Abbreviations

2D – Two-dimensional

3D – Three-dimensional

APED – Austin-Frisch-Petersson functional with dispersion

B3LYP – Becke, three-parameter, Lee-Yang-Parr exchange-correlation functional

B97-1 – Hybrid-GGA exchange-correlation functional due to Becke.

B97D – Grimme's modified B97 including the empirical D2 functional including dispersion

B97D3 – Grimme's modified B97 including the empirical D3 functional dispersion correction with Beck-Johanson damping method

BDB – butadiynedibenzoate

BDC – benzenedicarboxylate

BET – Brunauer-Emmett-Teller

BioMOF-11 – $Co_2(ad)_2(CO_2CH_3)_2$ .2DMF.0.5H_2O; Had: adenine

BPDC – biphenyl-4,4′-dicarboxylate

Bptc – biphenyl-tetracarboxylate

Btb – 1,3,5-benzenetribenzoate

BTC – 1,3,5-benzenetricarboxylate

BTE – 4,4′,44″-[benzene-1,3,5-triyl-tris(benzene-4,1-diyl)]tribenzoate

Bttb – Benzene-1,2,4,5-tetrayltetrabenzoate

def – N,N-diethylformamide

DMSO – Dimethyl sulfoxide

DOT – dioxidoterephthalate

DUT-6 – Zn_4O(2,6-ndc)$(btb)_{4/3}(def)_{16}(H_2O)_{9/2}$

HKUST-1 – Hong Kong University of Science and Technology $(Cu_3(btc)_2(H_2O)_3$

H_3ntb – $N(C_6H_4CO_2H)_3$

IRMOF – Isoreticular metal-organic framework

IRMOF-10 – $M_4O(bpdc)_3$, M: Mg, Zn, Cu

IRMOF-3 – $Zn_4O(BDC\text{-}NH_2)_3$

IRMOF-62 – $Zn_4O(BDB)_3$

M06 – The hybrid functional of Truhlar and Zhao

MCF – (2R,3S,4R,5R)-2-[(8S)-8-hydroxy-7,8-dihydro-6H-imidazo[4,5-d][1,3]diazepin-3-yl]-5-(methylsulfanylmethyl)tetrahydrofuran-3,4-diol.

MIL-100 – $Fe_3O(H_2O)_2(OH)(btc)_2.nH_2O$

MIL-101 – $Cr_3OF(bdc)_3$

MIL-53 – M(OH)(bdc) (M = Cr, Al)

MIL-88 – $Fe_3O(MeOH)(bdc)_3$

MOF – Metal-organic framework

MOF-177 – $Zn_4O(btb)_2$

MOF-200 – $Zn_4O(BBC)_2$; BBC: 4,4′,44″-benzene-1,3,5-triyl-tribenzoate

MOF-210 – $(Zn_4O)_3(BTE)_4(BPDC)_3$

MOF-5 – $Zn_4O(bdc)_3$

MOF-505 – $Cu_2(bptc)$

MOF-74 – M_2(2,5-DOT), M: Mg^{+2}, Zn^{+2}

MONs – Metal organic nanosheets

NDC – 2,6-naphthalenedicarboxylate

NU-100 – Cu_3(TTEI); TTEI: 5,5′,5″-(((benzene-1,3,5-triyl-tris(ethyne-2,1-diyl))tris(benzene-4, 1-diyl))tris(ethyne-2,1-diyl))triisophthalate

PBE0 – Perdow-Borke-Emzerhof exchange correlation functional

PCN-6 – $Cu_3(TATB)_2(H_2O)_3$

RRKM theory – Rice-Ramsperger-Kassel Marcus theory

TATB – triazine-2,4,6-triyl-tribenzoate

UiO-66 – $Zr_6O_4(OH)_4(bdc)_6$

UiO-67 – $Zr_6O_4(OH)_4(bpdc)_6$

UMCM-1 –University of Michigan Crystalline Material-1.

UMCM-150 –$Zn_4O(bdc)(btb)_{4/3}$

WB97XD – Head-Gordon and coworkers including empirical dispersion

ZTF-1 – Zeolitic tetrazolate Framework

λ – lagrangian multipliers

ρ – Electron density

Φ – Spatial function

Ψ – Wave function

Abstract

In this thesis, the properties of Metal-Organic Frameworks are investigated using theoretical methods in general and density functional theory in particular. These materials have interesting properties due to the interplay between the pores and the material itself, making them of use in e.g. adsorption of harmful gases.

The first set of MOFs studies focus on so-called Zinc paddlewheels and zirconium oxo-clusters. In particular, the adsorption properties of these materials with respect to a range of gases are investigated. Our studies show that the choice of functional and in particular the inclusion or exclusion of dispersion effects can have a significant impact on the adsorption of gases, particularly for those gases that bind quite weakly, the impact on strong binders, like e.g. CO_2 is much smaller. We also show that the local environment for the building blocks of the MOF are crucial as well. In particular, amine side chains are shown to be very effective in capturing CO_2. Finally, the presence of water is shown to be significant as well, particularly in the adsorption of nitrogen gas, where it enhances binding in many cases. However, for CO_2 adsorption the situation is more ambiguous.

The second set of studies focusses on the predictive capability of computational methods in regard to the generation of photoelectron spectra and nuclear magnetic resonance spectra, applying these techniques to copper paddlewheel and zirconium oxo-clusters, respectively. In both cases some success can be recorded. However, in both cases the predictive power of the methods is limited and more work is needed to resolve this properly.

Finally, our final set of calculations focusses on exfoliation in copper paddlewheel compounds. Here, the importance of side chains on the paddlewheel linkers is shown, particularly in relation to the analysis of the final structure through IR spectroscopy and the

calculation of IR spectra. It is also shown that the relative stability of the resultant structures is influenced by the nature of the side chains. Hereby, amine-based sidechains lead to more likely binding of the side-arms, whereas methoxy and mercapto groups allow axially bonded solvent molecules to be retained in the final exfoliated structure. The final calculated IR spectra show a reasonable agreement with the experimentally obtained ones, whereby in particular the large conformational freedom of the side-arms is highlighted as a potential reason for any discrepancies.

Contents

Author's Declaration 1
Acknowledgment 3
List of Abbreviations 4
Abstract 7
Contents 9
Chapter 1: Gas adsorption in metal-organic frameworks 1
1.1: Introduction 1
1.2: Porous Materials 1
1.3: Historical perspective 5
1.4: Metal-organic frameworks 9
1.4.1: General properties of metal-organic frameworks 10
1.4.2: Common microporous coordination polymers 12
1.4.3: Gas adsorption applications of metal-organic frameworks 19
1.4.3.1: Gas storage, and gas separation 19
1.4.3.2: Adsorption of gases 23
1.4.3.3: Carbon dioxide adsorption 24
1.4.3.4: Hydrogen adsorption 27
1.4.3.5: Methane adsorption 29
1.4.3.6: Adsorption of other gases 30
1.5: Theoretical aspects of gas adsorption 30
1.5.1: Physisorption and chemisorption 30
1.5.2: Measurement of gas adsorption characterisation 32
1.6: Challenges facing storage of gases using metal-organic frameworks 34
1.7: Problem statement and research objectives 36
Chapter 2: Computational Methods 37
2.1: Classical models 37
2.2: Quantum mechanical methods 40
2.2.1: Schrödinger equation 41
2.2.2: Born-Oppenheimer approximation 44
2.2.3: Variational principle 46
2.2.4: Hartree-Fock method 47

2.2.5: Density functional theory....58
2.3: Implementation of structure methods....64
2.3.1: Basis sets....67
2.3.2: Natural Bond Orbital (NBO) Theory....73
2.4: Conclusions....79
Chapter 3: A Theoretical Study of Gas Adsorption in series of Metal-Organic Frameworks....80
3.1: Introduction....80
3.2: Metal-Organic-Frameworks (MOFs)....80
3.3: Bonding Considerations in MOFs....83
3.4: DFT Methodology and Calculations....83
3.5: Application of DFT to Study Gas adsorption in Series of Metal-Organic Frameworks....84
3.5.1: Adsorption of Carbon Dioxide by Simple Zinc Paddlewheel Compounds....84
3.5.1.1: General Overview....85
3.5.1.2: Computational Details....87
3.5.1.3: Results and Discussion....87
3.5.2: Zirconium-based MOFs....93
3.5.2.1: General Overview....94
3.5.2.2: Defects in Zirconium based MOFs....95
3.5.2.3: Calculations on Zirconium metal organic frameworks....101
3.5.2.4: Results and discussion....108
3.5.3: Calculation of the Binding Energy for Carbon Dioxide Using Other Methods....120
3.5.4: Binding Energies of Carbon Dioxide and Nitrogen in the Presence of Water Using DFT:....121
3.6: Conclusions....129
Chapter 4: Computational analysis of spectroscopic data....131
Part 1: Natural Bond Orbital Calculations of Copper Paddlewheel Systems....131
4.1: Introduction....131
4.2: X-Ray Photoelectron Spectroscopy as an Analytical Technique....131
4.3: Computational Details....137
4.4: Results and Discussion....137
Part II: Calculations of NMR Chemical Shifts of Molybdenum Atoms....143
4.5: Introduction....143

4.6: Gauge Invariance Problem and Computational Error....146
4.7: Computation Methods....148
4.8: Computational Details....150
:4.9 Results and Discussion....155
4.10: Conclusions....162
Chapter 5: A Theoretical Study of the structure of the Exfoliation in Copper paddlewheel systems (2D)....163
5.1: Introduction....163
5.2: Layered Materials and Exfoliation....163
5.3: Layered Metal-Organic-Frameworks....164
5.4: Exfoliation....165
5.5: Results and discussion....170
5.5.1: Copper Methoxypropoxy benzoate systems [(Cu_2(**1**)(sol)$_2$], and [(Cu_2(**1***)(sol)$_2$]....175
:5.5.1.1 Calculation of the relative binding energies of solvent molecules for [Cu_2(**1**)$_4$(sol)$_2$] and [Cu_2(**1***)$_4$(sol)$_2$]....181
5.5.1.2: Infra-red spectra for [(Cu_2(**1**)(sol)$_2$], [(Cu_2(**1***)(sol)$_2$]....183
5.5.2: Copper methylaminopropoxy benzoate systems[(Cu_2(**2**)(sol)$_2$]....193
5.5.2.1: Infra-red calculations for [(Cu_2(**2**)(sol)$_2$]....197
5.5.3: Copper methylmercaptopropoxy benzoate systems [(Cu_2(**3**)(sol)$_2$]....201
5.5.3.1: Infra-red calculations for [(Cu_2(**3**)(sol)$_2$]....206
5.5.4: Comparison of binding energies in the three different ligands of copper systems [Cu_2(L)$_4$$X_2$]....209
5.6: Conclusions....211
Chapter 6: Conclusion and Future work....213
References....218
Appendix....238

Chapter 1: Gas adsorption in metal-organic frameworks

1.1: Introduction

This chapter presents the current state of research on porous materials, i.e. materials with a large surface to volume ratio. In particular, it will discuss gas adsorption in metal-organic frameworks, highlighting details of metal-organic frameworks synthesis, structural characteristics, and adsorbent characteristics.

1.2: Porous Materials

Porous compounds have long attracted the attention of chemists and physicists, because of their nanometre-sized spaces, which have interesting properties. Moreover, these materials have commercial application in separation, storage, and heterogeneous catalysis. Until the mid-1990s, two types of porous materials were mainly investigated: inorganic materials such as zeolites and carbon-based materials.[1] To quote Zhao: [2] "Porous materials are like music: the gaps are as important as the filled-in bits". The pores (holes) give the materials many useful properties compared to non-porous materials. This is qualified by the "porosity" of a material, which is volume ratio of pore space to the total volume of the material. Porous materials have a porosity between 0.2-0.95.[3] In general, there are two different types of pores: open pores, which connect to the surface of the material, and closed pores, which are isolated from the outside, (see figure 1-1). To facilitate the application of certain theoretical principles, a pore's shape is often supposed to be cylindrical, but this is rarely an accurate description of a real system. In fact, with some materials, it is more realistic to picture the pores as slits or interstices between spheroidal particles.[3] Pores can be straight or curved or with many turns and twists. The shape of these pores measured by the "tortuosity" (ratio of the average pore length to the

length of the porous medium along the major flow or diffusion axis used to describe diffusion in porous media).[4, 5] Tortuosity values typically range from 2–6.

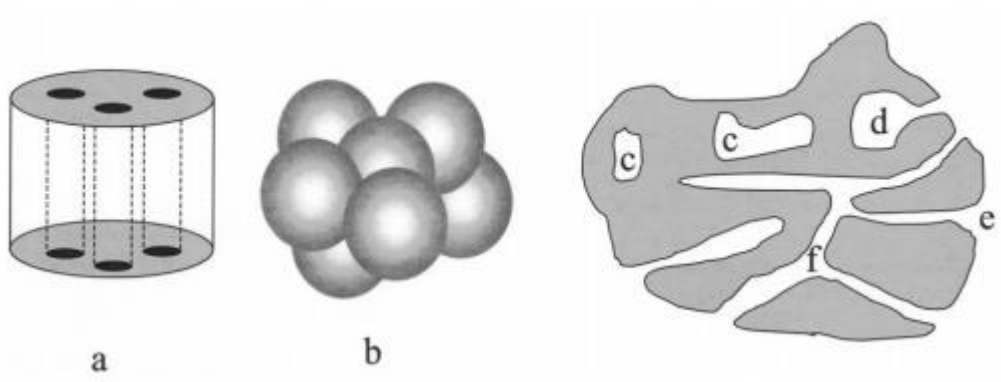

Figure 1-1: Idealized pore structures (a) cylindrical pores; (b) voids between packed spheres and schematic boundary structure showing (c) closed latent pores; (d) ink bottle; (e) funnel; and f open pores. Reproduced with permission from Ref 6**.**

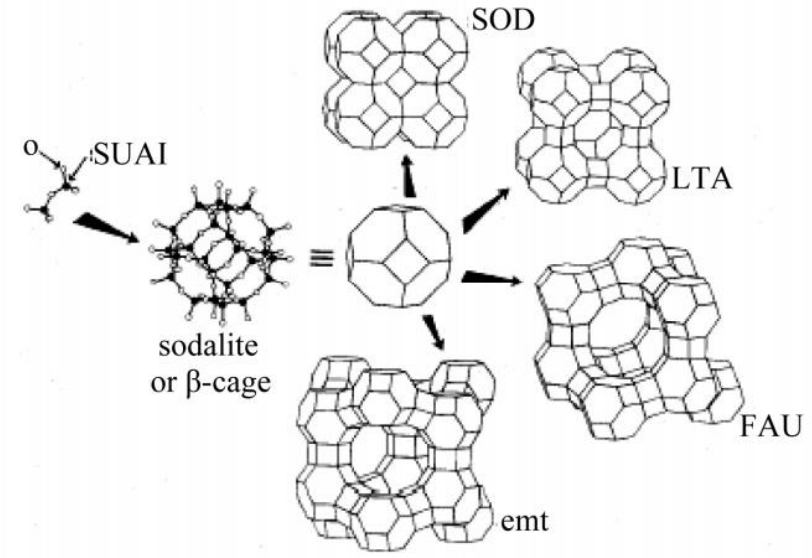

Figure 1-2: Building up zeolites structure. Reproduced with permission from Ref 7.

A particular well studied group of porous materials are zeolites, (see figure 1-2). Zeolites are aluminosilicate solid materials, which form through crystallization. There are many types of

zeolites. In general, they have relatively loosely bound cations in their lattice. They have a wide range of applications. For example, they can undergo cation-exchange and can be used to absorb species.[8]

Zeolites can absorb organic and mineral-based molecules in gaseous form without having to modify their structure. Zeolites have a high specific surface area of 40 to 800 m^2/g and also have hydrophobic-hydrophilic surfaces that affect their structure. Therefore, zeolites are used in industries as gas-treatment agents and also as a means of reducing bad odour in the production of some molecules. Some types of zeolites have a high affinity for water, reaching an adsorption capacity of 30% without any volume modification.[9] The ability of such zeolites to regenerate at high pressure and temperature make them important in industrial humidity stabilization. The separation of gases, as well as their purification through selective adsorption, is amongst the many other things zeolites are used for. This technique is essential in the chemical, medical, petrochemical, and gas industries.[10]

Porous adsorbents such as zeolites offer a wide choice as core adsorbents to be used in industry in gas separation and gas purification. Moreover, the discovery and creation of synthetic zeolites has made it possible to optimize them for gas drying and removal of toxic gases and heavier organic components, e.g. zeolites type A, X, and Y, which are synthesized from coal fly ash.[11,12] Gases with impurities, which are detrimental for certain chemical reactions, are purified using zeolites. Indeed, there is a growing use of zeolites and derivatives of zeolites in the purification industry, because they lower the cost and energy required for the separation of gases.[13] The primary advantage of zeolites in an industrial setup is the possibility to use zeolite membranes; this increases the surface area for the adsorption of the gases more economically than other gas separation and purification approaches.[14] Desorption from zeolites can be traditionally carried out by heating the zeolites to obtain the product gas in a thermal desorption

process. On the other hand, in a pressure-swing adsorption process the separation of the adsorbed gas from the zeolites is carried out through the lowering of the pressure, which results in the release of the gas from the zeolites, regenerating the original zeolites.[2]

Zeolites most used in gas separation are mordenite, chabazite, and clinoptilolite, which have hydrophilic properties, making them ideal for gas adsorption. The separation of gases by zeolites is made possible through three different properties and characteristics of zeolites. Firstly, zeolites use size, or steric exclusion. This refers to the ability of the zeolite's pores to accommodate some gases, which are adsorbed, whereas others cannot enter the pores. Secondly, the thermodynamic properties of zeolites lead to adsorption of certain gases over others, despite the ability of all gases to enter the pores. Lastly, kinetic selectivity is the ability of certain gases to enter the pores of the zeolites faster and be adsorbed, which limits the available space for the adsorption of other gases. Because of these properties, zeolites have been referred to as molecular sieves. The molecular size of the adsorbate molecules and the size of the pore openings in the zeolites make it possible for different zeolites to be used for the separation of different gases.[15]

Thus, the strength and selectivity of zeolites as an adsorbent depends on the size, shape, and structure of the zeolite's cavity as well as their cationic density. Other factors that affect the selectivity of zeolites include the permanent polarity and polarizability of the guest adsorbate molecules. Therefore, more polar molecules will be adsorbed by zeolites that have a larger cation density and smaller pores. The high strength and the selective adsorption of certain molecules is crucial for the removal of the trace impurities from a gas.[16]

It is important to note here that the discussion so far has presented zeolites as perfect crystals, which are physico-chemically homogeneous. Indeed, theoretically, they are often treated as such. However, commercial zeolites for use in gas separation can be heterogeneous as a result

of lateral defects, the presence of hydrated or dehydrated cations at different locations within the framework, non-uniform hydrolysis of the framework during regenerations, the variation in the silica/alumina ratio, and the presence of trace amounts of moisture. Heterogeneity can also be introduced by the binder phase as a part of pelletized zeolites.[17]

Zeolites may be one of the most heavily studied porous materials, but they are certainly not the only ones. Another important group of porous materials is formed by so-called metal-organic frameworks (MOFs) and their two-dimensional equivalents, Metal Organic Nanosheets (MONs) (see chapter 5). These are compounds comprising metal ions that are coordinated to organic ligands [for example 1,4-benzendicarboxylate (BDC)] in order to form 2D or 3D structures. The special feature of these coordination polymers is that they are inherently porous.[18] So far, over 70,000[19] different metal-organic frameworks have been identified and studied within the last 20 years. Organic units used in the preparation of the metal-organic frameworks are often either di-topic or polytopic organic carboxylates. However, other chemical substances with negative molecular charges may also be used for the same purpose.[18]

1.3: Historical perspective

Before MOFs are discussed in detail, it is important to note that coordination network materials have a long history. Some of these compounds have been used in the leather tanning process for centuries. When tanning a hide, Chromium(III) ions are incorporated into the hide's collagen, which results in collagen-metal ions crosslinking via olation.[20] It is through this crosslinking that these complex chromium coordination compounds help with resistance to decay and weathering of the treated hides. Another well-known historical coordination polymer is iron hexacyanoferrate(II,III) (Prussian Blue).[21] This polymer ($Fe_4[Fe(CN)_6]_3 \cdot xH_2O$) contains iron linked by the cyanide ligands in a 3D framework, (see figure 1-3). Of course, these coordination polymers were made by accident. Rational design formulation of molecular

organic frameworks only really took off when advanced chemical techniques paved the way for their formation.[22]

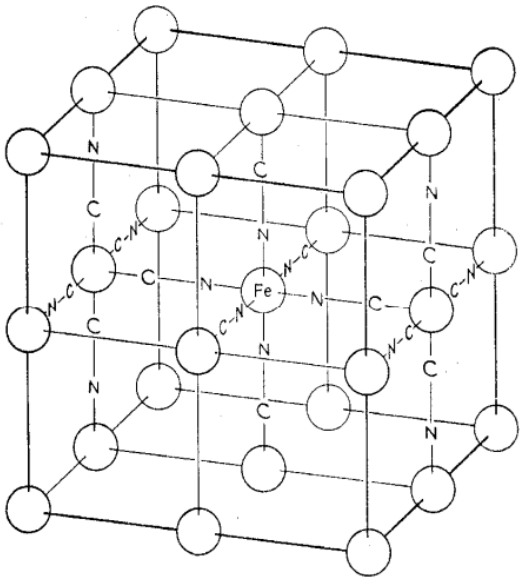

Figure 1-3: The unit cell of Prussian blue. Reproduced with permission from Ref 21. Copyright (1962) American Chemical Society.

The first porous coordination polymer (metal-organic framework) was reported by Hoffman *et al*. They reported on the synthesis of $[Ni(CN)_4Ni(NH_3)_2] \cdot C_6H_6$,[23] whose structure was later elucidated using X-ray diffraction.[24] This polymer contains extra-framework benzene between these layers. Therefore, one can describe this as a metal-organic framework, since benzene occupies what could be classed as a pore. Effective description of metal-organic frameworks started in the 1990s. For example, in 1990 the first fully-described coordination polymer was studied by Hoskins *et al*.[25-27] In their paper, they describe the 3D structure of coordination polymers as well as their characteristic porosity and catalytic activity. In 1995, the design, as well as synthesis of a layered material, was described by Yaghi *et al*. This paper used pyridine, cobalt (II) , and 1,3,5-benzenetricarboxylate.[28] The resultant material displayed an ability to selectively and reversibly adsorb aromatic compounds, which paved the way for

exploration of the potential for alteration by modifying the functionality of the frameworks. These developments have led to massive expansion of the field.[29]

Adsorption using porous materials has a long history as well. It was used already in antiquity. In fact, the ancient Egyptians, Romans, and Greeks utilized the adsorbent features of wood charcoal, sand, and clay to do e.g. water desalination, treatment of diseases, and clarification of fats. Indeed, some forms of charcoal are well-known to take up large volumes of gas. Charcoal has also been shown to exhibit decolorizing properties. This has been studied extensively for a long time. The first heat of adsorption measurements of various gases on charcoal was reported by Favre in 1854.[3]

The first modern scientific description of adsorption of hydrogen gas by carbon only happened in 1909.[30] In this case, the process was demonstrated to be a two-stage process, starting with a rapid stage of adsorption. This precedes a slow stage, which occurs in the solid's interior. In 1916,[31] adsorption of molecules on liquid and solid surfaces was described as a process that ends up in in the creation of a monomolecular layer. The publication of Brunauer-Emmett-Teller (BET) theory in 1938[32] was a crucial development in the fundamental description of adsorption. It highlighted the relative importance of physisorption and chemisorption in the overall process of adsorption at the molecular level. This theory paved the way for the studies of the significance of the surface area to volume ratio of the solid adsorbent materials in the adsorption of gases. Improvements have been made, because more adsorbents have been studied and because of better analysis techniques.[33]

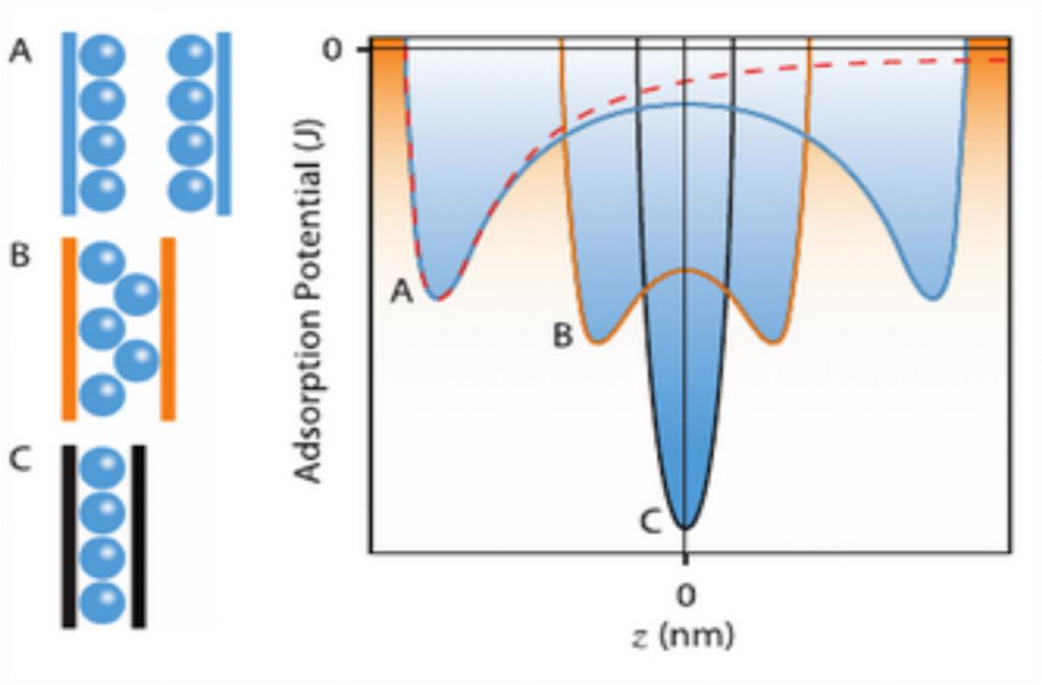

Figure 1-4: Adsorption potentials vs pore sizes, z represents the distance from the central plane between the two surface. Reproduced with permission from Ref 33.

In recent years, in particular, there has been a dramatic increase in the number of metal-organic frameworks available, making it possible to develop new materials for gas storage, separation, as well as purification. The classes of metal-organic frameworks developed recently have unique properties in terms of structural flexibility, pore structures, as well as tunable surface chemistry. These properties offer the potential for future applications – for example, high-pressure supercritical methane or hydrogen storage and transportation applications.[34] In addition, another area of application that is likely to feature prominently is carbon capture/storage, and separation of gas mixtures, such as xylenes/ethylbenzene,[35] acetylene/ethane,[36,37] alkanes/alkenes such as ethane/ethane,[38] and benzene/cyclohexane.[39] Different industrial separation processes will also be affected by the development of new nanoporous materials. This is an area, which is currently largely unexplored. Moreover, understanding the behaviour of gas adsorption will likely open ways to store gases from natural

reservoirs in geological formations.[40] It is through such applications that coordination polymers will contribute to the fight to reduce the natural causes of greenhouse effects all over the world and potentially reduce the problems associated with global warming.

1.4: Metal-organic frameworks

As mentioned above (section 1.2), these materials are made of metal ions that are assembled into an extended porous host structure that is held together by organic ligands. Thus, the bonding between the metal ion and the linker results in a porous structure. On the other hand, the incorporation of functional groups such as amino, thio, halogen, carboxy, nitro, and cyano groups on the organic linker allows the tuning of the structure in order to accommodate adsorption of some gases over others.

Metal-organic frameworks can be described as structures with joints and struts, where the joints represent metal-oxide polyhedra, which offer the points of extension that control the framework's geometry. On the other hand, the struts represent the polydentate organic ligands, for example, imidazolates, pyridine, and carboxylates – the common nitrogen and oxygen donors. A strut can be take a particular shape or size, have a specific number or position of donor atoms, and rigidities. In a framework, the inorganic or the organic components determine the one-, two or three-dimensional formations displayed. Often, the structures of the metal-organic frameworks are compared to those of zeolites because of the shared similarities in terms of their extended networks with microporous structures. In fact, some metal-organic frameworks have pores of a mesoporous range of between 2 and 50 nm.[41]

In order to understand the distinct details of the structures of MOFs, it is important to describe both the physical characteristics as well as the functional properties exhibited by a typical coordination polymer. In this case, it is also important to describe connectors/linkers and motifs. As mentioned above, a typical coordination polymer has two central components,

linkers and connectors. The principal framework of the coordination polymer is constructed with these starting reagents. They are augmented by such auxiliary components as counterions, template molecules, and blocking ligands.[1] The most commonly used group of connectors used as components of coordination polymers consists of transition-metal ions. The transition-metal ions commonly used in coordination polymers have coordination numbers of 2 to 7, as influenced by their oxidation state, and normally give rise to such geometries as tetrahedral, pentagonal-bipyramidal, square-planar, Y-/T-shaped and octahedral forms. For example, silver and copper ions have different coordination numbers and geometries. These can be realized by altering the reaction conditions of the ligands, counterions, and solvents. New as well as unusual network topologies can be formed by using lanthanide ions of coordination numbers above 7. Moreover, it is recommended to use metal-complex connectors instead of naked metal ions because of the formers' ability to control the bond angles as well as restrict the number of coordination sites, which frees specific sites for linkers.[1] If the product is a linear chain, it is referred to as a 1D motif. In this case, silver ions are known to form linear chains when combined with different linear linkers. This phenomenon is explained by Ag(I) affinity for a coordination number of two.[42] On the other hand, if the product is a square-grid network it can be termed a 2D metal-organic motif. Moreover, if the product exhibits tetrahedral nodes, it can be termed a 3D motif. A good example of a 3D motif is $\{[Zn(nicotinate)_2].MeOH.2H_2O\}_n$. It contains a $4^2 \cdot 8^4$ topology and tetrahedral nodes, which is a consequence of self-assembly of the 4-connected nodes under mild conditions.[43]

1.4.1: General properties of metal-organic frameworks

As already mentioned, one of the major characteristics of metal-organic frameworks is that they are a product of coordination between organic linkers and inorganic metal ions.[44] As

a result, they exhibit more complex mechanical properties when compared with any other inorganic porous materials – such as, zeolites and perovskites. For example, they have variable chemical interactions – such as strong coordination bonds, weak hydrogen bonds, and weak dispersion forces – which contribute to their high structural flexibility in response to uniaxial stress, hydrostatic pressure, as well as temperature.[44] Some metal-organic frameworks have the capability to undergo reversible or irreversible amorphization under the influence of mechanical stress.[45] Indeed, some metal-organic frameworks can undergo drastic pressure-induced phase transitions and striking rearrangement of bonds.[46,47] Moreover, metal-organic frameworks have pores that are capable of hosting different guest molecules, including solvents and gases, which generally influence the general mechanical behaviour of the metal-organic frameworks. These properties generally result from the blend of both the chemical and the physical properties of the constituent organic and metallic components of the metal-organic framework.[44] The mechanical properties of metal-organic frameworks are also enhanced using MOF-based composites, which promotes synergy between MOFs and inorganic nanomaterials leading to a variety of mechanical properties.[48]

Most metal-organic frameworks are rigid, which means that they experience no framework dimensional changes even after the removal of solvent molecules in the absence of mechanical pressure. However, there exists a group of metal-organic frameworks that exhibit distinctive structural changes under the influence of pressure, temperature or gas adsorption variations which contribute to the reversible expansion and contraction properties of the framework.[49,50] The MIL-88 and hydrated MIL-53 families show so-called this breathing effect. The linker has two separate carboxylate groups. Rotation occurs about the O···O vector of each carboxylate group, leading to a massively increased porosity of the material.

Manipulation of the size/morphology changes how these metal-organic frameworks could be used. Moreover, manipulation of the frameworks gives rise to crystals, composites,

and films/membranes.[52] The nanosized crystals of these materials result in particles that are suitable for diffusion-based applications. They are also used in the development of films and membranes. Manipulation of both the crystal size and morphology involve the modulations of such factors as the temperature programme, compositional process parameters, additives, and reverse micro emulsions.

Some of the compositional parameters that can be modulated as a way of tuning the size as well as the shape of metal-organic framework crystals include pH, reactant concentration, solvent, metal source, and the reactant's molar ratio. The process parameters of interest when tuning the size and shape of the metal-organic framework's crystals include pressure, time, heating source, and temperature. For example, the temperature programmes involved influence the crystal growth rates and the relative nucleation of the metal-organic framework crystals. On the other hand, additives influence the formation of the metal-organic framework crystals by stopping crystal growth and adsorbing on some crystal faces, which ultimately modulates the overall size and morphology of the crystals.[52] There are a variety of compositional and process parameters for different metal-organic frameworks that are prepared both at the micro- and the nanoscale levels.[52] For example, preparation of MOF-5 can be achieved at room temperature, or by applying ultrasound (US) irradiation, micro-wave (MW) radiation, and conventional electric (CE) heating.

1.4.2: Common microporous coordination polymers

Today, there are many examples of metal-organic frameworks. These materials are receiving increasing attention because of their potential applications. A few examples will be described below.

Commercially available metal-organic frameworks include UiO-66 and UiO-67. UiO-66 and UiO-67 belong to a group of metal-organic frameworks developed by combining

$ZrO_4(OH)_4$ with 1,4-benzene-dicarboxylate in case of UiO-66 and 4,4′ biphenyl-dicarboxylate in case of UiO-67.[53] The two metal-organic frameworks are both physically and chemically stable in the presence of high pressures, acids, bases, high temperatures, and a variety of solvents.[54] These MOFs are used in industry as catalysis and gas separation.

A number of MOFs, as mentioned below are used for liquid phase adsorption. One such MOF is MOF-5.[55] It contains Zn^{+2} metal ions that are linked together by 1,4-benzenedicarboxylate to form a three-dimensional cubic structure, (see figure 1-5). The BET surface area of MOF-5 is 3800 m^2/g.[56]

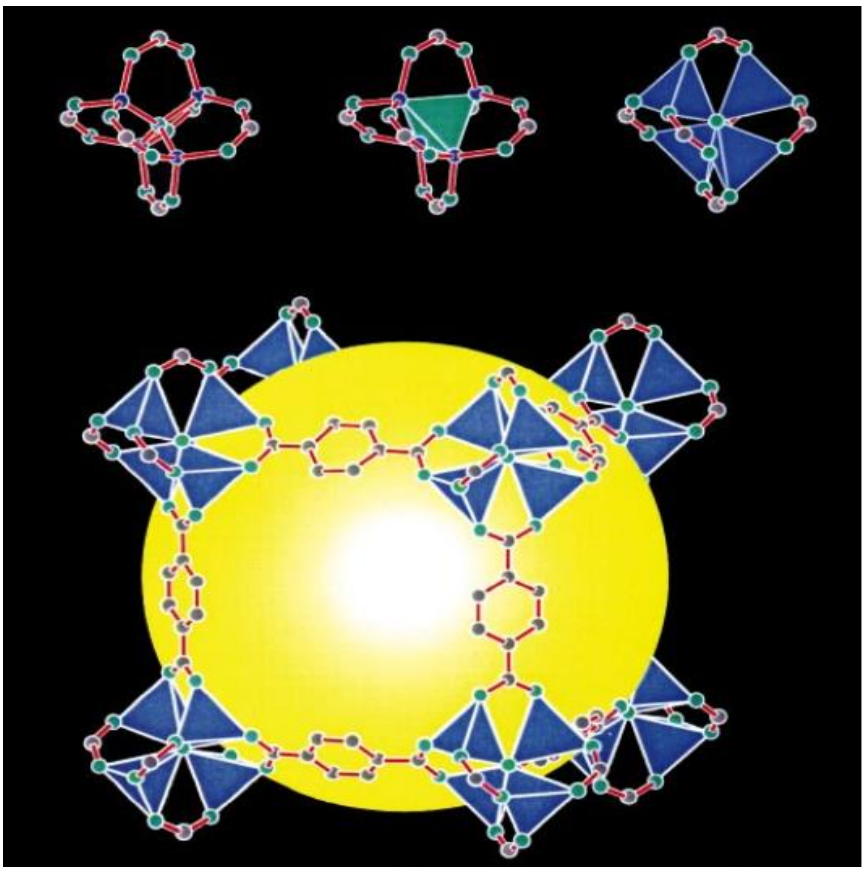

Figure 1-5: Crystal structure of MOF-5. Top, the $Zn_4(O)O_{12}C_6$ cluster. Left, as a ball and stick model (Zn, blue; O, green; C, grey). Middle, the $Zn_4(O)$ tetrahedron indicated in green. Right, the ZnO_4 tetrahedra indicated in blue. Bottom, one of the cavities in the $Zn_4(O)(BDC)_3$, MOF-5, framework. A large cavity, indicated by a yellow sphere. Reproduced with permission from Ref 55.

Another well-studied metal-organic framework is HKUST-1, [57] (see figure 1-6), which is an example of a copper-based metal-organic framework. This metal-organic framework contains metal clusters that are linked together by 1,3,5-benzenetricarboxylate. HKUST-1 is also known commercially as BASOLITE C 300 produced by BASF. It has a BET surface are of 1900 m^2/g. HKUST-1 is used for several applications, including liquid phase adsorption, gas phase adsorption, catalysis, and as a prototype for copper-based metal-organic frameworks.[58]

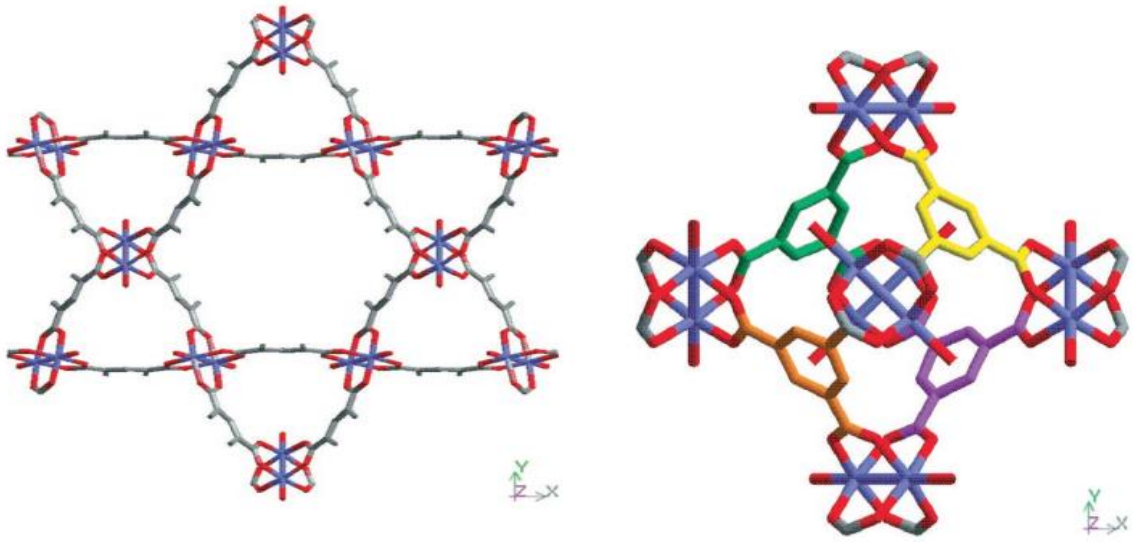

Figure 1-6: Crystal structure of HKUST-1(left), Secondary building unit for $[Cu_3(TMA)_2(H_2O)_3]_n$, TMA: benzene-1,3,5-tricarboxylate, viewed along the [100] direction. The Cu_2 dimers bridge to other such SBUs (right) (nomenclature taken from ref 57). Reproduced with permission from Ref 57.

MOF-177 is another example to highlight; (see figure 1-7).[59] This metal-organic framework has been described as the best microporous coordination polymer (MCP) for the storage of hydrogen as it has an uptake of 7.5 wt%.[60] This material has basic octahedral zinc carboxylate clusters that are linked to each other by 1,3,5-(triscarboxyphenyl)benzene. It has a BET surface area of 4700 m^2/g and a pore volume of 1.59 cm^3/g. It has a pore aperture that is sufficiently big to allow C_{60} to diffuse freely.

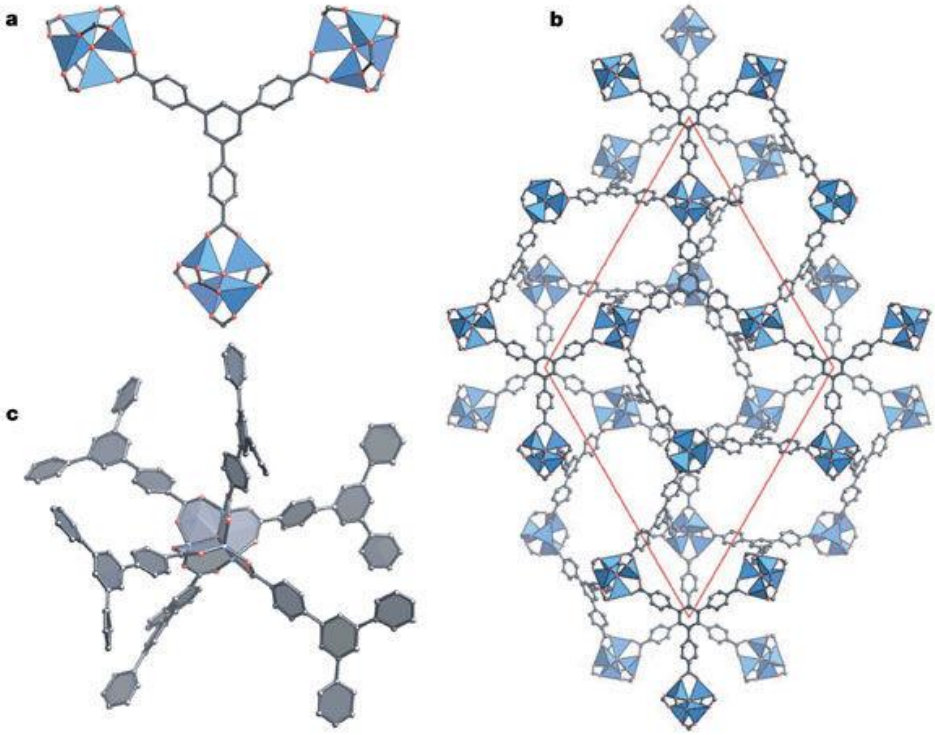

Figure 1-7: Crystal structure of MOF-177. a, A BTB unit linked to three OZn_4 units. b, the open three-dimensional structure of composition $Zn_4O(BTB)_2$. c, the structure of MOF-177 is entirely constructed of six-membered C_6H_4, C_6H_3 and OZn_2CO_2 rings. Reproduced with permission from Ref 59.

A fifth example to highlight is MOF-505, (see figure 1-8). This metal-organic framework is generally used for hydrogen adsorption. It is also used as a prototype for the generation of other metal-organic frameworks. It is produced by reacting copper nitrate with 3,3',5,5'-biphenyltetracarboxylic acid.[61] In its structure, MOF-505's copper paddlewheel metal clusters form two different size/shaped pores with a surface area of 1670 m^2/g.[62]

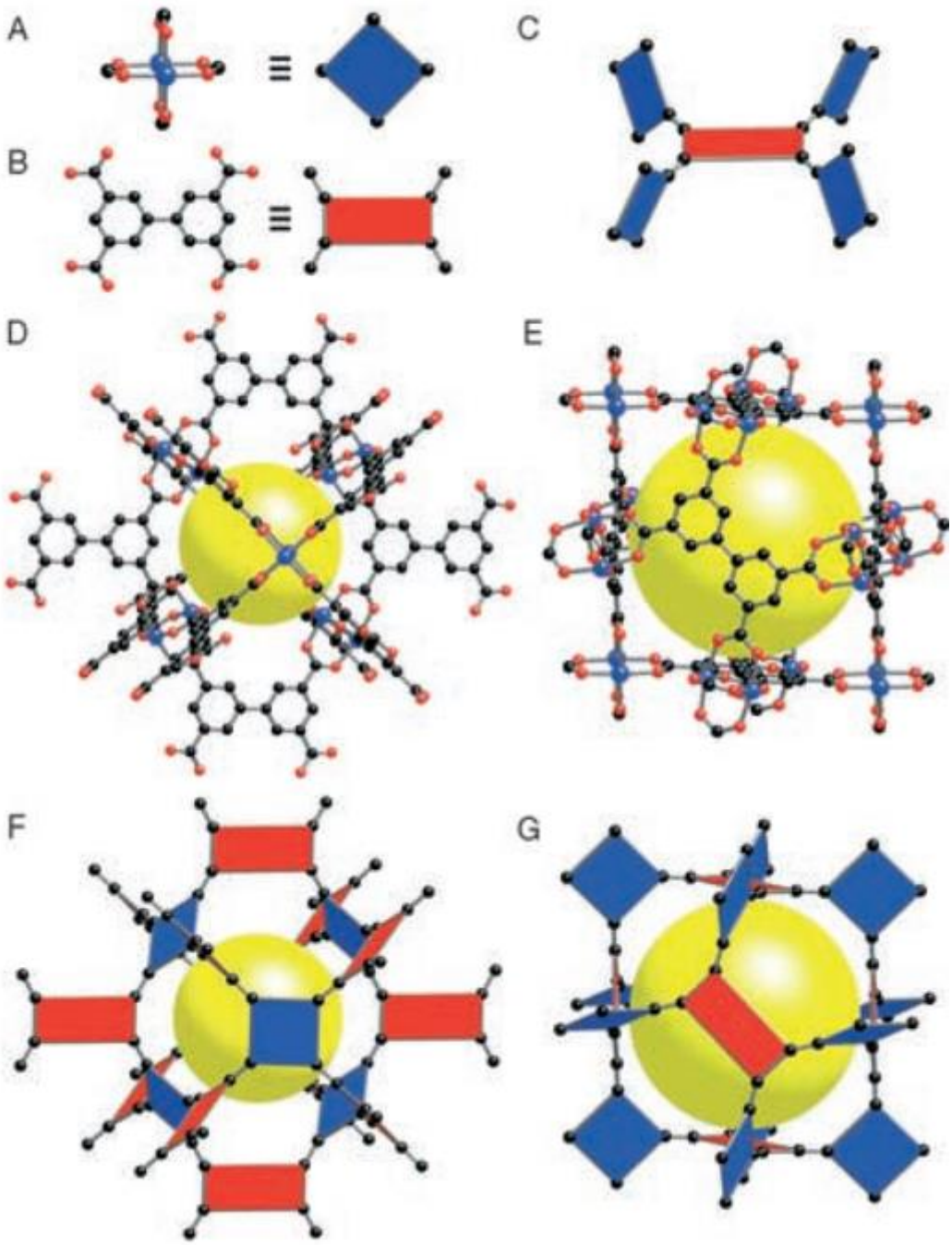

Figure 1-8: Crystal structure of MOF 505. A) $Cu_2(CO_2)_4$ units (blue, square SBUs) and B) $bptc^{-4}$ units (red, rectangular SBUs) that are C) orthogonally joined. The overall 3-periodic crystal structure (D,E); Cu blue, C black, O red, and the yellow sphere has two different types of pores and an underlying net (F,G). Reproduced with permission from Ref 61.

A sixth example is UMCM-150, (see figure 1-9), which is also commercially available. This material is primarily used for hydrogen storage as its uptake increases with increase in pressure.

Its basic unit contains a copper paddlewheel as well as copper trinuclear clusters that are linked together through 3,4′,5-biphenyltricarboxylate.[63] This MOF results from an organic linker that is unsymmetrically substituted. The structure possesses a BET surface area of 2300 m^2/g and forms two different copper metal clusters as well as three types of cages.

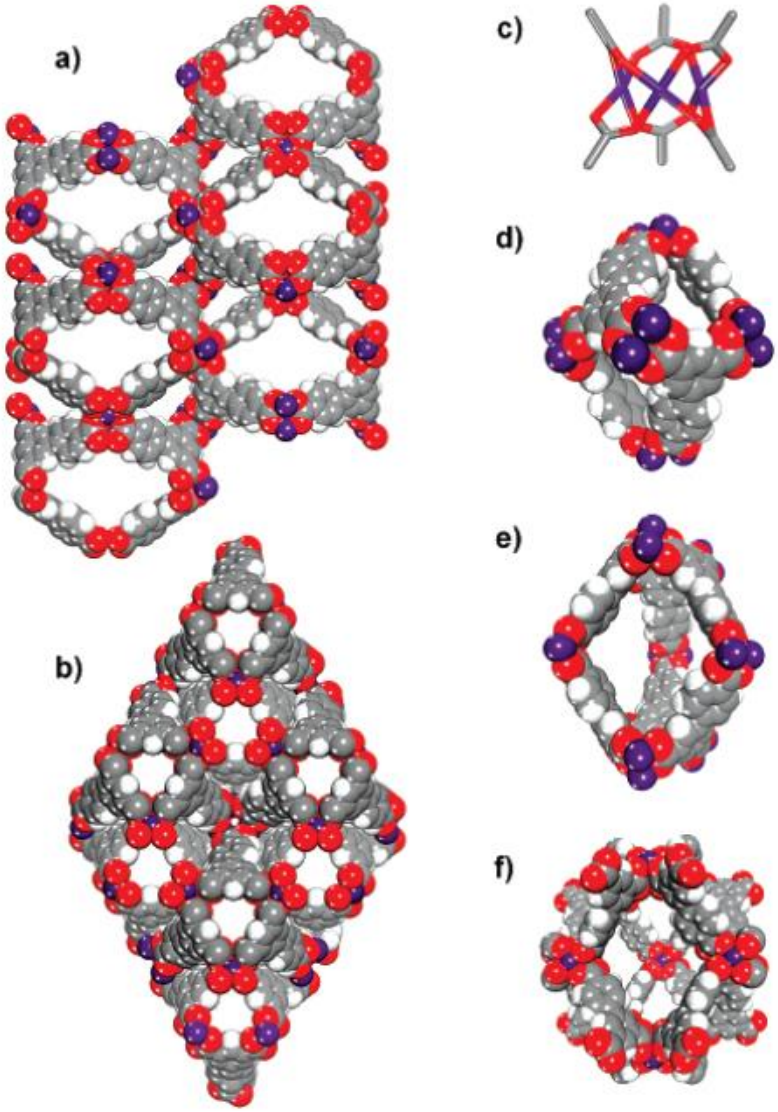

Figure 1-9: Crystal structure of UMCM-150. **(a)** Unit cells of the crystal structure of UMCM-150. C atoms (dark gray), H atoms (white), O atoms (red), Cu atoms (purple). **(b)** View along the *c*-axis. **(c)** Detail of a $Cu_3(O_2CR)_6$ cluster. **(d)** Hexagonal bipyramidal cage formed by six molecules of 4 linked by eight Cu clusters. **(e)** Trigonal bipyramidal cage formed by six molecules of 4 linked by nine Cu clusters. **(f)** Cage formed by twelve molecules of 4 linked by nine Cu clusters. Reproduced with permission from Ref 63.

Another metal-organic framework that is commonly used in gas adsorption is MIL-100, (see figure 1-10).[64] The compound is formed by reacting chromium(IV) oxide with 1,3,5-benzenetricarboxylic acid. MIL-100's surface area is 3100 m^2/g; [65] its pores contain three distinct pores whose dimensions are different. Of the three different pores, two are mesoporous. Some of the gases that have been demonstrated to be taken up by this material include hydrogen sulphide, [66] hydrogen, [67] methane, [68] and carbon dioxide.[69]

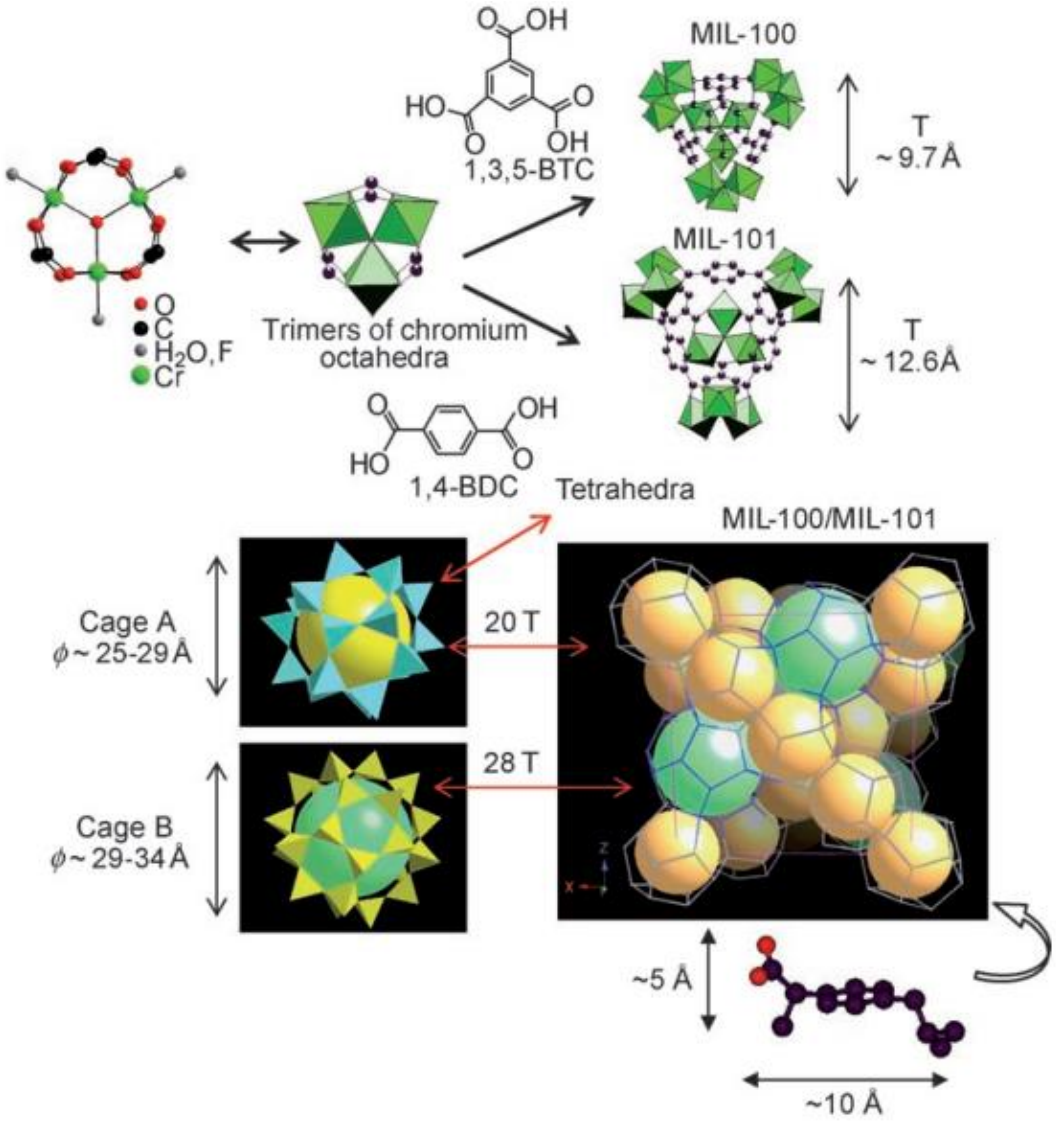

Figure 1-10: Top: Schematic 3D representation of the tetrahedra (T) built up from trimers of chromium octahedra and 1,4-benzenedicarboxylate moieties or 1,3,5-benzenetricarboxylate groups in MIL-101 and MIL-100, respectively. Reproduced with permission from Ref 64.

A final example of an extensively studied metal-organic framework is MIL-101. MIL-101 is a mesoscopic metal-organic framework that contains chromium terephthalate as the primary constituent,[70] (see figure 1-10).[64] Among the MIL series of metal-organic frameworks, MIL-101 stands out as it has a record carbon dioxide uptake of 40 mmol/g at 50 bar and 303 K. The material also has a high level of uptake of other gases such as methane. The structure of MIL-101 exhibits a high stability as a function of temperature. It resists attack by organic solvents and is stable under solvothermal conditions. As a result, it has attracted interest for use as an agent in catalysis, gas storage, and drug delivery.[64]

1.4.3: Gas adsorption applications of metal-organic frameworks

1.4.3.1: Gas storage, and gas separation

Like purely inorganic porous materials, metal-organic frameworks attract much interest as potential materials for use in the adsorption of gases as is clear from the discussion in section 1.4.2. However, metal-organic frameworks offer several advantages over porous inorganic materials. One of the advantages is the large pore volume of MOFs. Most metal-organic frameworks have pore volumes of at least one ml/g, while others (for example, DUT-6[71] and UMCM-1[72]) have pore volumes of more than 2 ml/g. Another advantage is the high surface area of MOFs. Many of them possess a surface area of more than 2000 m^2/g, and UMCM-2[73] possesses a surface area higher than 5000 m^2/g. Another advantage of MOFs is their pore size is adjustable. Thus, it is possible to get a variety of pore sizes, including mesoporous cages (for example, offered by DUT-6, MIL-101[70], and UMCM-1) and microporous channels (for example, in IRMOF-1[55] and Cu-BTC[74]). One of the classic examples of metal-organic frameworks with an adjustable pore size is the IRMOF series,[75] which comprises of dicarboxylate ligands of different lengths and Zn-O-C clusters.

Thus, MOFs show a large diversity of architecture, as shown in their geometry, and topology, as evidenced by crystallography. Furthermore, the metal-organic frameworks have many organic parts, which allows for easy post-synthesis modification. Overall, these advantages make metal-organic frameworks versatile for materials.

Indeed, more new MOFs structures are published every year compared to any other class of porous materials. The primary application of gas adsorption of metal-organic frameworks includes storage of methane, hydrogen, as well as selective gas adsorption. The interest in the use of metal-organic frameworks as storage methods for hydrogen gas has come from the increasing realisation that the supply of fossil fuels is limited in an era when energy-intensive machines have taken over. This makes it necessary to investigate the use of alternative energy sources, such as hydrogen. However, efficient use of hydrogen-powered machines is highly dependent on the presence of safe, efficient, and economic systems of storing hydrogen. Such factors influence the use of metal-organic frameworks as storage methods for hydrogen as the pore sizes, surface area/volume ratio, ligand functionalization, catenation, and unsaturated metal centres can all be changed.[76] In general, large pore sizes have a characteristic low hydrogen adsorption capacity, which is explained by the high surface area to volume ratio, which results in weak interactions between hydrogen molecules and the framework. Thus, by reducing the pore sizes, it is possible to enhance the uptake of hydrogen by the framework.

Another way to do this is through ligand functionalization. This affects not only the general properties of metal-organic frameworks, but also e.g. the hydrogen adsorption capacity. Increasing hydrogen adsorption capacity means it is necessary to increase the aromaticity of the organic ligands, by using such aromatic linkers as naphthalene, biphenylene, and phenylene in the 3D porous framework. Catenation (interpenetration; see figure 1-11) influences the capacity of a metal-organic framework in the adsorption of hydrogen by influencing the pore size. In this case, the use of longer linkers favours catenation. On the other hand, this reduces

the pore sizes leading to a consequent reduction in the surface area to volume ratio and enhancement of the hydrogen uptake by the framework. However, when choosing the extent of catenation, it is necessary to remember that catenation often helps the formation of stable as well as porous crystalline structures.[76]

Furthermore, it appears to that the impregnation of unsaturated metal centres into metal-organic frameworks results in the enhancement of the material's capacity to adsorb hydrogen. This is attributed to the nature of metal ions in porous MOFs.[77] The remarkable hydrogen adsorption capacity of unsaturated metal centres has been shown by an increase in the uptake of hydrogen gas by up to 20% in PCN-6 at one atmosphere.[78]

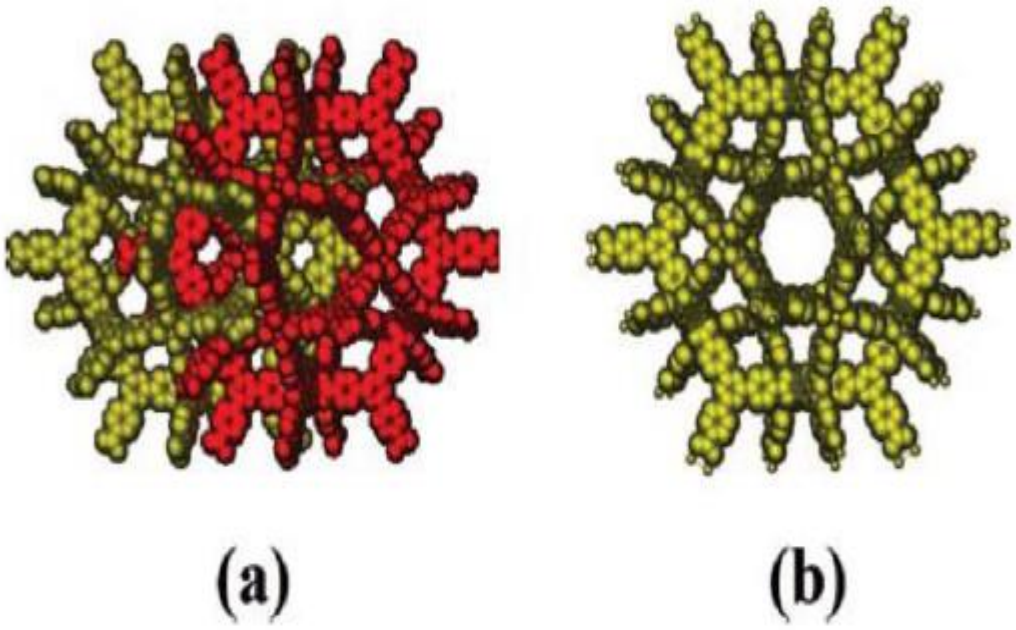

Figure 1-11: Catenated PCN-6 (a) and noncatenated PCN-6(b). Reproduced with permission from ref 79. Copyright (2008) American Chemical Society.

MOFs are also used to investigate storage of methane. Similar to hydrogen storage, interest in the use of metal-organic frameworks to store methane is a product of methane's potential use as an alternative source of energy to petroleum, because of its high energy content and low-carbon-emission potentials.[76] Metal-organic frameworks exhibit a high adsorption

capacity for methane gas, and as a result attract much interest for that purpose. Like hydrogen storage, storage of methane gas in metal-organic frameworks is influenced by several factors, including heat of adsorption, ligand functionalization, pore size, and surface area.

A third application of metal-organic frameworks in this area is selective gas adsorption. In this case, the frameworks are used for the separation of gas mixtures such as nitrogen/oxygen, carbon dioxide/hydrogen, and nitrogen/methane.[80,81] The basic principle behind this molecular sieving effect is to allow a molecule of an appropriate size/shape to enter open channels of the framework and excluding others.[76] Since the apertures of the metal-organic frameworks can be modulated, it is possible to promote selective adsorption of some gas molecules leading to molecular sieving. For example, by utilizing short bridging ligands, it is possible to restrict the pore sizes of organic molecular frameworks in line with the size of the target gas molecules. For example, if the metal-organic framework comprises of microporous $Mg_3(NDC)_3$, a magnesium based 2,6-naphthalenedicarboxylate MOF,[82] it is possible to have a selective uptake of hydrogen or oxygen over nitrogen or carbon dioxide. Also, it is possible to achieve a similar molecular sieving effect using a 2,4-pyridinedicarboxylate-based cobalt metal-organic framework to separate carbon dioxide from methane, oxygen from nitrogen/argon, and hydrogen from nitrogen.[83]

According to Eddaoudi et al.[75] isoreticular metal-organic frameworks can be designed with pore sizes suited for the storage of specific gases, for example, the storage of methane gas. In this case, the pore size of the MOFs built using octahedral Zn-O-C clusters and benzene can be expanded using long struts such as pyrene, tetrahydropyrene, biphenyl, and terphenyl to allow for the storage of methane gas.[75]

The pore size of metal-organic frameworks is also utilized in kinetic separation. Here, a MOF derives its usefulness from its ability to cause differential diffusion of gases through the framework. For example, in the case of chromatographic separation of gases, different

gases diffuse at different rates leading to the accumulation of different bands of gases with different diffusion characteristics. A good example of this application is the separation of different hexane isomers during petroleum processing.[84] However, for example, kinetic separation of propane and propylene, is complicated as these chemicals exhibit relatively similar volatilities and molecular sizes.[84] Another way to perform selective gas adsorption is through mesh-adjustable molecular sieves, MAMS. The first mesh-adjustable molecular sieve, MAMS-1, was constructed using 5-tert-butyl-1, 3-benzenedicarboxylate as a ligand.[76] A variable- temperature gas adsorption studies on MAMS-1 indicated that it displayed a temperature-dependent molecular sieving effect. Thus, the overall ability to attain a specific size of the mesh allows for molecular separation of gases.[85]

In the same vein, some metal-organic frameworks have a high capacity as well as a selectivity for harmful gases, which allows one to use them in their separation. These metal-organic frameworks include IRMOF-62, MOF-199, MOF-5, MOF-74, and IRMOF-3. They are capable of adsorbing gases such as ammonia, sulfur dioxide, carbon monoxide, ethylene oxide, benzene, tetrahydrothiophene, and dichloromethane. Some of these metal-organic frameworks have adsorption capacities of about 35 percent by weight.[86]

1.4.3.2: Adsorption of gases

Adsorption refers to the solid substances' capability to attract gas or liquid molecules to their surfaces. In this case, solid substances act as adsorbent materials while the liquid or gaseous substances are referred to as adsorbates. This process involves both chemical and physical processes, and the result is a major change in the concentration of a specific gas at the interface relative to the neighbouring phases.[87]

1.4.3.3: Carbon dioxide adsorption

The application of metal-organic frameworks for carbon dioxide storage has drawn significant interest due to the rising amounts of carbon dioxide in the atmosphere. MOFs are seen as effective carbon dioxide storage materials, since they have a large internal surface area and polar functional groups that increase the capacity of to take up carbon dioxide gas.[88] For example, MOF-210 has an internal surface area of 10,450 m^2/g and a high carbon dioxide uptake value of 2400 mg g^{-1}. Thus, it exceeds any other possible candidate. Indeed, MOF-210 offers a possible solution to carbon emission crisis by offering to store the gas and possibly dispose of it in a more environmentally friendly manner. Other examples of MOFs likely to be used in carbon dioxide storage include BioMOF-11, ZTF-1, MOF-200, HKUST-1, NU-100, MOF-5, and Mg-MOF-74.[88]

The adsorption and uptake of carbon dioxide in metal-organic frameworks depends on the pore size, the pore volume and its surface. Most metal-organic frameworks have a higher pore volume and surface area than zeolites or activated carbon, which explains the higher uptakes for MOFs. Typically, adsorption of carbon dioxide in rigid porous materials such as zeolites gives a type-I isotherm or in isolated cases, stepwise isotherms are observed. For example, in the case of MCF-19,[89] adsorption of carbon dioxide at low temperature adsorption occurs in a two-step process, while a similar stepwise adsorption of carbon dioxide, which gives sigmoidal isotherms, is observed especially if the metal-organic frameworks in the question have ultrahigh pores like in the cases of MOF-5, MOF-177, IRMOF-1and MOF-210 [90,91], (see figure 1-12).

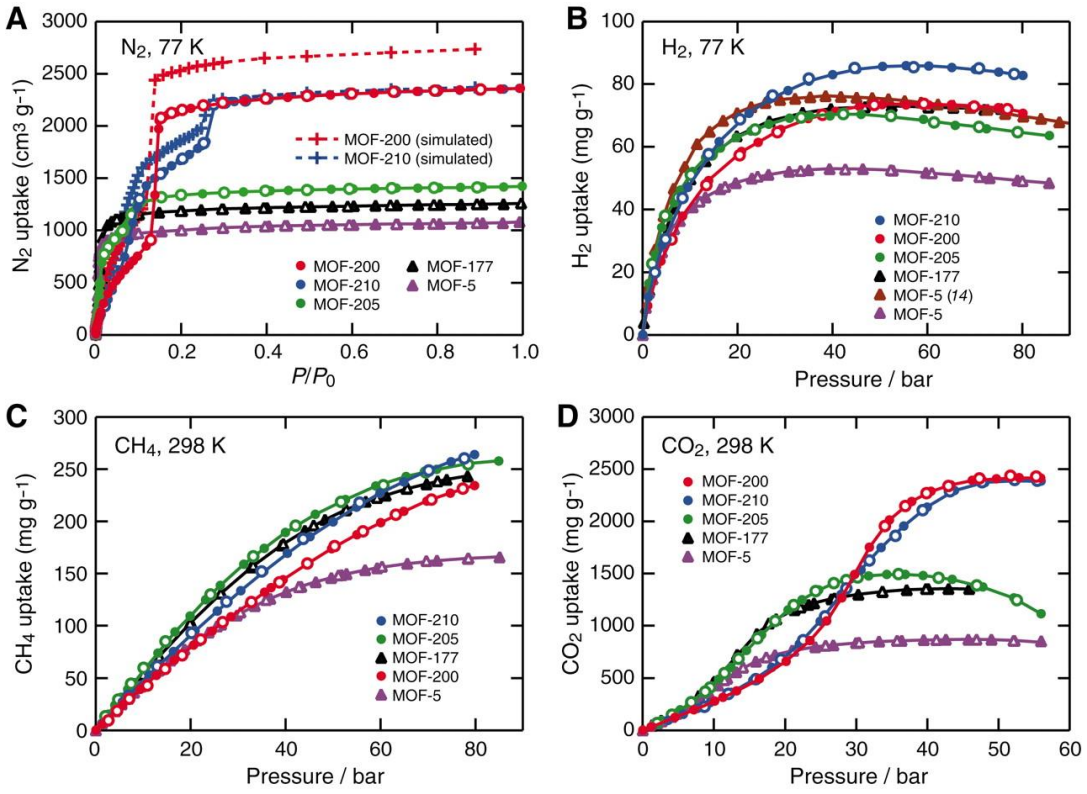

Figure 1-12: **(A)** Low-pressure N_2 isotherms of MOF-5, -177, -200, -205, and -210 at 77 K. Simulated isotherms of MOF-200 and -210 were overlaid. P/P_0, relative pressure. High-pressure H_2 isotherms were measured at 77 K **(B)**, **(C)** CH_4 and **(D)** CO_2 isotherms were measured at 298 K of the same MOFs. Reproduced with permission from Ref 91.

On the other hand, flexible MOFs normally exhibit stepwise adsorption isotherms for carbon dioxide. It is through this flexibility that some metal-organic frameworks exhibit both selective adsorption and separation of gas molecules.

The adsorption of carbon dioxide in metal-organic frameworks can be tuned by using different metal ions. In this case, metal ions influence the shrinkage/expansion of the structure and the gas adsorption properties. For example, the addition of cobalt ions to MOF-5-based materials results in an increased capacity to adsorb carbon dioxide.[92] The adsorption of carbon dioxide in metal-organic frameworks is also influenced by the adsorption sites as well as adsorption modes. In an amino-triazolate framework, $Zn_2(Atz)_2(ox)$, two independent adsorption sites exist – one near to the oxalates and the other one near the free amine group.[93] The interaction

of CO_2 with an amine could be via N-H···O hydrogen bonding or via the N lone pair and the C atom of CO_2. In an X-ray crystallographic study (see figure 1-13) it was found that one of CO_2 molecules was adjacent to the amine, with the electropositive C atom oriented toward the electronegative N atom [C(δ+)···N(δ –) = 3.151(8) Å; the other CO_2 was located between oxalate groups. Here, O(δ^-) of CO_2 interacts with the C(δ^+) of the oxalate [O(δ^-)(CO_2)…C(δ^+)(Ox) = 2.961(5) Å].

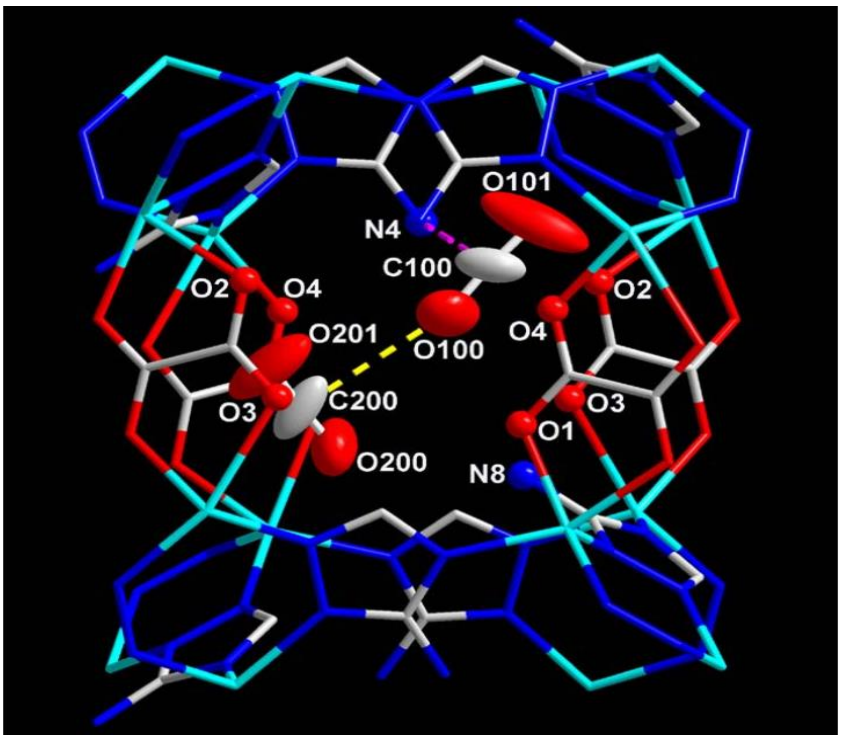

Figure 1-13: Structure of two crystallographically independent CO_2 molecules trapped in a pore. The CO_2···NH_2 interactions are represented as dotted purple bonds, while the CO_2···CO_2 interactions are indicated as dotted yellow bonds. Reproduced with permission from Ref 93.

Co-adsorption of carbon dioxide has been studied extensively using several techniques. Experimentally, it has been demonstrated that carbon dioxide-rich and equimolar carbon dioxide-methane mixtures result in a structural transition of MIL-53-Al from the large pore configuration (LP) to the narrow pore configuration (NP), before going back to the LP form after an increase in pressure. However, methane-rich mixtures result in a constant LP

framework. Consequently, the closing, as well as the opening of the structure, is dependent on the partial pressure of CO_2 with just a weak dependence on the partial pressure of methane. In fact, in some experiments, adsorption of methane gas was shown not to happen in the NP-form.[94]

The capability to adsorb gases selectively is the primary determinant of the ability of the metal-organic frameworks to separate them. In most cases, the material's selectivity factor is calculated using ideal adsorbed solution theory[95] or the single component isotherms.[96] In general, the selective adsorption of carbon dioxide instead of methane or nitrogen in rigid metal-organic frameworks is described to be a product of a favorable gas-pore surface interaction and size exclusion. Thus, separation occurs based on physical properties and size of gas respectively. For example, the kinetic diameter of carbon dioxide is smaller than those of nitrogen and methane, and its quadrupole moment is larger **(**CO_2, 13.4 x 10^{-40} $C.m^2$; N_2, 4.7 x 10^{-40} $C.m^2$; CH_4, 0 $C.m^2$). As a result, CO_2 has stronger interactions with the adsorbents' pore surface. Studies of the selectivity of carbon dioxide over nitrogen in modified metal-organic frameworks, for example, $Zn_2(bttb)(CF_3\text{-}py)_2$ (bttb = benzene-1,2,4,5-tetrayltetrabenzoic acid py = pyridine), have shown that its selectivity increases with pressure, because of the high polar CF_3 group which attracts CO_2 more than N_2. Often under these conditions, it surpasses the selectivity reported for such materials as carbon adsorbents and zeolites.[97]

1.4.3.4: Hydrogen adsorption

Adsorption draws significant attention in relation to hydrogen storage, since MOFs could be used to transport hydrogen.[98]

There are two different ways of measuring hydrogen adsorption. One of these is by gravimetric measurements, which is a direct method of adsorption measurement. The

gravimetric measurements involve correlating the sample with its equivalents. The other method consists of volumetric measurements, which allows for the indirect measurement of the known amounts of gas in a sample. Both of the two methods are reliable and robust methods of measuring hydrogen adsorption.[99]

It is difficult to characterize the porous structure of materials, because some MOFs are flexible. Different techniques and methods are used to characterize the porous structures by the use of a variety of isotherm equations and adsorptives.[99] At high pressure, an increase in the size of pores is related to a comparable increase in the amount of gas absorbed by the structure. However, at the atmospheric pressure the level of adsorption is minimal. [100,101] The hydrogen adsorption on the surface of porous materials is highly limited by the weak interactions between hydrogen and the adsorbent surface (weak physisorption). This attraction between the adsorbent surface and the adsorbate weakens further with an increase in the temperature of the contents. However, one of the advantages of metal-organic frameworks is a wide range of surface chemistry, which include open metal centres and hydrophobic surfaces, which are associated with the linker ligands.[102]

Seven factors influence adsorption of hydrogen in metal-organic frameworks. One of these factors is sample preparation, as it is most important to obtain repeatable as well as reliable data. Some of the sample preparation factors that influence the metal-organic framework's capacity to take up hydrogen are purity and activation. This has been shown for e.g. HKUST-1.[103] Therefore, any impurity phases contained within the pore should be eliminated by activation. Other factors that influence adsorption of hydrogen in metal-organic frameworks are chemical doping and spillover. In particular, chemical doping can increase the energy of binding between hydrogen and metal-organic framework. For example, Li^+ has shown a strong affinity for hydrogen.[104] Indeed, lithium-decorated MOF-5 exhibits a higher hydrogen binding capacity compared to free MOF-5.

The third factor that influences the capacity of metal-organic frameworks to adsorb hydrogen is the existence of unsaturated metal sites. Here, exchange of coordination polymers with coordinatively-bound guest particles result in a higher hydrogen binding affinity than without exchange. The fourth factor that influences the adsorption of hydrogen in metal-organic frameworks is the structure of ligands and their functionalization. In this case, the size, as well as the shape of the ligand, influences the uptake of hydrogen. The fifth factor is catenation, which influences pore size, which in turn influences the rate of adsorption of hydrogen gas. In this case, a high level of catenation is associated with a high rate of adsorption. The last two factors are pore size and geometry, which influences the adsorption and surface area to volume ratio, where a large pore size has a small surface area to volume ratio, which in turn decreases the ability of the material to adsorb hydrogen gas.[101]

1.4.3.5: Methane adsorption

The interest of the use of metal-organic frameworks as a storage medium for methane is rapidly developing because of the increased industrial use of methane gas, especially in the automobile industry. Here, the primary goals are to introduce strong interaction sites and a large accessible surface area to accomplish a high methane uptake. Generally, these goals are achieved by modifying organic linkers. So far, there are over 300 metal-organic frameworks that have been reported to be of importance for the storage of methane gas as a result of their good gas adsorption properties.[105]

One exemplar MOF used in the storage of methane gas is IRMOF-6, which adsorbs a higher volume of methane compared to all other members of the IRMOF series. This is caused by the functionality and the surface area of the ligand used in IRMOF-6.[106] In particular, an IRMOF-6 unit has been modified at the phenyl ring of the bdc ligand in order to form 1,2-cyclobutane-3,6-butane-3,6-benezenedicarboxylate. The result is a porous MOF that has an

uptake of 240cm^3/g of methane at room temperature (298 K) and 36 atmospheres,[75] larger than any other metal-organic frameworks or any zeolites.

1.4.3.6: Adsorption of other gases

If we consider gases other than those already mentioned, then it should be mentioned that it is possible to use MOFs to adsorb toxic gases and reduce their concentration in the atmosphere. Some of the gases primarily targeted include sulfur dioxide (SO_2) and ammonia (NH_3), as they are generally regarded as high-hazard gases. The two gases cannot be filtered effectively using activated carbon filters, because of their weak chemisorption strength. As a result, metal-organic frameworks appear to be the best alternative adsorbent. Other gases targeted this way, include carbon monoxide, ethylene oxide, chlorine, and dichloromethane, because of their obvious implications for public health.

Finally, research has recently been carried out to investigate the use of metal-organic frameworks in the adsorption of gases like oxygen.[86] Adsorption of oxygen in MOFs results a reduction of its storage pressure with obvious advantageous safety implications. The interest in the development of MOFs for oxygen adsorption results from the need to store and concentrate oxygen for use in industrial processes, aerospace industries, and health care settings, amongst others.[107]

1.5: Theoretical aspects of gas adsorption

1.5.1: Physisorption and chemisorption

Adsorption refers to the phenomenon resulting from interactions between fluidic molecules and solid phase particles leading to the movement of the fluidic molecules along the particles of the solid support phase. There are two types of adsorption involved in this movement, and they include physical adsorption (physisorption) and chemical adsorption

(chemisorption).[3] In general, the forces behind physisorption are the same forces that influence the transition from the gas to the liquid phase. These forces also cause the deviations from ideal gas behaviour. On the other hand, the forces involved in chemisorption are the same as involved in chemical reactions, leading to the formation of compounds. As a result, there are several fundamental differences between chemisorption and physisorption.

One of the differences between physisorption and chemisorption is that whereas chemisorption depends on the reactive characteristics of the adsorbent and the adsorbate, physisorption does *not* depend on the chemical characteristics of the adsorbent material and the adsorbate. Thus, by being a more general phenomenon, physisorption has a significantly lower degree of specificity. Another difference is that chemisorption, i.e. the linking of the reactive parts of the adsorbent and the surface, is generally confined to a monolayer, while on the other hand physisorption may involve multiple layers, especially if the process involves high pressures.[3] Moreover, physisorption is differentiated from chemisorption by the fact that in the former both the adsorbate and the adsorbent demonstrably retain their identity at the end of the process. Chemisorption is more energetic than physisorption. In fact, it involves a similar amount of energy as the comparable chemical reaction. Another difference is that chemisorption can involve an activation energy, and as a result, if the system is at low temperature it could have not enough energy to attain the thermodynamic equilibrium. On the other hand, physisorption does not generally involve an activation energy. As a result, physisorption processes tend to attain equilibrium fast, even though a rate-determining transport process may limit accomplishment of this equilibrium.

During adsorption, when a molecule interacts with the solid surface, it seeks to establish a balance between the intermolecular repulsive and attractive forces. Once the other molecules have been absorbed, the process is influenced by both adsorbent-adsorbate and adsorbate-adsorbate interactions. The process may include intricate energy dynamics, but for

physisorption, the interactions are dominated by short-range repulsion and the attractive dispersion interactions, which are non-specific and not dependent on the polar characteristics of the adsorptive or the adsorbent. The first theory of these attractive dispersion interactions was developed by London in 1930. In this theory, the interactions were described as a result of rapid fluctuations of the atomic electron density, creating an electrical moment in the nearby atoms. Adsorption is highly dependent on these attractive interactions, which dictate the amount of energy released by the system during adsorption. The amount of heat evolved during adsorption is referred to the molar heat of adsorption

1.5.2: Measurement of gas adsorption characterisation

Different materials exhibit different adsorption behaviours. As a result, it is important to have accurately measured data in order to facilitate research-led discovery or development of adsorbent materials. The description of both the physical and chemical properties of adsorbent materials in relation to their effects on the thermodynamics as well as the kinetics of the process of adsorption could act as an effective guide to the process of the development of metal-organic frameworks.[33] In this case, the techniques used for the measurement of single component adsorption are different from those employed for multiple component adsorptions. Single component measurements are conducted by determining the adsorption isotherms – the graphs that indicate the adsorption of a specific gas against pressure at constant temperature. When isotherms are analysed, it is possible to establish the capacity of materials and determine the enthalpy of adsorption at zero surface coverage, and as a result, it provides the measure of the adsorbent-adsorbate interaction.

Generally, when measuring gas adsorption, there are four typical methods that can be used. These methods include the pulse adsorption method, the dynamic method, the gravimetric

method and the volumetric method. However, the gravimetric and volumetric methods are the most widely used techniques in gas adsorption measurements.[33]

A typical apparatus used in the volumetric method has components such as a vacuum system, valves, and pressure systems.[108] A typical gravimetric apparatus comprises a magnetic suspension balance and a pressure sensor. On the other hand, both the pulse adsorption apparatus and the dynamic method have a detector (Thermal Conductivity Detector) as the most important component.

Single components are also measured by using volumetric and gravimetric techniques. In this case, one of the commonly used volumetric techniques is the manometric method. In this method, it is possible to determine the sorbed quantity of the gas by monitoring pressure changes in a fixed volume system.[33] In this indirect method, gas is dosed into a sample cell from a calibrated volume, followed by the calculation of pressure drop (in the absence of adsorption) by the ratio of the dosing volume against the total system's dead volume. After this, reduction in pressure is said to be a product of adsorption and its magnitude can be calculated using a molar balance expression. The gravimetric method, on the other hand is a direct method of making single component measurements by utilizing a microbalance, where measurement begins at vacuum – meaning that any weight gain experienced with an increase in pressure is a result of adsorption.

In addition, the two methods are important in determining the adsorption kinetics. For the gravimetric approach, it is possible to perform kinetic measurements under isobaric conditions to give data that can be used in the derivation of the diffusion equation, the stretched exponential,[109-111] the linear driving force,[112] and the double exponential models.[113]

The use of N_2, Ar, and CO_2 adsorption for the determination of pore volumes and pore size distributions includes the measurement of adsorption at sub-ambient pressure using a manometric apparatus.[114] However, this approach faces several challenges, including the

potential for experimental error,[115-117] the presence of impurities, and error propagation. At high pressures, there are two primary practical issues that influence the measurement of single component adsorption. These include the real (rather than ideal) behaviour description of the gas and the determination of the solid's volume.

Similarly, multicomponent adsorption can also be measured using the volumetric and the gravimetric techniques, even though it is necessary to employ other methods as well to determine the specific amounts adsorbed. There are different gravimetric approaches available.[33] For example, closed systems accomplish the adsorption measurement by circulating the mixture through an adsorbent bed, followed by analysis of the composition of the gas phase after equilibration. On the other hand, open systems generally involve the equilibration of the adsorbent bed with a mixture of gases before calculating the amount of the each adsorbate component by a molar balance expression or desorbing and analysing all the compositions of the bed. It is also possible to combine the volumetric and the gravimetric techniques to determine the total adsorption. However, this approach requires the molecular weights of the adsorbates under investigation to be different. The most important challenges facing the application of this method is the determination of the concentration of specific gases contained as part of the adsorbed phase. Besides, techniques applied in this approach are laborious, as measurements of such parameters as composition, temperature, and pressure require equilibration for each data point, which is time-consuming.[33]

1.6: Challenges facing storage of gases using metal-organic frameworks

Metal-organic frameworks face two major challenges with regard to the storage of gases, particularly carbon dioxide. The first challenge is its capacity for carbon dioxide uptake. Different metal-organic frameworks have different capacities for carbon dioxide uptake. Thus,

it requires assessment of every candidate to establish their capacities and validate their suitability for the purpose. The second challenge is the selectivity of the materials. Some materials are highly selective for a specific gas, which means that designing a microporous material only attracts interests of application in a particular gas over the others. Other challenges of importance with regard to the uses of metal-organic frameworks in gas adsorption include stability towards contaminants, the cost of design, and flexibility in terms of shaping.[118]

Most metal-organic frameworks have high levels of instability after exposure to water vapour. This hampers their large-scale applications in gas adsorption as well as in the separation of such gases as carbon dioxide, methane, and hydrogen, which often have a significant water content. The coordination bond existing between the metal secondary building unit and the ligands is relatively weak, which makes metal-organic frameworks susceptible to water molecules. Generally, the effects of water attack include structural collapse due to adsorption of water, leading to decreased gas adsorption capacity. Some of the metal-organic frameworks that have been studied with regard to their interactions with water include MOF-74. These metal-organic frameworks interact with water molecules at the ligand nodes leading to the displacement of the ligands and/or hydrolysis of the metal-oxygen groups. It has also been established that both stability and decomposition reaction pathway of the metal-organic frameworks after exposure to water molecules is dependent on their structure as well as the specific metal cations present in their basic units.[88]

The exposure of MOF-5 to water results in the protonation of its BDC linker, while the exposure of MOF-177 in water results in the loss of its crystalline structure. These changes have a general impact on reducing the capacity to take up the gas by adsorption.[119] For MOF-5, attack of the water involves the replacement of one of the ZnO_4 tetrahedra with the water oxygen leading to the ultimate release of the ligand. On the other hand, the interaction of water molecules and MOF-5, MOF-74 and IRMOF-10 involve the dissociation of water molecules

into OH^- and H^+ and the subsequent attachment of OH^- and H^+ to Zn^{2+} and the oxygen of BDC, respectively.[119]

1.7: Problem statement and research objectives

Every year new classes of metal-organic frameworks emerge from hundreds of research projects in this area. Characterization of most of these products appears to show advantages for adsorption applications compared to most other porous materials, which increases the general interest in their application in gas adsorption, However, the effectiveness of MOFs as gas adsorption agents remains poorly understood, which limits the choice of the metal-organic frameworks that could be used for adsorption applications with such gases as hydrogen, methane, carbon dioxide, nitrogen, oxygen, and carbon monoxide.

The primary objective of this work is to investigate gas adsorption in metal-organic frameworks. One of the specific objectives of the project is to study the interactions involved in the adsorption of different types of gases in metal-organic frameworks – with specific attention to such forms of attractions as electrostatic interactions, H-bonding and π-quadrupole interactions, and interactions between hydrogen molecules and functional groups. Another specific objective of the project is to explore different linker molecules for their applications in development and tunability of metal-organic frameworks as well as their influence on the gas adsorption characteristics of the microporous material in the question. Finally, this thesis is interested in determining how computational data can be used to elucidate spectroscopic studies on MOFs, in particular those using NMR, XPS, or IR spectroscopy.

Chapter 2: Computational Methods

Computational chemistry is the subfield within chemistry where mathematical methods are combined with the fundamental laws of physics to study processes of chemical relevance, such as the construction, transformation, or the properties of molecules.[120] The range of computational chemical methods is based on a wide range of levels of approximation. At one end of the spectrum are the atomistic models based on whole atoms or rigid molecules in which the species of interest (also referred to as classical models), followed by models that combine classical mechanics with quantum mechanics, and finally the pure by quantum mechanical methods. It is generally observed that, as one proceeds from the classical methods to the quantum mechanical methods, the accuracy and scope increases. However, as a consequance the size of the system that can be studied is reduced.

2.1: Classical models

The empirical classical models, known as 'molecular mechanics', are considered the simplest models for predictive chemistry due to their lack of pretence in elucidating the fundamental nature of molecules.[121] Atomistic (force field) models in general permit internal flexibility within the molecules, whereby there are models that treat molecules as rigid bodies with no internal flexibility. The interactions between these are treated by means of force fields. These force field-based methods are most effectively used in systems, where molecular transformations can be ignored. Hence, these models are commonly only used to study physical transformations such as phase transitions, conformational changes, or docking. The limitation in scope of systems that can be studied is counteracted by the size of systems to which these

methods can be applied. It is for this reason that atomistic methods are employed in molecular dynamics studies, where large molecules or large numbers of small molecules are studied.

The key approximation is the atoms in an atomistic model are treated as classical particles. In a rigid-molecule model, the interactions (energies) between atoms are taken to be the sum of electrostatic and van der Waals interactions.

$$E_{nb} = E_{es} + E_{vdW} \quad (1)$$

These energy contributions are computed as a function of position. The electrostatic energy is obtained through the Coulomb equation, whereas the van der Waals energy is obtained from fitting to more accurate models (and parameterising to simpler form).[122] The van der Waals interaction is considered to be due to the temporary (or instantaneous) dipole-dipole, dipole-quadrupole, quadrupole-quadrupole, and higher-order terms (The van der Waals interaction is known to be an effect of electron exchange and electron correlation). These terms decay as R^{-6}, R^{-8}, R^{-10}, etc., where R is the distance between the particles. The first of the listed terms is the London dispersion force.[120] which decays asymptotically as R^{-6}. At short distances, the interaction is highly repulsive. This combination of a highly repulsive short-range term and a (relatively) slowly decaying long-range term can be expressed in to the Lennard-Jones potential.[120]

$$E_{vdw} = \varepsilon \left(\frac{c_1}{R^{12}} - \frac{c_2}{R^6} \right)$$

In non-rigid methods, the energies of the molecules are computed in terms of the deformations of the bond lengths, internal angles, and torsions (dihedral angles).

$$E_{int} = E_b + E_a + E_t \quad (2)$$

In the simplest methods, the deformations are treated as Hookean springs. Hookean springs increase in energy as the square of the deformation.[120] The bond stretch takes the following form:

$$E_b = k_b(R - R_0)^2$$

Where R_0 is the bond length at equilibrium. In the above, the energy of the deformed bond (stretched or compressed) is given in terms of the bond spring constant k_b (analogous to the classical spring) and the deformation. This harmonic approximation is suitable for most systems of interest. However, the harmonic approximation does not have the correct behaviour in crowded systems or highly elongated systems. In such cases, a Morse potential can be used to describe the correct short-range and long-range behaviour. A similar argument can be made for angular deformations, especially for small deviations from the equilibrium. Some of the high-accuracy models have developed their angular dependence terms by fitting to spectroscopic data.[120]

The more complex models consider cross-interactions of the deformations. The models described above are unable to reproduce the changes that are observed in bond lengths when the associated bond angle is changed, or *vice versa*. This can be seen from the form of the energy expression. Since each term of the energy expression deals with only one geometric parameter, the optimisation would not be able to include the co-operative effects of strain induced on a molecule. Thus, a three-centre interaction takes the general form:

$$E^{ABC} = k^{ABC}(\theta^{ABC} - \theta_0^{ABC})[(R^{AB} - R_0^{AB}) + (R^{BC} - R_0^{BC})]$$

It is readily seen from the above that there is no restraining force in this form of the energy expression. Hence, it is possible to force one of the parameters to decrease inordinately, thereby

reducing the total energy. For this reason, these models tend to suffer from issues of numerical instability.

The classical models described above have a common feature: they treat atoms as indivisible particles with partial charges. Hence, they are unable to account for polarisation effects due to the changes in the chemical environment caused by neighbouring molecules. The immediate atoms and the neighbouring atoms would need to be re-assigned parameters before, during, and after the process. For obvious reasons, electron transfer reactions are beyond the scope of these models. However, bond formation, bond breaking, atomic rearrangement, spectroscopy, and electron transfer represent the bulk of chemical problems. Considering that these problems cannot be modelled using the techniques discussed so far, it is necessary to use more flexible models. Indeed, the essence of chemistry is the rearrangement of electrons. Hence, the models developed would need to adequately and accurately describe the motion and behaviour of electrons.

2.2: Quantum mechanical methods

Chemical change is defined as the modification of the position or distribution of electrons. Electrons cannot be adequately described using classical mechanics, but require quantum mechanics. Therefore, quantum mechanical (QM) methods are used when the process being studied involves a change in the positions or distributions of electrons.[122] In principle, QM methods can provide exact solutions to the systems being studied. However, in practice, the QM equations can only be solved exactly for one electron systems.[122] This is because the interacting three-body problem does not have a closed-form solution,[123] even in the classical realm. This forces the development of approximation methods to solve systems of chemical interest. Since the various approximation methods devised focus on the positions and distributions of electrons, they are also referred to as electronic structure methods.

2.2.1: Schrödinger equation

A system of quantum particles cannot be described exactly in terms of the positions and momenta of the particles. This is because the position operator and momentum operator do not commute.

$$[\hat{r}, \hat{p}] = i\hbar \qquad (3)$$

In the above, $\hbar$ is Planck's constant divided by $2\hbar$. This implies that position and momentum are not independent variables, unlike in classical mechanics. All pairs of variables commute and are therefore mutually independent. There, the quantum description involves the use of a wave function $\hbar$, which is itself a function of the positions of the constituent particles. Since the positions and momenta are not independent quantities, the wave function can only depend on one of the two. From a phenomenological point of view, it is simpler to describe the wave function in terms of the geometric positions. The wave function for a system of N particles in terms of the particle positions given by

$$\Psi = \Psi(r_1, \cdots, r_N) \qquad (4)$$

The wave function itself is not an observable quantity. However, the wave function of the system determines the values of all observable quantities relating to the system. The operators used to compute a particular property of the system can be likened to a projection operator. The general form of the projection in Dirac's *bra-ket notation*[124] is

$$\langle O \rangle = \langle \Psi | \hat{O} | \Psi \rangle \qquad (5)$$

where <O> refers to the expectation value of the property of interest and $\hat{O}$ is the corresponding operator.[125] When $\hat{O}$ is the unit operator, the property computed is the probability of finding the system.

$$\langle P \rangle = \langle \Psi | \Psi \rangle \quad (6)$$

If the wave function is constructed well, then this integral evaluates to unity. This is known as the normalisation condition. The probability of finding the first particle at r_1+dr_1, the second at r_2+dr_2, and so on, is obtained without integrating Equation 6.

$$\rho = \Psi^* \Psi \quad (7)$$

This form of the density distribution is not very useful; however, it is related to the electron density used as the fundamental variable in density functional theory (Section 2.2.5). In the same vein, using the Hamiltonian operator in Equation 5 yields the expectation value of the energy of the system.

$$\langle E \rangle = \langle \Psi | \hat{H} | \Psi \rangle \quad (8)$$

The preceding discussion assumes that the wave function is normalised. When the wave function is not normalised, Equations 5 and 8 become

$$\langle O \rangle = \frac{\langle \Psi | \hat{O} | \Psi \rangle}{\langle \Psi | \Psi \rangle} \quad (5')$$

$$\langle E \rangle = \frac{\langle \Psi | \hat{H} | \Psi \rangle}{\langle \Psi | \Psi \rangle} \quad (8')$$

Equations 8 and 8' are alternate means of representing the *time-independent Schrodinger equation*. The traditional representation of the Schrodinger equation is obtained by right-multiplying Equation 8 by the wave function Ψ. The choice of this process is dictated by the historical imperative wherein the zero-order Hamiltonian perturbation was the commonly used starting point of choice in calculating radiation-less conditions.[127]

$$\hat{H}\Psi = E\Psi \quad (9)$$

Equation 9 is an eigenvalue problem where E is the eigenvalue and Ψ is the eigenfunction. Hence, E is the eigenvalue of the operator $\hat{H}$.

The time-dependent formalism of the Schrödinger equation (Equation 10) is employed when one wants to study the time-evolution of a quantum system and is the more general form.

$$i\hbar\frac{d\Psi}{dt} = \hat{H}\Psi \qquad (10)$$

Equation 10 reduces to Equation 9 (with a multiplicative phase factor) when the Hamiltonian operator does not contain any time-dependent terms.

The general Hamiltonian is given in terms of the kinetic energy operator and the potential energy operator.

$$\hat{H} = \hat{T} + \hat{V} \qquad (11)$$

In principle, $\hat{V}$ is a generalised potential term. In practice, however, the major contribution to the potential energy is the Coulomb energy. Hence, in the absence of an external field, the potential energy term is the Coulomb operator. In molecular chemistry, the Hamiltonian operator is given by[125]

$$\hat{H} = \hat{T}_N + \hat{T}_e + \hat{V}_{eN} + \hat{V}_{NN} + \hat{V}_{ee} \qquad (12)$$

In Equation 12, the subscripts N and e refer to summations over the nuclear and electronic coordinates, respectively. Substitution of Equation 12 into Equation 9 provides the standard approach to solving the electronic structures of molecules.

Thus, the problem at hand is now one involving many nuclei and many electrons. Unfortunately, the Schrödinger equation is exactly soluble only for the simplest of systems,

such as a particle in a constrained potential. The only system of chemical interest for which the Schrodinger equation can be solved exactly is the hydrogenic (one-electron) atom.[122]

It is noted that the Schrodinger equation describes the non-relativistic physics involved in the system. Systems in which relativistic effects are appreciable (e.g. systems that contain third-row and heavier atoms) need to be treated using the Dirac equation,[124] which is a fully relativistic analogue of the Schrodinger equation.

2.2.2: Born-Oppenheimer approximation

The solution of complex systems was not tractable in an era before the advent of digital computers. M. Born and R. Oppenheimer[126] developed a method, which can be traced to the Franck-Condon theory of the radiationless process wherein 'accepting modes' of nuclear displacements (though incapable of coupling) can contribute to the process method by which systems of chemical interest could be calculated.[127] They took advantage of the fact that all nuclei are at least more than 1800 times more massive than the electron and suggested that nuclei be considered stationary. The electrons are then considered to move in the static electric field of the nuclei. This has been understood as the electrons adjusting quickly to the changes in nuclear positions. Hence, at any instant in time, the electrons experience a fixed nuclear framework.[128] The Born-Oppenheimer approximation effectively transformed the nuclei into classical particles since the positions (and hence momenta) are known exactly.

The Born-Oppenheimer approximation implicitly assumes the separability of electronic and nuclear motion in a bound system, with the only interaction between the two realms being through the electrostatic potential.[129] They separated the nuclear and electronic motions by expanding the kinetic energy term as a sum of single-particle terms. The ratio of electron and nuclear masses was treated as a perturbation to the Hamiltonian, wave function, and energy.[126]

In this way, nuclear motion is treated as a perturbation expanded about a mean position. The zero-order solution is the motion of electrons in the static nuclear field; this is commonly known as the Born-Oppenheimer approximation. The second-order equation yields the vibrational motion in the fixed field of the electrons while the fourth-order equation yields molecular rotation.[126, 129]

The Born-Oppenheimer approximation made it possible to perform quantum mechanical calculations on systems with more than one atom. Coupled with the most common implementation of the approximation (the classical nuclei approximation), it became possible to study the effect of the geometric configuration on the electron configuration. This leads directly to the possibility of calculating property surfaces for molecules and larger systems. A property surface is the variation in the property of interest as a function of the positions of the nuclei. The most commonly calculated surfaces are the potential energy surface (PES) and free energy surface (FES).[129] The PES refers to the variation of the sum of electronic and nuclear energies as a function of nuclear position.[130] This allows one to define the equilibrium geometry as the position on the PES, where the energy is at an absolute minimum. It is definitely possible for there to be several minima on the PES; these correspond to the equilibrium structures of different geometric configurations. Vibrational frequencies are typically calculated based on the curvature of the PES, and not using the perturbative approach of Born and Oppenheimer. Any two minima will be connected by a saddle point, a point where the energy is a maximum in one or more dimensions (and a minimum in all others). A first-order saddle point in the PES corresponds to a transition state. This allows the computation of reaction rates by transition state theory[131, 132] or RRKM theory,[133–139] as the situation warrants.

The Born-Oppenheimer approximation implies the decoupling of the electronic delocalisation from that of the nuclei. Under the traditional implementation of the Born-

Oppenheimer approximation, nuclei are treated as classical point charges. This causes the electronic states to be identical for all isotopic substitutions. Another implication is that the gradients and force constants – and hence optimised geometries – are independent of isotopic substitution.

2.2.3: Variational principle

The Born-Oppenheimer approximation reduces the magnitude and complexity of the description of molecular processes. The problem is now reduced to solving for the electrons in an external (nuclear) electric field. However, due to the fact that an analytic solution for the many-electron problem cannot be obtained, again approximation methods are required. One approach is to treat the electrons independently and then to treat the presence of other electrons as a perturbation (to each single-particle problem). This approach – though intuitive – is not taken as it violates the symmetry restrictions involved with Fermi statistics. However, other perturbative schemes[140] have been developed in which the exact solution is approached as a series expansion. The perturbation is applied to a similar system for which the exact solution is known. These perturbative methods are convergent methods, with the property that the computed energy at certain truncations of the expansion can be higher or lower than the true energy of the system. The physical interpretation of an energy below the ground state energy is an open question. A detailed overview of perturbative methods, which was addressed by Nayfeh,[141] is beyond the scope of the current discussion.

The other approximation scheme in use is the variational approach, based on the variational theorem.[125] The variational theorem states that the energy associated with a well-behaved wavefunction (a well-behaved function is one which is finite, continuous, single-valued, square integrable, and differentiable to the second order) cannot be lower than the exact

energy of the correct eigensolution to the Hamiltonian. Hence, assuming a trial orthonormal wavefunction, the following inequality holds.

$$\langle \varphi | \hat{H} | \varphi \rangle \geq E_0 \qquad (13)$$

Equation 13 becomes an equality when the trial wavefunction becomes equal to the exact ground state eigensolution. Any well-behaved function can be expanded as a linear combination of the exact eigensolutions (which incidentally are not known *a priori*).

$$\varphi = \sum C_i \Psi_i \qquad (14)$$

Substituting Equation 14 into Equation 13 yields

$$\sum (E_i - E_0) |C_i|^2 \geq 0 \qquad (15)$$

Since $(E_i - E_0)$ is necessarily always positive, the inequality in Equation 15 is true. Hence, Equation 13 is true. That means that the solution in a variational method always has an energy that is higher than the true ground state energy. This provides a means to improve the quality of the approximation. Since the energy of an approximation cannot be lower than the exact solution, any trial wavefunction that lowers the ground state energy is necessarily 'better' than other wavefunctions. In this sense, 'better' refers to 'more like the exact solution than the previous approximation' and does not necessarily imply an improved physical description of the system.[123] However, as the computed energy becomes close to the exact solution, the trial wavefunction becomes close to the exact wavefunction, and hence should also reproduce the correct physical behaviour.

2.2.4: Hartree-Fock method

The first step to approaching the exact solution is to generate a suitable trial function that can be improved upon. The Hartree-Fock method is an early method deriving from the

early work of D.R. Hartree[142] and V. Fock[143] on atomic systems. Hartree's method suffered from the drawback that it did not account for the correct anti-symmetric behaviour of electrons with respect to exchange. This method was later modified by J. C. Slater[144] to include the anti-symmetrisation of the electronic wavefunction. This method was developed to solve for the optimal wavefunction variationally. The total Hartree-Fock wavefunction of a closed-shell atom is given by the Slater determinant

$$\Psi = \frac{1}{\sqrt{(2n)!}} \det|\phi_1(1)\alpha(1) \cdots \phi_n\beta(2n)| \qquad (16)$$

A closed-shell system is one where n spatial wavefunctions are occupied by an even number ($2n$) of electrons, each electron having either α or β spin. This form of the wavefunction is a determinant of the $2n$ single-particle functions. Each single-particle function is the product of a spatial function ϕ and a spin function (α or β), this is possible as the spatial and spin functions are separable in the non-relativistic regime. This is clear from the structure of the Hamiltonian, which depends only on spatial coordinates. Therefore, the spin states of the electrons do not affect the overall energetics and can be factored out. The spatial functions (also referred to as orbitals) are commonly chosen to be orthonormal, or

$$\langle \phi_i | \phi_j \rangle = \delta_{ij} \qquad (17)$$

where δ_{ij} is the Kronecker delta, which has the property of being 1or 0 depending on whether i and j being the same or different. Unlike Valence Bond methods, which use non-orthogonal orbitals[145], the orthonormality restriction makes computations simpler by making it possible to neglect the overlap integrals, since these are uniformly zero for non-identical spatial functions. A system that has a wavefunction of the form described by Equations 16 and 17 has a total energy that is given by

$$E = 2\sum_{i}^{2n} \varepsilon_i^{(0)} + \sum_{i,j}^{2n} (2J_{ij} - K_{ij}) \tag{18}$$

In the above, the $\varepsilon_i^{(0)}$ are the single-electron energies and include the kinetic energies and electron-nuclear attraction energies. The second summation is over all pairs of electrons and includes the Coulombic repulsion (J_{ij}) and the (quantum mechanical) exchange contribution (K_{ij}). The exchange energy is a result of the anti-symmetry property of electrons and has no classical analogue. The exchange operator interchanges electrons between spatial functions. The Coulomb and exchange operators are defined as below.

$$J_i(\mu)\phi_j(\mu) = \left\langle \phi_i(\nu) \middle| \frac{1}{r_{\mu\nu}} \middle| \phi_i(\nu) \right\rangle \phi_j(\mu) \tag{19a}$$

$$K_i(\mu)\phi_j(\mu) = \left\langle \phi_i(\nu) \middle| \frac{1}{r_{\mu\nu}} \middle| \phi_j(\nu) \right\rangle \phi_i(\mu) \tag{19b}$$

Based on the above definitions, the Coulomb and exchange energy contributions are written as

$$J_{ij} = \langle \phi_i(\mu) | J_j(\mu) | \phi_i(\mu) \rangle = \langle \phi_j(\nu) | J_i(\nu) | \phi_j(\nu) \rangle \tag{20a}$$

$$K_{ij} = \langle \phi_i(\mu) | K_j(\mu) | \phi_i(\mu) \rangle = \langle \phi_j(\nu) | K_i(\nu) | \phi_j(\nu) \rangle \tag{20b}$$

The wavefunction needs to be optimised so that the energy corresponding to the wavefunction is minimised. The best possible wavefunction is required to be constructed to obtain the minimum energy. This is done by the method of Lagrangian multipliers (λ_{ij}). A functional $F[E]$ is constructed as below.

$$F[E] = 2\sum_{i=1}^{2n} \varepsilon_i^{(0)} + \sum_{i,j}^{2n} (2J_{ij} - K_{ij}) - 2\sum_{i,j}^{2n} \lambda_{ij} (\langle \phi_i | \phi_j \rangle - \delta_{ij}) \tag{21}$$

The method then requires one to find the conditions to be satisfied by the orbitals to make $F[E]$ a minimum. This implies that $\delta F[E] = 0$ for arbitrarily small variations $\delta\phi_i$ of the optimised orbitals. In other words, the functional $F[E]$ is a stationary state with respect to the set of spatial orbitals. The first-order variation in $F[E]$ is given by

$$\begin{aligned}\delta F[E] = 2\sum_{i}^{2n}\left(\langle\delta\phi_i|h_\mu|\phi_i\rangle + \langle\phi_i|h_\mu|\delta\phi_i\rangle\right) \\ + \sum_{i,j}^{2n}\left(\langle\delta\phi_i|2J_j - K_j|\phi_i\rangle + \langle\phi_i|2J_j - K_j|\delta\phi_i\rangle\right) \\ + \sum_{i,j}^{2n}\left(\langle\delta\phi_j|2J_i - K_i|\phi_j\rangle + \langle\phi_j|2J_i - K_i|\delta\phi_j\rangle\right) \\ - 2\sum_{i,j}^{2n}\left(\lambda_{ij}\langle\delta\phi_i|\phi_j\rangle + \lambda_{ij}\langle\phi_i|\delta\phi_j\rangle\right)\end{aligned} \tag{22}$$

In Equation 22, h_μ is the one-electron part of the Hamiltonian operator. The second and third terms are symmetric and can be collapsed into one term. Hence, Equation 22 becomes

$$\begin{aligned}\delta F[E] = 2\sum_{i}^{2n}\langle\delta\phi_i|h_\mu + \textstyle\sum_j^{2n}(2J_j - K_j)\,|\phi_i\rangle \\ + 2\sum_{i}^{2n}\langle\phi_i|h_\mu + \textstyle\sum_j^{2n}(2J_j - K_j)\,|\delta\phi_i\rangle \\ - 2\sum_{i,j}^{2n}\left(\lambda_{ij}\langle\delta\phi_i|\phi_j\rangle + \lambda_{ij}\langle\phi_i|\delta\phi_j\rangle\right)\end{aligned} \tag{23}$$

The first two terms are adjoins of each other, and $\langle\delta\phi_i|\phi_j\rangle$ and $\langle\phi_i|\delta\phi_j\rangle$ are mutual adjoints. Hence, Equation 23 reduces to

$$\delta F[E] = 2\sum_{i}^{2n}\left[\langle\delta\phi_i|h_\mu + \Sigma_j^{2n}(2J_j - K_j)\,|\phi_i\rangle - \sum_{j}^{2n}\lambda_{ij}\langle\delta\phi_i|\phi_j\rangle\right] + 2\sum_{i}^{2n}\left[\langle\delta\phi_i|h_\mu + \Sigma_j^{2n}(2J_j - K_j)\,|\phi_i\rangle^* - \sum_{j}^{2n}\lambda_{ij}\langle\delta\phi_i|\phi_j\rangle^*\right] \tag{24}$$

The conditions for $\delta F[E]$ to vanish now become

$$\left[h_\mu + \sum_{j}^{2n}(2J_j - K_j)\right]\phi_i = \sum_{j}^{2n}\phi_j\lambda_{ij} \tag{25a}$$

$$\left[h_\mu + \sum_{j}^{2n}(2J_j - K_j)\right]\phi_i^* = \sum_{j}^{2n}\phi_j^*\lambda_{ij} \tag{25b}$$

Subtracting the complex conjugate of Equation 25b from Equation 25a yields Equation 26.

$$\sum_{j}^{2n}\phi_j(\lambda_{ij} - \lambda_{ji}^*) = 0 \tag{26}$$

Since the spatial orbitals are linearly independent, it means that

$$\lambda_{ij} = \lambda_{ji}^* \tag{27}$$

Hence, the Lagrangian multipliers used to minimise the energy of the system form a hermitian matrix. Equations 25a and 25b are known as the Hartree-Fock equations and are equivalent as they are complex conjugates of each other. The Hartree-Fock equations can also be rewritten as

$$\widehat{\boldsymbol{F}}\boldsymbol{\Phi} = \boldsymbol{\Phi}\boldsymbol{\lambda} \tag{28}$$

Where, the Fock operator $\hat{F}$ is defined as

$$\hat{F} = h_\mu + \sum_{j}^{2n} \left(2J_j - K_j\right) \tag{29}$$

The Fock operator is a one-electron operator. The first term contains the kinetic energy of the electron and its attraction to the nucleus; the second term is the average potential experienced by the electron from all the other electrons in the system. There are no dynamic electron-electron interactions. For this reason, the Hartree-Fock method is called the mean-field approximation. The $\boldsymbol{\lambda}$ matrix is diagonalised by means of a unitary transformation to yield the solution

$$\hat{F}\phi_i = \varepsilon_i \phi_i \tag{30}$$

The set of ε_i are interpreted as being the orbital energies of the orbitals ϕ_i. The negative of the Hartree-Fock orbital energy has been shown (Koopmans Theorem)[146] to correspond to the energy of ionisation of an electron from that orbital.

The Hartree-Fock method was extended to molecules by Roothaan and Hall.[147-149] The Roothaan-Hall method invokes the Born-Oppenheimer approximation (Section 2.2). The reasoning was that the velocities and ranges of motion of the nuclei are expected to be much smaller than those of the electrons – owing to their significantly higher masses – and hence the nuclear motions are decoupled from the electronic motions.

Following from the Hartree-Fock method, the Roothaan-Hall method also allows the separability of the spatial and spin coordinates. In this model, the one-electron molecular spatial wavefunctions are expanded as a series of atomic spatial wavefunctions. This is known as the linear combination of atomic orbitals (LCAO) approach. The one-electron functions under the LCAO approximation are given by

$$\psi_i = \sum_{\lambda} C_{\lambda i}\phi_{\lambda} \tag{31}$$

This equation connects the atomic functions ϕ_λ to the molecular functions ψ_i through the coupling terms $C_{\lambda i}$. This can be written in matrix notation as

$$\boldsymbol{\psi} = \boldsymbol{C\Phi} \tag{32}$$

As before, the molecular wavefunction is constructed as a Slater determinant[150] of the one-electron functions.

$$\Psi = \frac{1}{\sqrt{(2n)!}}\det|\psi_1(1)\alpha(1)\cdots\psi_n(2n)\beta(2n)| \tag{33}$$

By means of a derivation analogous to that of the Hartree-Fock method, it was shown[147] that the following system of equations is satisfied. This is referred to as the Roothaan-Hall equation.

$$\boldsymbol{FC} = \boldsymbol{SC\varepsilon} \tag{34}$$

This can be written as the following set of equations

$$\hat{F}c_i = \varepsilon_i S c_i \tag{35}$$

Here, the index is over the molecular functions. The Fock operator is as defined in Equation 29. The Coulomb and exchange operators used to make up the Fock matrix are defined earlier (Equations 19a and 19b). The matrix $\boldsymbol{S}$ is defined as the overlap matrix, and its elements are the overlap integrals.

$$S_{pq} = \int \bar{\phi}_p \phi_q d\tau \tag{36}$$

It can be seen that the Coulomb and exchange operators depend on the coefficients, whereas Equation 34 aims to solve for the set of coefficients. The coefficients of one orbital can only be determined if the coefficients of all other orbitals are known.[120] This leads to a situation where the orbital coefficients need to be optimised cooperatively. This means that the Roothaan-Hall method (similar to the Hartree-Fock method) is not a true eigenvalue problem, as the eigenfunctions obtained are required to define the operator. A guess set of coefficients is used to compute the Fock matrix. The optimised coefficients are computed to satisfy the Fock matrix. This set of coefficients is used to generate a new set of coefficients. This process is continued until the two sets of coefficients are identical to within a pre-determined tolerance level. This process is known as the self-consistent field (SCF) procedure. For this reason, the Hartree-Fock and Roothaan-Hall methods are known as self-consistent or SCF procedures. Based on the variational theorem, the energy computed by this method is always an upper-bound to the true energy of the system.

The energy of the system is computed in terms of the orbital energies by

$$E = \sum_{i}^{n} \varepsilon_i - \frac{1}{2}\sum_{ij}^{n}\left(J_{ij} - K_{ij}\right) + V_{nn} \tag{37}$$

It is to be noted that there is an additional term in the Roothaan-Hall energy that was not obtained when deriving the Hartree-Fock energy. The third term in Equation 37 is the (classical) nuclear repulsion energy, which is a result of the Born-Oppenheimer approximation. Since the Hartree-Fock method is an atomic method, there are no nuclear repulsions. The orbital energies are given by

$$\varepsilon_i = h_i + \sum_{j}^{n}\left(J_{ij} - K_{ij}\right) \tag{38}$$

It is instructive to compare the Hartree-Fock and Roothaan-Hall equations.

$$\widehat{\boldsymbol{F}}\boldsymbol{\Phi} = \boldsymbol{\Phi\varepsilon} \tag{30}$$

$$\boldsymbol{FC} = \boldsymbol{SC\varepsilon} \tag{34}$$

It is readily seen that the two equations are equivalent; the Roothaan-Hall method is a direct generalisation of the Hartree-Fock method to molecules. For this reason, the Roothaan-Hall method is commonly referred to as the Hartree-Fock method.

In the Hartree-Fock method the many-electron Schrodinger equation is separated into several one-electron operators to solve for one-electron orbitals and one-electron energies. This one-electron operator describes the motion of an electron in the static field of all other electrons. However, the Hamiltonian of the Schrodinger equation is a two-electron operator. That means that the true solution to the Schrodinger equation must be obtained through a simultaneous solution of many two-electron equations, which means that the Hartree-Fock method misses some important physics, mainly through the correlated motion of the electrons. Thus, the Hartree-Fock cannot obtain the true energy of the system, but will have a higher energy. The difference between the Hartree-Fock energy and the true energy of the exact solution to the Schrodinger equation is known as the correlation energy, as it describes the lowering of the total energy due to the correlated motions of the electrons.

For its physical failing, it is to be noted that the Hartree-Fock method in practical calculations recovers ~99% of the total energy of the system. However, the ~1% of energy that is not recovered is most important in describing chemical phenomena.[120] Hereby, it should be noted that correlation effects depend on the relative spin of the two elections. The correlation between electrons with opposite spins has both intra- and inter-orbital contributions, hence it will in general be larger than the correlation between electrons with the same spin. The opposite

spin correlation is called Coulomb correlation and the same spin correlation is called Fermi correlation. Another way of looking at correlation is in terms of the electron density. In this picture, the correlation due to electrons with opposite spin is called a Coulomb hole and the corresponding correlation due to electrons with the same spin is called a Fermi hole. This latter definition is commonly used in the development of density functional theory and its various flavours (Section 2.5).

Since the Hartree-Fock method recovers about 99% of the total energy, it is often used as a starting point for improvements. The Hartree-Fock method provides the best single-determinant wavefunction. Therefore, to improve the descriptions beyond the Hartree-Fock method, it is necessary to have a trial wavefunction that is constructed from more than one Slater determinant. This also means that the mental picture of electrons residing in orbitals is inaccurate. A generic multi-determinant wavefunction is given by

$$\Psi = a_0 \Phi_{HF} + \sum_{i>0} a_i \Phi_i \qquad (39)$$

In the above, the coefficient a_0 is usually close to 1. Electron correlation methods differ in how the other determinants and their coefficients are computed. The coefficient of the Hartree-Fock determinant is then obtained from the normalisation condition.

The construction of the additional determinants and the computation of the coefficients are the subject of the remainder of this section. The Roothaan-Hall equations for a spin-restricted system with N electrons and M spatial functions yield $N/2$ occupied and M-$N/2$ virtual orbitals (the total number of molecular orbitals is equal to the number of atomic orbitals because the coefficient matrix is a square matrix, which is needed for it be invertible). The Slater determinant is determined by the $N/2$ spatial orbitals each being multiplied by two spin functions to produce N spin orbitals. A multitude of determinants can be generated by replacing

occupied MOs from the Hartree-Fock solution with unoccupied MOs. This is akin to expanding the wavefunction in terms of determinants, similar to how the Hartree-Fock wavefunction is a function expanded in a non-linearly-dependent basis (the set of spatial orbitals). The determinants formed in this manner can be denoted based on how many occupied Hartree-Fock MOs are replaced with unoccupied MOs. These Slater determinants are considered to be singly, doubly, triply, quadruply, etc. excited relative to the Hartree-Fock determinant when one, two, three, four, etc. MOs are exchanged between the occupied and unoccupied realms, respectively.[120] These determinants are often referred to as singles (S), doubles (D), triples (T), quadruples (Q), etc. This process can be continued until all *N* electrons are excited relative to the Hartree-Fock determinant. The number of determinants available in the phase space to expand the wavefunction (Equation 39) depends on the number of electrons and the number of spatial functions used to describe the system and increases in a combinatorial manner. When all possible determinants are included in the expansion, the exact (non-relativistic, within the Born-Oppenheimer approximation) solution is obtained.[120] However, for most practical applications, the inclusion of all possible excitations is not feasible. This means that one needs to choose which excitations to include and which to exclude.

There are four families of schemes that are used to choose the excited determinants. These methods are known as configuration interaction (CI), many-body perturbation theory (MBPT), multiconfiguration self-consistent field (MCSCF), and coupled cluster (CC). A brief overview of these methods follows; further information on these methods is available elsewhere.[120,123] Configuration interaction is based on the variational energy principle. The trial wavefunction is a linear combination of determinants with the expansion coefficients optimised by requiring that the energy be a minimum. In this method, the spatial MOs are unchanged from the Hartree-Fock solution. Conversely, many-body perturbation theory is based on the

premise that the problem to be solved is only slightly different from a problem for which a solution is readily available.[140] The final solution should therefore be similar to the approximating function. Since the Hartree-Fock solution is close to the exact solution (recovering 99% of the energy), the Hartree-Fock wavefunction becomes a good approximating function to the exact solution. It is to be noted that MBPT is not a variational method, and hence the energy obtained is not an upper-bound to the exact energy. The perturbation methods include contributions from all types of excitations (singles, doubles, triples, etc.) to a given order (2, 3, 4, etc.).[120] Meanwhile, the MCSCF method has two components that are variationally optimized: the configuration function coefficients (A_K) and the MO expansion coefficients ($C_{\mu i}$).[151] These two components make the method distinct from CI, which only has the configuration mixing coefficient variationally optimized. Finally, the coupled cluster method instead includes all corrections of a given type to infinite order.[152] As a perturbative method, it is also not variational. However, it is well-behaved and converges faster than the Møller -Plesset expansion.

Since the properties of interest generally involve changes to the valence electrons, it is reasonable to ignore the excitations from the orbitals representing the core. This is referred to as the frozen-core approximation, and within the frozen-core approximation the core electrons are not correlated. This approximation allows one to focus the computational effort on correlating the valence electrons and improving the density distribution in the regions far from the nucleus (including improving the tail behaviour).

2.2.5: Density functional theory

Meanwhile, another approach, referred to as density functional theory (DFT), is built on the premise that the energy and properties of the system being studied are completely

determined by the electron density. This premise was originally defined in the Hohenberg-Kohn Theorems, which are the major pillars that provide the necessary foundation of contemporary DFTs.[153] Nevertheless, this premise implies a one-to-one correspondence between the electron density and the ground state energy.[120] Recall that in the Hartree-Fock method the system is defined by $3N$ coordinates. In principle, the electron density is a function of three dimensions, and hence the DFT approach is only dependent on three dimensions and is independent of the number of electrons. In general, it can be shown that[153]

i. $\int \rho(\bar{r}_1) d\bar{r}_1 = N$, or the electron density integrates to the total number of electrons.

ii. $\rho(\bar{r}_1)$ has maxima at the positions corresponding to the nuclei, and

iii. $\lim_{r_{iA} \to 0} \left[\frac{\partial}{\partial r} + 2Z_A\right] \rho(\bar{r}_1) = 0$, or the density at the nucleus contains information regarding the charge of the nucleus.

It is thus seen that the electron density has the characteristics required to create a system-specific Hamiltonian and the density suffices for a complete description of molecular properties. It can therefore be surmised that DFT is an alternate approach to solving the molecular Schrodinger equation. In terms of implementation, it can be shown that the DFT Hamiltonian operator can be separated into kinetic, Coulomb, and exchange terms, analogous to the Hartree-Fock method.[120,153]

The Hartree-Fock-Slater (X_α) method was one of the earliest DFT-based schemes to be applied to multi-atomic systems. This method is based on the work of Slater,[154] who proposed an improvement to the non-local exchange contribution under Hartree-Fock theory, and it was found that the exchange-correlation potential could be represented by a function that is

proportional to the 1/3 power of the electron density. The exchange energy arises from the anti-symmetry of the true wavefunction and can be expressed as the interaction between the charge density of spin α and the Fermi hole of the same spin.

$$E_X = \frac{1}{2}\int\int \frac{\rho(r_1)h_X(\bar{r}_1:\bar{r}_2)}{r_{12}} d\bar{r}_1 d\bar{r}_2 \tag{40}$$

Hence, the exchange contribution could be calculated easily if a reasonable approximation to the Fermi hole could be developed. Slater assumed that the Fermi hole is spherically symmetric and that it is centred on the electron at $\bar{r}_1$. Further, it was assumed that the exchange-hole density is constant within the sphere, being the negative of $\rho(r_1)$, and zero outside the sphere. The Wigner-Seitz radius[155,156] is calculated based on the fact that each Fermi hole contains exactly one elementary charge.

$$r_s = \left(\frac{3}{4\pi}\right)^{\frac{1}{3}} \rho(r_1)^{-\frac{1}{3}} \tag{41}$$

It is a result of standard electrostatics that the potential of a charged sphere of radius r_s is given by $\frac{1}{r_s} = \rho(r_1)^{\frac{1}{3}}$. The exchange functional is thus given by

$$E_X[\rho] \cong C_X \int \rho(r_1)^{\frac{4}{3}} d\bar{r}_1 \tag{42}$$

The quantity C_X is a numerical constant. An adjustable parameter α was included in C_X to improve the quality of the approximation. It was for this reason that the method was called the X_α method. The exchange functional in the X_α method is given by

$$E_{X_\alpha}[\rho] = \frac{9}{8}\left(\frac{3}{\pi}\right)^{\frac{1}{3}} \alpha \int \rho(r_1)^{\frac{4}{3}} d\bar{r}_1 \quad (43)$$

Typical values of α ranged from 2/3 to 1. When α takes the value of 2/3, the exchange functional is identical to the Dirac exchange functional.

A formal proof for the assumption that the energy of an electronic system could be expressed in terms of its density came when Hohenberg and Kohn,[157] particularly their first theorem, showed that the ground-state energy of an electronic system is uniquely defined by its density. The exact dependence between the two remained unknown. The Hamiltonian and thus the ground-state wavefunction of an *N*-particle system interacting with a given inter-particle interaction are completely determined by the specification of the external field ϕ(r). This is expressed as the ground state energy is a functional of the external field. Hohenberg and Kohn showed that there is a unique one-to-one correspondence between the external field and the single-particle density, and that it is possible to express the ground-state energy as a functional of the density.

$$E[\rho] = E_0[\rho] + \int dr\phi(r)\rho(r)\, d\bar{r}_1 \quad (44)$$

In the above equation, $E_0[\rho]$ is a functional that is independent of the external potential. In their second theorem, Hohenberg and Kohn proved that for any trial density $\rho(r)$ that satisfies $\int \rho(\bar{r}_1) d\bar{r}_1 = N$,

$$E[\rho] \geq E_g \quad (45)$$

Here, E_g is the true ground state energy. The equality is only valid when the trial density is equal to the true ground-state single-particle density. Hence, the second theorem of Hohenberg

and Kohn is the DFT analogue of the variational theorem. The Hohenberg-Kohn theorems apply specifically to the ground state and are strictly valid only at zero absolute temperature.[158]

In a further improvement, Kohn and Sham[159] derived a set of one-electron equations. In principle, one could obtain the exact electron density and hence ground-state energy from these one-electron equations. In general, the total energy of an *N*-electron system can be written as

$$E_{el} = -\frac{1}{2}\sum_{i} \phi_i(\bar{r}_i)\bar{\nabla}^2\,\phi_i(\bar{r}_i)d\bar{r} + \sum_{A}\frac{Z_A}{|R_A - r_1|}\rho(r_1)dr_1 + \frac{1}{2}\int\frac{\rho(\bar{r}_1)\rho(\bar{r}_2)}{|\bar{r}_1 - \bar{r}_2|}d\bar{r}_1 d\bar{r}_2 + E_{XC} \tag{46}$$

The first term in Equation 46 corresponds to the kinetic energy of *N* non-interacting electrons that have the same density as the actual system of interacting electrons. This form of the kinetic energy operator is identical to the form used in Hartree-Fock theory. The second term describes the Coulomb attraction between electrons and nuclei, and the third term describes the Coulomb repulsion between the electrons. The last term E_{XC} is called the exchange-correlation energy. The one-electron orbitals of Equation 45 are solutions to the set of one-electron (Kohn-Sham) equations

$$\left[-\frac{1}{2}\nabla_1^2 + \frac{Z_A}{|R_A - \bar{r}_1|} + \int\frac{d\bar{r}_2\rho(\bar{r}_2)}{|\bar{r}_1 - \bar{r}_2|} + V_{XC}\right]\phi_i(\bar{r}_1) = \hat{h}_{KS}\phi_i(\bar{r}_1) = \varepsilon_i\phi_i(\bar{r}_1) \tag{47}$$

The exchange-correlation potential V_{XC} is the functional derivative of E_{XC} with respect to the density.

$$V_{XC} = \frac{\delta E_{XC}[\rho]}{\delta \rho} \tag{48}$$

It is important to remember that the exchange-correlation energy in DFT is different than the traditional definition of the exchange-correlation energy being the sum of the Hartree-Fock exchange and the correlation energy. The correlation is traditionally defined as the difference between the Hartree-Fock energy and the exact energy. The traditional definition has the advantage that the reference Hartree-Fock energy does not contain unknown quantities and can be calculated to arbitrary accuracy. This is not the case with the Kohn-Sham equations, as E_{XC} and its functional derivative V_{XC} are only known approximately. Obtaining them is exactly equivalent to a full solution of the many-electron problem.[158,160]

A cursory look at Equations 37 and 47 shows a close resemblance between the Kohn-Sham and Hartree-Fock equations. However, the consequence of the differences in the implementation is that the Kohn-Sham[159] orbitals are different from the Hartree-Fock orbitals, even though they both are one-electron spatial orbitals. This is because the Koopmans theorem is not applicable to the Kohn-Sham orbitals and their energies. Hence, the Kohn-Sham orbitals do not have the same physical meaning as the Hartree-Fock orbitals. Koopmans theorem would only be valid if the exact exchange-correlation functional is used.[120] However, the exact form of the exchange-correlation functional cannot be known[157] and hence this functional must be approximated. It is possible that the common assumption that the exchange and correlation functional contributions may be inaccurate.[120,153] If so, the application of this assumption would prevent solution of the exact exchange-correlation functional. Nevertheless, this close

resemblance suggests that the means of computation and the computational expense of both methods are similar.

Thus, summarizing, the Hohenberg-Kohn theorems[157] offer the first formal proof of the applicability of using the electron density to compute energy and molecular properties. This was done by showing that there exists a one-to-one correspondence between the electron density and the ground-state energy. Moreover, it was shown that the computed energy is an upper-bound to the exact energy. These are analogous to the wavefunction formalism. The wavefunction formalism asserts that there exists an exact solution to the Hamiltonian, and that the energy of the computed wavefunction is necessarily an upper-bound to the exact energy. This shows that the wavefunction approach and the density approach are essentially equivalent, the only difference being in the implementation.

2.3: Implementation of structure methods

The Hartree-Fock (including Roothaan-Hall) method and the Kohn-Sham method have similar implementation schemes. The Hartree-Fock method is a self-consistent field method. The Kohn-Sham scheme is also a set of one-electron eigenequations (with two-electron contributions to the operator), and hence can also be implemented as a self-consistent field method. The difference between the methods lies in the construction of the Fock matrix. The implementation of the Hartree-Fock method is described below,[161] with suitable modifications to account for differences in the Kohn-Sham method.

When solving for the self-consistent field, it is useful to separate the constant and flexible terms of the operator. This separation simplifies the computation by reducing the number of terms that need to be computed at each iteration. The Fock matrix **F** is separated into the (constant) core **H** matrix and the variable **G** matrix.

$$\mathbf{F} = \mathbf{H} + \mathbf{G} \tag{49}$$

The core matrix contains the terms that are invariant during the course of the self-consistency optimisation as its contents are constant for a fixed nuclear configuration. The terms of **H** are the one-electron kinetic energy and nuclear attraction terms expanded in terms of the set of atomic spatial functions $\{\phi_i\}$.

$$H_{\mu\nu} = \int d\boldsymbol{r_1}\phi_\mu^*(1)\left(-\frac{1}{2}\nabla_1^2 - \sum_A \frac{Z_A}{|\boldsymbol{R_A} - \boldsymbol{r_1}|}\right)\phi_\nu(1) \tag{50}$$

The **H** matrix is a one-electron matrix and does not contain any information relating to the spin. For this reason, the **H** matrix is unchanged between the spin-restricted and spin-unrestricted cases.

The **G** matrix contains the information regarding all the terms that change from iteration to the next. In a self-consistency calculation, the only property that change is the distribution of the electrons. The G matrix is thus made up of all the electron-electron interactions, such as the Coulomb and exchange interactions. The difference between the Hartree-Fock and Kohn-Sham-based methods is in how the **G** matrix is constructed. In some implementations, the elements of the **G** matrix are set to zero before the first iteration. The first iteration yields a guess density matrix **P**. Under the more general spin-unrestricted formalism,[162] the electronic density is expressed in terms of the α and β densities.

$$P_{\mu\nu}^{\alpha} = \sum_a^{N^\alpha} C_{\mu a}^{\alpha}(C_{\nu a}^{\alpha})^* \tag{51a}$$

$$P_{\mu\nu}^{\beta} = \sum_a^{N^\beta} C_{\mu a}^{\beta}\left(C_{\nu a}^{\beta}\right)^* \tag{51b}$$

Two other matrices are defined under the unrestricted formalism. The total density matrix is

$$\mathbf{P}^T = \mathbf{P}^\alpha + \mathbf{P}^\beta \tag{52}$$

The spin-density matrix is given by

$$\mathbf{P}^T = \mathbf{P}^\alpha - \mathbf{P}^\beta \tag{53}$$

In comparison, the spin densities of the spin-restricted case are equal. Hence, the total density matrix is twice the α (or β) density matrix, and the spin-density matrix is uniformly zero. The spin-density matrix is of chemical interest, but is not involved in the computation of the method. The terms of the **G** matrix are obtained through the **P** matrices. The **G** matrix deals exclusively with two-electron interactions and hence two equivalent **G** matrices are generated. These are the $\mathbf{G}^\alpha$ and $\mathbf{G}^\beta$ matrices, defined as below.

$$G_{\mu\nu}^{\alpha} = \sum_{\lambda}\sum_{\sigma}\left(P_{\lambda\sigma}^{T}(\mu\nu|\lambda\sigma) - P_{\lambda\sigma}^{\alpha}(\mu\lambda|\nu\sigma)\right) \tag{54a}$$

$$G_{\mu\nu}^{\beta} = \sum_{\lambda}\sum_{\sigma}\left(P_{\lambda\sigma}^{T}(\mu\nu|\lambda\sigma) - P_{\lambda\sigma}^{\beta}(\mu\lambda|\nu\sigma)\right) \tag{54b}$$

It can be seen from Equations 54a and 54b that the α and β electrons interact with each other through the **G** matrices. Further, it can be seen that the electrons of opposite spin interact only through the Coulomb term. The exchange term only contains contributions from electrons with the same spin. The differing spin makes the particles distinguishable (magnetically). There is therefore no exchange interaction between the electrons of opposite spin. In implementations of Kohn-Sham theory, the **G** matrix only contains the Coulomb term. The exchange interactions between the electrons are introduced through the exchange-correlation potential V_{XC}.

The Pople-Nesbet equations[162] are solved to yield the orbital energies and coefficient matrices.

$$\mathbf{F}^{\alpha}\mathbf{C}^{\alpha} = \mathbf{S}\mathbf{C}^{\alpha}\boldsymbol{\varepsilon}^{\alpha} \tag{55a}$$

$$\mathbf{F}^{\beta}\mathbf{C}^{\beta} = \mathbf{S}\mathbf{C}^{\beta}\boldsymbol{\varepsilon}^{\beta} \tag{55a}$$

The **S** matrix in the above equations has the same meaning as in Equation 36 and is the matrix containing the overlap integrals between the various spatial functions. Since this matrix is based on the spatial coordinates, it is invariant between the two equations. Hence, the **S** matrix only needs to be computed once for each nuclear orientation. The coefficient matrices $\mathbf{C}^{\alpha}$ and $\mathbf{C}^{\beta}$ that are obtained from solving Equations 55a and 55b are used to generate new **P**, **G**, and **F** matrices. This procedure is done recursively until the energy of the system is minimised (variational optimisation) within a set tolerance. The energy of the system is computed to be

$$E_0 = \frac{1}{2}\sum_{\mu}\sum_{\nu}\left[P^{T}_{\nu\mu}H_{\mu\nu} + P^{\alpha}_{\nu\mu}F^{\alpha}_{\mu\nu} + P^{\beta}_{\nu\mu}F^{\beta}_{\mu\nu}\right] \tag{56}$$

An alternate convergence criterion is the convergence of the density matrices **P**. This automatically leads to an optimised energy as the energy depends only on the density matrices.

2.3.1: Basis sets

In the discussions about the Hartree-Fock method and the Kohn-Sham method, the molecular wavefunction is defined in terms of atomic orbitals. This is known as the linear combination of atomic orbitals (LCAO) approximation. In strict terms, the LCAO approximation assumes that the set of atomic spatial functions is known. It has also been seen that the exact set of spatial functions cannot be obtained for any element larger than hydrogen.

At best, hydrogenic spatial functions can be obtained. However, the hydrogenic functions are a solution to the one-electron problem, whereas what is required is a solution to the many-electron atomic problem. This itself requires an optimisation study as the solutions to the one-electron problem are not expected to be good spatial solutions to the many-electron problem. The effects of electron-electron repulsion will cause the outermost electron shells to be more diffuse than predicted by the one-electron solutions. It is thus seen that exact atomic spatial functions are not obtainable. This raises the question of how to construct the wavefunction in Equations 31 and 47.

Looking at Equations 31 and 47, it is obvious that optimised atomic functions are not required. They are only what are desired. The equations are equally valid with any set of spatial functions. Moreover, the solution to the Hartree-Fock or Kohn-Sham equations that is obtained is relative to the set of basis functions used. This means that the quality of the solution depends on the quality of the set of spatial functions used to describe electron motion. In general, if the molecular orbital is expanded in a (mathematically) complete set of basis functions, the obtained molecular orbital is exact. This implies the use of an infinite number of basis functions. When a finite basis set is used, the quality of the molecular orbitals, and hence the molecular wavefunction depends on the truncation. A smaller basis set leads to a poorer representation of the system. Therefore, a larger basis set is in general preferred. Considering that the scaling of the computational effort for a Hartree-Fock calculation increases formally in terms of the number of basis functions as M^4, it is necessary to minimise the number of basis functions to describe the system. When the individual basis functions describe the electronic motion more accurately, fewer basis functions are required to obtain the same or higher levels of accuracy.[120]

Two types of spatial functions are commonly used in electronic structure calculations: Slater-type orbitals (STOs) and Gaussian-type orbitals (GTOs). Slater-type orbitals are constructed with an exponential dependence on the distance between the nucleus and the electron, which mirrors the exact orbitals of the hydrogen atom. This includes the cusp at the nucleus and the long-range decay of the tail of the spatial function. The general form of the Slater-type orbital is

$$\chi(r,\theta,\varphi) = NY_{l,m}(\theta,\varphi)r^{n-1}e^{-\zeta r} \tag{57}$$

It is seen that the STOs do not have radial nodes, unlike the exact orbitals of the hydrogen atom. The radial nodes are introduced by making linear combinations of STOs. Due to their favourable behaviour, the energy and wavefunction (and hence properties) converge quickly with respect to an increase in the number of basis functions. This is balanced by the fact that the three- and four-centre integrals (used to generate the **G** matrix) do not have an analytic solution. This means that these integrals need to be computed numerically. Hence, the practical use of STOs is in general limited to small systems where high accuracy is required.[120] Since the use of STOs requires numerical integration, they can in principle be used in density functional calculations since, the exchange-correlation term in DFT is integrated numerically anyway.

Gaussian-type orbitals have the general form

$$\chi(r,\theta,\varphi) = NY_{l,m}(\theta,\varphi)r^{2n-2-l}e^{-\zeta r^2} \tag{58}$$

Gaussian-type orbitals, by their construction, have a slope of zero at the nucleus. This is to be contrasted with the Slater-type orbitals, which have a cusp (discontinuity, with slope approaching infinity) at the nucleus. Under the Born-Oppenheimer approximation, the basis functions should have a cusp at the nucleus. This is obvious from the functional form of the

Coulomb attraction term. Because of this, the behaviour of the GTOs at short distances is erroneous. Moreover, the tails of the GTOs decay more quickly than the tails of the exact hydrogenic solution. However, it is possible to reproduce the behaviour of a Slater-type orbital using linear combinations of GTOs. As with the case of Slater-type orbitals, the exact solution can also be attained at the complete basis set limit with Gaussian-type orbitals. However, the complete basis set limit being unachievable, the next best option is a sufficiently large basis that can reproduce the behaviour of Slater-type orbitals. It requires many more Gaussian-type orbitals to reproduce the behaviour of Slater-type orbitals. However, this can be done at significantly lower computational expense as the integrals involving Gaussian-type orbitals can be evaluated analytically. A rough guideline is that it takes approximately thrice as many GTOs as STOs to achieve the same level of accuracy.[120]

The preceding discussion related to the types of basis functions used in constructing a basis set. The next consideration is the radial flexibility. The simplest type of basis set possible is the minimal basis. In a minimal basis, the number of basis functions for a given atom is sufficient to contain all the electrons of the neutral atom. The next level of improvement is provided by doubling the basis functions. Such a basis set is referred to as a double-zeta basis set, since zeta refers to the pre-factor to the radial term in the exponential term. Hence, zeta determines the rate at which the function decays from the nucleus. A double-zeta (DZ) basis would thus need basis functions with two different rates of decay for each 'real' atomic function. If they have the same rate of decay, the two functions become linearly dependent. For example, a double-zeta basis for the hydrogen atom requires two *s* spatial functions to describe the 1*s* atomic function. Since bonding primarily affects only the valence electrons and their distribution, it is customary to instead double only the valence functions; the core orbitals are described by a minimal basis. A basis set that is constructed in this manner is referred to as a

valence double-zeta basis set. Similarly, basis sets can be constructed that are true triple-, quadruple-, quintuple-zeta basis sets, or larger. These are abbreviated, TZ, QZ, 5Z, etc. Basis sets constructed with large numbers of zeta tend to be split-valence basis sets, with very few basis functions (usually a minimal number) being used to describe the core. The addition of basis functions with different decay constants affords radial flexibility to the basis set. This radial flexibility helps to improve the description of the electron density distribution as a result of bonding and non-bonding interactions.

A common disadvantage to energy-optimised basis sets is that the region of the inner shell electrons largely determines the energy. Therefore, minimising the energy as the procedure for optimising the basis set leads to a situation where the basis set is optimum for the core electrons and generally less than optimum for the valence electrons. This is because the atomic energy is dominated by the core orbitals. On the other hand, the processes of chemical interest depend primarily on the valence electrons; the core electrons can largely be assumed to be inert. Additionally, several molecular properties like the polarisability depend on the wavefunction tail, which is energetically unimportant. Therefore, energy-optimised basis sets that give a good description of the outer part of the wave function need to very large.[122] This is an inefficient method for improving the description of the tail. Instead, energy-optimised basis sets usually have diffuse functions – basis functions with small exponents – added explicitly to improve the description of the electron density distribution in the tail region. Diffuse functions are used whenever there are loosely-bound electrons or the property of interest depends on the tail.

It was mentioned above that many basis functions are used to describe the energetically important but chemically unimportant core electrons. This is the reason for the development of contracted basis sets. The computational cost increases as the fourth power of the number of

basis functions. However, the majority of basis functions in an energy-optimised basis set are used to describe the chemically inert core electrons. There is very little change in the MO coefficients of the core basis functions during a chemical process. Hence, there is no justification for spending most of the computational effort on computing the core electrons. For this reason, the basis functions describing the core electrons are contracted, i.e. their orbital coefficients are made constant. By doing this, the coefficients of the core electrons are no longer parameters to be optimised using the variational principle. This has the effect of reducing the number of basis functions to be used in the variational optimisation. The original basis functions used are referred to as primitive basis functions. The primitive functions are combined in set combinations to produce the contracted functions. These contracted basis functions are then used in the variational optimisation of the system. Contraction is typically only performed with Gaussian-type orbitals. A large number of Gaussian-type orbitals are required to properly describe the cusp region. This becomes more severe for the innermost orbitals (1*s*) than the outer core orbitals. Contracting a basis set will always increase the energy. This is because contraction reduces the number of variational parameters and hence reduces the flexibility of the basis set. However, contraction significantly reduces the computational expense. The user must then determine the balance between accuracy and computational efficiency.[120]

The canonical basis functions have certain preferred orientations for the electron density based on the orientations of the basis functions. For example, the *p*-orbitals are oriented at 90° from each other. When these are the valence orbitals, the molecular geometry around the atom gets 'forced' into bond angles of 90°. Consequently, ammonia (NH_3), in its minimal basis set, is geometrically flat rather than pyramidal. This is in spite of the fact that the molecule may optimise to a different geometry if there were sufficient basis functions of suitable energy to

direct the electron densities to these other positions. This situation is overcome by adding polarisation functions to the valence shell. Polarisation functions are additional basis functions that have higher angular momenta than the valence shell, and yet have energies and decay properties similar to the valence basis functions so that the two sets of functions can 'mix' during variational optimisation. In effect, these functions provide angular flexibility to the valence basis functions.

2.3.2: Natural Bond Orbital (NBO) Theory

The concept of natural bond orbitals was introduced as a means of describing a unique set of orthonormal one-electron functions that are intrinsic to a multi-electron wave function. They can be generalized in this role as the ψ_n component wave functions of the multi-electron wave function $\Psi(\psi_1, \psi_2, \psi_3,...)$. Thus, the natural orbitals are selected as satisfying by Ψ itself as being natural for its own description. These natural bond orbitals are symmetry adapted in the same sense that canonical molecular orbitals of Hartree-Fock theory are symmetry adapted.[163] Natural bond orbitals allow a more condensed description of Ψ than does Hartree-Fock theory, such that a minimal description of the core and valence shell natural orbitals is often adequate for describing chemical behaviour that is intimately related to standard valence concepts. One criticism of natural bond orbitals and NBO theory in general is that the valence sense of standard orbital overlap is lost when natural bond orbitals are employed in the description of the wavefunction Ψ. This is misleading, however, and can be rationalised by considering that the standard orbital overlap component of other descriptions of Ψ have been reframed as an integral component of the natural bond orbital wavefunctions ψ_n. Thus, bond orbital overlap effects are included intrinsically in the computation of Ψ when it is described in terms of natural bond orbitals. Another aspect of natural bond orbital theory derives from the classic Lewis octet rule for localized bonding in common main group elements. For higher

elements such as the transition metals, this can be extended from the eight electrons of a Lewis octet occupying a maximum of eight orbitals about an atom to an analogous dodectet of twelve electrons in accord with the higher orbital numbers of heavier elements. Thus the natural orbital concept automatically includes natural bond angles about any particular atom. This is applicable to metal-metal bonds in organometallic compounds such as copper paddlewheel frameworks (see chapter 4).

Natural orbital theory has been applied to many aspects of chemical behaviour that have otherwise proved to be not satisfactorily amenable to other theory approaches. Typically, this has been for reasons of the computational cost associated with obtaining accurate descriptions of the phenomena being addressed. It has been noted by Reed and Weinhold that classical bonding descriptions are closely tied to minimal basis set concepts computationally.[164] Natural bonding orbital theory in their study of the near-Hartree-Fock water dimer provides a significant insight regarding the extent to which orbital interactions other than basic σ and π orbitals are involved in chemical behaviour, as the n→σ* charge transfer interaction was revealed to be a significant contributor to the formation of hydrogen bonds between the two water molecules in the dimeric structure, as well as to the thermodynamic stability of the dimer itself. The computational approach utilised by Reed and Weinhold in that study was two-fold, beginning with the transformation of a set of atomic orbitals as input into an orthonormal set of natural atomic orbitals having optimal occupancy of electrons. Manipulation of these natural atomic orbitals divides them neatly into a natural set of core and valence orbitals that are highly occupied, and a residual set of 'Rydberg orbitals' having low or zero electronic occupancy values. Rydberg orbitals are vacant higher-energy orbitals that are available to accept an electron that has been appropriately excited. Atoms and molecules in which this has occurred are defined as being in a Rydberg state.

The second step in this approach was to form an optimal orthonormal set of directed hybrid orbitals and polarization coefficients to generate the final set of natural bond orbitals having maximal electronic occupancy properties that are localised on one or two centres rather than being delocalized over the entire molecule. Localisation on one centre corresponds to orbitals containing a 'lone pair' of electrons, while localisation on two centres corresponds to a molecular bond orbital. Reed and Weinhold further applied natural bond orbital theory to the study in steric interactions in molecules in regard to steric hindrance and internal rotation barriers as functions of hyperconjugation involving bonding and non-bonding or anti-bonding orbitals.[165] They reported that hyperbonding interactions, or interactions between bonding and antibonding orbitals, lends stabilization to certain conformations in molecules, while destabilizing others. This is understandable in that a bond geometry within a molecule in which bonding-antibonding orbital interaction tends to minimize the energy state of the molecule will be favoured over a molecular geometry in which such interaction would require the molecule to exist in a conformation that increases the energy state of the molecule. This kind of interaction should exist only along bonds separated by two or more atoms, such as the C—H bonds on the two carbon atoms of ethane, due to the geometric alignment of the appropriate orbital structures. In consideration of this restriction, Reed and Weinhold also found that interactions between geminal bonds and interactions involving Rydberg orbitals made little or no contribution and were relatively unimportant. The natural bond orbital approach used by Reed and Weinstein was found to be consistent across the series of compounds used in their studies, testifying to the utility of the methodology. A more complex study was reported by Badenhoop and Weinhold in an examination of various measures of steric repulsion.[166] Steric repulsion energy values had been typically obtained from linear free energy relationships or by fitting structural and transport properties obtained experimentally to assumed functional forms. However, proper identification of the terms contributing to the assumed functional forms was

controversial at best and problematic at worst. Badenhoop and Weinhold noted that low-level *ab initio* Hartree-Fock theory could yield accurate descriptions of repulsive interactions between closed shell systems, suggesting that natural bond orbital theory would yield equally good results at lower computational costs. In regard to computation, the natural bond orbital method can be applied to any wave function for which a Fock matrix can be generated, assuming that the package being used for computation contains a suitable programme for use with natural bond orbital theory. As mentioned above, natural bond orbital analysis partitions the wave function into a localised bond orbital and lone pair orbital description corresponding to the formal Lewis structure of the molecular system, and a residual set of low- occupancy orbitals. These latter are valence antibond orbitals and Rydberg orbitals existing outside of the valence sphere of the molecular system. They are normal in the sense of maximum electronic occupancy of the molecular system as they are necessary for retaining strict orthonormality and localisation that leads to high transferability of bond energies and close correspondence to chemical bonding concepts. Together, all these orbitals cover the entire span of the orbital basis set.

Each of the natural bond orbital functions is written as a linear combination of natural atomic orbitals derived from an associated non-orthogonal set that has the familiar shapes of the *s*, *p*, *d*, etc. atomic orbitals of the free hydrogen atom, and differs from their natural counterparts only in that they do not have a final orthogonalisation with other atoms in their descriptions. The natural bond orbitals can therefore be used to assess the relative strengths of interactions that lead to chemical bonding, as the sum of occupied natural bond orbital energy changes. Thus, steric repulsion, for example, can be expressed in terms of the relative energy changes of natural bond orbitals upon orthogonalisation, yielding results that are consistent with the classical 'Pauli repulsion' energy. The total exchange repulsion can be approximately

separated into local natural bond orbital interactions that add in a pairwise manner, using local partial deorthogonalisation. This allows the separation of purely steric or exchange contributions from delocalisation, charge transfer, induction, electrostatic and other effects. However, steric effects observed experimentally reflect the complex interactions of the complete *N*-electron distribution within a molecule, and not the theoretical construct obtained from natural bond orbital theory. The steric interaction energy is not necessarily just the simple repulsive exponential form obtained from empirical potentials. Natural bond orbital theory is particularly useful in illustrating energy relationships that exist in molecular interactions. According to Sajan and coworkers,[167] the most important orbitals in molecules with regard to molecular interactions are the highest occupied molecular orbital, the HOMO, and the lowest unoccupied molecular orbital, the LUMO. All 'normal' chemical activities occur only at the level of the outermost, or valence, electrons and atomic orbitals of the atoms involved in the interaction. By extension, this necessarily also means that normal chemical interactions between molecules only occur at the level of the outermost electrons and electronic orbitals in the system. Accordingly, the HOMO and LUMO determine how a molecule interacts with other species. The difference in energy between between the two, known as the HOMO-LUMO gap, characterises both the chemical reactivity and the kinetic stability of the system.[167] A small gap between the HOMO and LUMO energy values is associated with a molecular structure that is more polarisable and more chemically reactive. The HOMO functions as an electron donor in processes, and the LUMO necessarily functions as the electron accceptor in those processes. It is intuitively obvious that as the HOMO-LUMO energy gap in a molecular system decreases, less energy is required to excite an electron from the HOMO level to the LUMO level. The closer the HOMO and LUMO energies are, the easier it is for the HOMO to donate an electron to the LUMO, and the easier it is for the LUMO to accept an electron from the HOMO.

Natural bond order analysis provides results that describe single 'free' molecules, on a par with more complex and more computationally expensive approaches. The implication is that natural bond orbital theory should be more generally applicable. Dunnington and Schmidt[168] have reported the application of generalised natural bond orbital analysis to bulk materials and periodic surface models. Natural bond orbital analysis provides a straightforward and computationally efficient methodology to decompose complex quantum mechanical results into a chemically intuitive representation in which molecular orbitals are described in terms of one- or two-centred orbitals. The one-centred molecular orbital corresponds generally to an orbital containing a 'lone pair' of electrons, while the two-centred molecular orbital corresponds to the orbital of a two-electron chemical bond. However, the delocalised bonding expected in metals is not well described by the one- and two-centred bonding interactions to which natural bond orbital implementation is currently limited. Dunnington and Schmidt bypass this limitation by the use of a projection method in the implementation that allows the description of bulk materials and periodic surfaces by natural bond orbital analysis. Bulk materials and periodic surfaces are essentially the image of metal-organic frameworks such as copper paddlewheel molecules. Petkov *et al*[169] have noted that the crystalline structure of metal-organic framework compounds puts all of the metal atoms in exactly the same environment, in a periodic arrangement both within the structure and across the surface of the crystal lattice. This allows for systematic spectroscopic studies such as nuclear magnetic resonance analysis on interaction with different chemical species, conducive to natural bond orbital analysis as well. The periodic natural bonding orbital method used by Dunnington and Schmidt yielded results that are directly comparable to those for isolated molecules, providing a localised perspective of bonding and reactivity.

2.4: Conclusions

This chapter outlined some of the basic computational theories and techniques employed to chemical systems. The discussion began with a brief overview of the atomistic models and why they are unsuitable for computing chemical systems. The discussion then shifted to the rationale behind electronic structure methods and the need to use quantum mechanics to solve the problem of obtaining the electronic structure. The importance of the Born-Oppenheimer approximation in electronic structure theory was considered. This led to a development of the Hartree-Fock-Roothaan method and an introduction to correlated methods. Due to the computational effort required to perform post-Hartree-Fock correlated calculations, an alternate approach to obtaining electron correlation (density functional theory) was outlined with respect to Kohn-Sham theory. The similarities and differences between the Kohn-Sham and Hartree-Fock equations (and wavefunctions) were elaborated. The chapter ends with a discussion of the basis set approximation and why it can be used instead of the atomic orbitals.

Chapter 3: A Theoretical Study of Gas Adsorption in series of Metal-Organic Frameworks

3.1: Introduction

The aim of this section is to provide a short review of the structure of zirconium clusters, the methodology of calculating the adsorption isotherms for various gases in a zinc 'paddlewheels' and zirconium clusters having an assortment of different functional groups on the organic linker molecules. Four cases will be examined in the calculations the binding energy of the different gases adsorbed in the clusters is calculated. The theoretical basis for the calculations used in this study is also reviewed, as a sound understanding of the concept is needed to justify the validity of the calculations.

3.2: Metal-Organic-Frameworks (MOFs)

Metal-organic frameworks have been well studied, and have been discussed in this study already (see chapter one). The electronic structure of metal atoms in metal-organic frameworks permits the coordination of ligands in specific geometries that reflect minimum electronic energy states of the central metal atoms. Depending on the specific type of coordination and electron distribution, an essentially infinite variety of such metal-organic compounds is possible. The basic details of metal-organic frameworks are reviewed briefly before discussing the experimental results for the systems under consideration in detail.

Metal-organic framework (MOF) molecules are a relatively new class of crystalline porous compounds, first synthesized and reported by Robson[26] in the early 1990s then by Yaghi, and now numbering in the thousands.[170] MOFs are hybrid materials that form from the interaction of metal atoms or ions and multifunctional organic ligands. The successful synthesis of an MOF compound that retained robust structural rigidity was first reported by Li, Eddaoudi,

O'Keeffe and Yahgi,[55] demonstrating the potential for the use of MOFs in many applications (see also Rowsell and Yahgi).[171]

In the crystal structure of MOF compound, the metal atoms are referred to as backbone atoms and the organic molecules that link the metal atoms together are called 'linkers'. The backbone atoms are generally present as clusters of two or more, depending on the specific MOFs. Due to the complexity of naming of MOFs according to IUPAC standards for the naming of metal-organic compounds,[172] MOFs are typically identified by a trivial designation taken from their point of origin and a chronological identifying number. Thus, e.g. the compounds produced by Yaghi's research group at University of California, Berkeley, are typically identified using MOF-xxxx as the identifier of any specific MOF compound.[173] UiO-xxxx is used to identify compounds developed at Universitet i Oslo, while MIL-xxxx for Materials Institute Lavoisier, and HKUST-xxxx for Hong Kong University of Science and Technology identify the points of origin of the corresponding MOFs. Yaghi's group have also elucidated the geometric and structural requirements of MOFs in regard to the nature of the ligands and coordination geometry of the metal atoms and clusters that make up the MOF.[173]

The interaction of metal atoms with bidentate organic ligands offers a substantially greater variety of structural variations due to the availability of multiple functional groups on a single organic molecule. It can be readily seen that for example two of the carboxylate groups can occupy coordination sites about one metal atom at one end, while the second carboxylate groups can occupy coordination sites about a second metal atom, forming a bridge between the two metal atoms. In a 'paddlewheel' complex, the two oxygen atoms of a carboxylate function of each occupy coordination sites on a cluster of two metal atoms. With the carbon atom of the carboxylate functional group a five-membered ring structure is formed, and when three additional carboxylate ligands are similarly coordinated about the same metal atom cluster, the overall structure can be likened to a paddlewheel.

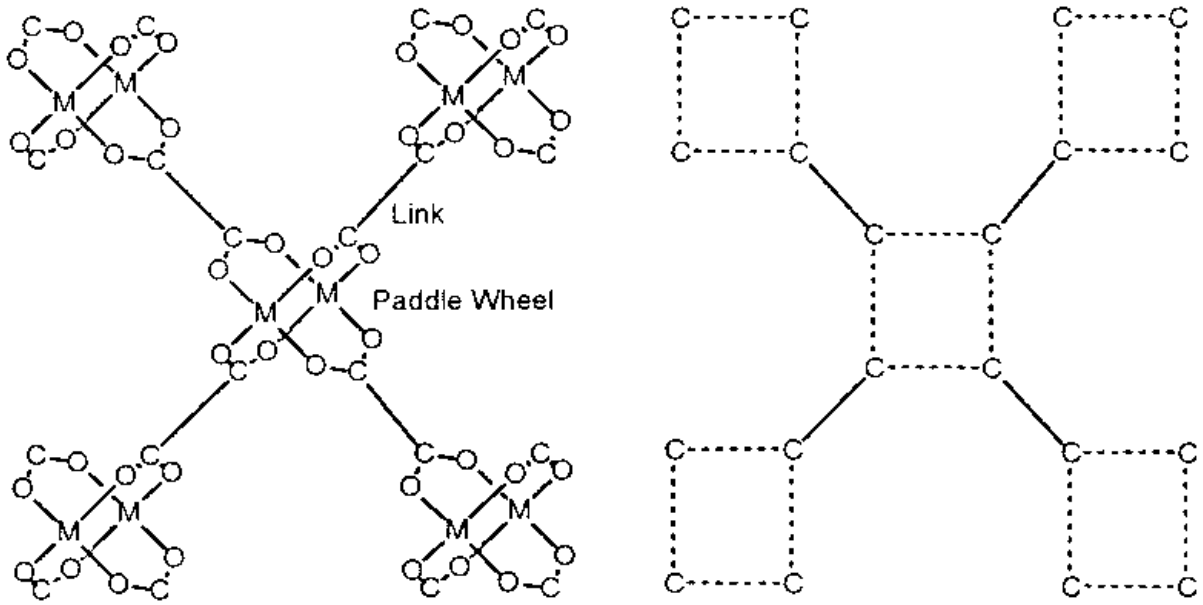

Figure 3-1: paddlewheel structure motif. Copyright (2002) National Academy of Sciences. Reproduced with permission from Ref 173.

The two central metal atoms form the axis of the paddlewheel, the four 'paddles' are formed by the four ligand molecules. This effectively extends the potential length of the resultant molecule to infinite size, depending of course on the availability of polymerisable material. Thus, the formation of the crystalline form of a paddlewheel compound can theoretically become an infinite two-dimensional array of conjoined paddlewheel structures that is described as a metal-organic network (MON). In this basic structure, in which the metal atoms are tetracoordinate, coordination is not saturated. That is to say, not all of the available coordination sites that are available on the metal atoms have been satisfied, and at least two sites are available to coordinate other ligands. The two sites are diametrically opposed to each other at opposite ends of the metal-metal axis. When a third functionality is added to the linker molecule, enabling it to coordinate to a different metal cluster, coordination extends in three dimensions and the resulting crystal structure of such an MOF is characterised by large interstitial pores that are able to accommodate a variety of molecules in a stable arrangement.

3.3: Bonding Considerations in MOFs

MOFs formed around *3d* transition metals have been studied and analysed extensively to obtain an understanding of the electronic nature of bonding within the structures. Such investigations invariably have a computational component. A variety of computational models employing defined bases sets and functional are available for application in such studies, using density functional theory (DFT) calculations. Chase, Rudshteyn, Psiuck *et al* recently reported that hybrid functionals identified as B3LYP, ωB97X-D, PBE0 and B97-1 used in combination with the basis set 6-311G(d,p) provide good agreement of computational results with experimental data.[174] (The present study uses the same basis set). Kim, Kang and Wei examined the interaction of adsorbed molecular hydrogen in paddlewheel MOFs based on copper with tetracarboxylate linkers, using DFT .[175] They found that orbital coupling between H_2 and Cu_2 in the molecule apparently occurs between the occupied σ molecular orbital of H_2 and the unoccupied *4s* orbitals of the copper atoms. The same type of bonding interaction was found for the corresponding zinc-based MOF. For similar MOFs based on manganese, iron, cobalt and nickel, it was found that the bonding interaction occurred between the H_2 σ bond and the d_z^2 orbital of the metal atoms. For scandium, titanium and vanadium-based MOFs, the binding mechanism was determined to be between the H_2 σ orbital and the d_z^2 of the metal atoms.

3.4: DFT Methodology and Calculations

Density functional theory (DFT) has become a very successful computational means of describing the electronic structure of matter. Beginning from the ground state properties of a system, DFT is applicable to a large variety of electronic systems, including atoms and molecules, nuclei, solid or condensed matter, as well as quantum and classical fluids. The methodology been used to investigate spin-polarized systems, multicomponent systems, free energies at real temperatures, super conductance, kinetic phenomena, molecular dynamics, and

many others. Some particular molecular properties that are successfully described by DFT include molecular structure, vibrational frequencies, atomisation and ionisation energies, electromagnetic properties, and reaction pathways. For a more extensive discussion of DFT, see chapter 2.

3.5: Application of DFT to Study Gas adsorption in Series of Metal-Organic Frameworks

3.5.1: Adsorption of Carbon Dioxide by Simple Zinc Paddlewheel Compounds

In order to test and become familiar with the computational methodology, a small study of carbon dioxide adsorption in zinc-based paddlewheel MOFs was carried out prior to the application of the methods to the zirconium-based systems that are the major focus of this study. Alzahrani and Deeth had carried out a modelling study of zinc paddlewheel MOFs, in which they utilized DFT-optimized model systems with an all-atom first-principles force field to describe the pore structure of the compounds.[176] However, their study was intended to account for the structural changes that occur in the particular MOFs upon adsorption of dimethylformamide or benzene, rather than small molecule gases like carbon dioxide. This approach produced good agreement between calculated and observed structural changes. In comparison, other approaches have been applied to the calculation of physicochemical properties of MOFs. Coudert and Fuchs described the application of the Grand Canonical Monte Carlo method for the calculation of adsorption properties and short-range interactions of MOFs, though they also report this approach is ultimately unsatisfactory for calculating host-guest interactions with coordinative unsaturated metal sites.[177] For this, Coudert and Fuchs state that *ab initio* DFT methods are needed.

3.5.1.1: General Overview

Numerous reports of e.g. zinc coordination motifs with benzenedicarboxylate ligands exist. One of the common flexible paddlewheel MOFs contains a zinc motif, with a square paddlewheel grid. Such as structure called MOF-2, [Zn(BDC)·(DMF)(H_2O)] was first reported by Yaghi et al.[55] It has a calculated 270 m^2/g Langmuir apparent surface area for N_2 and 310 m^2/g for CO_2. Later, Yaghi and coworkers,[178] synthesized 2-D and 3-D network solids by reacting H_2-BDC (BDC= 1,4-benzenedicarboxylate) with $Zn(NO_3)_2$ under various conditions using the diffusion method. MOF-46 was the first reported amine-functionalized MOF with a robust three-dimensional (3D) framework, constructed by using 2-amino-1,4-benzene-dicarboxylate (NH_2BDC) linkers and Zn^{+2} ions. It is worth noting that some substituents on the benzene ring result in a rotation of the benzene ring out of the plane of the carboxylate group. As a consequence, certain side groups such as methyl groups will hinder formation of the MOF, since the side groups will clash with each other. Other substituents, for example amino groups, do not give this rotation due to favourable intramolecular N-H···O hydrogen bonds, which mean that there is a large apparent barrier to rotation.

In investigating the thermochemical behaviour of the compound MOF-5, prepared from ZnO, 1,4-benzenedicarboxylic acid and diethylformamide, results were obtained that suggested that entrained diethylformamide in the MOF structure as occluded solvent played only a space-filling role in the structure and did not affect the energetics of the compound.[179]

Millward & Yaghi 2005[90] reported a series of IRMOFs. They found that at 35 bar, MOF-177 can adsorb more CO_2 than for example, zeolite 13X and MAXSORB due to the high internal surface area of MOFs, figure 3-2. They also found that the amine-functionalized MOFs have a significant affinity towards CO_2. Despite a decrease in the BET surface area from 2833 to 2160 m^2/g, $Zn_4O(BDC)_3$ (IRMOF-1 or MOF-5) adsorbs approximately 4.6 wt % CO_2 whilst

the amine-functionalized variant $Zn_4O(NH_2\text{-}BDC)_3$ (IRMOF-3) adsorbs 5.0 wt % CO_2 at 298 K and 1.1 bar. The explanation for this is the CO_2 can bind to the nitrogen of amine either via hydrogen bonding or via an interaction with the lone electron pair. In fact, alkylamine solutions are commonly used in acid gas removal.[90]

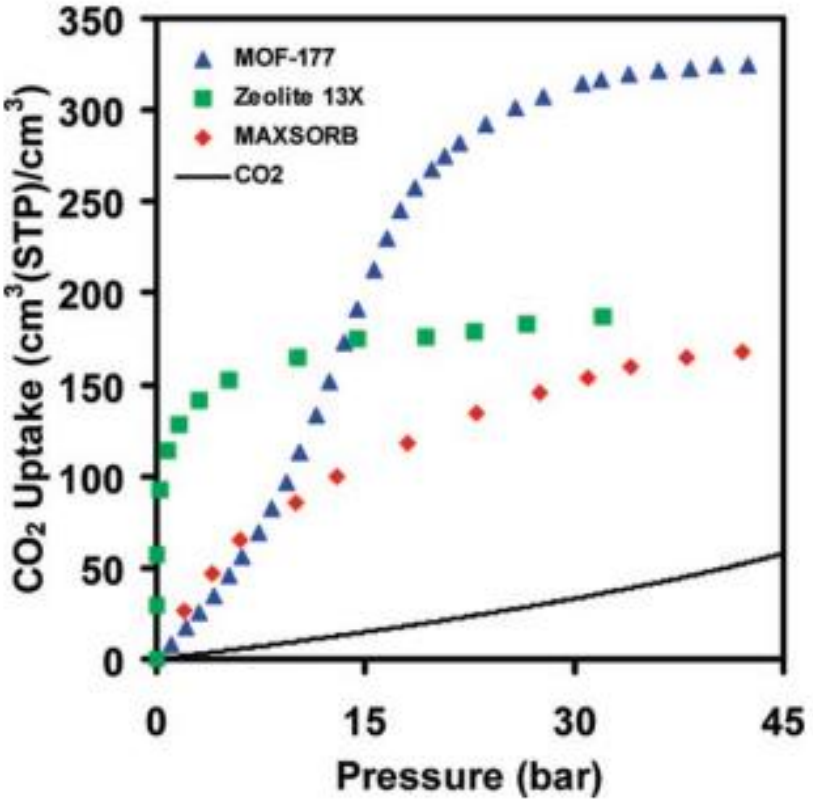

Figure 3-2: Comparison of the volumetric CO_2 capacity of crystalline MOF-177 relative to zeolite 13X pellets, MAXSORB carbon powder, and pressurized CO_2. Reprinted (adapted) with permission from Ref 90. Copyright (2005) American Chemical Society.

Howe et al.[180] examined the potential of a series of MOF-2, M-BDCs (1,4-benzenedicarboxylic acid) MOF, M = Zn, Cu, and Co in capturing flue gas molecules (NO_2, SO_2, CO_2, CO, H_2S and H_2O). They found that MOFs exhibiting open-metal sites (OMS) display strong adsorption sites for acid gases. SO_2 gas shows the strongest binding to the open metal site in Zn-BDC MOFs, a result of "strong electrostatic and orbital interactions enabling an energetically favourable distortion of the Zn-BDC open-metal site toward a preferred

tetrahedral or trigonal bipyramidal geometry from its square planar geometry in MOF-2 and M-BDC nanosheets."[180]

3.5.1.2: Computational Details

In this preliminary study, the adsorption of carbon dioxide on a series of simple zinc-based paddlewheel complexes was evaluated. These consisted of a pair of Zn^{2+} ions coordinated to one or two bridging bidentate *o*-aminoterephthalate monanions and a corresponding number of bridging formate anions to enable a paddlewheel structure. The remaining coordination sites about the metal atoms are occupied by coordinated dimethylformamide or water molecules. Our calculations were carried out using density functional theory with the B3LYP functional[181] and the 6-311G(d,p)[182, 183] basis set for H, C, O, N and SDD[184] for Zn as implemented in Gaussian 09.[185] The binding energies of the adsorbed gases, in kJ/mol, were calculated using the equation:

$$E_B = E_{GAS + CLUSTER} - E_{CLUSTER} - E_{GAS}$$

3.5.1.3: Results and Discussion

Table 3-1: Binding energies of CO_2 in selected Zn paddlewheel systems.

Zn Paddlewheel MOF	**B.E. kJ/mol**	
$[Zn_2(\mu\text{-}O_2C(syn\text{-}C_6H_3NH_2)COOH)(\mu\text{-}O_2CH)_3(H_2O)_2]$	-28.3	Figure 3-3
$[Zn_2(\mu\text{-}O_2C(anti\text{-}C_6H_3NH_2)COOH)(\mu\text{-}O_2CH)_3(H_2O)_2]$	-14.0	Figure 3-4
$[Zn_2(\mu\text{-}O_2C(syn\text{-}C_6H_3NH_2)COOH)(\mu\text{-}O_2CH)_3(DMF)_2]$	-7.8	Figure 3-5
cis-$[Zn_2(\mu\text{-}O_2C(syn\text{-}C_6H_3NH_2)COOH)(\mu\text{-}O_2C(C_6H_4)COOH)((\mu\text{-}O_2CH)_2(H_2O)_2]$	-12.7	Figure 3-6
$[Zn_2(\mu\text{-}O_2C(anti\text{-}C_6H_3NH_2)COOH)(\mu\text{-}O_2CH)_3(H_2O)_2]_2$	-17.8	Figure 3-7

The simplest structure of the zinc series, shown in figure 3-3, has the formula [Zn_2(μ-O_2C(*syn*-$C_6H_3NH_2$)COOH)(μ-$O_2CH)_3(H_2O)_2$]. The two coordinated water molecules occupy the axial positions of the structure, one on either side of the paddlewheel formed by the aminoterephthalate and formate ligands. The precise locations of adsorbed species are determined by the sum of both chemisorption and physisorption interactions. In this case, adsorbed carbon dioxide occupies a position between the *o*-amino group of the terephthalate ligand and the adjacent axial water molecule. As can be seen in figure 3-3, the binding energy is -28.3 kJ/mol. The oxygen atoms of the carbon dioxide molecule are situated at 1.98 Å from the hydrogen atom of the axial water molecule and 3.59 Å from the nearest hydrogen atom of the amino group on the terephthalate ligand. This represents the closest binding of the adsorbed carbon dioxide molecule in the series.

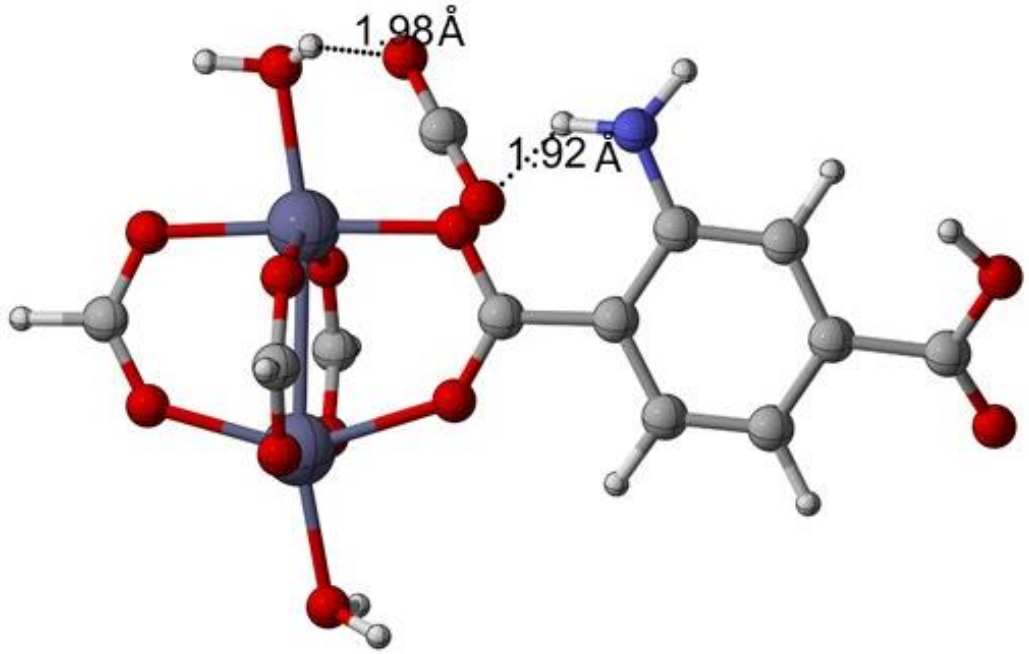

Figure 3-3: CO_2 capture in a [Zn_2(μ-O_2C(syn-$C_6H_3NH_2$)COOH)(μ-$O_2CH)_3(H_2O)_2$] single zinc paddlewheel with bridging terephthalate and capping formate ions in the equatorial positions and water in the axial position. CO_2 is shown in a H-bonding arrangement with one of the axial water molecules as well as with the amino-group on the benzene ring.

Figure 3-4 shows the isomeric structure [Zn_2(μ-O_2C(*anti*-$C_6H_3NH_2$)COOH)(μ-$O_2CH)_3(H_2O)_2$], in which the *o*-amino group of the terephthalate ligand is distant from rather than adjacent to the zinc cluster. The binding energy is -14.0 kJ/mol. In this case, here, it can be seen that at the minimum energy configuration of the adsorbed carbon dioxide molecule has one of the oxygen atoms at a distance of 2.02 Å from the hydrogen atom of the axial water molecule, and 2.49 Å from the nearest hydrogen atom of the *o*-amino group of the terephthalate ligand.

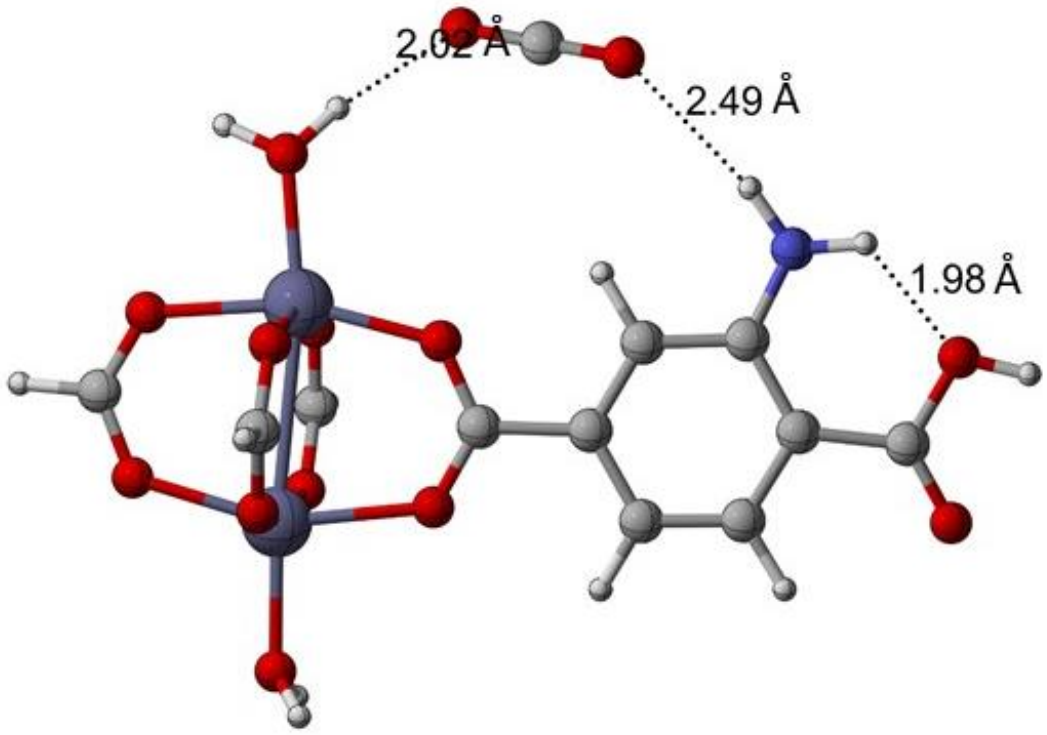

Figure 3-4: CO_2 capture in a [Zn_2(μ-O_2C(*anti*-$C_6H_3NH_2$)COOH)(μ-$O_2CH)_3(H_2O)_2$] single zinc paddlewheel with bridging terephthalate and capping formate ions in the equatorial positions and water in the axial position. CO_2 is shown in a H-bonding arrangement with the amino-group on the benzene ring and one of the axial water molecules.

As the only difference between the structures in figures 3-3 and 3-4 is the position of the *o*-amino group relative to the zinc atoms, it is clear that the amount of carbon dioxide that a given quantity of the complex would be able to adsorb, and the strength with which the adsorbed molecules are bound to the surface of the complex structure, are greatly affected by

such structural variations.

For the configuration shown in figure 3-5, the binding energy is -7.8 kJ/mol. In this case, the axial water molecules have been replaced by molecules of dimethylformamide (DMF), giving the compound $[Zn_2(\mu\text{-}O_2C(syn\text{-}C_6H_3NH_2)COOH)(\mu\text{-}O_2CH)_3(DMF)_2]$ with the structure analogous to that of the compound with axial water molecules. Here, it can be seen that at the minimum energy structure an adsorbed carbon dioxide molecule has one of the oxygen atoms at a distance of 2.45 Å from the nearest hydrogen atom of the *o*-amino group on the terephthalate ligand. The other oxygen atom is situated at a distance of 2.75 Å from the nearest hydrogen atom of the adjacent axial DMF molecule. The two remaining compounds studied in this series have notably different structures.

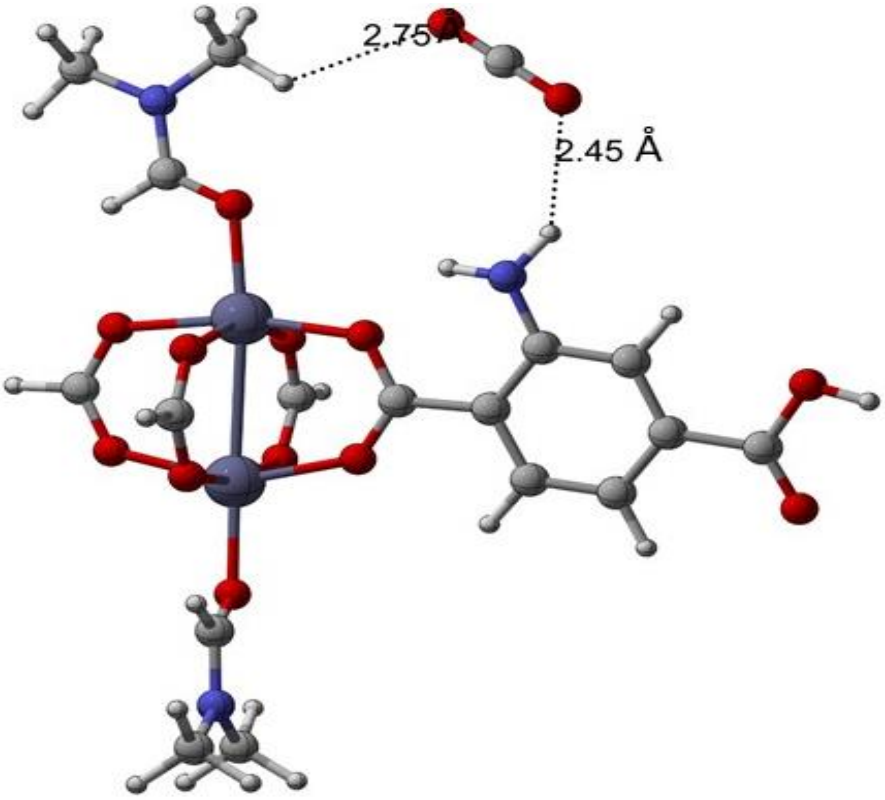

Figure 3-5: CO_2 capture in a $[Zn_2(\mu\text{-}O_2C(syn\text{-}C_6H_3NH_2)COOH)(\mu\text{-}O_2CH)_3(DMF)_2]$ single zinc paddlewheel with bridging terephthalate and capping formate ions in the equatorial positions and DMF in the axial position. CO_2 is shown in a H-bonding arrangement with the amino side-group of benzene and one of the axial DMF molecules.

Figure 3-6 illustrates the structure formed when one of the bridging formate groups in [Zn_2(μ-O_2C(*syn*-$C_6H_3NH_2$)COOH)(μ-$O_2CH)_3(H_2O)_2$] is replaced by a bridging terephthalate mono anion in the *cis*- position relative to the *o*-aminoterephthalate ligand, as cis-[Zn_2(μ-O_2C(syn-$C_6H_3NH_2$)COOH)(μ-$O_2C(C_6H_4)$COOH)(μ-$O_2CH)_2$ ($H_2O)_2$]

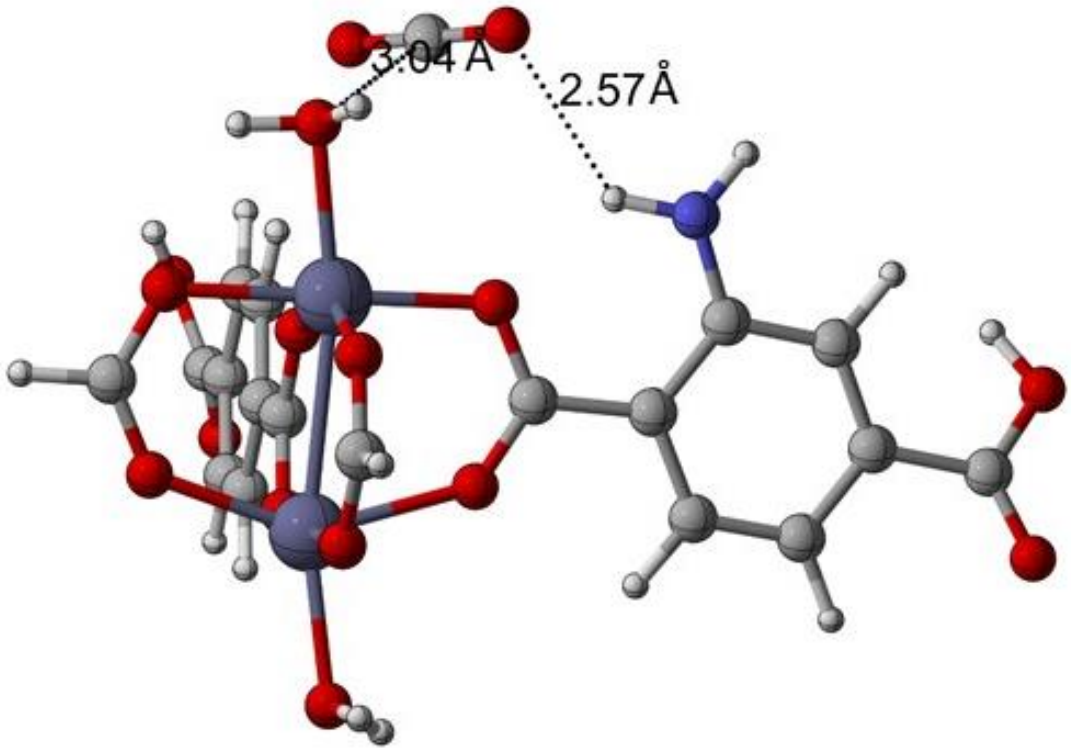

Figure 3-6: CO_2 capture in a *cis*-[Zn_2(μ-O_2C(*syn*-$C_6H_3NH_2$)COOH)(μ-$O_2C(C_6H_4)$ COOH) (μ-$O_2CH)_2(H_2O)_2$] single zinc paddlewheel with bridging terephthalate and capping formate ions and extra terephthalate in the equatorial positions and water in the axial position. CO_2 is shown in a H-bonding arrangement with the amino side-group of benzene and with a weak H-bond with one of the axial water molecules.

In this structure, for the minimum energy configuration, the binding site of the adsorbed carbon dioxide molecule has changed, such that the central carbon atom is now situated 3.04Å from the oxygen atom of the axial water molecule, and one of the terminal oxygen atoms of the carbon dioxide molecule is located 2.57Å from the nearest hydrogen atom of the *o*-amino function on the *o*-aminoterephthalate ligand. The binding energy is -12.7 kJ/mol in this case.

Finally, in figure 3-7, a very different structure is represented by the double-paddlewheel

structure in which a single *o*-aminoterephthalate dianion acts as a bridging ligand to two separate zinc clusters. In this structure, the binding energy is -17.8 kJ/mol. The minimum energy structure has the terminal oxygen atoms of the carbon dioxide molecule coordinated at one end to the nearest hydrogen atom of the *o*-amino group, and at the other end to the nearest hydrogen atom of an axially-coordinated water molecule, at distances of 2.43Å and 2.01Å respectively.

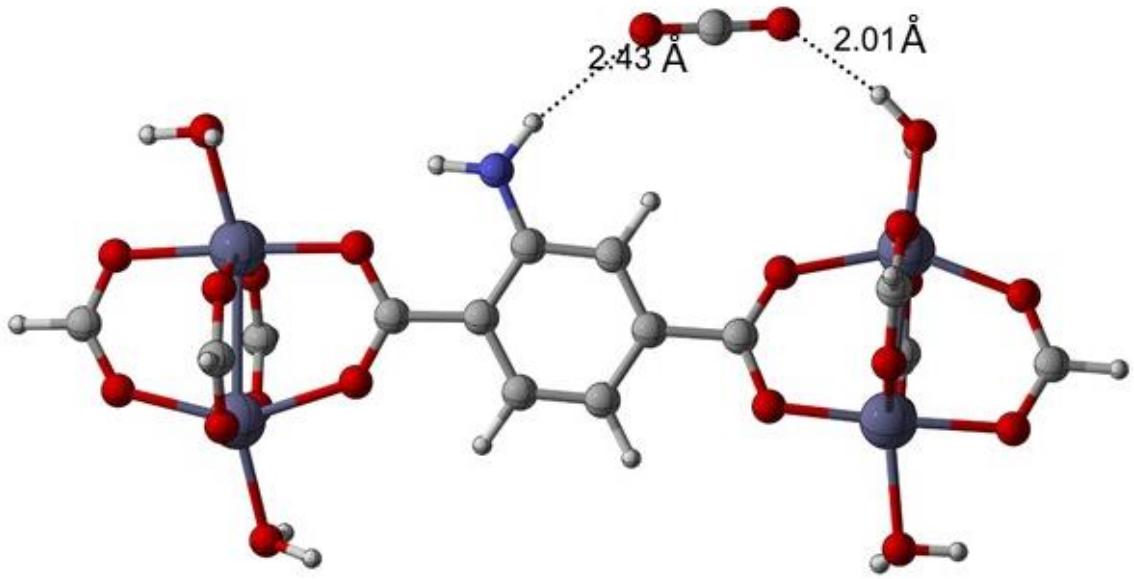

Figure 3-7: CO_2 capture in a $[Zn_2(\mu\text{-}O_2C(anti\text{-}C_6H_3NH_2)COOH)(\mu\text{-}O_2CH)_3(H_2O)_2]_2$ double zinc paddlewheel with bridging terephthalate and capping formate ions in the equatorial positions and water in the axial position. CO_2 is shown in a H-bonding arrangement with the amino side-group of benzene and one of the axial water molecules.

These distances suggest that the adsorbed carbon dioxide molecule may experience a stronger binding energy (calculated as suggested on page 87) in what corresponds to a larger pore size as would exist in a fully structured metal-organic framework material.

As a preliminary or introductory examination of the methodology to be used with zirconium cluster metal-organic framework compounds, this series of zinc-based compounds provides some valuable clues for the properties that might be expected. Specifically, by viewing

the rigid structure of the zinc-formate paddlewheel as analogous to the rigid structure of the zirconium cluster in those compounds, the terephthalate ligand can be viewed as the linker molecule of the framework. Since this determines the pore size and shape in a metal-organic framework, these factors and the 'landscape' within the pore structure with respect to functional groups and weak attractive forces determine the binding energy of adsorbed materials. As a first approximation, the larger the pore size, the more material that can be adsorbed on a metal-organic framework. The presence of specific functional groups within the pore can have either a strengthening or a weakening influence on the binding energy of adsorbed molecules, which should be reflected in the distances between the adsorbed molecule and its neighbouring atoms within the pore structure of the framework. The approach of tailoring the structure of the pore interior of metal-organic framework materials to suit adsorption of a particular material or type of materials has been stated and described in the literature.[186] In addition, pore structure in metal-organic frameworks can be changed by a process of ligand exchange, providing another approach to tailoring of pore properties.[187] In light of these aspects, the calculation of binding energy in metal-organic frameworks is fundamental to understanding the dynamics of adsorption on metal-organic frameworks.

3.5.2: Zirconium-based MOFs

The main focus of the work in this chapter is on gas adsorption of a number of different gases in Zr-based MOFs. Thus, we are interested in how modifications in the ligands changes the adsorption characteristics of the MOF (section 3.2.1) and how the presence of contaminants (in particular water) change adsorption energies. Furthermore, it is clear from the literature that the choice of DFT functional in the calculations can have a significant effect. Therefore, we have investigated this as well.

3.5.2.1: General Overview

The development of MOFs can be shown through the progression from simple metal ions to complicated secondary building units (SBUs).[188-190] In particular, we are interested here in Zr_6O_8 clusters, which form part of a variety of clusters involving Zr.[191-195] An Zr_6O_8 cluster has the formula $[Zr_6(\mu_3\text{-}O)_4(\mu_3\text{-}OH)_4]^{+2}$. Two common forms are observed during exposing to high temperature: hydroxylated and dehydroxyated phases leading to a distorted $Zr_6(\mu_3\text{-}O)_4(\mu_3\text{-}OH)_4$ cluster, UiO-66. Since the discovery of $Zr_6(\mu_3\text{-}O)_4(\mu_3\text{-}OH)_4$ clusters and their properties, mostly Zr (IV) carboxylates have been reported in the literature.[196-201]

Zirconium-based MOFs have great potential for gas storage, catalysis, and drug delivery, and offer possibilities for research and development as well. For example, Ganesh, Hemalatha, Peng *et al* prepared a Zr-fumarate MOF using zirconium chloride and fumaric acid under solvothermal conditions and without adding formic acid for modulation. They then determined that the material is able to adsorb up to 8% carbon dioxide by weight.[202] The best-known and most well-studied zirconium-based MOF is UiO-66. The compound is described as having exceptional hydrothermal stability due to the strong bonds formed between the Zr^{4+} ion and the carboxylate functionality of the linker ligands. This structure is characterized by the presence of both octahedral and tetrahedral 'cage' pores connected by triangular 'window' channels. The material retains its crystalline structure in polar protic solvents such as water and alcohols, and is similarly robust through treatment with hydrochloric acid at pH = 1 or with aqueous sodium hydroxide at pH = 14.[203]

The development of zirconium-based MOFs has received considerable attention recently, due to the high availability and low cost of zirconium itself, and the high thermal and structural stability of zirconium-based MOFs.[204] The desirable properties of zirconium-based MOFs have thus spurred on the development of more effective synthetic methods for the materials that includes high through-put methods, as reported by Kelty *et al* for the synthesis

and characterization of zirconium-porphyrin MOFs on a nanocrystalline scale,[205] and "green" synthetic methods, as reported by Reinsch *et al*.[206] The former illustrates a common feature of zirconium-based MOFs, which is that the coherence of the crystal structure of the compounds is greatly enhanced by the presence of a mediating acid in the reaction medium. The crystal structures of the porphyrinic MOFs produced by Kelty *et al*. typically reveal structures that are supported by octahedral clusters of six zirconium atoms, and the dependency of product identity on both the molecular size and the acid strength of the mediating acid used in the synthetic procedure.[205] Most zirconium-based MOFs that have carboxylate linkers are built upon clusters of six zirconium atoms that are capable of coordinating as many as twelve carboxylate functional groups. Using zirconium sulphate in an aqueous medium, Reinsch *et al*. avoided the use of both a mediating acid and DMF as the reaction medium, to produce several ziroconium-based MOFs.[206]

3.5.2.2: Defects in Zirconium based MOFs

The larger coordination sphere of $ZrO_6(\mu_3\text{-}O)_4(\mu_3\text{-}OH)_4$ in MOF structures not only enables the coordination of a greater number of linker molecules, it also increases the probability that as the crystal structure of the MOF forms, coordination sites can be missed in such a way that the crystal structure encloses vacant sites that would normally be occupied by a linker molecule.

Such missed sites constitute missing linker defects in the crystal structure. Hereby, the defect structures may have different types including vacancies, substitutions, and "dangling" linkers. Szilágyi *et al.* pointed out that introducing defects into MOFs can make them promising adsorbers due to the large resultant pores.[207] In fact, they observed enhanced methane uptake of treated MIL-101(Cr) by 33% compared to the original MOF. They found that by introducing $NH_2\text{-}BDC_2^-$ (BDC_2^- = 1,4-benzenedicarboxylate), 20% of the BDC_2^- linkers were exchanged through solvent-assisted linker exchange (SALE). They established that these defects (see

figure 3-8) have an important role as it allows access of CH_4 into MIL-101 superclusters.

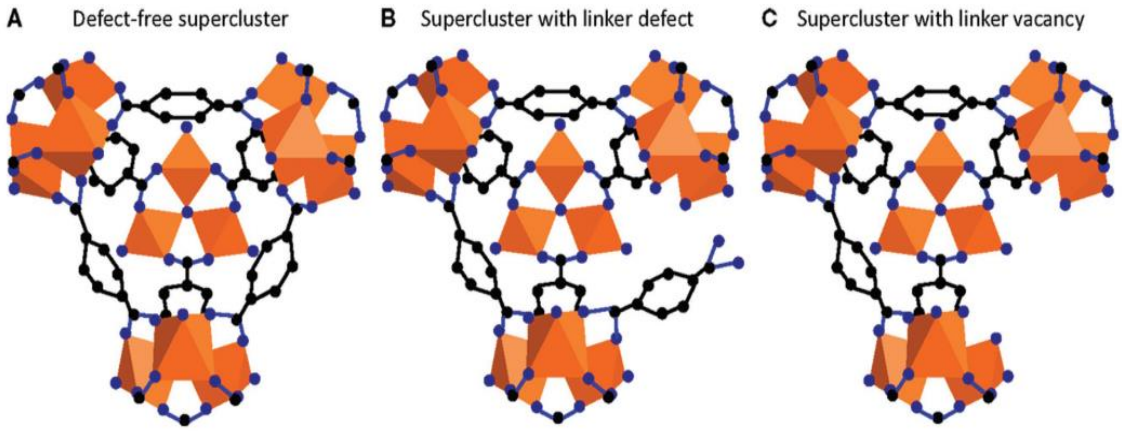

Figure 3-8: MIL-101 supercluster A) defect-free, B) with dangling linker, and C) with linker vacancy. The orange polyhedra represent the cationic units,whereas C and O atoms are depicted in black and blue, respectively. Reproduced with permission from P. Á. Szilágyi et al., Frontiers, 2016, Ref 207.

Lee *et al.*[208] reported on MUF-32 (Massey University Framework) (see figure 3-9), which is constructed from, 1,4-diazabicyclo[2.2.2]octane (dabco), 4,4′-bipyridine (bipy), 4,4′,4″-nitrilotrisbenzoate, (ntb) as ligands, and zinc (II) as metal. Subsequently, vacancy defects were introduced by partial removal of the dabco and bipy ligands. Those defects were successfully correlated with CO_2 adsorption. They found that samples with more bipy vacancies showed higher CO_2 uptake than pristine MUF-32, indicating that defects improve the adsorption efficiencies. In this case at the bipy vacancies, dabco ligands act as a N-donor, coordinating to the axial sites of the Zn PW, which can then interact with CO_2.

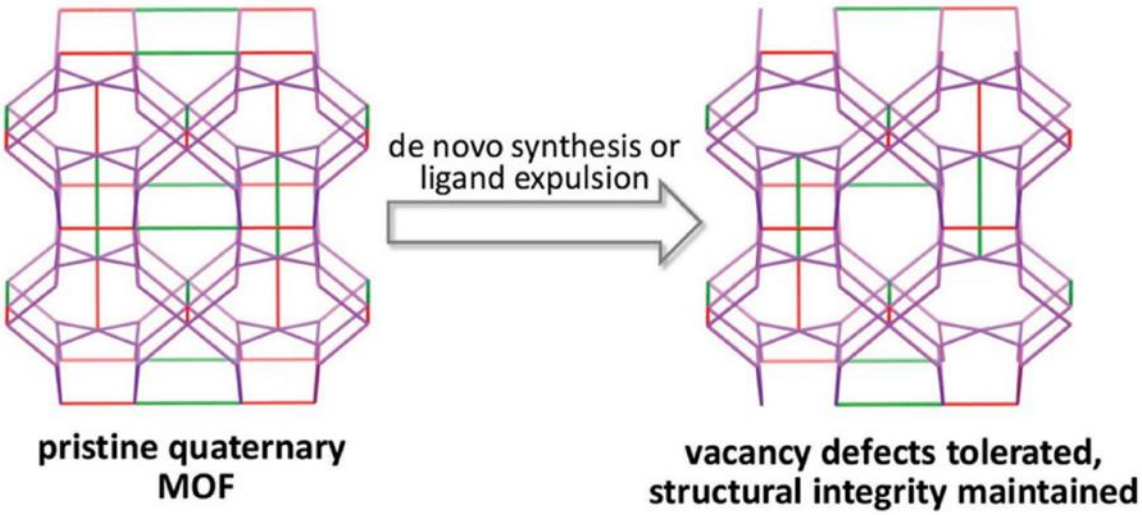

Figure 3-9: Formation of vacancy defects in MUF-32. Reproduced with permission from Ref 208. Copyright 2016, American Chemical Society.

Defective MOFs, in particular UiO-66 and its isoreticular versions, have been extensively researched in the literature.[209-212] The missing linker defects in UiO-66 based MOFs were first reported by Valenzano *et al*.,[54] where a significant weight loss of aromatics was noted by thermal treatment in conjunction with the observation of FT-IR bands which were associated with OH groups at high temperature. Hu et al.[213] reported a series of modified UiO-66 based MOFs using metalated-ligand exchange. They obtained UiO-66 with a high BET surface area of 1730 m^2 g^{-1} and extra mesopores of 3.9 nm. The new series of UiO-66-type MOFs: UiO-66-$(COONa)_2$-EX and the UiO-66-$(COOLi)_4$-EX MOFs is generated effectively through the metalated-ligand-exchange reactions (EX) (see figure 3-10), was found to have a high CO_2 uptake as a result of electrostatic and van der Waals interactions.

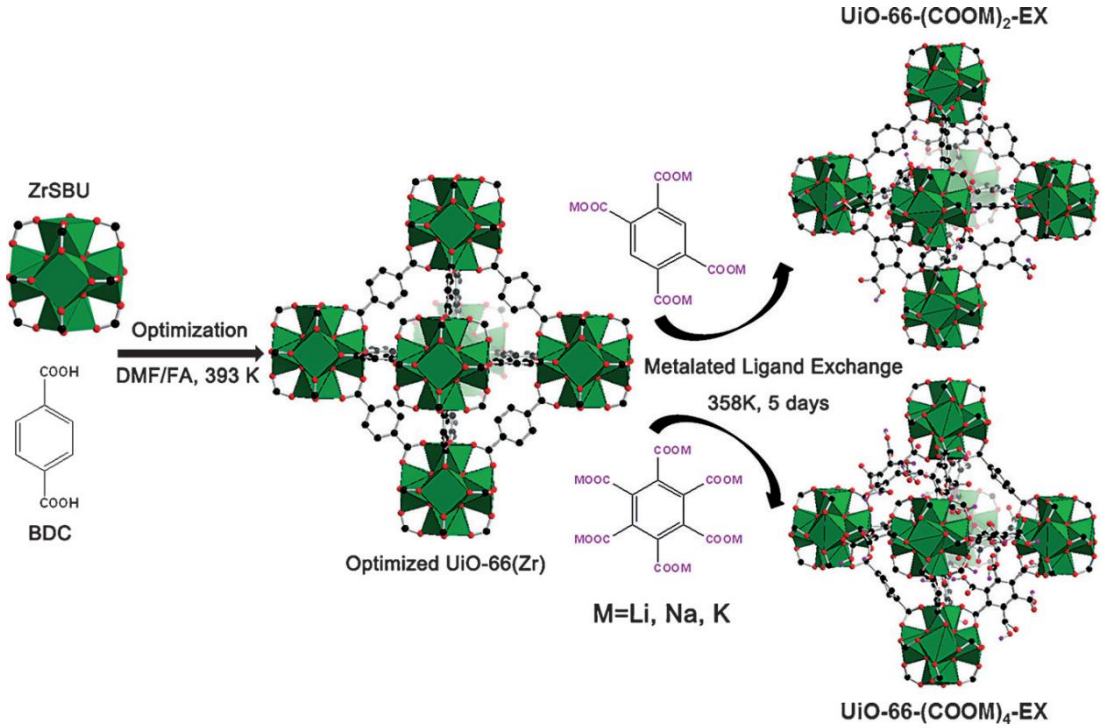

Figure 3-10: Optimization and metalated ligand exchange in UiO-66. Reproduced with permission from Ref 213.

Wu et al. reported that the mediating acid plays a key role in controlling the occurrence of missing linker defects in the crystal structure.[214] The types and number of defects can be controlled by the synthesis conditions and the type of modulators.[215,216] Wu *et al*. stated that the stability of Zr based UiO-66 comes from the twelve coordination sites compared to for example HKUST-1, which has only four coordination sites.[217] The missing linker would probably reduce the overall cluster stability. However; it was pointed out by De Voorde et al.[218] that the replacement of the Zr-based UiO-66 linker with an acid modulator such as (trifluoroacetate) increased the physical stability under ball-milling treatment. It was also an important factor in controlling the porosity, particle size and morphology of the final product. Gutov, Hevia, Escudero-Adfan and Shafir[219] found that the occurrence of missing linker defects in the formation of the zirconium-based MOF with biphenyl-4,4'-dicarboxylate linker molecules being studied was highly dependent on the nature of the modulator acid. This, in

turn, affected the physical and chemical properties of the compound.

A detailed study of the UiO-66 and UiO-67 MOFs by single-crystal X-ray diffraction revealed an accurate depiction of the electron density and atomic structure of the compounds in question.[220] The results revealed large irregularities in electron density about the carboxylate oxygen atom in UiO-66, while computational results indicated that the hydroxylated clusters have 50% μ_3-O and μ_3-OH. However, the study precluded missing linker defects in the materials being examined by focusing solely on the examination of single microcrystals that were presumed to have formed without missing linker defects.

A modified linker defect can be introduced *via* replacement of the DBC ligands in UiO-66. This can be done through using formate, chloride and/or hydroxyl anions with different acid modulators such as trifluoroacetic acid, formic acid, or hydrochloric acid.[221,222] Such modifications have shown to give high CO_2 uptake in defective UiO-66 compared to ideal UiO-66 at high pressure. On the other hand, at pressures below one bar, the CO_2 uptake of defect-free UiO-66 is increased.[222] Hereby, it was noted that hydrochloric acid modified UiO-66 showed better affinity to CO_2 than the formic acid modified one. These studies were qualitatively compatible with the computational study by Thornton *et al*.[223] In addition, it was found that water adsorption on defective Zr-based MOFs has a hydrophilic effect.[60, 224-225]

An important study of missing linker defects in UiO-66 was carried out that identified the role played by such defects with respect to gas adsorption.[214] In a perfect crystal of UiO-66, and similar MOFs, the crystal structure is a twelve-connected framework, built on clusters of six zirconium atoms. Clearly, the greater the percentage of missing linker defects present in the structure, the weaker the structure must become. In addition, the vacant space that would otherwise be occupied by a linker molecule represents additional space that is available for the entrainment or adsorption of extraneous materials such as gases. Wu *et al*.[214] demonstrated directly that the presence of missing linker defects in the crystal structure of UiO-66 means

that the effective pore volume of the crystal structure could be systematically increased by as much as 50% relative to that of the perfect UiO-66 crystal. Thus, the Brunauer-Emmett-Teller surface area of the crystals could also be increased by about 60% relative to that of the perfect UiO-66 crystal.

Wu *et al*. speculate that the increased formation of internal voids in the crystal structure on increasing the concentration of mediating acid that was employed in the synthesis is due to blocking of coordination sites by the mediating acid during crystal formation. Such blocking would act to prevent linker molecules from occupying those coordination sites, resulting in the formation of missing linker defects in the crystal structure. Moreover, they found that in the UiO-66 crystal structure, two different structures were present, one in which the zirconium cluster was capped with a hydroxyl group, and one in which the hydroxyl group was not present. Thus, there were three different sites for adsorption on the zirconium clusters, identified according to the capping unit that is normally present at a particular site. These three were the –OH site (OH exist), the –O site, which was similar to the OH site with one of the hydrogens moved to another sites, and the void site (in which, the Zr cluster has lost a single water molecule). Wu and coworkers determined by neutron diffraction measurements that gas adsorption in the hydroxylated structure occurs preferentially at the 'cup' sites, (OH site), of the zirconium clusters. Thus, the decision was taken to calculate the static binding energies of adsorption with regard to methane and carbon dioxide using dispersion-corrected density functional theory (DFT-D) for each binding site (*vide infra*).

3.5.2.3: Calculations on Zirconium metal organic frameworks

The structure of zirconium-based metal-organic frameworks is fundamentally different from that of the zinc paddlewheel compounds that were studied (*vide supra*). Whereas the zinc-based compounds were based on a pair of Zn atoms, the zirconium-based compounds are built on octahedral clusters of six zirconium atoms. As described in the introduction section, the coordination of the metal atom clusters with appropriate "linker" molecules that bind metal clusters to each other can form a structurally stable crystalline material characterised by large pore spaces and channels within which free compounds can be adsorbed. This is analogous in manner to hydrogel formation, in which an interconnected network of hydrophilic polymeric materials is able to accumulate and coordinate very large amounts of water within the network, sequestering it until released by physical or chemical means.[226,227] In the present study, the /7minimum energy position and binding energy of a molecule of one of the four selected adsorbed gases is calculated.

The work presented here explores a series of defects introduced within Zr-based MOFs in order to understand the effect of such defects on gas adsorption by DFT calculations. The Zr-cluster was built from a crystal structure, where each Zr-cluster is capped by 12 formate groups based on the crystallographic information files from Cambridge Crystallographic Data Centre (CCDC code: RUBTAK).[228] From this starting point three formate groups were turned into benzoate in a similar arrangement to Wu et al.[214] Functional groups were then placed on the benzene ring in a single position, ortho to the acid group. Thus, in this MOF all sites are capped by formate anions, except for three sites surrounding a single O, OH, or empty site, where a (substituted) benzoate has been placed (*vide infra*). The gas molecules are then placed in the cavity of these three benzoic acid molecules in order to compute the binding energy. The calculations started with the adsorption of CO_2. In these calculations, CO_2 was placed in the cavity in a position to maximize H-bonding interaction with the present NH_2 groups (i.e. at

approximately 2.0 Å distance), using our experience from the Zn-paddlewheel calculations. Then, the geometry was optimized in the normal fashion. Calculations were performed for adsorption of CO_2, CH_4, N_2, and H_2. To simplify our calculations, the final optimum geometry for CO_2 absorption was used as starting point for the optimizations for absorption of CH_4, N_2, and H_2.

Two different calculation methods were used. In the first, we used standard B3LYP.[181] In the second, we introduced dispersion via the gd3 keyword.[229] In all cases, the basis set used was SDD[184] for the Zr atom and 6-311G (d, p)[182,183] on all other atoms using Gaussian 09.[185] Other functionals were also explored, including APFD,[230] B97D,[231] B97D,[231] MO6,[232] and WB97XD,[233] to study just carbon dioxide adsorption on zirconium clusters. The effect of water on the efficiency of adsorption of carbon dioxide and nitrogen was also studied using B3LYP as the functional.

The calculations examined the binding energy of the specific gas for four situations, or defects. The defect situations reflect the availability of a particular site of coordination on the zirconium cluster. In the crystal structure of a metal-organic framework compound, failure of the structure to completely form with the full complement of linker molecules can leave coordination sites vacant, hence a defect is formed. The presence of defect sites has been demonstrated to have the effect of increasing the available space for adsorbed materials, effectively by increasing the available pore size in the structure (*vide supra*). The three defect situations that are identified for computation in this study are:

- The trivial case in which no defect is present, so the adsorption happens around an OH group, figure 3-11.
- The H-defect, loss of H^+, in which the coordination site normally occupied by an OH group, only has an oxygen atom. The released H is then moved to one of the (μ_3-O) oxygen sites, figure 3-12. This can also be considered as a different

choice of adsorption position around the Zr-cluster.

- The H_2O-defect, in which a coordination site normally occupied by OH is vacant, leaving a hole. In addition, an H atom is lost from an adjacent site, leading to overall loss of H_2O, figure 3-13.

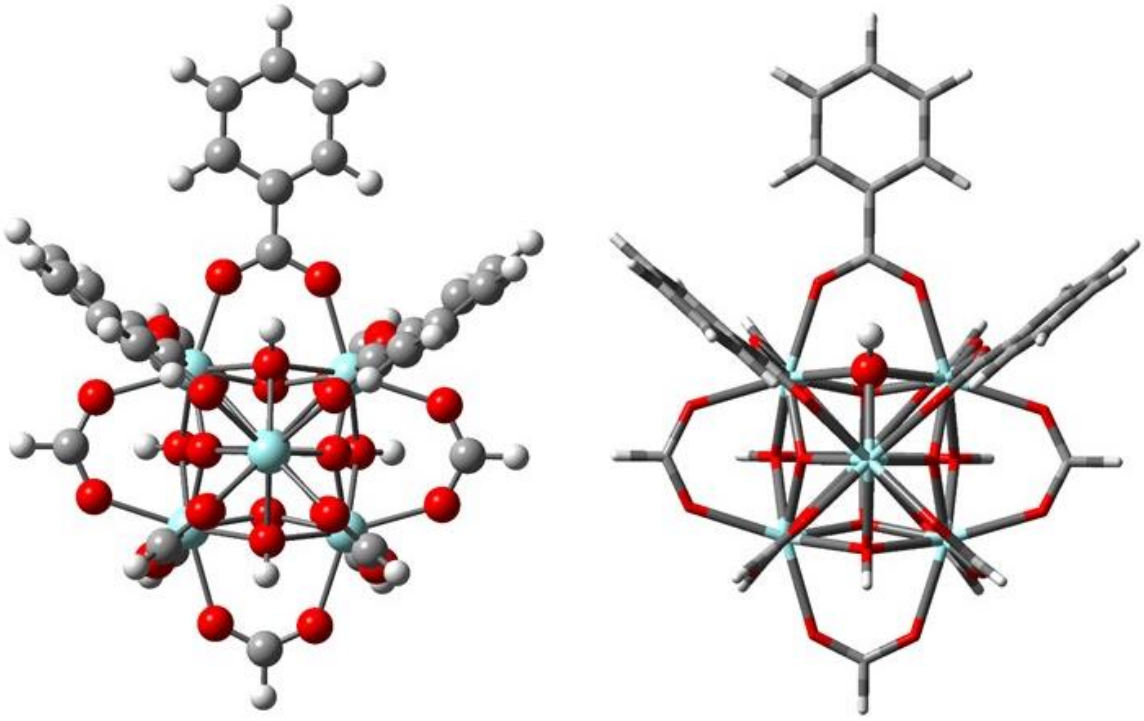

Figure 3-11: Structure of $[Zr_6(\mu_3\text{-}O)_4(\mu_3\text{-}OH)_4(O_2CH)_9(O_2CPh)_3]$ with adsorption occurring one of the $(\mu_3\text{-}OH)_4$ sites. This absorption geometry will be described as "No Defect," (left: ball and stick), (right: stick)

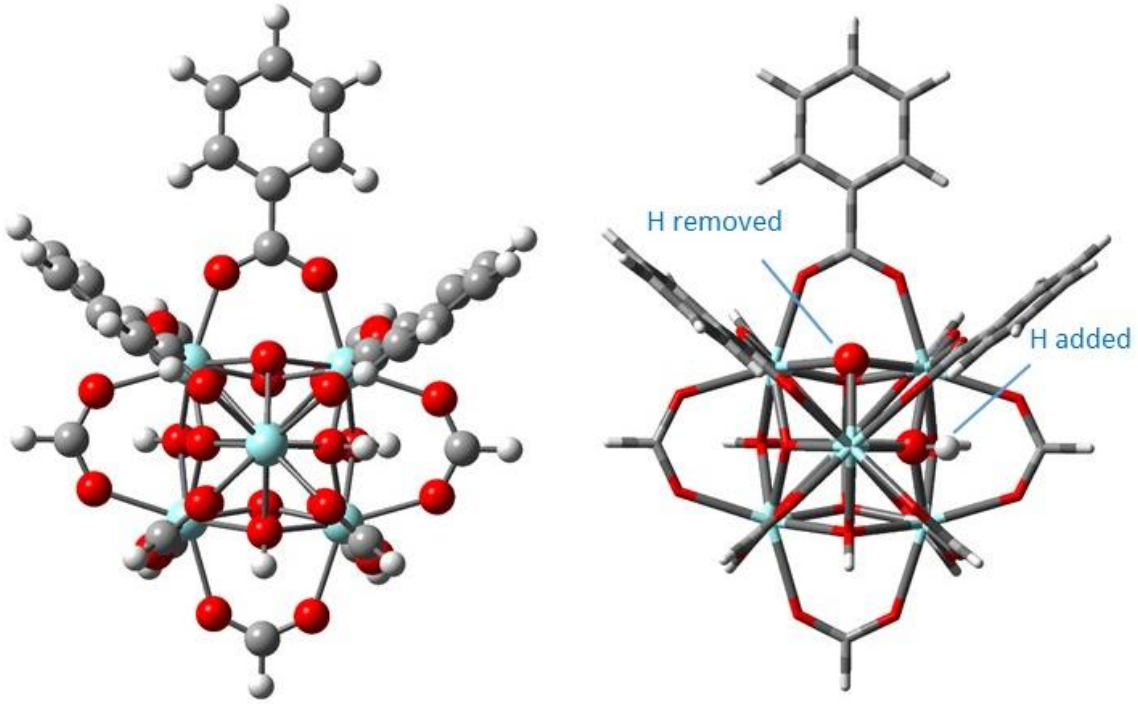

Figure 3-12: Structure $[Zr_6(\mu_3\text{-}O)_4(\mu_3\text{-}OH)_4(O_2CH)_9(O_2CPh)_3]$ with adsorption occurring one of the $(\mu_3\text{-}O)_4$ sites. This absorption geometry will be described as "H Defect," (left: ball and stick), (right: stick). Here, an H atom is removed from a $(\mu\text{-}OH)_4$-site and then is added to one of $(\mu\text{-}O)_4$ sites.

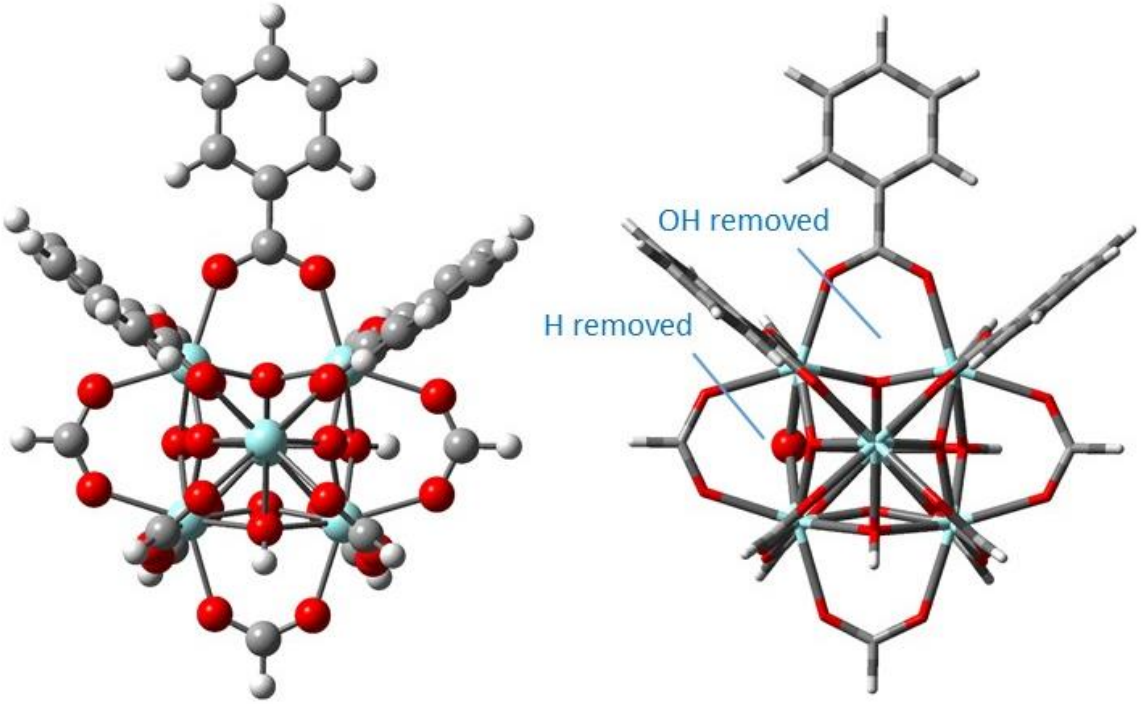

Figure 3-13: Structure of $[Zr_6(\mu_3\text{-}O)_3(\mu_3\text{-}OH)_2(O_2CH)_9(O_2CPh)_3]$, (left: ball and stick), (right: stick) with adsorption occurring one of the $(\mu_3\text{-}O)_4$ sites. This absorption geometry will be described as an "H_2O Defect," where OH is removed from the binding site together with an H atom of one of the $(\mu_3\text{-}OH)_4$ sites.

The binding energy of an adsorbed gas molecule in each situation will be influenced by the geometry of the adsorbed molecule, its molecular volume (steric influence), the presence of dipoles and the overall polarity of the adsorbed molecule, and the relative electronegativity of its component atoms. In this study, the effect of changing the substituent on the benzoate ligands is our major focus, keeping other elements as fixed as possible, so that their influence is constant. Thus, the influence on binding energy by a particular defect in the zirconium cluster should be consistent throughout the series of benzoate substituents. Subsequently, up to three benzoic acid molecules were modified with a single substituent group, X, in the ortho position on the benzene ring. These substituents, X, were: NH_2, CH_2NH_2, CH_2OH or CH_2CONH_2. For all substituents, calculations were performed with a single modified benzoic acid. For the NH_2 substituent, calculations were also performed where 2 benzoic acids (2 isomers) or 3 benzoic acids were substituted.

Thus, the clusters (depicted in figures 3-14a/3-14b) have the general formula $[Zr_6(\mu_3\text{-}O)_4(\mu_3\text{-}OH)_4(O_2CH)_9((O_2CC_6H_4X)(O_2CC_6H_5)_2)]$, $[Zr_6(\mu_3\text{-}O)_4(\mu_3\text{-}OH)_4(O_2CH)_9((O_2CC_6H_4X)_2(O_2CC_6H_5)]$, or $[Zr_6(\mu_3\text{-}O)_4(\mu_3\text{-}OH)_4(O_2CH)_9((O_2CC_6H_3X)_3)$ respectively.

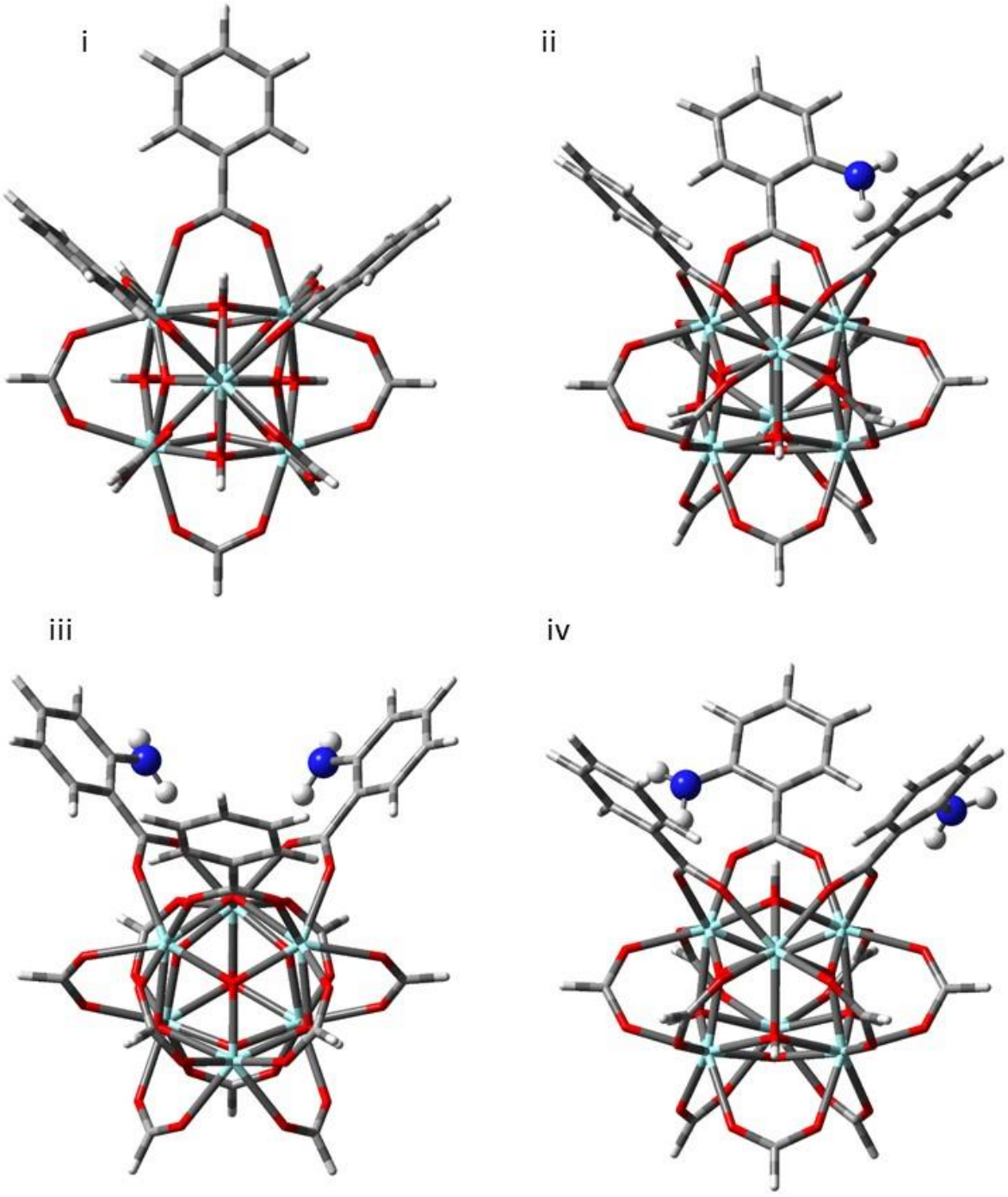

Figure 3-14a: Subsequent substitutions in Zr-clusters. Unsubstituted (panel i), and where one or two benzoate ligands are replaced by $O_2CC_6H_4NH_2$, panels (ii) to (iv) respectively.

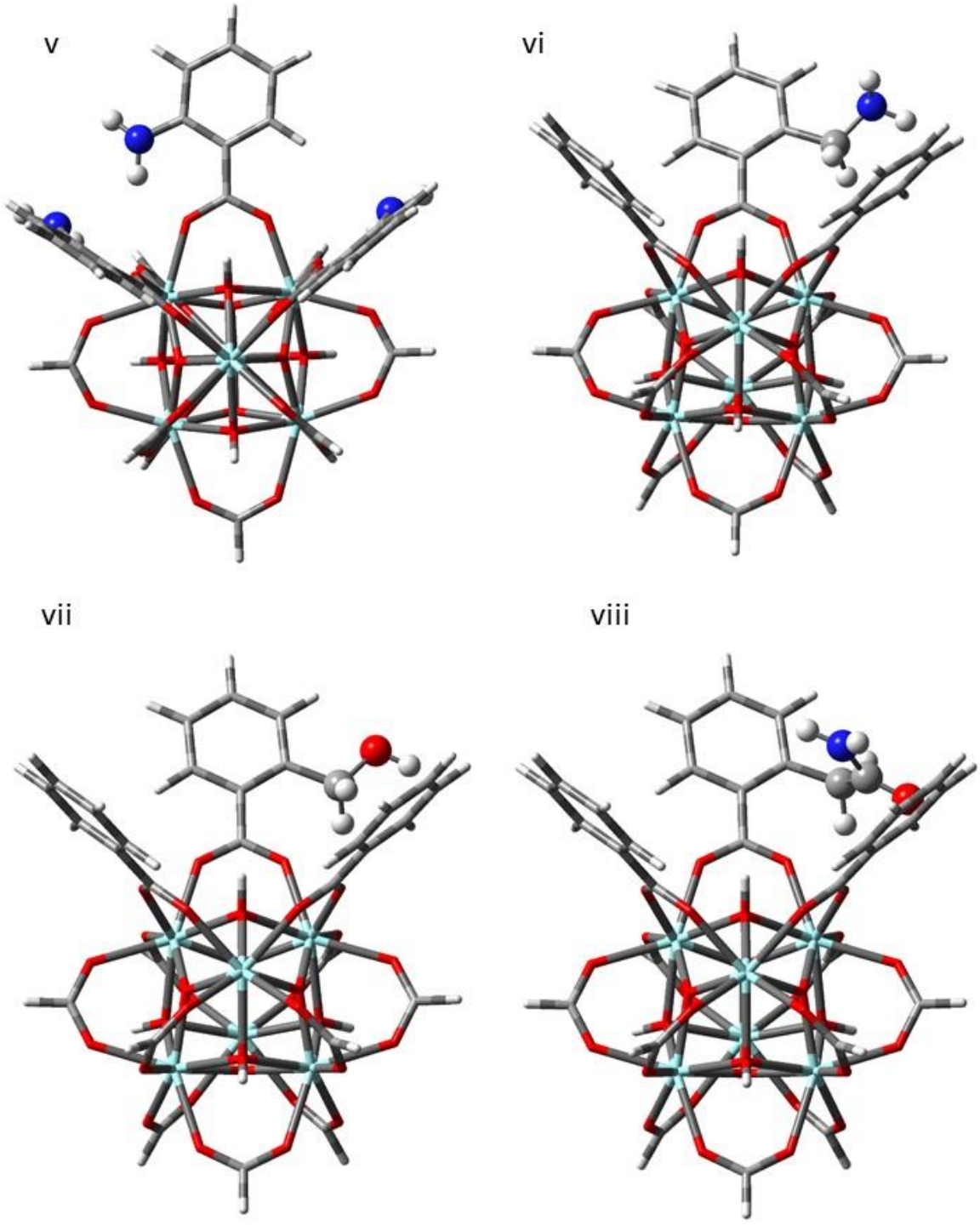

Figure 3-14b: Different substitutions in Zr-clusters. *Three* benzoate ligands are substituted by $O_2CC_6H_4NH_2$ (panel v), or where *one* of the benzoate ligands is replaced by $O_2CC_6H_4X$, X: methylamine(panel vi), methylalcohol (panel vii), and methylamide (panel viii).

These clusters were used to study the adsorption of four gases: carbon dioxide, methane, nitrogen, and hydrogen.

3.5.2.4: Results and discussion

The computed binding energies for the four gases in the various combinations of defects and substituents using the DFT and DFT-D method are shown in Tables 3-2(a-d), and plotted in figures 3-16 and 3-17 respectively. (The binding energies for the OH site are presented separately in Appendix table A3-1).

Table 3-2a: Computed Binding Energies for CO_2 using B3LYP//6-311G(d, p)+ SDD(Zr) in kJ/mol. (R is the unsubstituted benzoate ligand).

Linker	No Defect		O Defect		H_2O Defect	
	DFT	DFT-D	DFT	DFT-D	DFT	DFT-D
3R	-15.5	-50.1	-6.2	-35	-10.2	-40.5
2R+R-NH_2	-16.3	-49.2	-9.9	-39.3	-9.6	-41.1
R+2R-NH_2	-15.7	-52.8	-6.9	-34.9	-9.6	-42.3
R+2R-NH_2(iso)	-17	-52.4	-11.8	-45.8	-9.4	-40.7
3R-NH_2	-16.9	-59.8	-10.4	-36.8	-3.4	-34.1
2R+R-CH_2NH_2	-15.7	-53.8	-7.7	-36.2	-17.8	-39.1
2R+R-CH_2OH	-16.1	-64.3	-7.8	-39.9	-11.8	-34.2
2R+RCH_2CONH_2	-14.9	-49	-8.1	-46.9	-11.9	46.6

Table 3-2b: Computed Binding Energies for CH_4 using B3LYP//6-311G(d, p)+ SDD(Zr) in kJ/mol. (R is the unsubstituted benzoate ligand).

Linker	No Defect		O Defect		H_2O Defect	
	DFT	DFT-D	DFT	DFT-D	DFT	DFT-D
3R	-0.6	-31.5	-0.4	-19.2	-0.8	-26.3
2R+R-NH_2	-0.7	-32.4	-0.7	-25.7	-0.86	-26.7
R+2R-NH_2	-0.8	-35.2	-0.8	-18.2	-0.69	-27.3
R+2R-NH_2(iso)	-0.69	-33.2	-0.81	-29.7	-0.4	-26
3R-NH_2	-1	-36.3	-0.98	-19.6	-2	-27.5
2R+R-CH_2NH_2	-0.7	-33	-0.72	-7.2	-0.39	-27.4
2R+R-CH_2OH	-0.67	-33.7	-0.7	-25.1	-0.6	-33
2R+RCH_2CONH_2	-0.9	-34.1	-0.7	-34.1	-4.8	-37.4

Table 3-2c: Computed Binding Energies for N_2 using B3LYP//6-311G(d, p)+ SDD(Zr) in kJ/mol. (R is the unsubstituted benzoate ligand).

Linker	No Defect		O Defect		H_2O Defect	
	DFT	DFT-D	DFT	DFT-D	DFT	DFT-D
3R	-10.4	-33.9	-4.3	-22.9	-5.2	-27.4
2R+R-NH_2	-11	-34.6	-4.9	-27.9	-5.1	-28.7
R+2R-NH_2	-11.5	-38.8	-4.48	-20.9	-5.2	-29.3
R+2R-NH_2(iso)	-11.5	-35.2	-5.2	-50.9	-5	-27.2
3R-NH_2	-11.9	-40	-5	-18.8	-5.5	-30
2R+R-CH_2NH_2	-4.6	-37.9	-5.1	-22.8	-5.4	-29.5
2R+R-CH_2OH	-10.5	-38.4	-4.9	-26.1	-5.5	-29.2
2R+RCH_2CONH_2	-8.7	-34.4	-5.2	-32.2	-10.5	-40.3

Table 3-2d: Computed Binding Energies for H_2 using B3LYP//6-311G(d, p)+ SDD(Zr) in kJ/mol. (R is the unsubstituted benzoate ligand).

Linker	No Defect		O Defect		H_2O Defect	
	DFT	DFT-D	DFT	DFT-D	DFT	DFT-D
3R	-0.28	-10.6	-0.35	-4.3	-0.4	-11
2R+R-NH_2	-0.07	-13.5	-0.58	-9.9	-0.67	-11.8
R+2R-NH_2	-0.19	-15.7	-0.48	-6.1	-2.13	-11.4
R+2R-NH_2(iso)	-0.27	-13.5	-0.48	-18.4	-1.8	-10.3
3R-NH_2	-0.74	-16.3	-0.48	-5.5	-0.52	-11.8
2R+R-CH_2NH_2	-0.5	-15.1	-0.43	-5.7	-0.3	-12.0
2R+R-CH_2OH	-0.14	-15.1	-0.32	-8.9	-0.51	-11.4
2R+RCH_2CONH_2	-0.36	-14.7	-6.3	-16.9	-4.2	-21.1

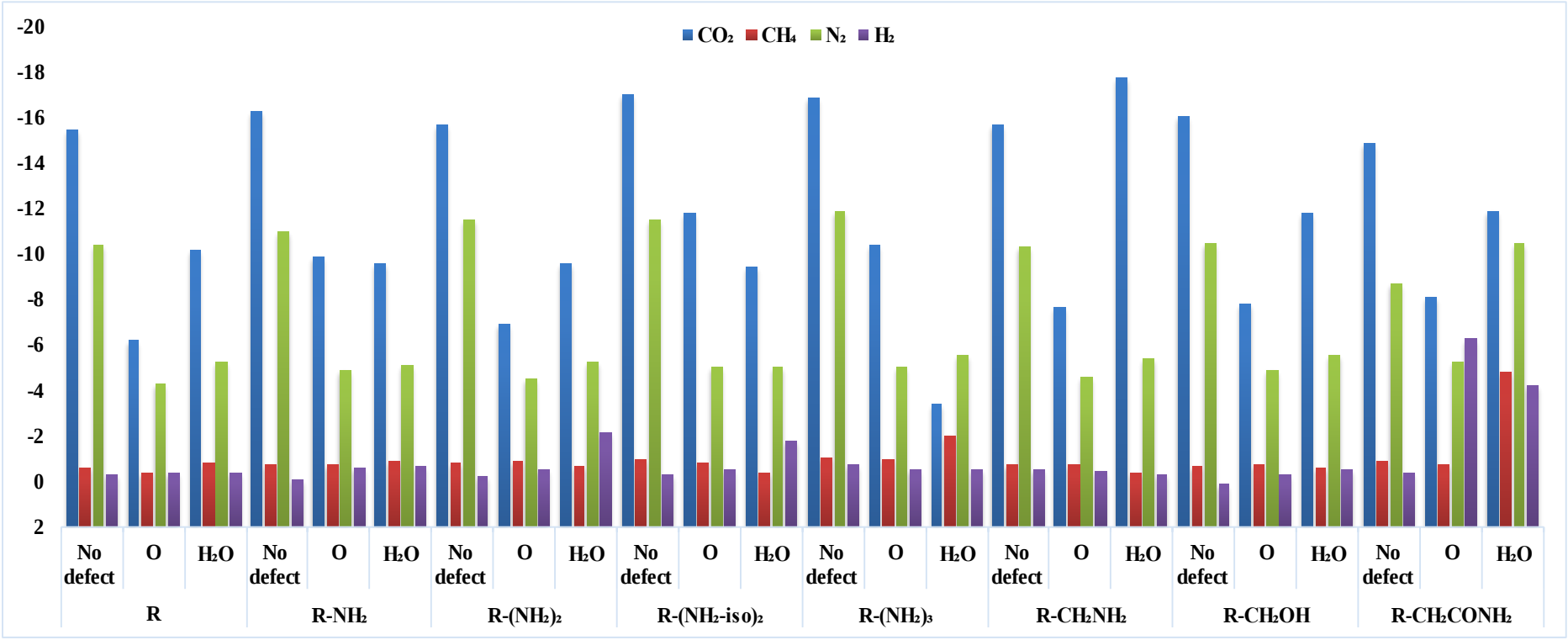

Figure 3-15: Binding Energy of CO_2, CH_4, N_2 and H_2 in Zr Clusters Using B3LYP-GD3//6-311G (d, p) + SDD(Zr), R is the unsubstituted benzoate ligand.

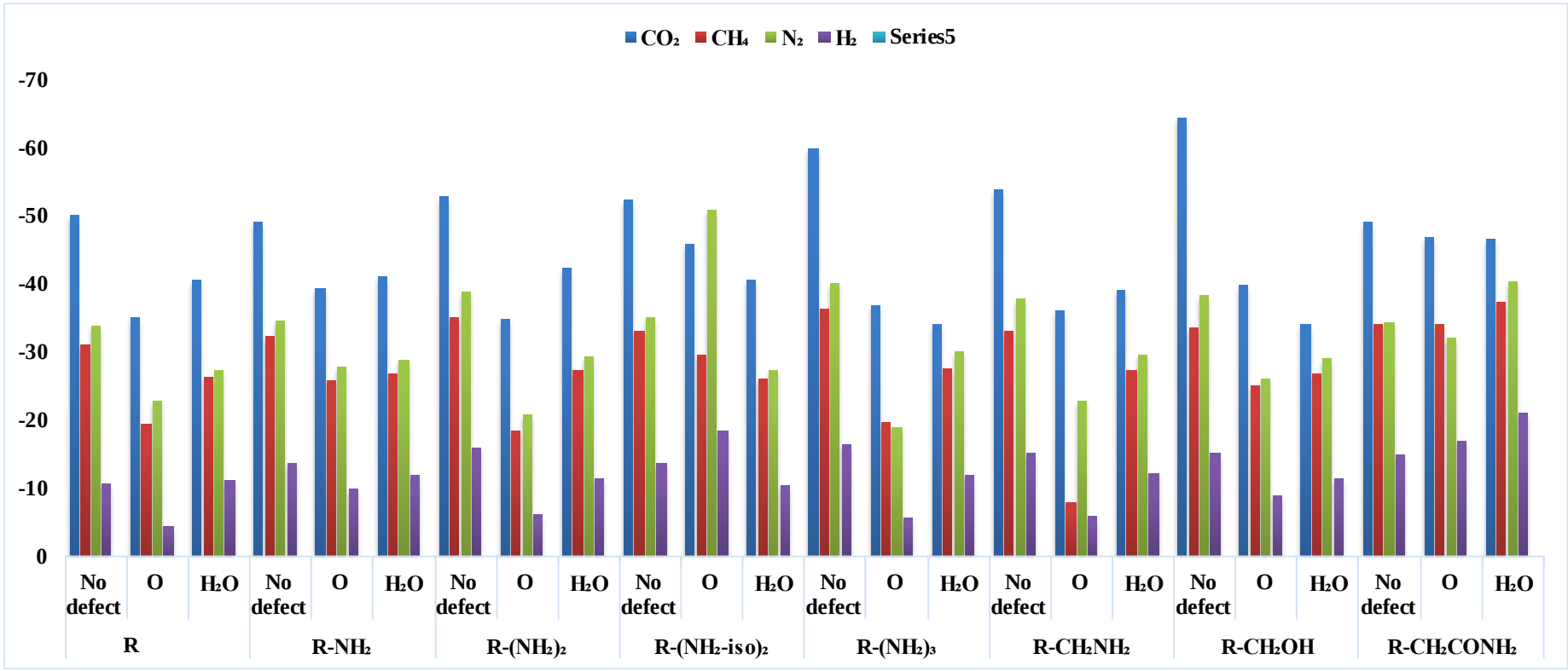

Figure 3-16: Binding Energy of CO_2, CH_4, N_2 and H_2 in Zr Clusters Using non-dispersion-corrected B3LYP//6-311G(d, p)+ SDD(Zr), R is the unsbstituted benzoate ligand.

In figures 3-15, 3-16, it can be seen that the computed values of binding energy for all four gases vary across the substituent series with the least variation shown for the H_2 molecule and the CH_4 molecule. The uniformity of the values begins to break down and become more widely variable for the CO_2 and N_2 molecules, presumably due to the polarizability and electron density of the two molecules as these enable greater interaction with the *ortho* substituent groups.

As might be expected from the above qualitative discussion, the most polar or polarisable molecules (CO_2 and N_2) are associated with the largest binding energies, while the lightest and non-polar molecules (H_2 and CH_4) exhibit lower binding energies. Table 3-3 below illustrates some general properties of these gases. Across the series of substituent groups on the benzoate molecules, it appears that the *ortho* substituents on the benzoate ligands have very little effect until the molecular size of the adsorbed molecules becomes such that there can be close proximity between the adsorbed molecule and the substituent group.

As may be readily seen, the pattern of adsorption energies for the four gases using the DFT and DFT-D methods is essentially identical in all cases. The order of binding energy under the DFT-D method, with very few exceptions, is

$$H_2 < CH_4 < N_2 < CO_2$$

as it is under the DFT method. The major difference between the results obtained using the two methods, however, is striking in its magnitude of the binding energy. The binding energies calculated using the DFT-D method are significantly larger than those calculated using the DFT method. Thus, inclusion of London dispersion forces in the calculations greatly increases the calculated binding energies. It has been reported elsewhere[234] that the inclusion of dispersion forces in calculations is necessary in order to obtain accurate energetics of a system. It is

particularly noteworthy that in the case of H_2 absorption dispersion accounts for almost all of the interaction energy.

Table 3-3: Quadrupole moment and polarizabilities of gas CO_2, CH_4, N_2 and H_2[235]

Gas	Quadrupole moments C m^2	Polarizabilities C m^3
CO_2	-13.4×10^{-40}	31×10^{-25}
CH_4	0	26.0×10^{-25}
N_2	-4.72×10^{-40}	17.6×10^{-25}
H_2	2.2×10^{-40}	8×10^{-25}

The work in Ref 234 focused primarily on hydrogen-bonded systems. The energetics of those are dominated by electrostatics. In the present study, hydrogen bonding is not thought to be a prominent feature for N_2, CH_4, or H_2. If that were the case, one might expect that large variations in binding energy would occur for some combinations of a particular adsorbed gas and a particular *ortho*-substituted benzoate ligand. Indeed, the calculated binding energies for CH_4, N_2, or H_2 (table 3-2 b-d) using DFT-D seem to remain within a well-defined range of values throughout. This is different for carbon dioxide (table 3-2a) where the calculated binding energies for carbon dioxide associated with a particular defect tend to increase with the presence of ligands that are capable of hydrogen bonding. Indeed, this is clear from table 3-2a which shows the DFT-D calculated binding energies for carbon dioxide with respect to the different *ortho* substituents on the benzoate ligands. In the 'No Defect' series, the trend to increasing binding energy with increasing opportunity for hydrogen bonding between the carbon dioxide molecule and the *ortho* substituent can be clearly seen. When a defect is present, however, the geometry of the void is changed. Thus, the orientation of the adsorbed molecule

in its minimum energy state does no longer appear to be affected by hydrogen bonding in a regular or linear manner.

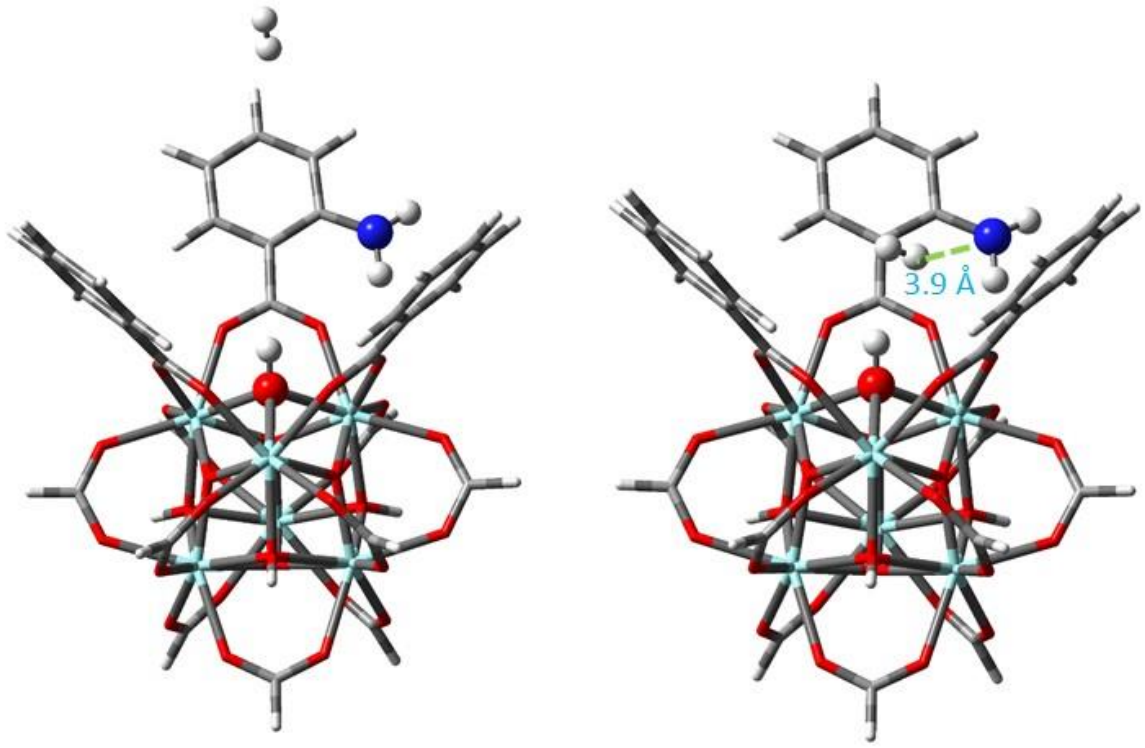

Figure 3-17: DFT(left) and DFT-D(right) Minimum Energy Structure for Adsorbed H_2 in 'No Defect' Configuration with Single Amino Substituent.

The difference between DFT and DFT-D calculations is illustrated by looking at the minimum energy structures for H_2 adsorption, which is the most apolar molecule. As explained in section 3.5.3.2, in all our calculations on H_2, the calculations were started with H_2 at the position CO_2 had in its optimal geometry, which was invariably approximately in the centre of the adsorption site. Figure 3-17(left) shows that the adsorbed hydrogen molecule in the straight DFT calculation has shifted significantly from its starting position in the approximate centre of the cavity. Indeed, it is now far removed from the single amino substituent (7.9 Å), and thus has little or no interaction with that functional group. In comparison, in DFT-D calculations for the same case the adsorbed hydrogen molecule remains in closer proximity to the amino

substituent, as shown in figure 3-17 (right), where the distance from H_2 to the amino group is 3.9Å. Similarly, the minimum energy structure for an adsorbed hydrogen molecule in the "no defect" configuration for the case in which the substituent side chain is an aminomethyl group is shown in figure 3-18 (left). While this side chain is able to extend the farthest away from the phenyl ring, and presumably has the greatest opportunity to interact with the hydrogen molecule, it can nevertheless be seen that there is apparently little or no interaction between them. Indeed, the distance of H_2 to the amine group is 4.5 Å for the DFT calculations. On the other hand, for the DFT-D calculations for the same case, the adsorbed hydrogen molecule is in closer proximity to the hydroxyl substituent, as shown in figure 3-18 (right). Here, the distance from H_2 to the methylamine group is 4.3 Å, similar to the amino case (figure 3-17 right). Again, in both cases, the starting point of the H_2 molecule in the optimization was in the middle of the cavity of the cluster at the optimum geometry for CO_2.

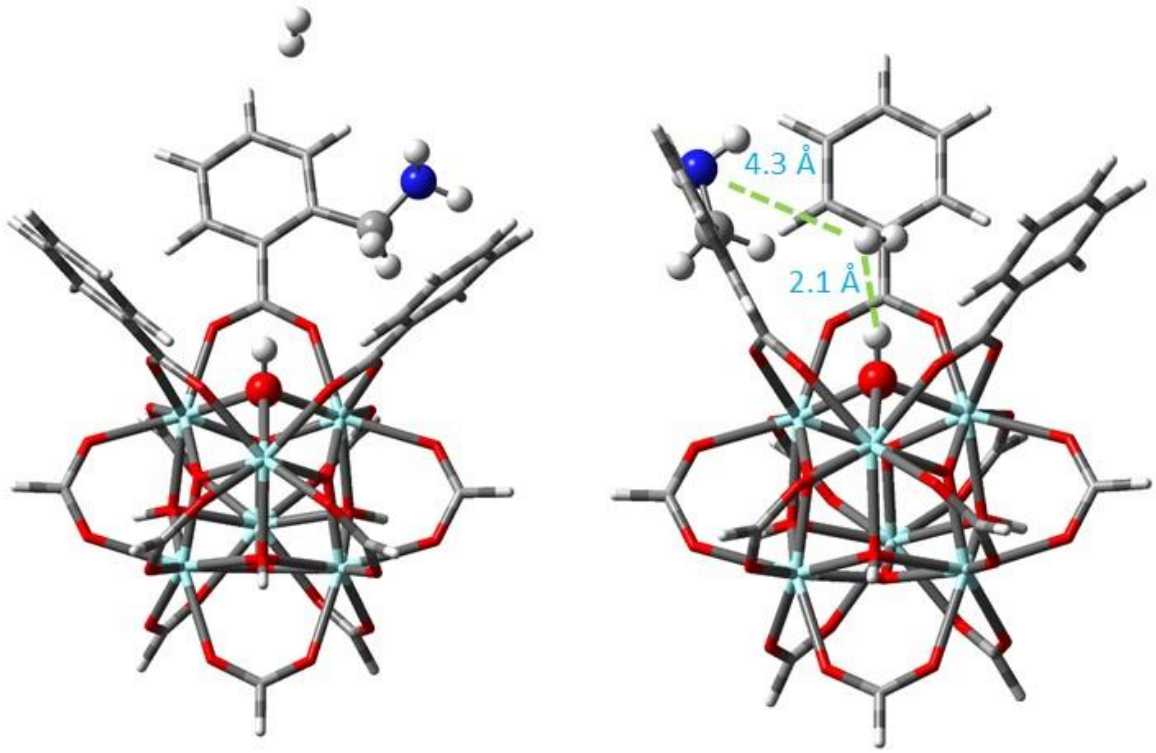

Figure 3-18: DFT(left) and DFT-D(right) Minimum Energy Structure for Adsorbed H_2 in 'No Defect' Configuration with aminomethyl Substituent.

The largest and most polar of the four gas molecules studied is carbon dioxide, CO_2. Here, the two oxygen atoms, with their lone pairs of electrons exposed, represent localised regions of high electron density in the molecule, while the localised electron density of the single carbon atom is significantly depleted by the electron-withdrawing capacity of the two electronegative oxygen atoms. The carbon atom therefore represents a local region of relatively high positive character, making the two carbon-oxygen bonds highly polarised. Interaction between the substituent side chains and an adsorbed molecule of carbon dioxide should therefore be more prominent than for the hydrogen molecule, which will be dominated by dispersion. In figure 3-19(left), it can be seen that carbon dioxide molecule stays close to the amino substituent, but that there is a clear interaction with the OH group on the Zr-cluster as well. It is also clear that the addition of dispersion forces has less effect than in the case of H_2 adsorption.

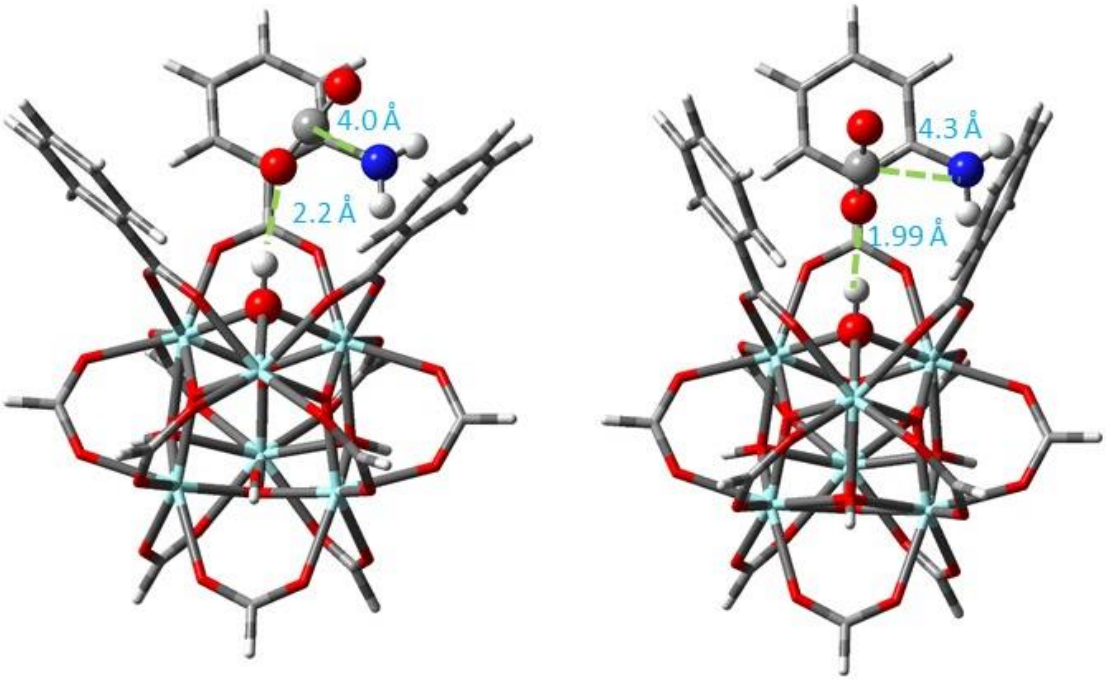

Figure 3-19: DFT(left) and DFT-D(right) Minimum Energy Structure for Adsorbed CO_2 in 'No Defect' Configuration with Single Amine Substituent.

The interaction between the adsorbed carbon dioxide molecule and the aminomethyl substituent side chain is shown in figure 3-20, Here, interaction between the carbon dioxide molecule and the aminomethyl group appears to have caused the carbon dioxide molecule to adopt a position somewhat more distant from the metal centre than in its single amine counterpart figure 3-19. However, in this case, it is still the OH ··· CO_2 interactions, which dominate the structure of the complex.

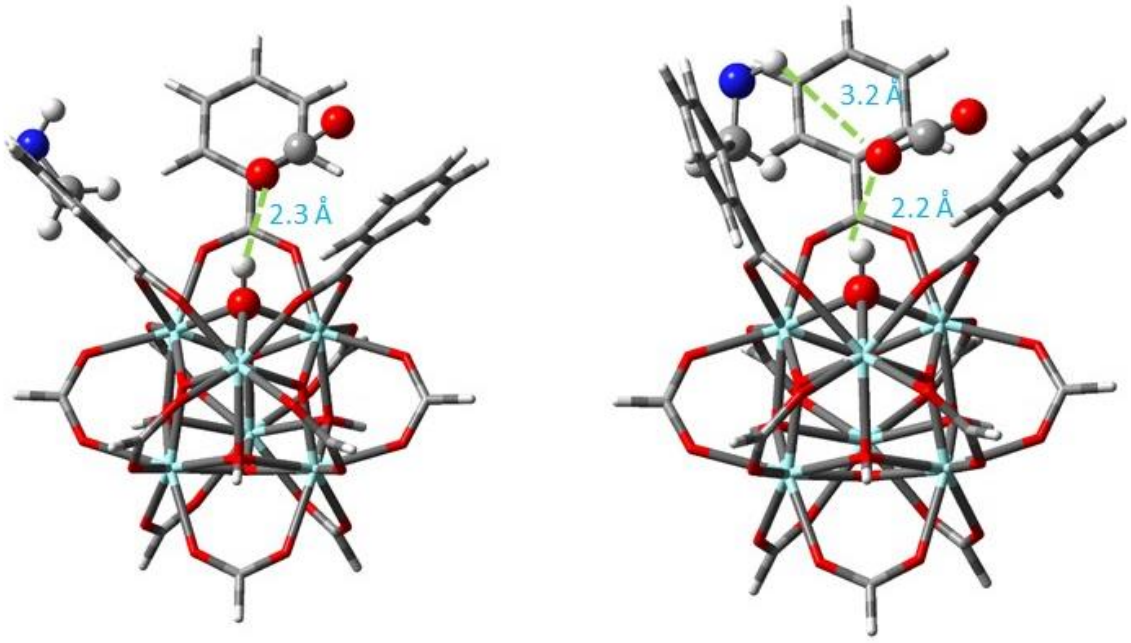

Figure 3-20: DFT (left) and DFT-D(right) Minimum Energy Structure for Adsorbed CO_2 in 'No Defect' Configuration with Methylamine Substituent.

The trend to higher binding energy for the adsorbed carbon dioxide molecule through the series of *ortho* substituents for any particular defect situation is more erratic and less apparent in the binding energies calculated using DFT-D than in the binding energies calculated using DFT (shown in Table 3-2a). The corresponding values, apart from being much lower than those calculated using the DFT-D method, do not indicate any increase in binding energy corresponding to an increase in *ortho* substituents on the benzoate ligands. Finally, analysing the data in tables 3-2 a-d, it is clear that the strongest binding energy does depend which

modification for which gas is investigated, but it also depends on the exact DFT methodology used. However, it is also clear that amides are generally a good choice for adoption. This relevant structures for N_2, CH_4, H_2, and CO_2 adsorption are given for the H_2O defect and the DFT-D approach in figure 3-21.

The study presented by Wu et al using the DFT-D computation method, as described previously, gave values of binding energies in UiO-66 relevant to the cases in which the structure of the zirconium centre has either no defect (OH site), -O defect, or - OH defect. For both methane and carbon dioxide, the highest static binding energy of adsorbed molecules was determined to be that of the -OH site (no defect) by a significant margin. The calculations of Wu et al were repeated for the present study. In this case, no side chain substituents are present on the phenyl ring of the terephthalate linkers. Interestingly, the computed values for the binding energy are significantly larger than those presented by Wu et al, (figure 3-21, table 3-4).

Table 3-4: Binding energy of CO_2 comparison between Wu et al.[214] and this thesis in kJ/mol using the DFT-D method.

Zr cluster	**B.E CO_2**		**B.E CH_4**	
	Wu et al work	**Current work**	**Wu et al work**	**Current work**
No defect	-29.9	-50	-24.8	-31.1
O defect	-23.2	-35.2	-21.9	-19.2
OH defect	-22.4	-40.5	-22.3	-26.2

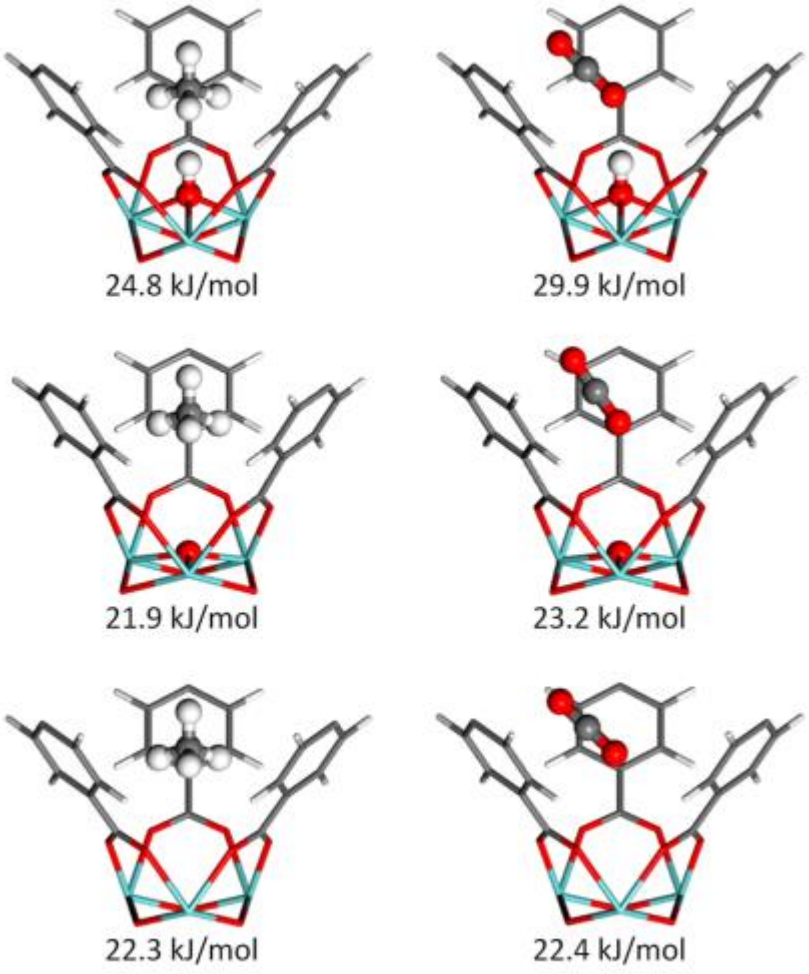

Figure 3-21: Optimized structure of CH_4 (left), CO_2 (right) in UiO-66 using DFT-D method, from top to bottom: the -OH site, the -O site, and the void site**.** Reproduced with permission from Ref. 213. Copyright (2014) American Chemical Society.

In particular, it is clear that our results for CH_4 adsorption are in line with the Wu *et al.* results. In fact, any remaining differences can be ascribed to differences in the precise methodology used. In particular, Wu *et al*. used quantum Espresso, which uses a plane-wave basis rather than the Gaussian basis used by us. However, our results for CO_2 are significantly different. Whereas Wu *et al*. calculate CO_2 adsorption to be of similar energy to CH_4 adsorption, our results clearly show that CO_2 adsorbs much stronger in line with what one would expect. Our results are in line with the experimental results.[213]

3.5.3: Calculation of the Binding Energy for Carbon Dioxide Using Other Methods

In the above, we looked at the variation in binding energy for a series of substituents and a number of defects given a specific DFT functional. However, it is well-known from the literature that the choice of functional can have a significant effect on structure and energetics of a system. Therefore, the minimum binding energy for an adsorbed carbon dioxide molecule was also calculated for one, two, and three *ortho* amino substituents on the benzoate ligands, and the 'No Defect' structure of the complex with an array of different functionals. The functionals used were APFD, B97D, B97D3, WB97XD and M06, with the 6-311G(d,p) + SDD (Zr) basis set. The results for these calculations, as well as those for the B3LYP and B3LYP-GD3 methods, are shown in Table 3-5. Again, as before, the calculations were started with CO_2 in a hydrogen-bonding position relative to one of the amino-groups.

From this table, it can be seen that there is consistent agreement in the results between the B3LYP-GD3 method and the other methods. A notable exception to this are the results obtained with the APFD method. All of these are higher than the values calculated by any of the other methods. The data in Table 3-5 also shows that there is a trend to higher binding energy with increasing opportunity for van der Waals interactions. As the number of *ortho*-amino substituents increases from one to three, the calculated binding energy also increases.

It can be safely concluded from these results that when van der Waals interactions are possible in the minimum energy orientation of an adsorbed molecule of carbon dioxide, and presumably of other molecules that are similarly polarised, then it becomes an important factor in determining the binding energy of the molecule within the complex, and by extension within the void space of a metal-organic framework structure.

Table 3-5: Binding Energy of Carbon Dioxide in Zr Clusters Using Other Dispersion Methods. (R is the unsubstituted benzoate ligand)

Method	R+R-NH_2	R+2R-NH_2	R+3R-NH_2
APFD	-62.8	-69.6	-71
B97D	-40.5	-44.3	-44.5
WB97XD	-45.2	-51.1	-55.1
M06	-47.8	-48.2	-56.4
B3LYP	-16.3	-15.7	-16.9
B3LYP-GD3	-49.2	-52.8	-59.8

3.5.4: Binding Energies of Carbon Dioxide and Nitrogen in the Presence of Water Using DFT:

Our calculations so far have concentrated in vacuo, where no other molecules are present for absorption. However, in any real-case situation, water, in particular, will be present and will therefore have an influence on gas absorption. Thus, the effect of water on the binding energy of carbon dioxide and nitrogen was examined using B3LYP with the 6-311G(d,p)+SDD (Zr) basis set. The calculated binding energies shown in Table 3-6, 3-7 and plotted in figure 3-26, are calculated using the expression below:

$$E_B = (E_{GAS+ECLUSTER+EWATER}) - E_{GAS} - (E_{CLUSTER+EWATER}),$$

i.e. the assumption is made that water will be absorbed first.

Table 3-6: Comparison of binding energies of CO_2 in presence and absence of water using B3LYP//6-311G**(O,H,N,C)+SDD(Zr) in kJ/mol. (R is the unsubstituted benzoate ligand)

Linker	**No defect**		**O defect**		**H_2O defect**	
	Water present	Water absent	Water present	Water absent	Water present	Water absent
3R	-17.3	-15	-15.4	6.2	-15.1	-10
2R+R-NH_2	-10.2	-16.3	-17.1	-9.9	-21.2	-9.6
R+2R-NH_2	-14.9	-15.7	-17.2	-6.9	-10.1	-9.6
R+2R-NH_2(iso)	-21.8	-17	-16.3	-11	-17	-9.4
3R-NH_2	-19.3	-16.9	-14.7	-10.4	-16.2	-3.4
2R+R-CH_2NH_2	-3.1	-15.7	-15.8	-7.7	-17.0	-17.8
2R+R-CH_2OH	-22.1	-16.1	-20.4	-7.8	-18.3	-11.8
2R+R-CH_2CONH_2	-16.4	-14.9	-14.1	-8.1	-15.6	-11.9

The presence of water in the system provides an environment in which hydrogen bonding is expected to play a significant role with respect to the binding energy of an adsorbed gas. Two mechanisms of action with regards to the defects of the system may be operational. In the simplest case, water molecules that are present may become coordinated to the zirconium cluster and eliminate the H_2O defect. In the other mechanism the gas molecule, will actually primarily interact with a water molecule coordinated to the Zr-cluster rather than the cluster itself. Here, also, two mechanisms can function. In the first, the binding energy is reduced due to competition between water and the absorbed molecule for the most advantageous coordination site. In the other, binding of the adsorbed gas molecule occur with the water molecule rather than the Zr-cluster. In this case, the effect of hydrogen bonding within the

complex structure would be a more important factor than if water was absent. In almost all cases, the pre-adsorption of water increases the binding energy of CO_2. The only exceptions observed to this are for the cases of a single amino group on the benzoate ligands, either as the amino group itself or as the aminomethyl substituent. In these cases, the competition between water and CO_2 pushes CO_2 further out, which means that the binding site for CO_2 is less favourable.

The computed minimal energy structures for all of the zirconium-based structures and adsorbed gases are provided in the Appendices A 3-1 to A 3-4. Computer-generated images of the minimum energy binding sites of a carbon dioxide molecule in the complex $[Zr_6(\mu_3\text{-}O)_4(\mu_3\text{-}OH)_4(O_2CH)_9(O_2CC_6H_3X)_3)]$ were produced for each combination of ortho ligand and defect, for both DFT and DFT-D, as well as for the effect of the presence of water. These images show the minimum energy conformation of the structure, the location of the adsorbed molecules and free water molecules, and the interatomic distances relevant to those molecules.

In figure 3-22(left), the minimum energy binding site of a carbon dioxide molecule in the no-defect configuration of the zirconium cluster with three 2-aminobenzoate ligands demonstrates the central location of the carbon atom. The nitrogen atoms of the amino functions of the ligands appear to be radially distributed about the carbon atom, suggesting that they each exert an equal influence in regard to the minimum energy configuration. The two 2-aminobenzoate ligands (right) on the other hand show slightly higher distance from OH site by 2.21 Å.

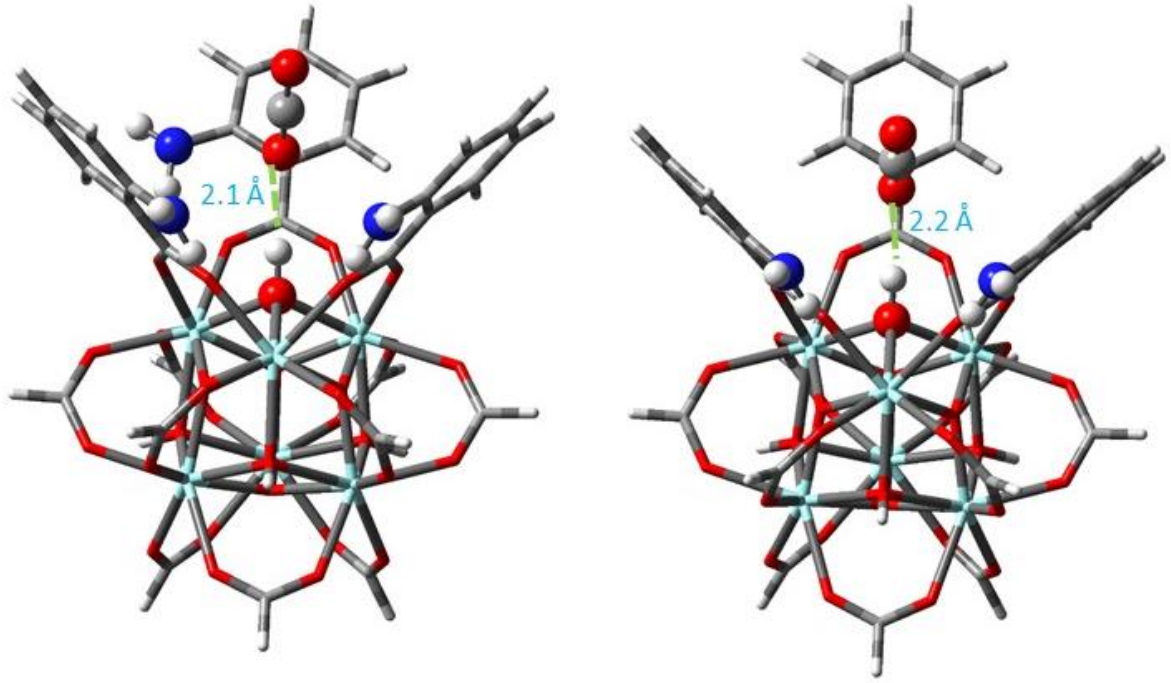

Figure 3-22: DFT Minimum Energy Structure for Adsorbed CO_2 in 'No Defect' Configuration with Three 2-Aminobenzoate Ligands (left) and Two 2-Aminobenzoate ligands (right).

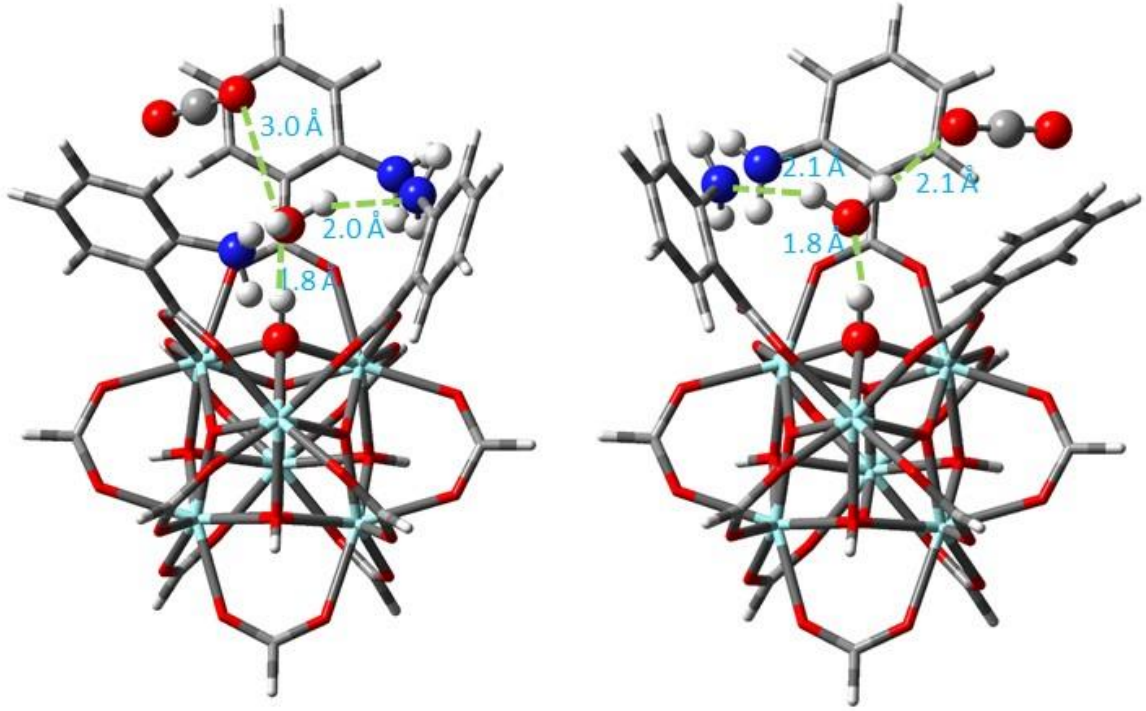

Figure 3-23: DFT Minimum Energy Structure for Adsorbed CO_2 in 'No Defect' Configuration with Three 2-Aminobenzoate Ligands (left) and Two 2-Aminobenzoate ligands (right) with Water Present.

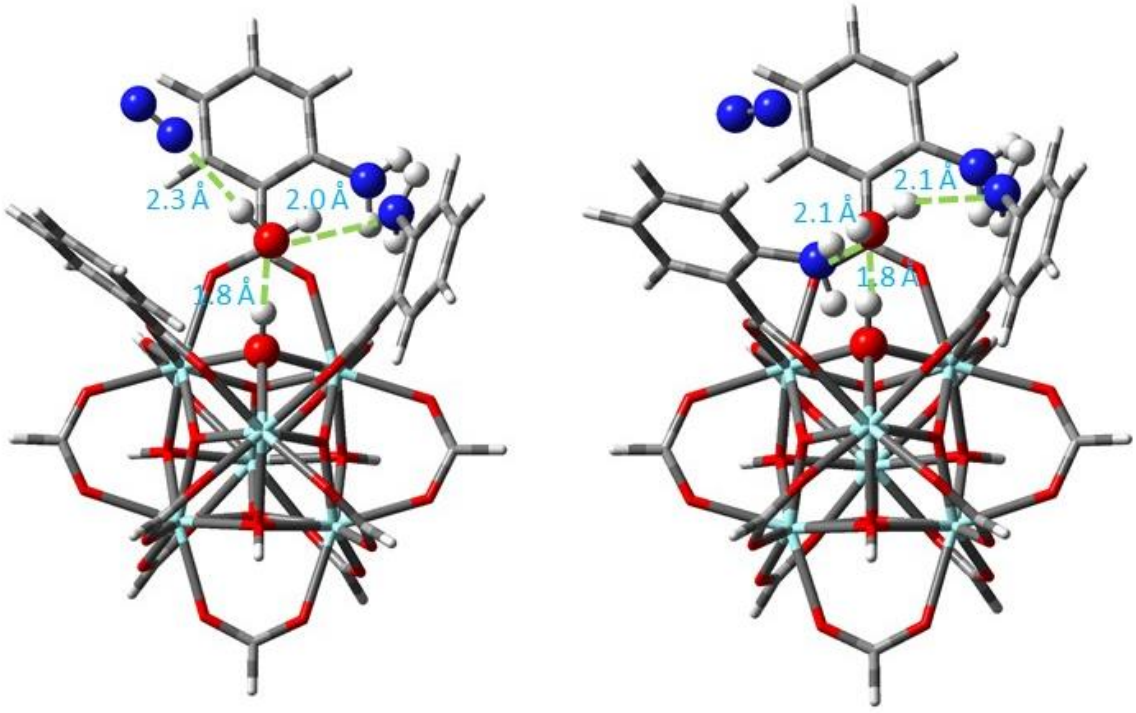

Figure 3-24: DFT Minimum Energy Structure for Adsorbed N_2 in 'No Defect' Configuration with Three 2-Aminobenzoate Ligands (left) and Two 2-Aminobenzoate ligands (right) with Water Present.

In the presence of water, however, the orientation of the adsorbed carbon dioxide molecule is quite different, as shown in figure 3-23. In that case, the carbon dioxide molecule is significantly removed from its position shown in figure 3-22. The adsorbed molecule appears to be rotated through 90°, assuming a horizontal orientation relative to the adsorption site rather than the vertical orientation found in the absence of water.

The most apparent difference between the calculated binding energies across the series of benzoate ligand structures is the marked slightly increasing in binding energy when water is present. As water also appears to significantly affect the location and orientation of the adsorbed carbon dioxide molecule in relation to the binding site, it is easy to rationalise these effects with the influence of hydrogen bonding between the carbon dioxide molecule and surrounding water molecules. Remark that in the figure 3-23 right, water is on top rather than

below, which may explain the difference here. However, the reason for this is unclear. Therefore, additional calculations with different starting points would be needed to resolve this.

The principal difference between carbon dioxide and nitrogen in regard to binding energy may be found in the polar nature of the molecules, relative to each other. Carbon dioxide has a linear structure, which is conducive to hydrogen bonding, dipolar interactions and electrostatic attraction. The nitrogen molecule, on the other hand, is completely non-polar, and has only the π bond electron cloud to augment the interaction of the single lone pair on each nitrogen atom with regard to interaction with the appropriate molecular orbitals of the zirconium clusters to facilitate binding. This interaction should not compete well with the hydrogen bonding interaction of the local water molecules in the binding site of the complex.

Table 3-7: Comparison of binding energies of N_2 in presence and absence of water using B3LYP//6-311G**(O, H, N, C) +SDD(Zr) in kJ/mol

Linker	**No defect**		**O defect**		**H_2O defect**	
	Water present	Water absent	Water present	Water absent	Water present	Water absent
3R	-9.6	-10.4	-5.8	-4.3	-6.2	-5.2
2R+R-NH_2	-8.7	-11.0	-6.1	-4.9	-5.9	-5.1
R+2R-NH_2	-8.3	-11.5	-7.0	-4.4	-6.9	-5.2
R+2R-NH_2(iso)	-8.5	-11.5	-7.7	-5.4	-6.9	-5.0
3R-NH_2	-9.8	-11.9	-7.2	-5.0	-7.2	-5.5
2R+R-CH_2NH_2	-7.4	-14.6	-6.7	-5.1	-8.8	-5.4
2R+R-CH_2OH	-10.3	-10.5	-10.2	-4.9	-9.3	-5.5
2R+R-CH_2CONH_2	-8.6	-8.7	-6.4	-5.2	-8.3	-10.5

However, data, as presented in table 3-7 and figure 3-25, shows that the precise behaviour for nitrogen depends on the precise nature of the defect studied. For the “No defect” case, the binding energy for nitrogen goes up on removal of water, wheras for the “O defect” and the “H_2O defect” the binding energy on the whole decreases upon water removal, except for a small number of cases. Thus, this suggests that in the case of the O and H_2O defects, the fact that N_2 has more room to manoeuvre in is detrimental to its binding. However, having water there to “plug the hole” allows for a stronger interaction with the π-system of the aromatic rings. Similarly, the presence of water allows for hydrogen bonding with the side groups of the benzoate rings, also lowering the energy.

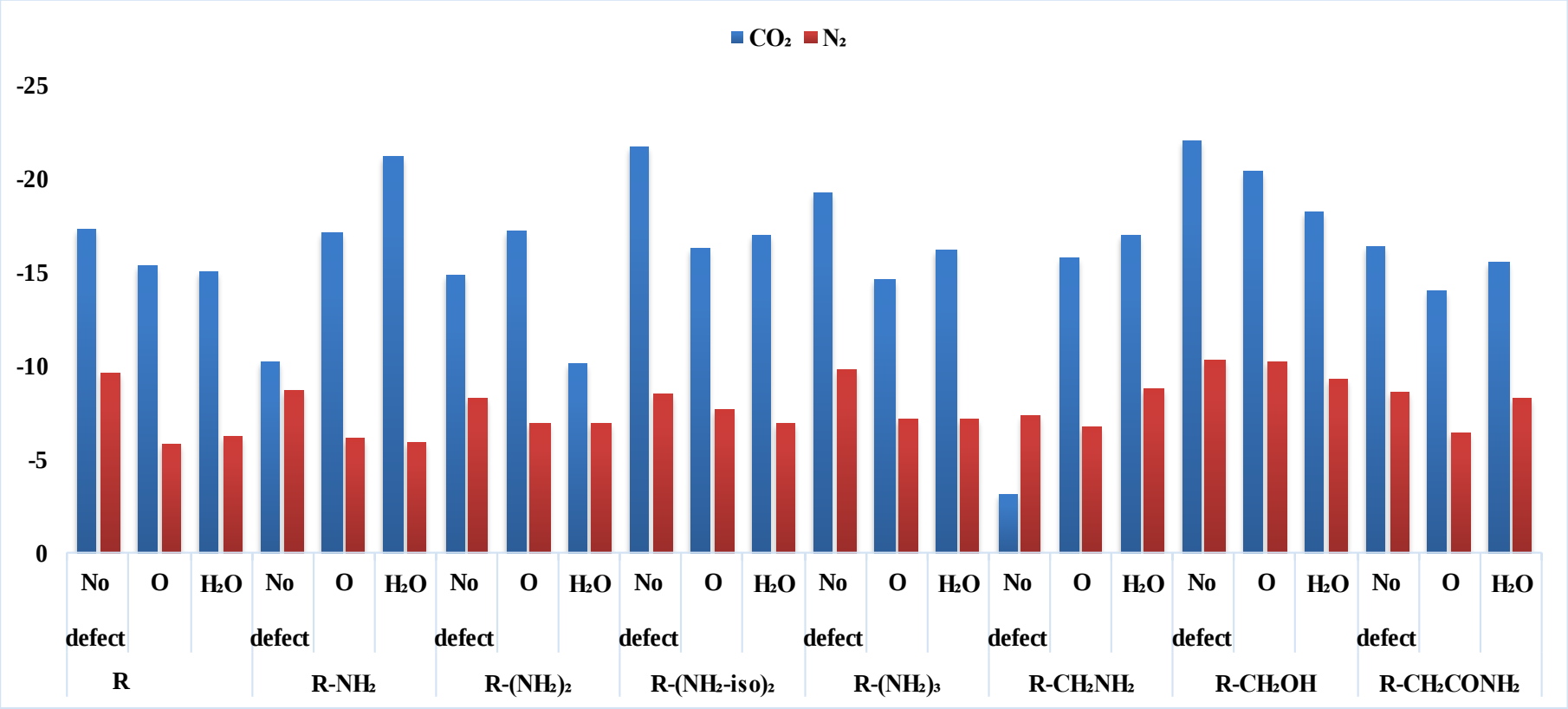

Figure 3-25: Binding Energies of CO_2 and N_2 in Presence of Water Using B3LYP//6-311G(d, p)+ SDD(Zr), R is the unsbstituted benzoate ligand.

3.6: Conclusions

The study carried out and presented in this chapter examined the minimum energy conformations of the complexes $[Zr_6(\mu_3\text{-}O)_4(\mu_3\text{-}OH)_4(O_2CH)_9(O_2CC_6H_5)_3]$, $[Zr_6(\mu_3\text{-}O)_4(\mu_3\text{-}OH)_4(O_2CH)_9(O_2CC_6H_4X)\ (O_2CC_6H_5)_2]$, $[Zr_6(\mu_3\text{-}O)_4(\mu_3\text{-}OH)_4(O_2CH)_9\ (O_2CC_6H_3X)_2\ (O_2CC_6H_5)]$, $[Zr_6(\mu_3\text{-}O)_4(\mu_3\text{-}OH)_4(O_2CH)_9(O_2CC_6H_2X)_3]$ where X represents a series of *ortho* substituents on bidentate benzoate ligands. The structure of the complex is defined to consist of an octahedral cluster of six zirconium atoms, with twelve edge binding carboxylate groups. As such, the structure models the basic building blocks of a larger metal-organic framework structure. The minimum energy conformation of the binding site models the corresponding portion of the interior voids of the metal-organic framework structure. The binding energy of adsorbed molecules in such locations is a significant determining factor in regard to the adsorption of various molecules onto metal-organic frameworks. The information that is generated in studies such as this is crucial to the development of new materials, with the field of metal-organic frameworks rapidly becoming of great importance and potential. It is clear from our calculations that designing a MOF for use in separating CO_2 from e.g. N_2 or H_2 is clearly possible. In particular, amines and alcohols appear to be give a large differential binding energy in this case, whereby it should be noted that the precise site around which adsorption happens affects the binding energy to a large extent.

The precise method for describing the interactions turns out to be crucial as well. Whereas different functionals largely give consistent binding energies for identical systems, the effect of including dispersion corrections is large. In particular, for hydrogen absorption most of the interaction energy is due to dispersion. It is therefore of importance in future work to look at wave function (*ab initio*) methods for investigating these systems to allow a more defined handle on the role van der Waals interactions play in these systems.

The effect of the presence of water in the system is an important factor in comprehending the functioning and design of new materials. While water tends to be present in multi-molar abundance relative to the binding sites and any adsorbed material within the binding sites, the quantification of the effect of the presence of water is nevertheless important. We did not address the question of to what is the maximum amount of water that the system will tolerate without affecting the binding energy of an adsorbed material, but we showed that for a polar molecule like carbon dioxide, the presence of water can greatly enhance the binding energy when the compound is adsorbed onto the binding site of a complex such as the material that was used for computational studies. It was also determined that the presence of water in the system is slightly enhances binding energies for non-polar molecules such as molecular nitrogen. This factor would be essential knowledge for the application of such materials to processes such as the isolation of specific compounds for specific purposes. In light of the necessity to reduce the amount of carbon dioxide that is being released into the atmosphere each day, the development of materials that can effectively adsorb and sequester carbon dioxide is an important goal. Given the results of the computations carried out for this study, for metal-organic frameworks built on the basis of the complex and the binding site studied for this chapter, it would seem that adsorption of carbon dioxide on a “wet” MOF would be more effective than adsorption from a dry medium.

Chapter 4: Computational analysis of spectroscopic data

Part 1: Natural Bond Orbital Calculations of Copper Paddlewheel Systems

4.1: Introduction

There are many methods that scientists use to experimentally to characterize the materials they make. Whilst methods like X-ray diffraction or IR spectroscopic methods are well established (see e.g. chapter 5 or Ref.127), other are less so. As such there are also fewer computational studies of those methods as well. Therefore, in this chapter we will look at a computational comparison for two such methods, XPS and NMR spectroscopy.

In our theoretical description we will use Natural Bond Orbital theory, which has been discussed in a short review in chapter 2. Therefore, this first section will be about how natural bond orbital (NBO) theory applies to copper paddlewheel metal-organic frameworks in particular. It begins with a brief discussion of copper paddlewheel metal-organic frameworks, with reference to the literature. Finally, the section concludes with analysis and interpretation of computations carried out for copper paddlewheel systems in the present work. Whereas the specific literature reference work was carried out only for a copper acetate paddlewheel system, the present work includes methyl and phenyl-substituted terephthalate linker molecules. Theoretical results are compared to experimental results in the analysis.

4.2: X-Ray Photoelectron Spectroscopy as an Analytical Technique

The basic principle of X-ray photoelectron spectroscopy is the use of X-rays to excite inner, or core, electrons from within atoms. The energy required for the excitation of an electron in this manner is effectively a direct measure of the energy of the particular orbital from which the

electron has been excited. Accordingly, the range of energies are exhibited as a spectrum with peaks corresponding to the individual atoms types within their respective environments within a molecular structure. Natural bond orbital methods and density functional theory can be used to calculate orbital energies and therefore could be used to predict spectra. Experimental X-ray photoelectron spectroscopy data could then be used for comparison and assessment of the validity of the calculation method. Such comparisons are typically made as described above, by plotting calculated spectra against experimentally observed spectra. As mentioned above, the closer the calculations are systematically to the observations, the more 'correct' is the computational model being used.

X-ray photoelectron spectroscopy (XPS) has been used to study MOFs in the literature.[236-238] For example, Kang et al.[239] studied HKUST-1@GO membranes (Graphene oxide) performance for H_2 and CO_2 gas adsorption. Here GO acts as a matrix membrane and HKUST-1 acts as a filler, which is used to maintain the ultra-thin membrane. The copper-based MOF was deposited on the GO surface using the layer-by-layer method. The XPS spectra of Cu $2p_{3/2}$ and Cu $2p_{1/2}$ revealed peaks at 935.0 and 954.9 eV, respectively. The C1s peaks of HKUST-1 @GO membrane were –C–OH at 286.5 eV, –COOH at 288.4 eV, and – C=C–/–C–C– at 284.8 eV. Noteworthy is that HKUST-1 @GO has one more peak compared to pure HKUST-1, which is attributed to the GO material. In addition, the O–Cu peak (530.0 eV) disappeared and the –COOH peak (532.1 eV) grew after CuO NS@GO was transformed into HKUST-1 NS@GO (here NS refers to nanosheets). The change in the XPS spectra provided the evidence for the fabrication of HKUST-1 on the GO surface.

Kim et al.[240] examined the growth of oriented metal-organic framework thin films on a thermal SiO_2 surface by the deposition of copper acetate $Cu(OAc)_2$ on SiO_2. This was followed by ligand exchange, incorporating BTC ligands into the MOF, resulting in a $Cu_3(BTC)_2$. xH_2O

(HKUST-1) MOF on top of SiO_2 layers of varying thickness. The variation in the SiO_2 thickness was used to examine its effect on the HKUST-1 deposition. The XPS study characterized three different substrates: bare thermal SiO_2, thermal SiO_2 immersed in a $Cu(OAc)_2$ solution, and thermal SiO_2 immersed in a BTC solution. Again, XPS was used to follow the formation of layers on SiO_2. One of the conclusions drawn was that e.g. BTC does not interact directly with the SiO_2 surface, as evidenced by the disappearance of the carbonyl peaks of BTC upon immersion of an SiO_2 surface into an H_3BTC solution. (see Figure 4-1)

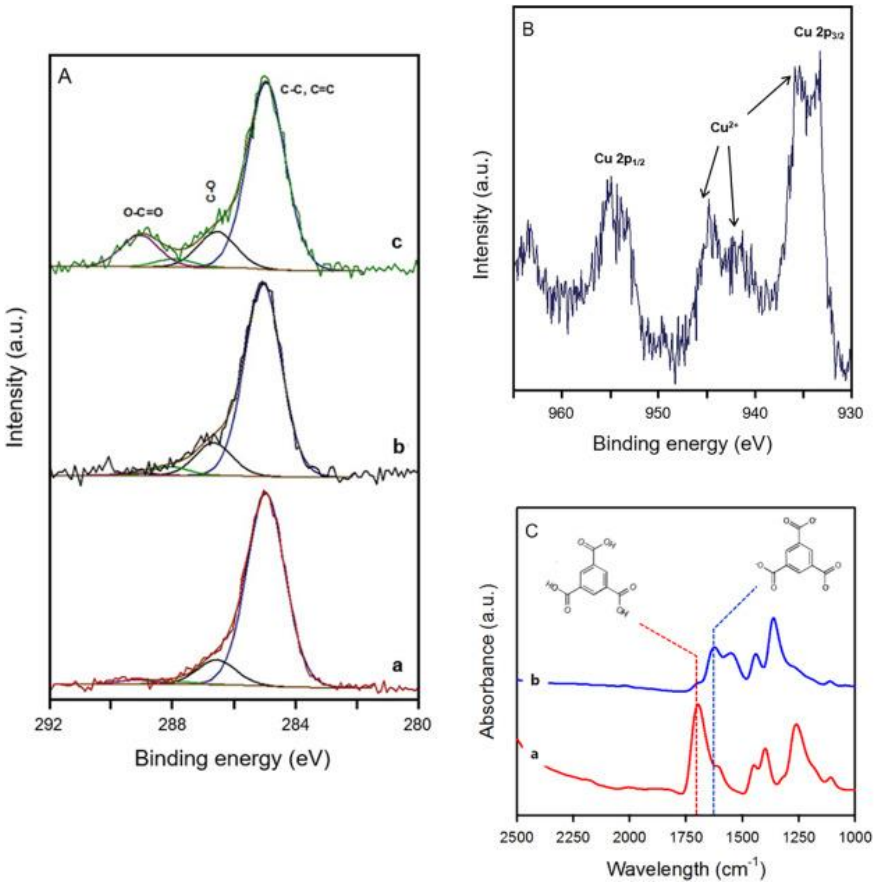

Figure 4-1: XPS spectra in the (A) C 1s (a: bare thermal SiO_2, b: after immersion into H_3BTC solution, c: after immersion into copper acetate $Cu(OAc)_2$ solution) and (B) Cu 2p after immersion into $Cu(OAc)_2$ solution. (C) FT-IR spectra of (a) BTC and (b) HKUST-1 indicating a deprotonation reaction occurred in the synthesis of HKUST-1 from BTC. Reproduced with permission from Ref 240.

Tardio and Cumpson[241] employed natural bond orbital (NBO) analysis to predict the core binding energy for a series of polymers including atoms of the second and the third row of the periodic table. They used Hartree Fock (HF) and density functional theory (DFT) methods with a 6-311 G (d, p) basis set. The results were compared to experimental XPS data. They found that good agreement was obtained both through using Koopmans's theorem (employing both DFT and HF) and through using a self-consistent field (SCF) calculation. However, fluorine shows a large deviation, because not enough electron correlation is included in the calculations.[241]

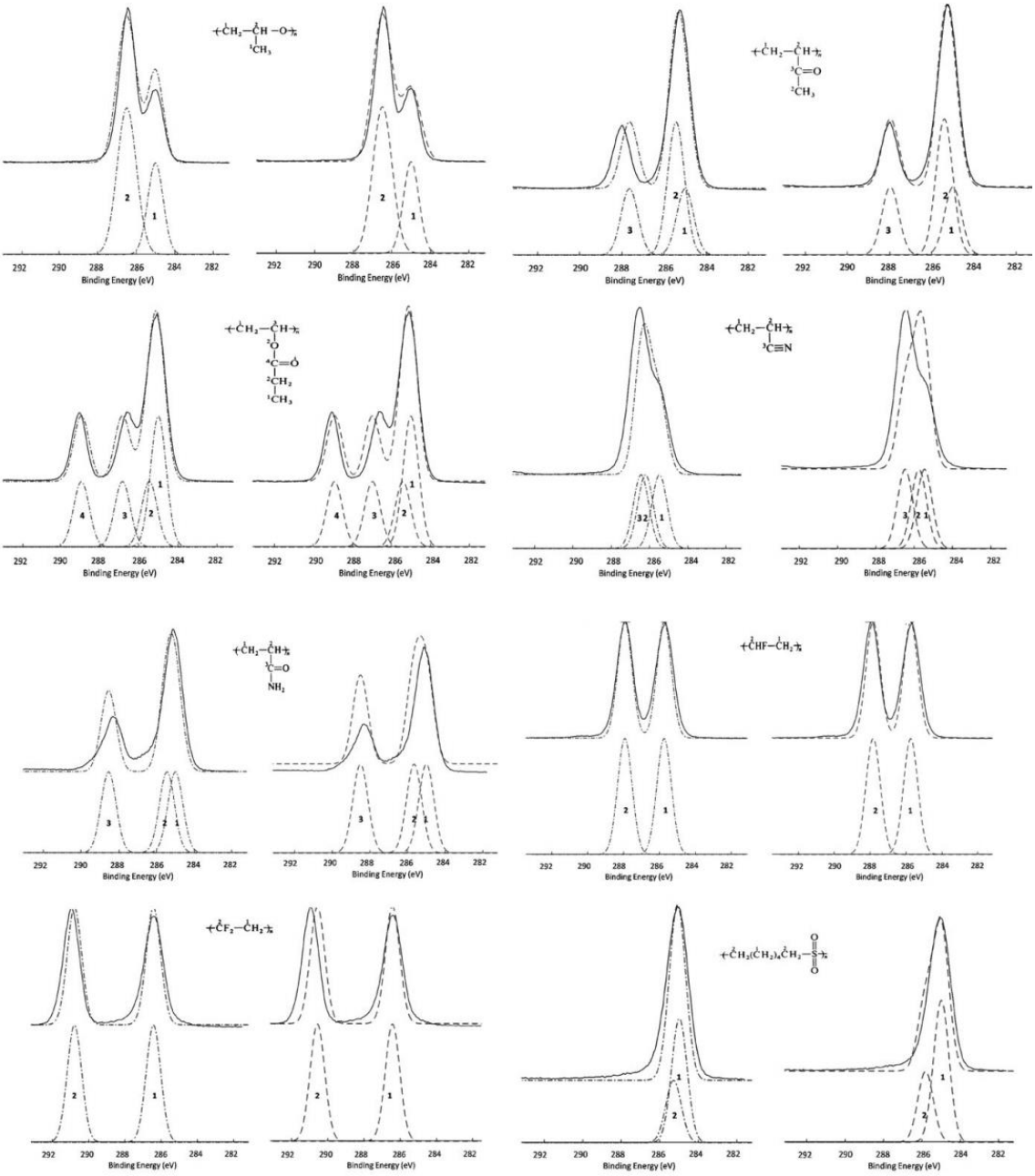

Figure 4-2: Comparison of experimental spectra [polyethylene, polypropylene glycol, polyvinyl methyl ketone, polyvinyl propionate, polyethyleneimine, polyacrylonitrile, polyacrylamide, polyvinyl fluoride, polyvinylidenefluoride, polyvinyl chloride, polyvinylidene chloride, polyethylene sulphide, polyhexamethylene sulphone (solid line) with the theoretical spectra obtained from the values calculated with Koopmans's theorem (dashed line) and ΔSCF method (dashed and dotted line). Reproduced with permission from Ref 241.

In the present study, experimental data obtained by R. Smith[242] is used. She studied the synthesis of HKUST-1 on oxide surfaces. In particular, in her experiments she attached phosphonate SAMS (self-assembled monolayers)[243-246] onto a TiO_2 substrate, because of the thermal stability of such material. This material forms an excellent platform to study MOF fabrication methods. In the experiments, five different phosphonate SAMs were exposed to a copper acetate solution. Then, copper Kα radiation was used to measure the Cu (2p) to P(2p) ratio. It is also noted in ref. 236 that the carbon 1s and copper (2p) XPS spectrum can potentially be used to elucidate the mechanism of copper acetate adsorption on surface- bound SAMs.

In the current study, natural bond orbital analysis is used in a computational study of copper paddlewheel systems, extending the work of Giesbers and coworkers[238] and comparing the results obtained computationally with results obtained experimentally by R. Smith. Giesbers and coworkers reported the results of computational simulation of X-ray photoelectron spectra using quantum chemical methods, particularly density functional theory and second-order Moller-Plesset theory in conjunction with the 6-311G(d,p) basis set.[238] It should be noted at the outset that Giesbers *et al* did not include copper paddlewheel systems in their study. Rather, the important feature of their work is its examination of the use of computation to calculate the energies of electrons and comparing those results with the electron energies obtained from X-ray photoelectron spectroscopic studies of various organic monolayers. In particular, their work looked at the energetics of the carbon 1s region for a variety of organic compounds on a silicon substrate. The calculated results obtained from computation were compared with those obtained experimentally and yielded a correlation factor of 0.9698 with R^2 value of 0.98361. These results suggest that confidence can be placed in the NBO analysis for these types of systems.

4.3: Computational Details

All our calculations were perfomed using density functional theory (DFT) as implemented in Gaussian09 v. D.01.[185] The functional used was B3LYP.[181] The basis set used was 6-311G(d,p).[182,183] Thus, all electrons were taken into account in our calculations. No simplifications due to symmetry were made. Moreover, the paddlewheels were assumed to be dry. Therefore, no solvent effects were taken into account. The NBO method was used as implemented in Gaussian09 and conforms to version 3.[247]

The starting geometry for the copper paddlewheels was built from scratch, using a similar structure in the thesis of J. Loader as a guide.[272]

For each structure, the geometry was optimized in the usual fashion. After this, the convergence to a minimum was checked through the calculation of frequencies in the harmonic approximation. No imaginary frequencies were found for any of the structures under consideration below. All NBO calculations were performed following the procedure outlined in the work by Giesbers et al.[238]

4.4: Results and Discussion

The paddlewheel structure of copper(II) acetate dihydrate is shown in Figure 4.3.

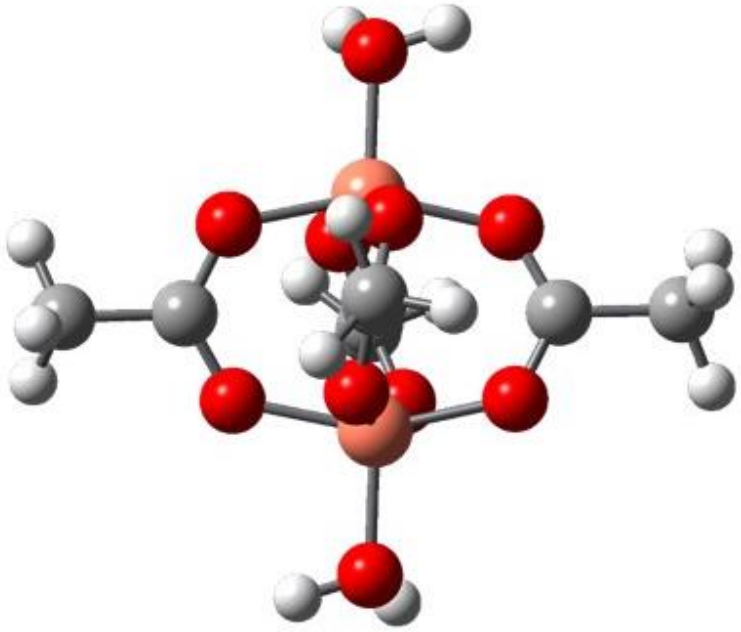

Figure 4-3: Paddlewheel Structure of $Cu_2(acetate)_4.2H_2O$, calculated using B3LYP//6-311G(d,p). The Cu-Cu distance is 2.57 Å. The Cu-O distances are in the range 2.3-2.36 Å.

X-Ray photoelectron spectroscopy of the 1s electrons of the carbon atoms in copper acetate yielded the result shown in figure 4-4. The spectrum obtained for the 2p electrons of the copper atoms is shown in figure 4-5. The calculated orbital energies for the C 1s and Cu 2p orbitals are given in table 4-1. Computations of the C 1s and Cu 2p electron binding energies were carried out for copper paddlewheel systems with terephthalate, benzoate and acetate linker molecules as well.

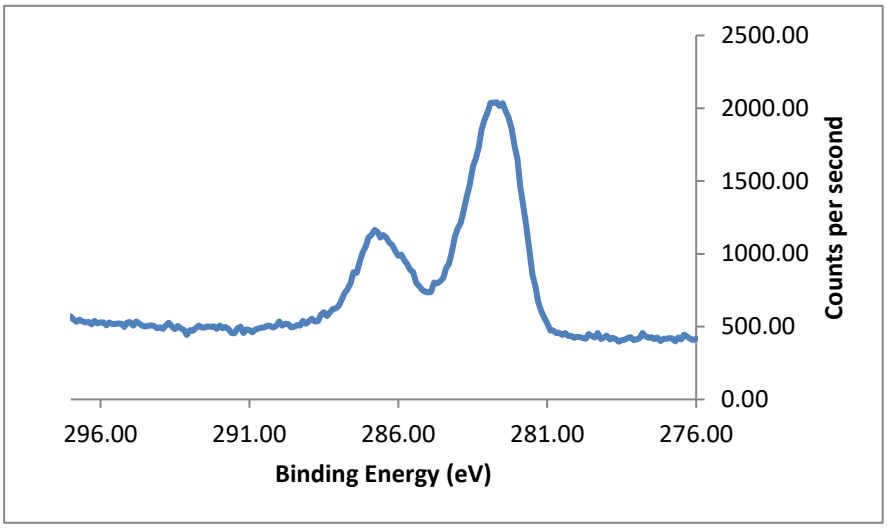

Figure 4-4: X-Ray Photoelectron Spectrum of C 1s Electrons in Copper (II) Acetate. Reproduced with permission from R. Smith, PhD thesis, University of Sheffield, 2017, Ref 242.

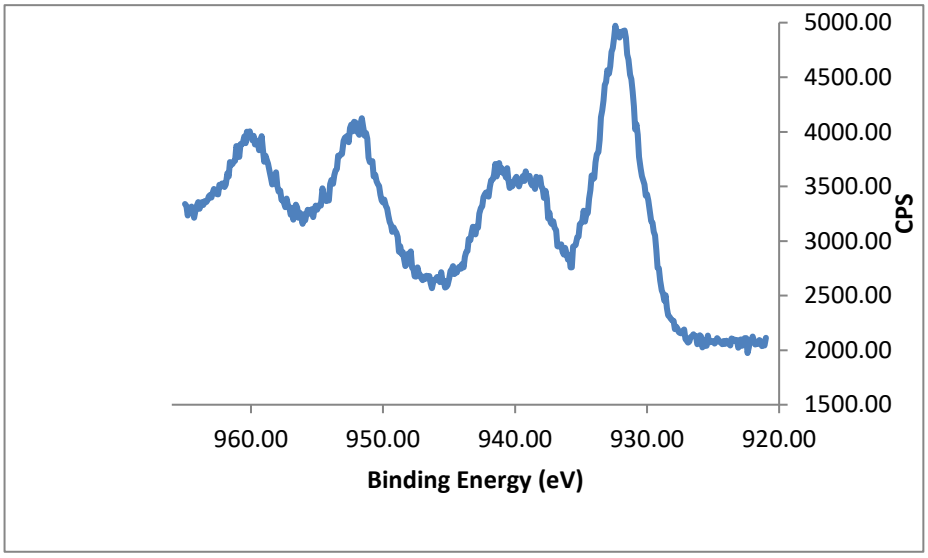

Figure 4-5: X-Ray Photoelectron Spectrum of Copper 2p Electrons in Copper (II) Acetate. Reproduced with permission from R. Smith, PhD thesis, University of Sheffield, 2017, Ref 242.

The major peak in the C 1s spectrum occurs at a binding energy of 282.70 eV, and the lesser peak occurs at a binding energy of 286.8 eV. In the Cu 2p spectrum, several peaks are observed. The major peak occurs at a binding energy of 931.20 eV, and secondary peaks occur at 941.20

eV, 952.20 eV and 961.10 eV. A consistently broadened peak occupies the range of binding energies between 941.20 eV and 937.60 eV.

The structures for these calculations are given in figures 4-3, 4-6, and 4-7, respectively.

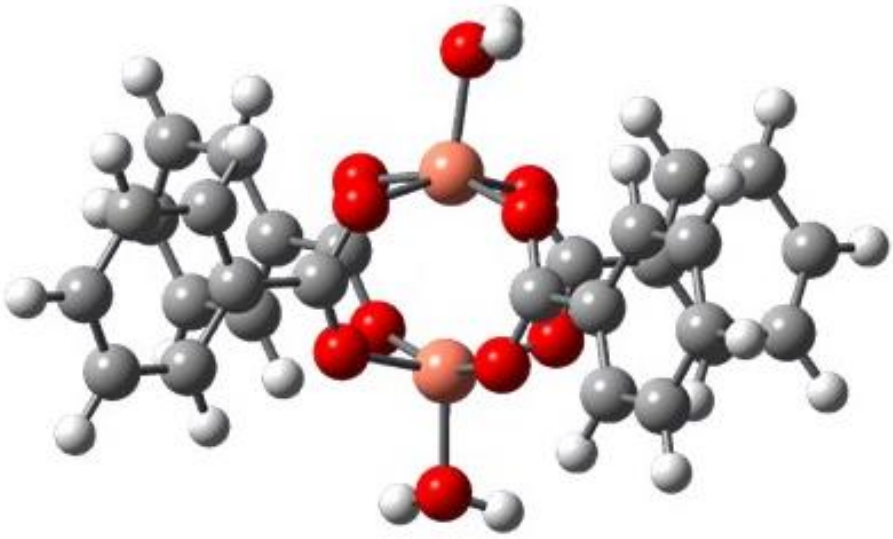

Figure 4-6: Paddlewheel Structure of $Cu_2(benzoate)_4.2H_2O$, calculated using B3LYP/ 6-311G(d,p). The Cu-Cu distance is 2.55 Å. The Cu-O distances are 2.3 Å.

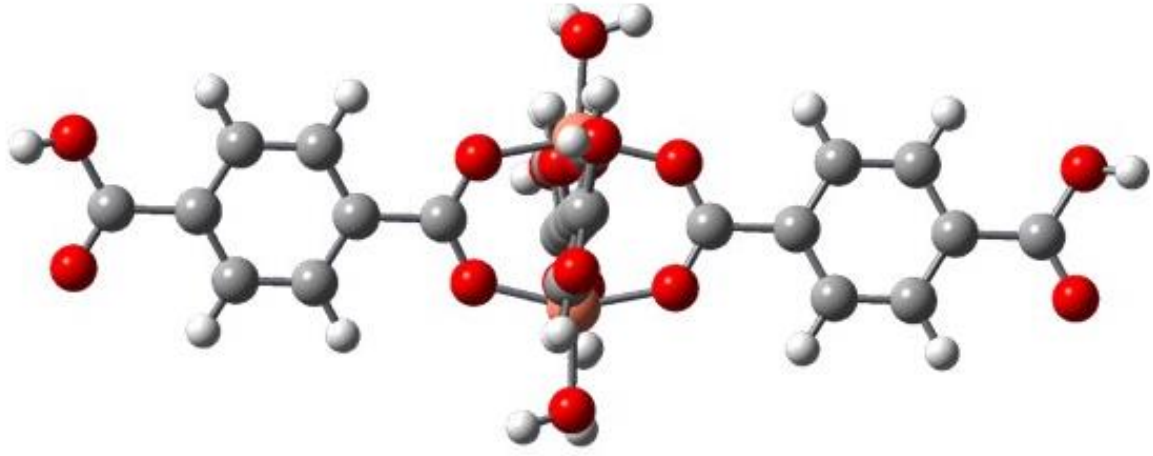

Figure 4-7: Paddlewheel Structure of $Cu_2(terephthalate)_4.2H_2O$, calculated by B3LYP/ 6-311G(d,p). The Cu-Cu distance is 2.59 Å. The Cu-O distances are 2.3 Å.

Table 4-1: Calculated Binding Energies (in eV) of C 1s and Cu 2p Electrons in Cu(II) Paddlewheel Systems built from Cu-acetate, Cu-benzoate, and Cu-terephthalate.

a: Cu-acetate system

Cu-acetate	C_{1s}(acetate)	C_{1s} (alkyl)	Cu_{2px}	Cu_{2py}	Cu_{2pz}
NBO(theory; eV)	277.02 (286.44)*	273.31 (282.60)*	924.45	924.48	924.14

b: Cu-benzoate system

Cu-benzoate	C_{1s}(benzoyl)	C_{1s} (benzene)	Cu_{2px}	Cu_{2py}	Cu_{2pz}
NBO(theory; eV)	277.10 (286.52)*	273.07 (282.35)*	924.89	924.92	924.58

c: Cu- terephathalate system

Cu-terephthalate	C_{1s}(benzoyl)terminal	C_{1s}(benzene)	C_{1s}(benzoyl)
NBO(theory; eV)	277.30 (286.73)*	273.58 (282.86)*	277.60 (287.04)*

* Number between brackets is scaled by 1.033

From table 4-1, it is clear that for the C1s orbitals the energies are close to the experimental energies, but that the difference between the calculated and experiment numbers requires a correlation offset (or scaling factor) to get agreement between the two. Two ways to calculate

such a scaling factor were attempted through a least-squares fit of the experimental data to the calculated energies. If only linear scaling is assumed, i.e. just a simple scaling factor, then the scaling factor is 1.033, which is tabulated in table 4-1. Alternatively, we could also have introduced a fixed offset. In that case, a scaling factor of 1.10051 with an offset of -19.54 eV should be used. Then, the calculated binding energies are 282.49 and 286.59 eV, respectively, for the Cu-acetate system, which is also very close to the experiment. It is noted, that this is somewhat different from the literature scaling value of 0.965 with an offset of 20.34 eV. [238] The reason for this is not exactly clear, but may have to do with the precise system under consideration. Given the qualitative differences between theory and experimental for the Cu 2p orbitals no scaling was attempted here (*vide infra*).

In general, it is worth noting that the calculated binding energies for the C 1s electrons, as tabulated in table 4-1(a-c), give a correct value for each of the bonding environments, despite the fact that the C 1s is generally not considered to be participating in chemical bonding. This is already mentioned (*vide supra*) not the case for the Cu 2p orbitals, which all show a very similar energy in contrast to the experimental results.

The major peak in the C 1s spectrum (see figure 4-4) occurs as a binding energy of 282.70 eV with a smaller peak at 286.8 eV. These can be described to the two different types of C atoms in a Cu-acetate paddlewheel. The first line in table 4-1 shows that this assertion is correct and using the calculations can be assigned to the C 1s orbital of the carbon in the carboxylate group, whereas the peak at 282.7 eV is assigned to the 1s orbital of the carbon atom in the methyl group. The situation is less straight forward for the Cu 2p peaks. The experimental spectrum shows four separate peaks at 931.20 eV, 941.20 eV, 952.20 eV and 961.10 eV, whereby the peak at 941.20 eV is significantly broadened, suggesting the contribution of one of more peaks to this one peak. The calculated results show only three peaks, which are all very close together.

If we were to use the same scaling factor as for C1s, then the energies would be around 956 eV. At that energy, there clearly is no experimental intensity. As a result, no clear assignment of experimental peaks can be made in this case. The reason for the lack of splitting is not entirely clear, but e.g. relativistic effects could play a role in this, which would be the subject of future work.

Ostensibly, these computations were carried out to test the correlation of the calculated results against physical experimental results. Such comparisons provide an 'acid test' of the ability of theoretical principles to calculate real-world results, on the assumption that comparable values indicate the trustworthiness of computations carried out using the same methodology with different structures and systems, and of different measurable properties such as nuclear magnetic resonance shifts. On the basis of our results so far, the only conclusion that can be drawn is that, despite some successes, more work is needed to understand the correlation between theory and experiment for XPS spectroscopy.

Part II: Calculations of NMR Chemical Shifts of Molybdenum Atoms

4.5: Introduction

The signals recorded in nuclear magnetic resonance spectra reflect the magnetic environment of the particular atoms in a molecular structure, and as such are affected by numerous environmental effects, primarily the relative locations of the atoms with respect to the other atoms in the molecule. Computation of nuclear magnetic resonance spectra should account for these effects as completely as possible. An example can be taken from the work of Alkorta and Elguero,[248] who studied the conformations of amines computationally. They noted

that the application of calculated chemical shifts to conformational analysis depends on differences in the absolute shielding responsible for the signals. This is governed by the dihedral angles in the compounds, which correspond to either the H–C+N–LP bond or the H–C···N–LP interaction across two atoms that are not bonded to each other. It was also noted by Alkorta and Elguero that only *large* differences in the absolute shielding provide unambiguous assignments. In the amine compounds used in the study, the differences in δ values between calculated and observed nuclear magnetic resonance shifts depended on the dihedral angles of the bonds in the molecule, and on the distance of the particular atom from the nitrogen atom of the amino group. Additionally, anisotropy of the lone pair depended on the ring size of heterocyclic amines, whether the atoms of interest are in the α, β, or γ position relative to the amine, and on the substituents that may be bonded to the amino nitrogen atom. Typically, the lone pair corresponds to a local minimum in the Laplacian description of electron density, and all of the preceding factors come into play in the accurate prediction of a nuclear magnetic resonance spectrum by computational means. As stated by Grimblatt and Sarotti,[249] the calculated nuclear magnetic resonance results are expected to have a very high statistical correlation with observed spectra. Yet for complex molecular structures, they indicated that the pattern of peaks in the experimental and calculated spectra is often a better indicator of molecular identity that the specific chemical shifts of the nuclear magnetic resonance signals. Indeed, complex structures are identified in such cases with the proposed structure for which the peak pattern of the experimental spectrum is the closest match to the calculated spectrum. This is echoed in the work of Pankratyev, Tolyabaev and Khalilov[250] (*vide supra*) who state that quantum mechanical nuclear magnetic resonance obtained from computations and experimental data taken together offer a good possibility of removing ambiguity in spectral assignments. At the same time, however, those authors point out that the different computational approaches utilised to calculate chemical shifts in nuclear magnetic resonance

spectra each has an inherent error in its methodology. The calculated δ values of chemical shift must be subjected to the application of a correction factor to improve their correlation with the observed values from experimentally obtained spectra.

An additional complication comes from the fact that the chemical shifts of specific atoms in ^{1}H and ^{13}C nuclear magnetic resonance spectra are typically determined relative to an internal standard, e.g. tetramethylsilane (TMS). This compound is used as an internal standard in prepared samples, because it does not react with either the compounds being analysed or the solvent in which the sample has been prepared. Moreover, it is easily and completely removed from the sample afterwards due to its high volatility. Finally, it provides a single, sharp peak in the spectra that are obtained. Accordingly, the peaks due to the atoms of interest in nuclear magnetic resonance spectra are described by the extent to which they are shifted from the TMS peak. Solvents that are typically used for the preparation of samples for nuclear magnetic resonance spectroscopy are required to have no atoms that would produce an interfering signal within the spectra that are obtained. Thus, solvents that do not contain hydrogen atoms are use*f*ul for ^{1}H (proton) nuclear magnetic resonance studies. The most useful of these is the deuterated form of chloroform, $CDCl_3$ due to the general applicability of chloroform as an organic solvent and the lack of paramagnetic character in the deuterium nucleus. Unfortunately, the presence of exchangeable protons in the compound of interest generally results in the formation of a certain amount of normal chloroform in the prepared sample. Depending on the number of exchangeable protons in the sample, and the rate at which the exchange takes place, the interfering peak due to $CHCl_3$ can be very problematic. Accordingly, solvents tend to be chosen for specific applications that depend on the nature of the compound to be analysed. This has ramifications for the computation of the chemical shifts. As has been pointed out in ref 250, chemical shifts (δ) and spin-spin coupling constants (*J*) depend on the magnetic shielding of

magnetically resonant nuclei by electrons and other nuclei, and the particular solvent being used is a major factor in determining these values due to solvent-solute interactions with the compounds of interest. This would indicate that the chemical shift of a particular atom under study in one solvent will necessarily differ to an extent from the same study carried out in a different solvent. Furthermore, as has been addressed by Sarotti and Pellegrinet,[251] chemical shifts in the absolute sense are virtual only. While the nuclear magnetic resonance signal is real, its 'location' can only be identified relative to that of another compound that is used as a standard. Indeed, this relative sense is for practical purposes the only one by which the nuclear magnetic resonance spectra can be comprehended and utilized routinely.

4.6: Gauge Invariance Problem and Computational Error

In calculating nuclear magnetic resonance shieldings and chemical shifts, a peculiar difficulty arises due to the so-called 'gauge invariance problem'. This is the non-physical dependence of the results on an arbitrary 'gauge' of the vector potential which, appears in the Hamiltonian as a vector potential with no fixed origin.[252] A common gauge origin can be chosen as the origin of the magnetic field, but the effectiveness of this approach is limited by the finite nature of the basis sets used in computation. This results in magnetic properties that are dependent upon the choice of gauge origin. As a consequence, they are not universal. To completely overcome this problem one would need to the use an infinite basis set. Since this is infeasible, the use of truncated basis sets in *ab initio* computation results in significant error. One particular method to circumvent this problem is the Gauge Including Atomic Orbital (GIAO) method. This is a combined approach to minimising the gauge invariance problem by utilising gauge origins that are distributed as intrinsic components of the atomic and molecular orbitals. Thus, it is necessary to consider what the gauge origins are, and how adequate the basis set is with respect to the Hartree-Fock limits. Last, but not least, it is also necessary to examine the predicted

results as a function of the overall computational method. Baldridge and Sieget[252] stated that one can, in principle, generate a simple correction factor relating the calculated and experimental chemical shift δ values. Based on the assumption that in the ideal case the calculated and empirical values are identical, a plot of one against the other would yield a linear regression plot having a slope of exactly one. This, of course, assumes that there are no extraneous factors that disrupt a linear relationship between the calculated and observed values of the form

$$\delta_{absolute} = m\delta_{empirical} + b \qquad \text{Equation 4.1}$$

Here, the δ values are the calculated and observed quantities and *b* is an axis offset value reflecting the incomplete nature of the selected basis set. In the case of the 'infinite basis set', b equals 0. Variations from the slope value m from unity are dependent on the computational method and the basis set used. Generally, the effect of increasing the basis set size lowers the value of $\delta_{absolute}$ in Equation 4.1. For the compounds used in ref 246, it was found that the addition of polarisation functionality in the calculation decreased the predicted value of δ by as much as 1 ppm, while simple solvent effects caused a 0.1 ppm change in the δ values. Interestingly, also found that using DFT calculations in the computations also decreased predicted values of δ by as much as 1 ppm. It is important to note that they examined and compared a number of computational approaches in their study, including Single Gauge Origin (SGO), Continuous Set of Gauge Transformations (CSGT), Individual Gauge for Atoms in Molecules (IGAIM) and Individual Gauge for Localised Orbitals (IGLO), in addition to the GIAO method. They stated that the latter gave the best results of all approaches tried. In a similar vein, using a different set of compounds for study, Lampert *et al*[253] agree that the GIAO method is the most straightforward formulation for computing δ values of nuclear magnetic resonance spectra. As a consequence, it has become the most widely used. The development of

the GIAO method has included accounting for electron correlation effects in molecules containing multiple bonds. This feature is essential for obtaining reliable nuclear shielding data. What must be considered in practical terms are the differences between the pure calculation of 'ideal' molecular spectra, and the actual spectra of condensed matter, and real temperature effects (versus zero temperature). There are also practical limitations arising from the available computational availability and accuracy, all of which combine in ways that necessarily result in incomplete agreement between experimental and calculated values of δ from nuclear magnetic resonance studies. As has been mentioned above, the pattern of spectra peaks is therefore more important in practical utility than the absolute agreement of δ values. Lampert *et al*[253] also found that the average differences between experimental and calculated values of δ decreased by adding diffuse functions to the methodology, which is to say that the more complete the systematic model used in the computation, is the closer the results are to the values.

Pankratyev and coworkers[250] also describe the use of side-by-side comparison of calculated and experimental spectra in structure elucidation as a valuable technique for clarifying spectral assignments. Correlations between calculated and theoretical δ values, in their estimation, is improved by adding correction factors to the calculated δ values. In common terms, this is essentially just a 'fudge factor', however, designed to force the observations to fit the theory, or vice versa. But it is also a necessary evil since each different approach to 'correcting' the calculations to match the observed values contains inherent inaccuracies due to the unavoidable trade-off between accuracy and computation costs.

4.7: Computation Methods

Most quantum mechanical computation methods in the literature appear to allow good prediction of ^{1}H and ^{13}C nuclear magnetic resonance chemical shifts, though all require the use

of a scaling factor to remove systematic errors in the calculation process. The agreement between theoretical and calculated δ values is significantly improved by this technique, but as Sarotti and Pellegrinet[251] point out the technique is limited by the fact that experimental results are required as reference for the theoretical results, and the real challenge is the computation of accurate nuclear magnetic resonance chemical shifts using only quantum mechanical calculations. Second-order Moller-Plesset theory (MP2) is known to yield excellent computational results, but the method is demanding of computation time and cost. Density functional theory has become the viable alternative, as it provides acceptable accuracy at comparatively low computational cost, and is typically performed using the GIAO computation methodology. Sarotti and Pellegrinet[251] identify the main problem with practical computation against experimental observation as the choice of reference standard, and question whether a reference standard can be found that performs better than tetramethylsilane (TMS) at any level of theory for GIAO observations of ^{13}C spectra. Their approach to this was to propose a multistandard reference system using different reference standards such as methanol for sp^3 carbon atoms and benzene for *sp* and sp^2 carbon atoms. In their investigation of this approach, it was found that this approach performed much better than just using TMS as a reference standard, especially when GIAO calculations were carried out using density functional theory methods. In fact, there was no evident dependence on the quality of the results by changing from the low computational cost of the 6-31G(d) basis set to the higher computational cost and more time consuming 6-311+G (2d, p) basis set using B3LYP method.

Buhl and van Mourik[254] note that the majority of computational studies of atomic and molecular structures are carried out for pristine static 'theoretical' structures that have been optimised at an appropriate quantum mechanical level that then require the inclusion of thermal motion and solvation effects that become more noticeable with increasing nuclear mass. This

also is an important consideration for computational studies of metal-organic frameworks. However, it was not considered here.

4.8: Computational Details

In this work, an attempt was made to elucidate the experimental work done by R. Smith,[242] where molybdate anions were absorbed onto Zr-oxo clusters (UiO-66), figure 4-8.

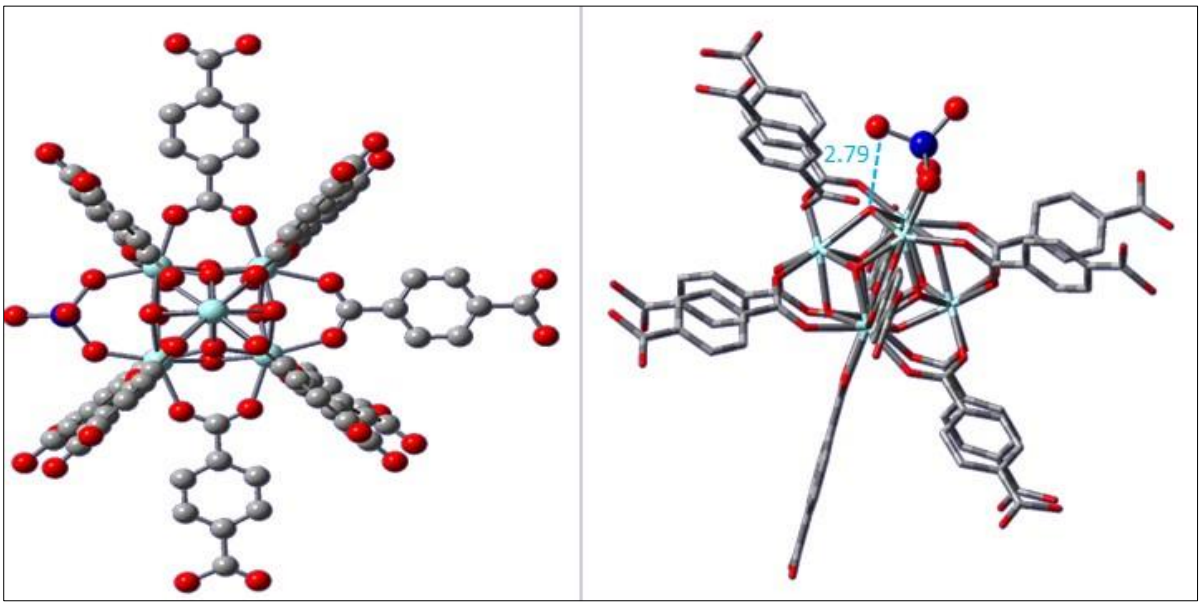

Figure 4-8: Geometry optimised model of molecular cluster $[ZrO_4(OH)_4(C_8H_5O_4)_{11}(MoO_4)]^-$. Reproduced with permission from R. Smith, PhD thesis, University of Sheffield, 2017.[242] Image on the right shows hydrogen bonding interaction between Mo=O and μ_3-OH. Colour scheme: blue = Zr, red = O, grey = C, purple = Mo. Hydrogens removed for clarity.

Initial attempts to understand these materials were unsuccessful, since the crystals were not large enough for use in single crystal X-ray diffraction. Thus, Mo MAS NMR (Magnetic Angle Spinning) studies were carried out to further our understanding of the modified UiO-66 materials,[242] figure 4-8. The experimental NMR spectra for molybdate-modified UiO-66 $[ZrO_4(OH)_4(C_8H_5O_4)_{11}(MoO_4)]^-$ are shown in figures 4-9 to 4-12 for three different

references.[242] The NMR spectrometer measurements were performed at ω_0 (^{95}Mo) = 55.394 MHz. The spectrometer-spinning rate was set to 6 kHz for all experiments. Series of molybdate modified UiO-66 materials were prepared with different molybdate loadings by varying the concentration of Na_2MoO_4 in solution.[242] In summary, the experimental NMR studies suggested that molybdate replaced a benzenedicarboxylate (bdc) ligand, which was bound to a Zr node.

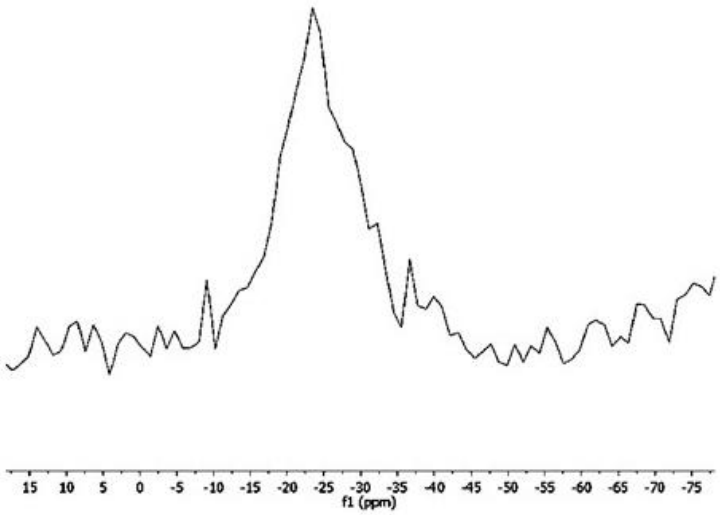

Figure 4-9: ^{95}Mo Solid-State NMR Experiments, Mo-UiO-66 loading (Mo per node) is 0.8 with magic angle spinning at 6 KHz. Reproduced with permission from R. Smith, Ref 242.

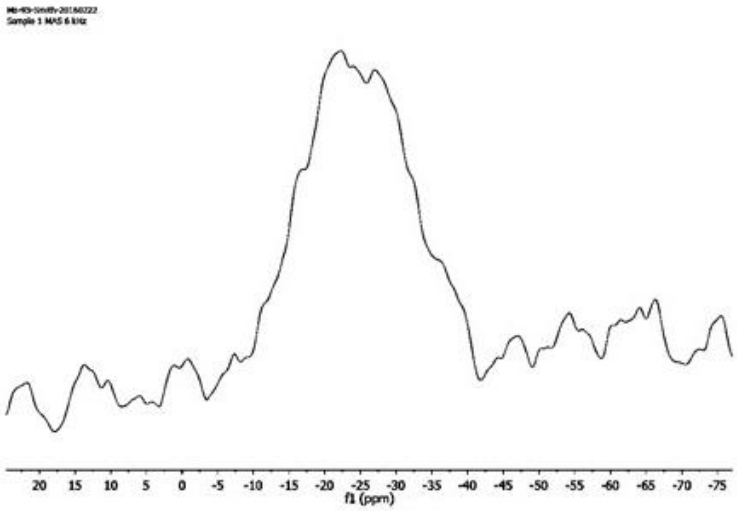

Figure 4-10: ^{95}Mo Solid-State NMR Experiments, Mo-UiO-66 loading (Mo per node) is 1.23 with magic angle spinning at 6 KHz. Reproduced with permission from R. Smith, Ref 242.

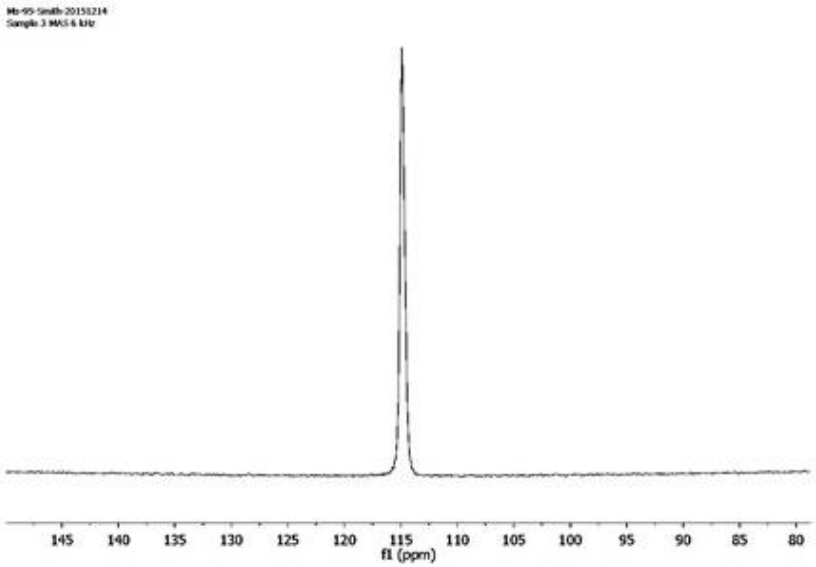

Figure 4-11: ^{95}Mo Solid-State NMR Experiments of Ag_2MoO_4 obtained at 18.8 T using a single-pulse sequence with magic-angle spinning at 6 KHz. Reproduced with permission from R. Smith, Ref 242.

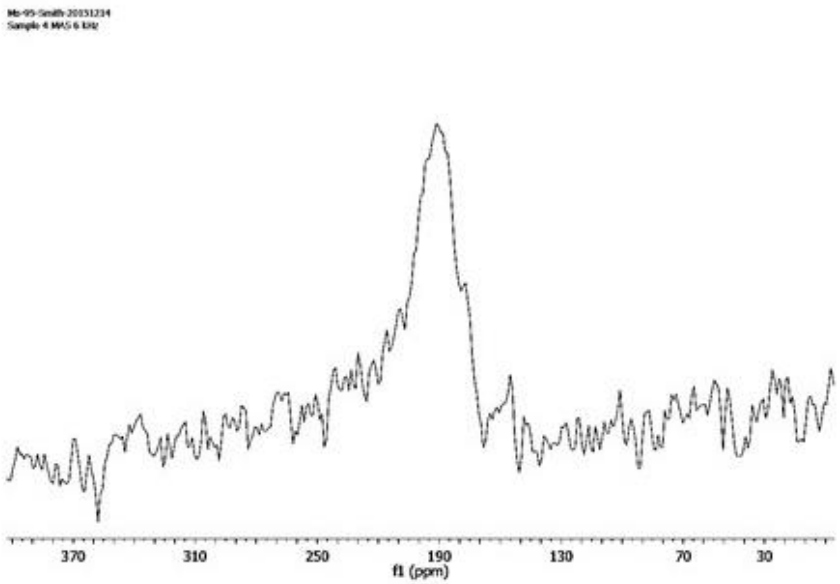

Figure 4-12: ^{95}Mo Solid-State NMR Experiments Mo-UiO-66, Reference: $MoO_2(OSiPh_3)_2$ – 6kHz MAS. Reproduced with permission from R. Smith, Ref 242.

In our computational work, the nuclear magnetic resonance shifts of the molybdenum atoms in three different sites of zirconium clusters were calculated using the GIAO NMR method[252] using B3LYP[181] as implemented in Gaussian09.[185] The 6-311G(d,p) basis set was used[182, 183] on all atoms except for the metal ions which used the SDD pseudo-potential.[184] The results were compared to the experimentally observed spectra. The general formula of the Zr cluster is $[Zr(\mu\text{-}O)_4(\mu\text{-}OH)_4(O_2CH)_{12}]$. One of the formate group in our calculations, is replaced by molybdate oxide $(MoO_4)^{2-}$. The number of benzoate groups replaced by formate ligands is: 0, 2, 4, and 11.

Table 4-2: Different ligands in molybdate modified Zr cluster

Mo Zr-oxo cluster	MOF formula	Formate	Benzoate
L_1	$[Zr(\mu\text{-}O)_4(\mu\text{-}OH)_4(O_2CH)_{11}(O_2MoO_2)]^-$	11	0
L_2	$[Zr(\mu\text{-}O)_4(\mu\text{-}OH)_4(O_2CH)_9(O_2CC_6H_5)_2(O_2MoO_2)]^-$	9	2
L_3	$[Zr(\mu\text{-}O)_4(\mu\text{-}OH)_4(O_2CH)_7(O_2CC_6H_5)_4(O_2MoO_2)]^-$	7	4
L_4	$[Zr(\mu\text{-}O)_4(\mu\text{-}OH)_4(O_2CC_6H_5)_{11}(O_2MoO_2)]^-$	0	11

The total charge of these MOFs is -1. The shift of the molybdenum atom is defined as equal to the shielding of the cluster containing the molybdenum atom minus the shielding of the molybdate. That is

$$\delta_{Mo} = \delta_{(vcluster + Mo)} - \delta_{(molybdate)}$$

The molybdenum chemical shift reference compound was taken to be one of: Na_2MoO_4, $MoO_2(OSiphy_3)_2$ and Ag_2MoO_4. The last two references were studied to be able to compare to the Mo shift of Na_2MoO_4 associated with Zr-oxo cluster.[242] The shifts were calculated for the molybdenum atom in the (μO- μO) site, the (μO- μOH) site and the (μOH- μOH) site of the zirconium cluster structures. Finally, we note that in our calculations, an ECP is used for both Zr and Mo. Thus, it is assumed that the core electrons of Mo, in particular, are not sensitive to the change in bonding environment from the reference compound to the cluster and that any shifts are caused by the valence electrons.

4.9: Results and Discussion

The results obtained for the calculation of the Mo shift in our Zr clusters with 3 different references are shown in Table 4-3.

Table 4-3: Calculated NMR Shifts of Mo Atom in Zr Clusters, a: No- benzoate -ligand systems, b: Two- benzoate -ligand systems, c: Four- benzoate -ligand systems and d: Twelve-terpathalate-ligand systems.

a: No-benzoate-ligand systems (L_1)

Mo-Position	**NMR shift for ^{95} Mo in $[Zr(\mu\text{-}O)_4(\mu\text{-}OH)_4(COOH)_{11}(O_2MoO_2)]^-$**		
	References		
	Na_2MoO_4	**$Mo_2(OSiPh_3)_2$**	**Ag_2MoO_4**
(μO-μO)	8.24	15.12	-13.33
(μOH-μOH)	8.0	14.8	-13.5
(μO-μOH)	6.2	13.1	-15.3

b: Two-benzoate-ligand systems (L_2)

Mo-Position	**NMR shift for ^{95} Mo in $[Zr(\mu\text{-}O)_4(\mu\text{-}OH)_4(O_2CH)_9(O_2CC_6H_5)_2(O_2MoO_2)]^-$**		
	References		
	Na_2MoO_4	**$Mo_2(OSiPh_3)_2$**	**Ag_2MoO_4**
(μO-μO)	10.2	17.0	-11.3
(μOH-μOH)	8.8	15.6	-13.1
(μO-μOH)	10.0	16.9	-11.5

c: Four-benzoate-ligand system (L_3)

Mo-Position	**NMR shift for ^{95} Mo in $[Zr(\mu\text{-}O)_4(\mu\text{-}OH)_4(O_2CH)_7(O_2CC_6H_5)_4(O_2MoO_2)]^-$**		
	References		
	Na_2MoO_4	**$Mo_2(OSiPh_3)_2$**	**Ag_2MoO_4**
(μO-μO)	8.8	15.7	-12.7
(μOH-μOH)	8.4	15.3	-13.1
(μO-μOH)	9.7	16.6	-11.8

d: Eleven-Benzoate-ligand system (L_4)

Mo-Position	**NMR shift for ^{95} Mo in $[Zr(\mu\text{-}O)_4(\mu\text{-}OH)_4(O_2CC_6H_5)_{11}(O_2MoO_2)]^-$**		
	References		
	Na_2MoO_4	**$Mo_2(OSiPh_3)_2$**	**Ag_2MoO_4**
(μO-μO)	8.8	15.7	-12.7
(μOH-μOH)	7.7	14.6	-13.8
(μO-μOH)	6.4	13.3	-15.1

It is well-known that the magnetic interaction between an atom and its environment is very much a 'two-way street', in that they affect each other to an equal degree. In examining the data presented, it can be seen that within each set of complexes of a particular number of benzoates ligands (0, 2, 4, 12) (figures 4-13 to 4-16) the exact position of the Mo atom has a small effect on the chemical shift. However, it is also clear that the shift in each of the cases is underestimated by the calculations and that even the sign of the shift is not consistently reproduced. Our main assumption was that the bonding environment i.e. the valence electrons are the main driver behind the chemical shift. Our results presented in table 4-3(a-d), indicate that it is not as straight-forward as that, since for different bonding environments, the shift

calculated is very similar. As a consequence, we have to conclude that it is not possible to reproduce the chemical shift accurately and consistently while leaving out core electrons.

However, we would like to note that the number of terephthalate ligands does affect the chemical shift in the complex. In particular, the presence of just two terephthalate ligands appears to result in a noticeable displacement of the shift relative to the cases in which 0, 4 or 12 benzoate groups are present in the structure. It is difficult to pin down the reason for this exactly, but if one could speculate that this may indicate the effect of dissymmetric fields resulting from the delocalisation currents of the benzene rings in the terephthalate ligands in regard to their position and orientation relative to the molybdenum atom in the cell space of the structure. In a computational study of the ^{13}C nuclear magnetic spectra of various 1-X-bicyclo[1.1.1]pentanes, Della and coworkers[255] indicated that electron delocalisation from a local environment of a polarised bond to an antibonding orbital should have a deshielding effect on the associated carbon atom. Furthermore, the effect should be larger the greater is the difference in electronegativity between the atoms involved, as polarization along the bond axis creates an electric field that induces an 'opposite sense' polarity in adjacent bonds. It is reasonable to suggest that a similar effect could take place here. It is also noted that the calculations for the (O-OH) site appear to have found a local minimum, since the structures look different. This does not affect the chemical shift significantly. However, clearly more work is needed to explore the PES for this system.

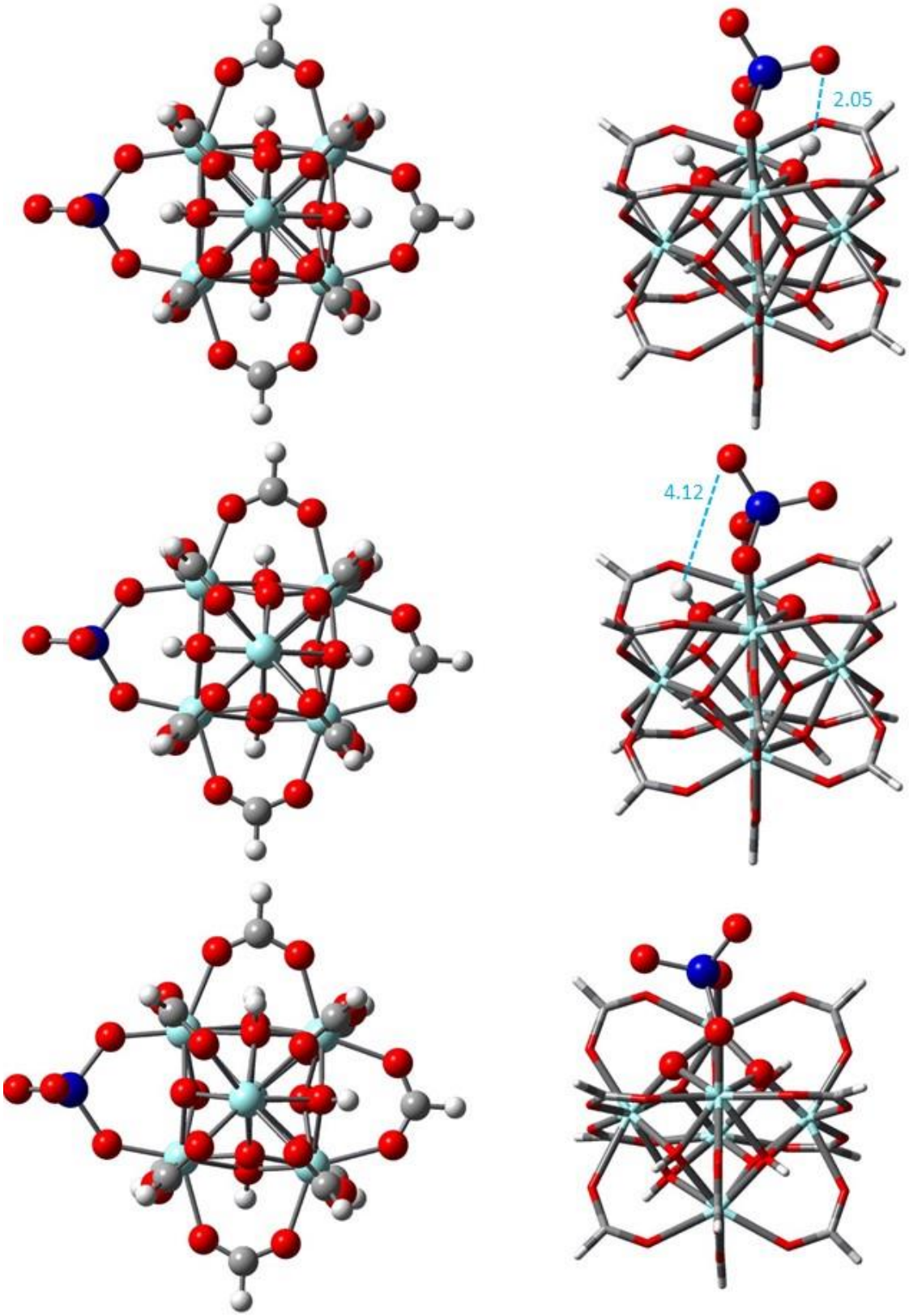

Figure 4-13: Geometry optimised model of two different views of molecular cluster $[Zr_6O_4(OH)_4(O_2CH)_{11}(MoO_4)]^-$ for OH-OH, O-OH, and O-O sites (top to bottom). Colour scheme: Cyan = Zr, red = O, grey = C, purple = Mo. H= white. It is noted that in the figure of the (O-OH) site potentially a local minimum is displayed.

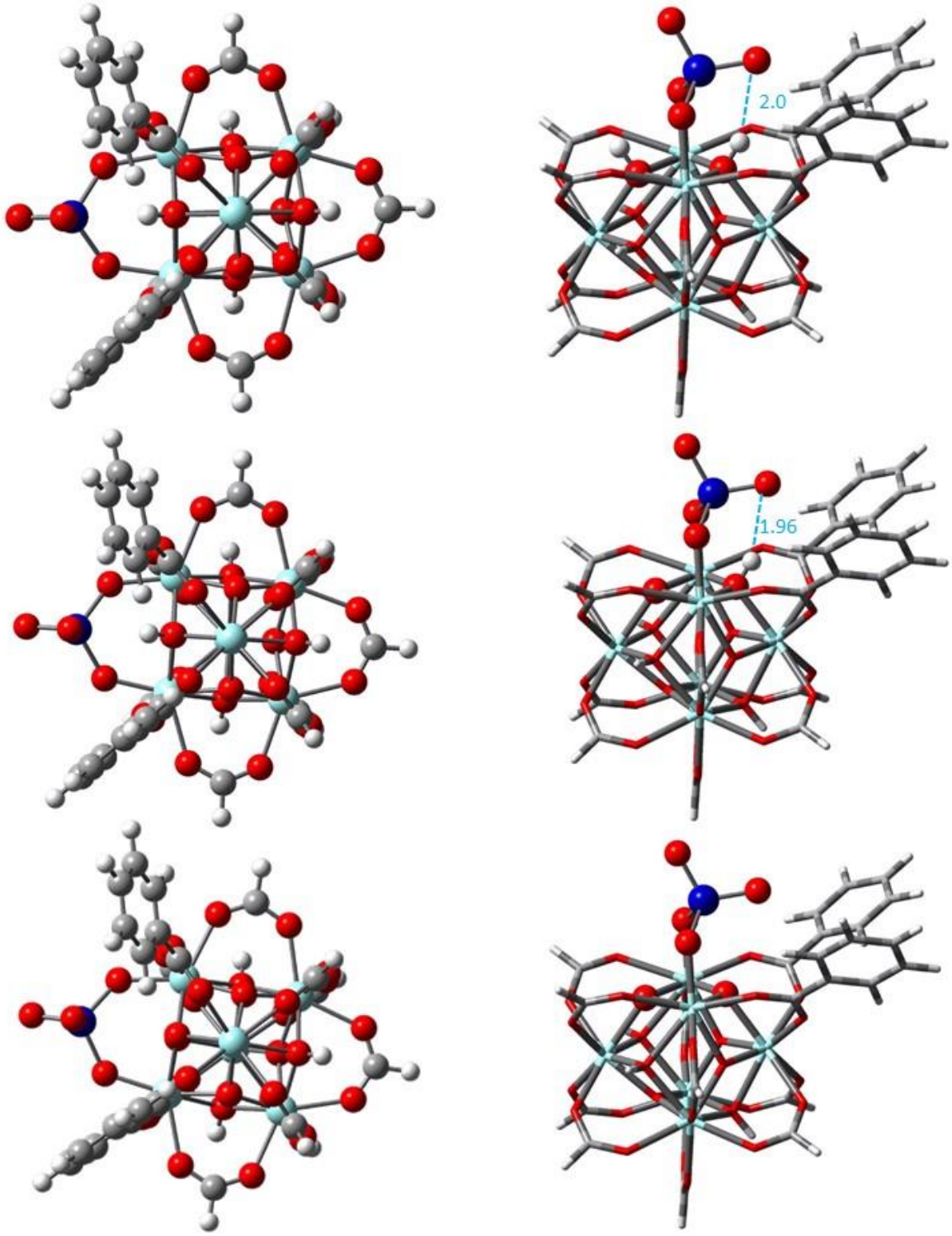

Figure 4-14: Geometry optimised model of molecular cluster $[Zr_6(\mu\text{-}O)_4(\mu\text{-}OH)_4(O_2CH)_9(O_2CC_6H_5)_2(O_2MoO_2)]^-$ for OH-OH, O-OH, and O-O sites (top to bottom). Colour scheme: Cyan = Zr, red = O, grey = C, purple = Mo. H= white.

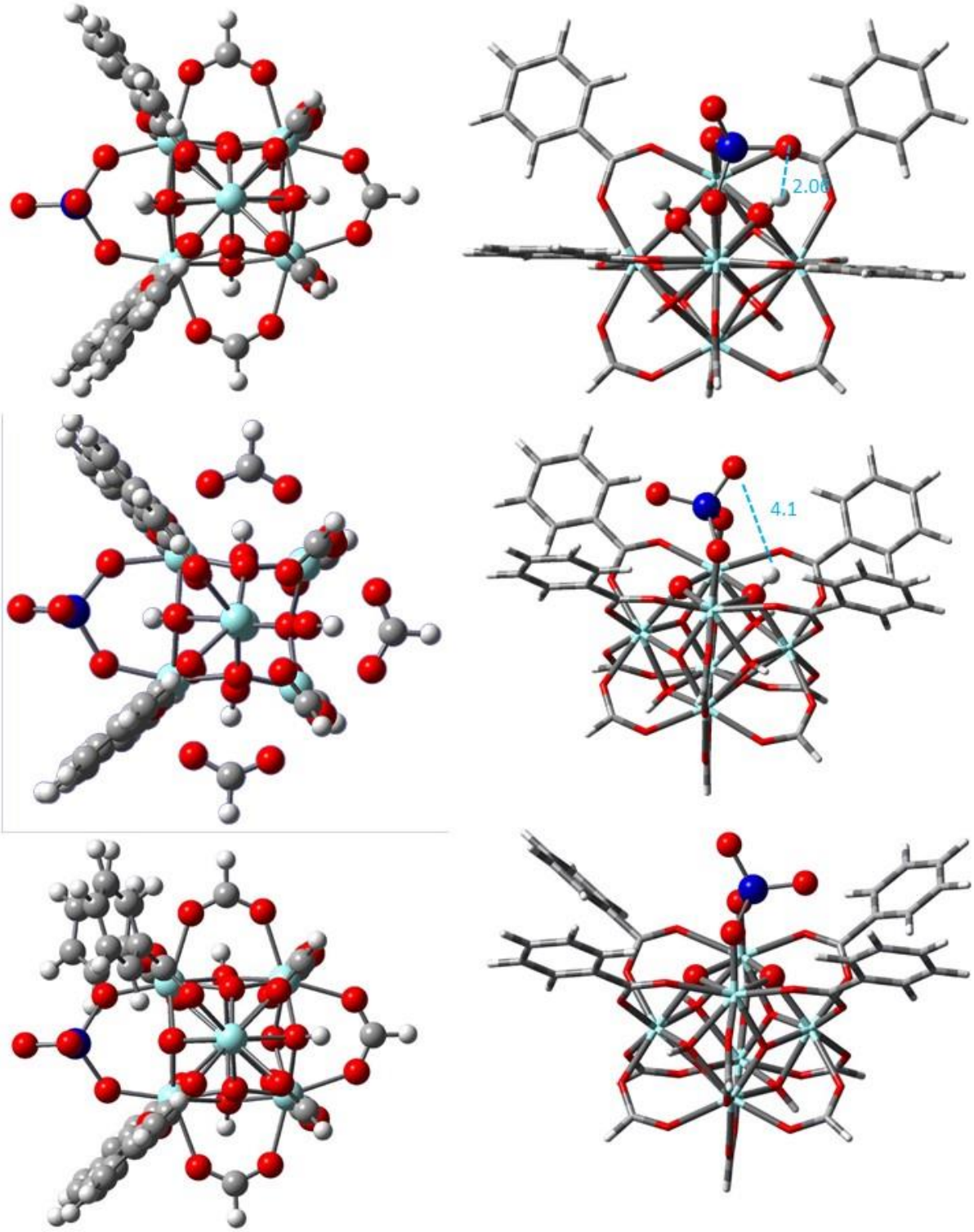

Figure 4-15: Geometry optimised model of molecular cluster[$Zr_6(\mu\text{-}O)_4(\mu OH)_4(O_2CH)_7(O_2CC_6H_5)_4(O_2MoO_2)]^-$for OH-OH, O-OH, and O-O sites (top to bottom). Colour scheme: Cyan = Zr, red = O, grey = C, purple = Mo. H= white. It is noted that in the figure of the (O-OH) site potentially a local minimum is displayed.

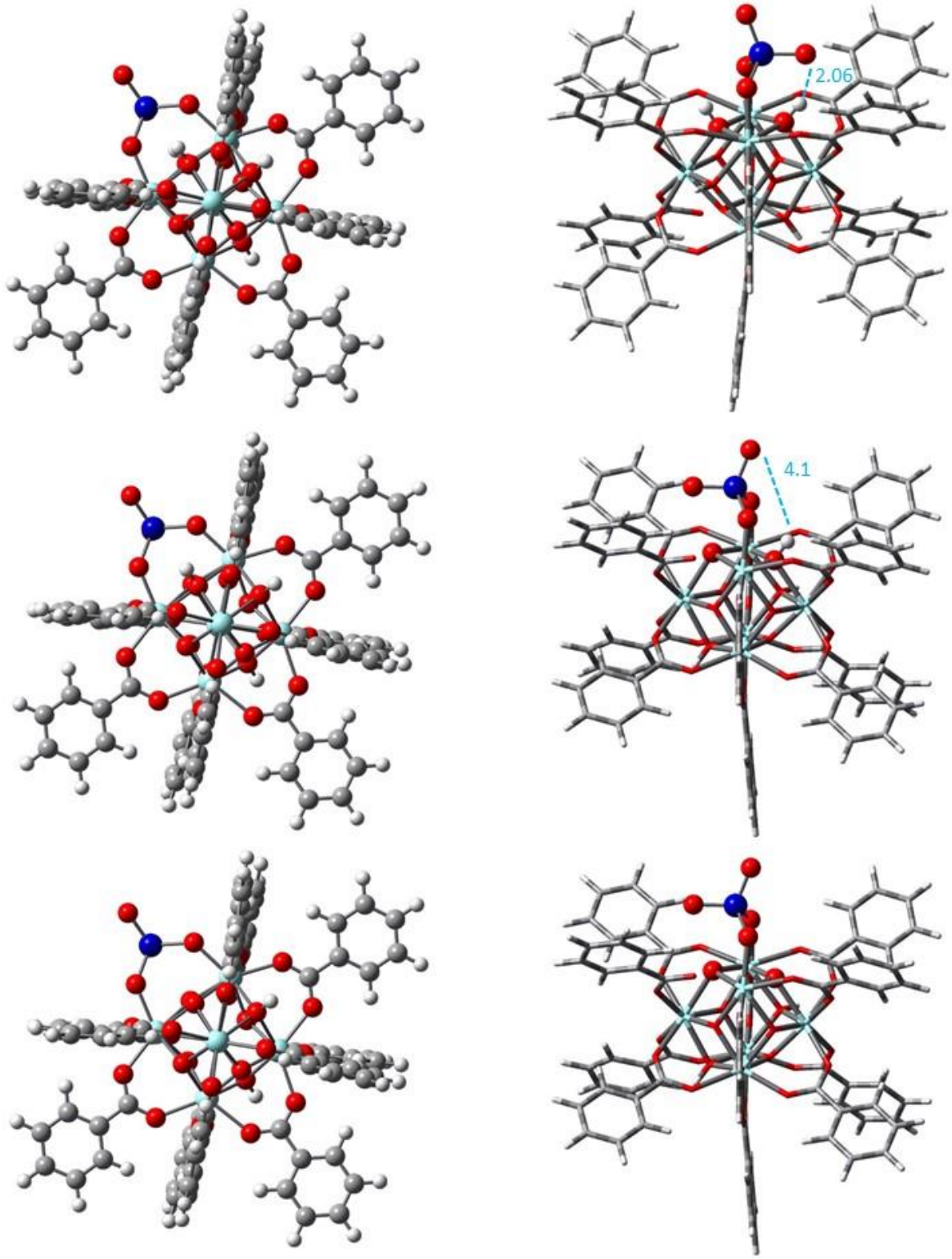

Figure 4-16: Geometry optimised model of molecular cluster $[Zr_6(\mu\text{-}O)_4(\mu\text{-}OH)_4(O_2CC_6H_5)_{11}(O_2MoO_2)]^-$ for OH-OH, O-OH, and O-O sites (top to bottom). Colour scheme: Cyan = Zr, red = O, grey = C, purple = Mo. H= white. It is noted that in the figure of the (O-OH) site potentially a local minimum is displayed.

4.10: Conclusions

Our assumption was that the core electrons of a transition metal atom such as molybdenum are too tightly bound by the nucleus to have an effect on calculation of the chemical shift. Another interpretation of that feature is that the core electrons are bound so tightly to the nucleus that their influence on chemical shift is invariant and that the valence electrons are in fact the determining factor in the real chemical shift. Based on the computational results of this study, it can be reasonably stated that, while calculation of nuclear magnetic resonance spectra by the use of GIAO and density functional theory methods may offer an opportunity for determining absolute chemical shifts as well as the fine detail of spectra, neglect of the core electrons is not an approximation which can be made, since different bonding environments and different references lead to qualitatively different results that do not compare well to experiment. More research is therefore needed to determine the minimum basis set size/ combinations needed to reproduce the experiment results qualitatively and consistently. Hereby, it should be noted that there are no reports in the literature of ^{95}Mo chemical shift calculations, which would enable us to ascertain whether our conclusions are reproduced in other types of complexes.

Chapter 5: A Theoretical Study of the structure of the Exfoliation in Copper paddlewheel systems (2D)

5.1: Introduction

The aim of this chapter is to investigate the possibilities for the computational evaluation of the structure of exfoliated layered materials. Thus, the chapter begins with a brief review of the nature and structure of layered materials, with particular emphasis on metal-organic frameworks. This is followed by an examination of the process of exfoliation with regard to the techniques that have been successfully employed in achieving exfoliation for the production of two-dimensional nanosheet materials. Computations carried out in this regard are expected to provide insight into the structure and properties of exfoliated copper paddlewheel metal-organic frameworks properties and structures.

5.2: Layered Materials and Exfoliation

There are many natural and synthetic materials are known that exist as intrinsically layered structures. Perhaps the most well-known of these in the present time is graphene, isolated mechanically by Novosolov and coworkers[256] in 2004. Since then, many other materials have been identified that have a similar structure of two-dimensional sheets stacked together to form a bulk three-dimensional structure. Examples of such materials include hexagonal boron nitride, molybdenum disulfide, tungsten disulfide, niobium diselenide, dibismuth tritelluride, dibismuth triselenide, and many others, notably metal-organic frameworks. A number of such compounds have been reviewed at length by Nicolosi and coworkers with respect to the layered nature of their structures.[257] Separation of the layers, or exfoliation, of the structure can produce two-dimensional sheet structures of the corresponding material. This greatly increases the surface area. Moreover, it potentially provides a large increase in the effectiveness of the catalytic and sorptive properties of the material. However,

layered materials must be exfoliated to produce two-dimensional materials, if these enhanced characteristics are to be accessed.

5.3: Layered Metal-Organic-Frameworks

As discussed in chapter 1, metal-organic frameworks are materials with a characteristic structure consisting of an array of metal atoms interconnected by organic 'linker' molecules. The two-dimensional structure arises from preferred geometry of linkers plus metal-ions/clusters. The linkers generally need to be rigid in order to limit their degree of freedom and to ensure the expected geometry is obtained.[258] Here, we point out that the coordination environment and the extent of inorganic connectivity can vary considerably between different layered structures when different linker molecules are used with the same metal framework atoms. It is also notable that for metal-organic frameworks to be stable, they often need solvent molecules to create the pore space in the structure. Indeed, sometimes the structures collapse when the solvent is removed. This is one of the reasons rigid aromatic linkers are often used. In the case of a paddlewheel (PW) secondary building unit the solvent molecules from the solvent can coordinate to the axial sites. In some cases, such as HKUST-1, they can be removed without a problem. In other cases, removal of solvent results in structural rearrangements.[259]

A more obviously layered structure is attained when there is intercalation between layers of a 2D metal-organic framework. Such a material may be exfoliated into two-dimensional sheets that can potentially be utilised for their unique electronic and catalytic properties. These *two-dimensional* metal-organic frameworks or metal-organic nanosheets (MONs) provide a very large surface area relative to their three-dimensional counterparts, as well as an enhanced ability for targeted materials to enter the pore space of the framework, where catalysis and separation activities take place.

For metal-organic framework materials, exfoliated layers of molecular thickness offer significant advantages, particularly in the areas of adsorption, catalysis, and separation of specific components from mixtures and solutions. An area of particular application is the area of metal-organic framework membranes, or membranes that act as molecular sieves prepared with metal-organic frameworks.[260] Indeed, Zheng, Grunker, and Feng[261] identify two-dimensional materials obtained from metal-organic frameworks such as 2D Zn_2(benzimidazole)$_4$ by exfoliation as ideal candidates for the development of separation membranes for such applications as gas and ion separation and water desalination, amongst others. One additional example of such a potential application is the use of two-dimensional metal-organic framework nanosheets as sensors.[261] These are particularly attractive, due to the highly diversified metal-organic framework structures that can be produced, their high surface area characteristics, and their specific adsorption affinities. In regard to this latter characteristic, the framework's flexibility and elasticity are important factors in determining the selectivity of adsorption.

5.4: Exfoliation

The ultimate goal of exfoliation methods is the production of two-dimensional nanosheets.[262] Various methods have been reported for the preparation of two-dimensional layered materials. These can be designated as either synthetic or mechanical methods. The most commonly used methods are mechanical in nature, ranging from Novosolov's simple isolation of graphene monolayers by the use of sticky tape on graphite to variations relying on mechanical grinding or ball milling, and ultra-sonication. Others include mechanical cleavage, liquid exfoliation, ion intercalation and exfoliation, anion exchange and exfoliation, chemical vapour deposition, wet chemical synthesis, and selective etching and exfoliation. In general, the separation of individual layers from an existing three-dimensional structure is referred to

as the 'top-down' approach. In contrast, direct synthesis methods are considered 'bottom-up' approaches. However, direct synthesis of two-dimensional nanosheets with acceptable properties of structure and functionality over extended dimensions requires very precise control of all aspects of the synthetic procedure.[263] As this renders the formation of defect-free nanosheets of the corresponding material more complicated, top-down methods of exfoliation are greatly preferred.

While the separation of layers of such materials sounds simple in principle, and has in fact been achieved by a variety of means with many different layered materials, the actual mechanisms of exfoliation are not well known and very little information on this aspect of the exfoliation of layered materials is found in the literature. There is therefore considerable value in examining the process of exfoliation, especially as they will apply to the exfoliation of metal-organic framework materials.

Hillier, Marwa, and Rice[264] studied the exfoliation of the mineral vermiculite in detail. Vermiculite exfoliates and expands when heated quickly to temperatures of about 900°C. Typically, the layers of the structure separate in an accordion-like manner in directions perpendicular to the plane of the layers, causing the material to expand to approximately twenty to thirty times its original thickness. Some vermiculite minerals can also be exfoliated by treatment with hydrogen peroxide, causing scission of interfacial hydroxide layers in the hydroxybiotite minerals. Hillier and coworkers[264] found that the pattern of chemical exfoliation among different vermiculite minerals corresponds to the same pattern of exfoliation in those minerals when subjected to thermal shock treatment. Exfoliation by thermal shock treatment is believed to be due to the rapid expansion of steam generated by the vaporisation of entrained water molecules within the fine structure of the mineral. A secondary and additional effect is thought to be due to thermolysis and dehydration of the hydroxide units in the octahedrally

coordinated sheets of the layered structure. However, Hillier and coworkers[264] cast doubt onto this explanation as they observed that the minerals with the most interfacial water content underwent the least amount of exfoliation and expansion. They also found, as had been known within the vermiculite industry for some time that the extent of exfoliation and expansion of vermiculite minerals is directly related to particle size, whilst the bulk density of the exfoliated material is inversely related to particle size. That is to say that the larger the size of the vermiculite particles, the more they are able to expand when exfoliated. Similarly, the greater the increase in volume due to expansion of the material, the lower its density becomes.

For metal-organic framework materials this appears to work in the opposite way. As catalysts, metal-organic framework materials function by adsorbing materials into the pore spaces of their crystal structure, where they interact with the metal atoms directly. In the three-dimensional structure, this process is limited by the extent to which materials can diffuse into and out of the framework structure. Filled pore spaces prevent the entry of materials into the structure, stopping them from reaching the majority of pore spaces within the material structure. Thus, the larger the particle size in this application, the smaller the amount of material that can be incorporated into its structure. Indeed, incorporation reaches a maximum when the particle size is a two-dimensional sheet of molecular thickness.

Exfoliation of vermiculite upon heating is a physical process, with some features in common with exfoliation of a metal-organic framework compound and other layered materials. However, because H_2O_2 breaks down the fixed hydroxide interfacial layers, exfoliation for vermiculite also occurs chemically on treatment with hydrogen peroxide. In terms of energetics, factors that reduce the energy required to effect exfoliation should greatly favour the process.

In the case of vermiculite, an intercalated layer of hydroxide ions and entrained water molecules, as shown in figure 5-1[265] facilitates the process of chemically-induced exfoliation. In a similar way, for MOFs an appropriate intercalated layer of some kind should also facilitate the process of exfoliation. As will be shown below, this is precisely the case.

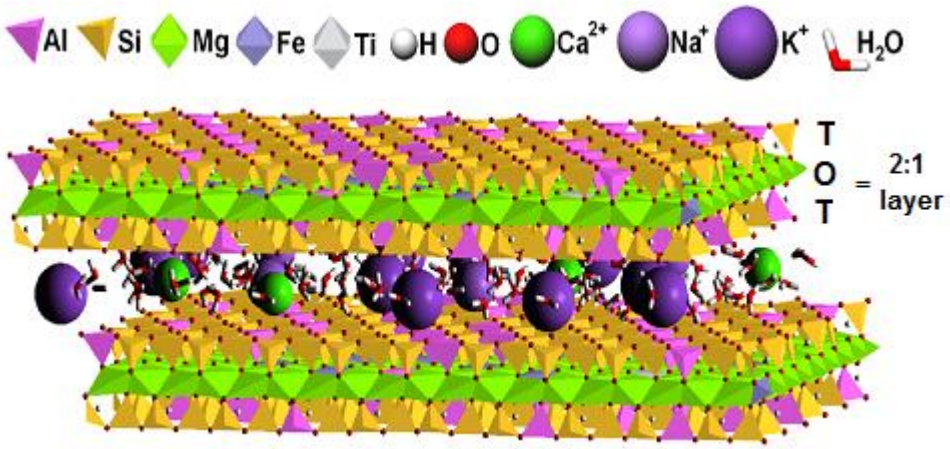

Figure 5-1: Layered Structure of Vermiculite.

Image Source: Clay Minerals in Nature - Their Characterization, Modification and Application, Marta Valaškova and Gražyna Simha Martynkova, eds. (2012), Published by InTech, Croatia, ref 265.

The most trivial method of obtaining two-dimensional nanosheets by exfoliation is simply to exfoliate the desired two-dimensional sheet structures from an existing three-dimensional bulk material consisting of two-dimensional layers that are held together by weak intermolecular forces, as is the case for graphene lifted physically from graphite. A somewhat more elegant method of exfoliation is achieved by intercalation of an appropriate layer between the desired nanosheet layers. The intercalated layer can be formed from an external or environmental agent, or by incorporation of a labile layer within the three-dimensional structure of the bulk material. Li and coworkers[266] utilized the former approach to delaminate δ-MnO_2 'flowers' for the subsequent formation of α-MnO_2 nanotubes. It was found that in the presence of tetra (*n*-butyl) ammonium hydroxide, the manganese dioxide flowers delaminated

into thin platelets that subsequently scrolled into the α-MnO_2 nanotube form. However, in that study no consideration was given to the actual mechanism of exfoliation to form the platelets or to the role of the manganese atoms in that process.

This type of intercalation method is not useful for metal-organic frameworks that have a symmetrical three-dimensional structure, as the ionic intercalation can be performed perpendicular to the plane of the desired constituent layers of the material as well as in the designed plane. Ionic intercalation in two or three orthogonal directions would not lead to the production of single layers. However, the approach works well with metal-organic frameworks that have a built-in intercalating agent, as was demonstrated by Ding and coworkers[263] through the synthesis of a metal-organic framework that incorporated a disulfide linker. The disulfide linkers formed a distinct layer between the metal framework layers, and being labile, chemical scission of the disulfide bonds resulted in the facile formation of individual metal-organic layers or nanosheets. Gallego[267] employed a similar strategy in synthesizing a copper-based metal-organic framework comprised of dipyrimidinedisulfide linker molecules and bridging chlorine atoms. Again, chemical scission of the disulfide bonds resulted in exfoliation of individual layers of copper framework structures. Moreover, it was found that solvent included in the crystal network prevented strong layer-to-layer interactions and that the voids or pore spaces were not selective in solvent capture with this material. Furthermore, exfoliation became more pronounced when the number of water molecules inside of the pore spaces and interstitial cavities was at a maximum.[267]

It has been noted by Coleman *et al*[268] that layered materials must be exfoliated in order to access the potential capabilities that are intrinsic in their molecular structure. Focusing on layered materials composed of transition metal dichalcogenides, they examined the use of ultrasonication in different solvents as one particular method of exfoliation. Hansen solubility

parameter theory indicated that successful solvents for exfoliation are those having a combination of dispersive, polar, and hydrogen-bonding components in the description of their cohesive energy density. Therefore, as suggested above, solvents that would be most successful as exfoliating solvents are those that minimize the energy required for exfoliation.

An interesting variation on the application of solvent properties to the formation of two-dimensional nanosheets was used by He and coworkers[269] for the *in situ* formation and exfoliation of a cobalt-based metal-organic framework material from cobalt acetate tetrahydrate and potassium hydroxide. After preparing the metal-organic framework precursor by refluxing the cobalt acetate tetrahydrate salt in ethanol, the dehydrated acetate was added to an aqueous solution of potassium hydroxide and the resulting cobalt acetate hydroxide metal-organic framework crystals were subjected to ultrasonication *in situ* to effect exfoliation. Thus, it can be seen that the solvent used can not only facilitate the formation of the metal-organic framework structure, but the same solvent can also assist in its exfoliation.

5.5: Results and discussion

In the present study, calculations on alkyl-ether functionalized metal-organic framework systems were carried out based on work published by Foster *et al.*[270] and Henke *et al.*[271] to assess the involvement of ether side chains in the exfoliation mechanism.

Foster and coworkers[270] studied the liquid exfoliation of copper-based metal-organic frameworks in acetone, acetonitrile, ethanol, water, and dimethylformamide. They studied Zn and Cu paddlewheels with 2,5-Bis(3-methoxypropoxy)-1,4-benzenedicarboxylate as a ligand. These compounds are labelled Zn($\overline{\mathbf{1}}$) and Cu($\overline{\mathbf{1}}$), respectively (see figure 5-2).

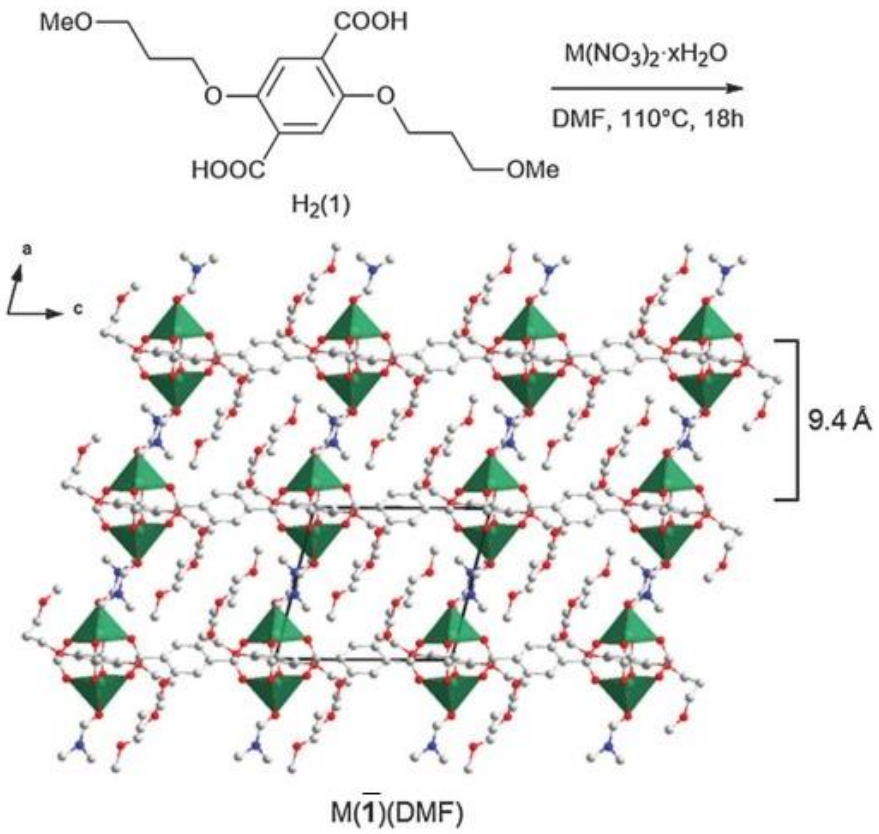

Figure 5-2: Scheme for the synthesis of M(($\overline{\mathbf{1}}$)(DMF) (with M = Cu, Zn) showing the crystal structure of Zn($\overline{\mathbf{1}}$)(DMF). Reproduced with permission from ref 270.

Their experimental study (including IR, XRPD, TGA, and elemental analysis) shows that after exfoliation in DMF, the resultant solid material after drying retains DMF in an axial position. Exfoliation in H_2O with 10% DMF also yields Cu($\overline{\mathbf{1}}$).DMF. However, after exfoliation in acetonitrile, ethanol, and acetone, the solvent is lost during drying of the samples.

Foster and coworkers hypothesized that these long side chains would be positioned between copper paddlewheel layers and would assist in the exfoliation process as well as enhance the dispersion of the exfoliated layers. They hypothesised that the 3-methoxypropoxy chains would coordinate to the axial position of the paddlewheel structures following exfoliation in acetone, acetonitrile, and ethanol. The proposition of Foster *et al*[270] is that "the methoxy oxygen atoms of the flexible 3-methoxypropoxy chains intramolecularly (or

intermolecularly) coordinate to the paddlewheel (PW) in place of more weakly coordinating volatile solvent molecules." Photochemical changes observed in the use of the exfoliated layers as sensors for the detection of pyridine were interpreted as being consistent with the substitution of pyridine for water molecules in the axial positions of the copper paddlewheel structures.

Systems studied by Foster *et al.* were investigated as part of this work. Our calculations were carried out using density functional theory with the B3LYP functional[182] and the 6-311G(d,p)[183,184] basis set for H,C,O, and N and the SDD pseudo potential for Cu as implemented in Gaussian 09.[185] In the current work the copper paddlewheel systems were investigated, which have the formula of $[Cu_2(\mathbf{L})(sol)_2]$. Three different systems using three different ligands were studied: First, a methoxy system, $[(Cu_2(\mathbf{1})(sol)_2]$, where **1** is [2-(3-methoxypropoxy) benzoate]. Second, a methylamino system, $[(Cu_2(\mathbf{2})(sol)_2]$, where **2** is [2-(3-methylaminopropoxy) benzoate]. Third, a methylmercapto system, $[(Cu_2(\mathbf{3})(sol)_2]$, where **3** is [2-(3-methylmercaptopropoxy) benzoate] (see figure 5-3). sol, coordinated axially is one of the solvents: acetone $(Me)_2CO$, acetonitrile (MeCN), dimethylformamide (DMF), ethanol (ETOH), and water (H_2O). In the case of the methoxy system, two different systems were taking into account in order to investigate the structure differences: the full system **1***, which includes two alkyl ether groups in position 2 and 5 [i.e. 2,5-Bis-(3-methoxypropoxy) benzoate], and the pruned system **1,** [2-(3-methoxypropoxy) benzoate], where one of the methoxypropoxy groups was eliminated (see figure 5-4). We undertook DFT modelling to visualize the structure of the MONs and confirm the assignments of the structure. Coordinates from the known crystal structure of Zn(**1***)(DMF) were used to generate starting coordinates for the pruned system (**1**) by replacing Zn atoms with Cu atoms. Structures of **1** and **2**, and **3** were initially modelled using a single PW formed using model monocarboxylate ligands functionalized with only a

single methoxy propyl, methoxy amino, and methoxy mercapto, respectively, to speed up the calculation. Previous studies by J. R. Loader[272] of PW MOFs have shown that using isolated fragments of unit cells produces very comparable results to calculations performed on extended structures. The structure was then modified, replacing DMF with water, acetonitrile, acetone, and ethanol. The fourth iteration removed any solvent from the axial position. In this final iteration, we manipulated the arms, so that the ether functionality could conceivably coordinate in the axial position.

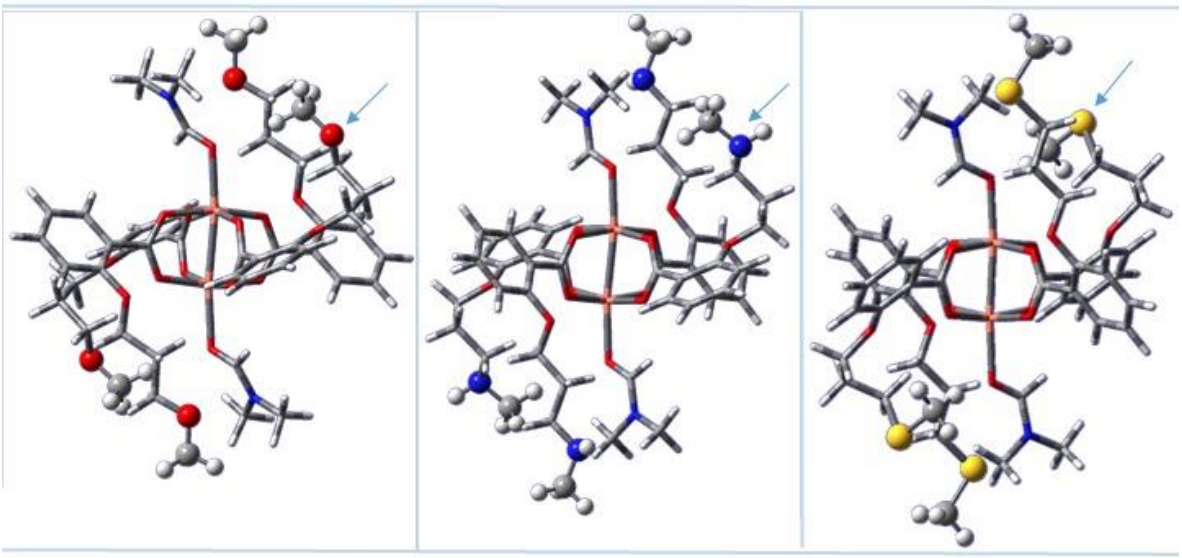

Figure 5-3: DFT calculated structures of the Cu-PW motif using ligand **1**, **2**, and **3**. (From left to right) with DMF coordinated axially.

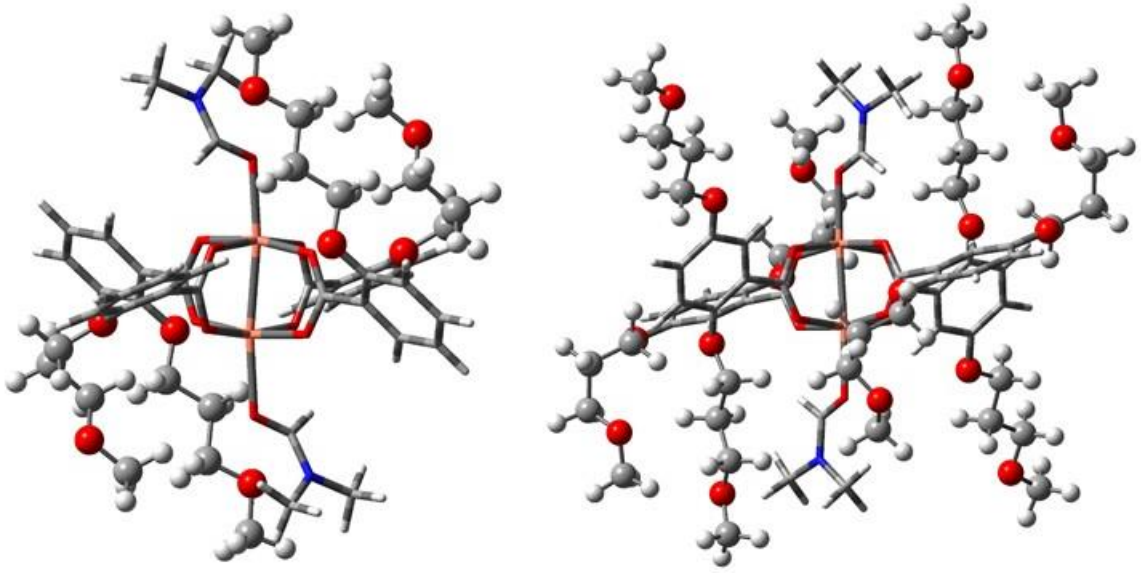

Figure 5-4: DFT calculated structures of the Cu-PW motif show the structure with coordinated DMF using ligand **1**(left), ligand **1***(right). Where **1** is 2(3-methoxypropoxy) benzoate, **1*** is 2,5-bis(3-methoxypropoxy)benzoate.

The input file was generated from the cif file of $Zn(\overline{\mathbf{1}})_4(DMF)_2$ structure, changing Zn to Cu. It is appreciated that for these kinds of flexible systems, there will be many potential conformations of the copper paddlewheel structure. All of these will have a similar energy and may well be sampled at room temperature. However, calculations cannot be done for all conformations. Therefore, only one chemically reasonable conformation has been chosen. It is noted that the ether (methoxy) version, (figures 5-5) is the only one studied experimentally.[270] Thus, to study the amino and mercapto version, rather than start from a crystal structure, the oxygen atoms of the alkyl ether were replaced by sulphur or nitrogen atoms respectively, keeping the correct valences. It is appreciated that the precise starting point for our calculations on these latter compounds has an effect on the geometry. However, these differences are expected to be small.

After geometry optimisation, IR spectra were calculated in the harmonic approximation. To account for an harmonicity and basis set incompleteness, the infrared spectra were modified using two scaling factors because they describe different types of vibration with,

therefore, different amounts of anharmonicity. For values below 2000 cm^{-1} a scaling factor of 0.973 was used,[273] while for values above 2000 cm^{-1} a scaling factor of 0.95 was used. Finally, theoretical and experimental IR spectra were superimposed using the Octave programme.[274] The optimal values were determined by visual inspection. To generate the spectrum from the frequencies, Lorentzian line shapes were used with a half-width half-height of 4 cm^{-1}. The strongest peaks were scaled to have zero transmittance. The consequence of this turns out to be that most peaks have a similar intensity to the experimental peaks apart from the case of water. Thus, here a scaling was chosen that matches up the experimental and theoretical intensities as well as possible.

The Cu paddlewheels used in the experiments were dried. Therefore, there should be no excess solvent present in the spectra. The theoretical infrared spectra were obtained of the copper paddlewheel systems with solvent molecules, and with solvent replaced by coordination of the methoxy, methylamino and methylmercapto sidechains. All spectra for ligand **1** and **1*** were compared with the experimental spectra for $Cu(\overline{\mathbf{1}})_4(DMF)_2$ exfoliated in the corresponding solvents where the $\overline{\mathbf{1}}$ is the 2,5-bis(3-methoxypropoxy) teraphtalate ligand. As noted by J. R. Loader[272] in cases like these the IR spectrum of the single paddlewheel is qualitatively similar to the IR spectrum for the full system, particularly where the position of the peaks is concerned. This is particularly useful in this case, since in contrast to Ref 272, we do not have access to the single-crystal structure for the material, which makes complete calculations impossible.

5.5.1: Copper Methoxypropoxy benzoate systems [$(Cu_2(1)(sol)_2]$, and [$(Cu_2(1^*)(sol)_2]$

As noted above, an analysis of the target system was carried out using a model system in which one of the arms on the benzoate ligands was eliminated from the calculations (the

pruned system). The goal of this was to obtain a quick indication of the viability of the coordination of a terminal methoxy group to the copper centre in the axial position. Additionally, the viability of a particular solvent molecule undergoing coordination in the same position was investigated.

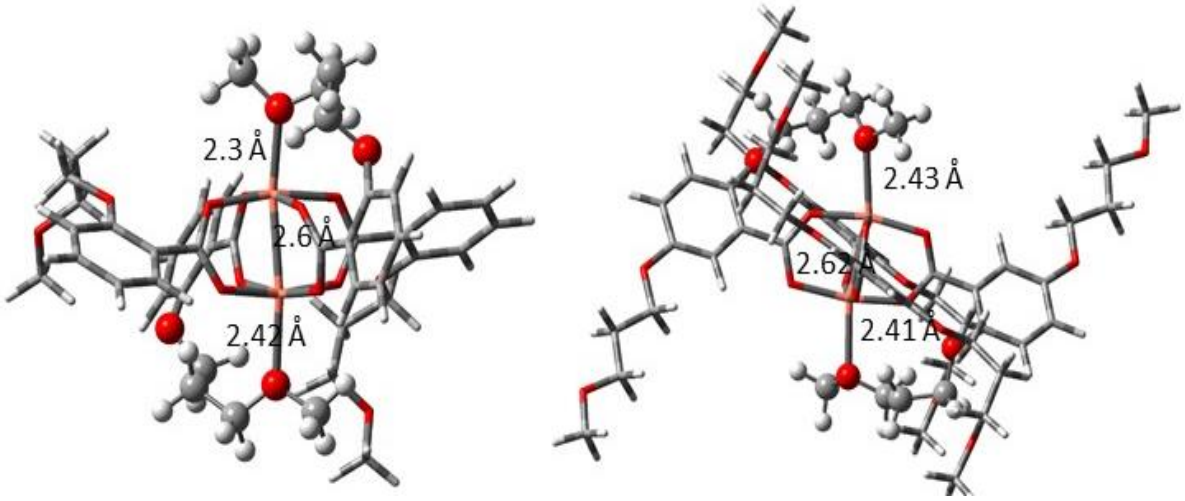

Figure 5-5: DFT calculated structures of the Cu-PW motif show the structure with no solvent coordinated using ligand **1**(left), ligand **1***(right).

First, a "No solvent coordinated" system is considered, whereby there is no residual solvent coordinated to Cu. Instead, methoxy group of the chains are coordinated as can be seen in figure 5-5 (left). The terminal methoxy groups are coordinated to the copper centres of the paddlewheel structure in the axial position. Similarly, figure 5-5 (right) presents an optimized structure of the full copper PW, where the additional methoxypropoxy groups are pointing away from the centre of the paddlewheel. Obviously, they would be available to bond at the next Cu-Cu unit in a 2-D structure.

Comparing figures 5-5 (left and right) in detail shows that the Cu-Cu distance in both cases is very similar. This is not surprising, since this distance will be largely determined by the distances between the oxygens of the carboxylate group. Similarly, the distance between

Cu and the coordinated oxygen does not change significantly from the pruned to the full PW system. This suggests that the pruned system is a viable alternative for studying this system.

Figures 5-6 to 5-10 show the optimized coordination sphere of the paddlewheel copper atoms for the pruned and full systems where the axial position is one of the solvent molecules: acetone, acetonitrile, dimethylformamide, ethanol and water, respectively. In all cases, the Cu-Cu distance is very similar to that in figure 5-5. Again, this is to be expected, since this distance will be governed to a large extent by the distance between the two oxygen atoms of the carboxylic acid group of the benzoate. The distance between Cu and the solvent molecules varies across the set. There does not appear to be a dependency on the sp^2 or sp^3 characters of the solvent molecule. However, MeCN has a shorter distance than any of the other molecules. In terms of orientation, the solvent molecules orient themselves along what is normally presumed to be the direction of the lone pair. However, surprisingly MeCN shows 2 different binding modes, an η^1 and η^2 motif.

As noted before, the differences between the pruned and the full systems is small. However, interestingly, the largest change happens again for the MeCN system for both distance and orientation. Thus, the potential energy surface in which MeCN operates appears to be flat in both the angular and radial direction, suggesting a relatively weak bond.

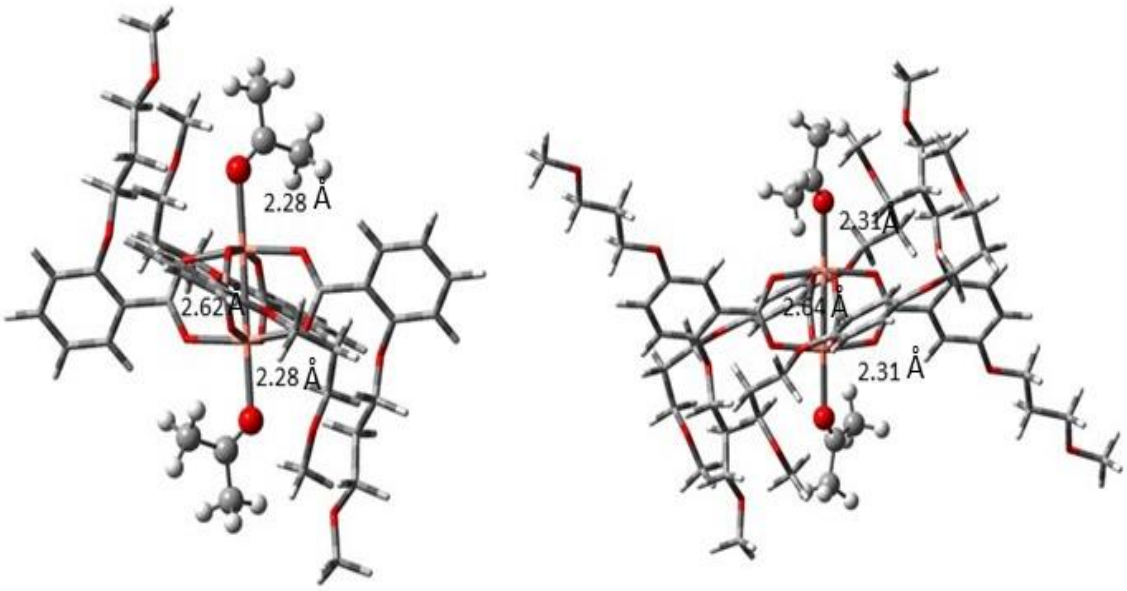

Figure 5-6: DFT calculated structures of the Cu-PW motif show the structure with coordinated acetone using ligand **1**(left), **1***(right).

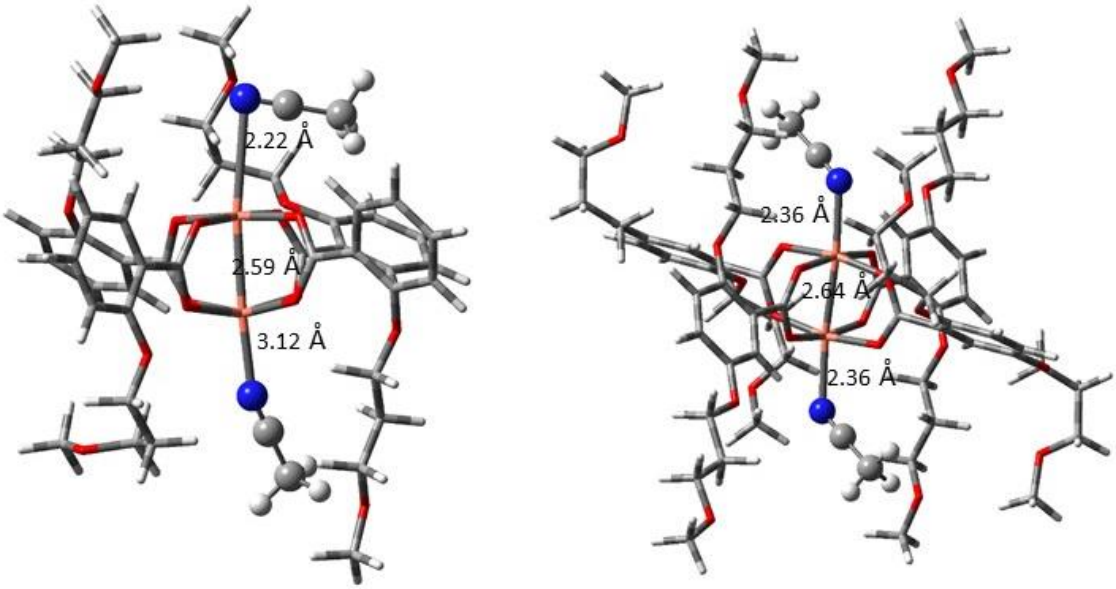

Figure 5-7: DFT calculated structures of the Cu-PW motif show the structure with coordinated acetonitrile using ligand **1**(left), **1***(right).

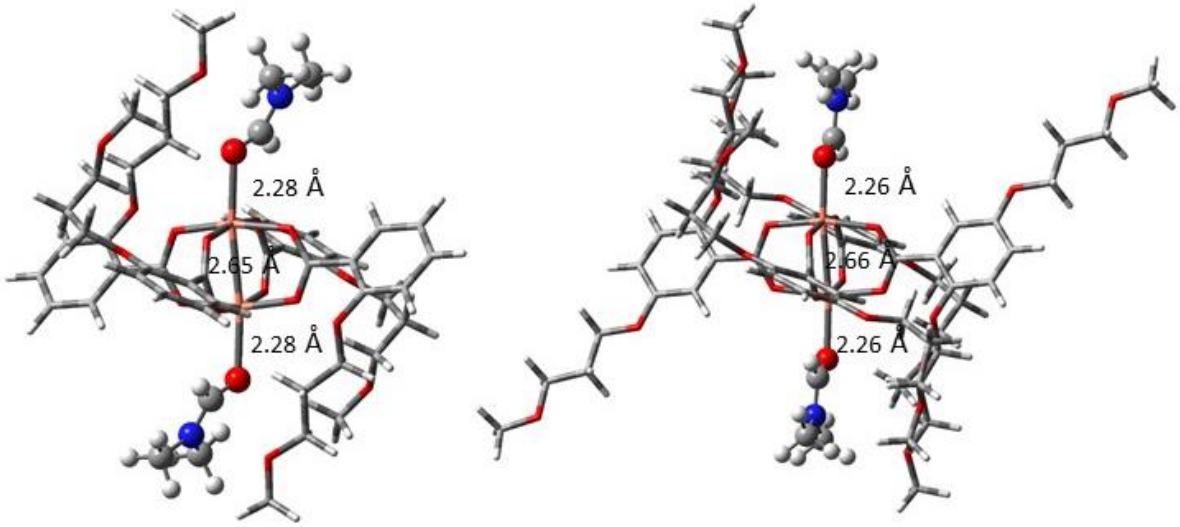

Figure 5-8: DFT calculated structures of the Cu-PW motif show the structure with coordinated DMF using ligand **1**(left), **1***(right).

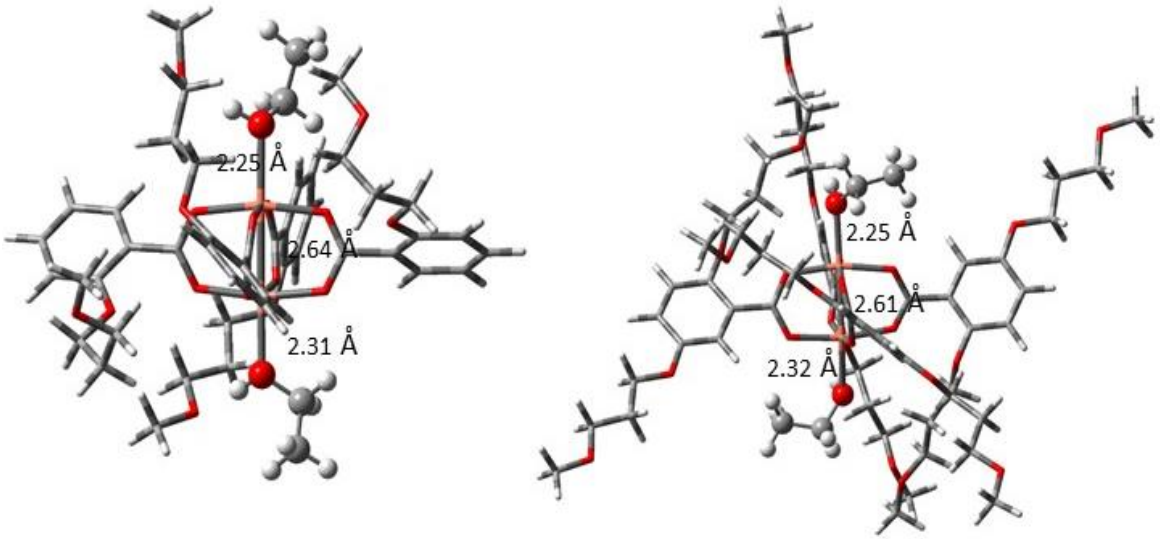

Figure 5-9: DFT calculated structures of the Cu-PW motif show the structure with coordinated ethanol using ligand **1**(left), **1***(right).

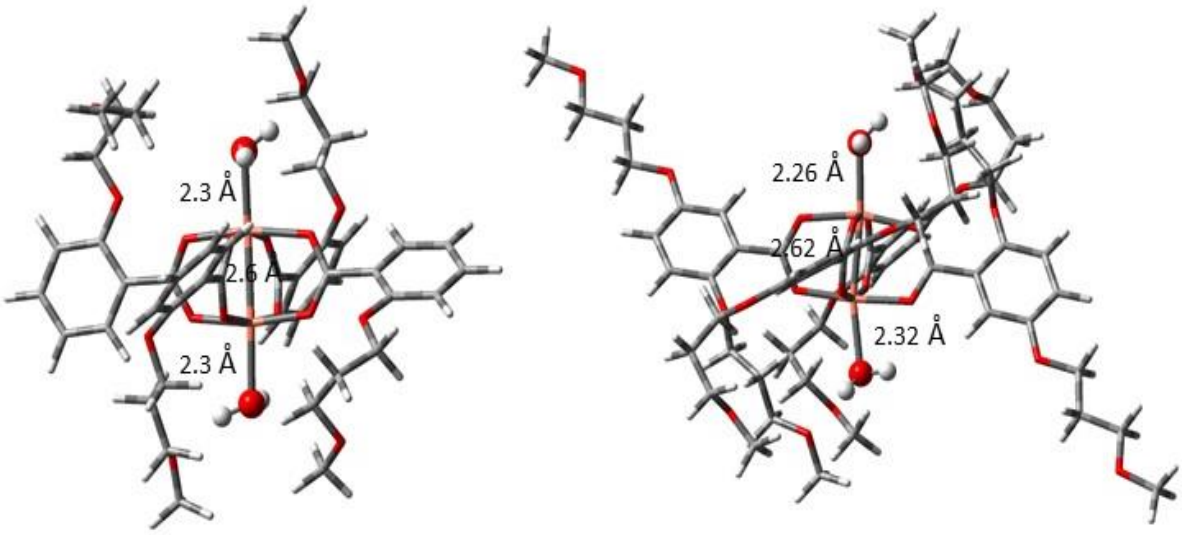

Figure 5-10: DFT calculated structures of the Cu-PW motif show the structure with coordinated water solvent using ligand **1**(left), **1***(right).

While the terminal methoxy groups are undoubtedly sufficiently flexible to attain coordination in the axial position, the electron-donating ability of the ether linkage in comparison with the polarities of the oxygen and nitrogen atoms of any of the five solvents will be crucial in its competition with any of those molecules for the axial positions of the copper centres or the displacement of any of those molecules from the axial position of the copper centres during exfoliation. Of course, there could be an equilibrium during exfoliation, in which a fraction of the axial positions is occupied by terminal methoxy groups and a fraction of the axial positions by the corresponding solvent molecules. The question, then, in such a case must be which of the two equilibrium situations leads to exfoliation, or do they both according to their relative role in the equilibrium? The question can then be asked as to whether the exfoliation mechanism is a multistep process in which coordination of the terminal methoxy groups is the rate-determining step, followed by coordination of the solvent or whether the inverse is true.

Examination of the optimized orientations of the terminal methoxy groups relative to the axial solvent molecules may provide a clue in this regard. In both the pruned system and the full system, the terminal methoxy groups are seen to extend well beyond the range of the axial solvent molecules, i.e. the terminal methoxy group is further away from the Cu atom than the the terminal carbon or oxygen atom of the solvent molecule, except in the cases of dimethylformamide and ethanol, where their respective extensions outward from the copper centres appears to be about equal. The steric bulk of the particular solvent molecule appears to be an important factor in this regard, as it appears that the smaller the solvent molecule, the closer it is able to coordinate to the copper atoms in the axial position. Dimethylformamide, having the largest steric bulk of the five solvent molecules is the least able to coordinate in close proximity to the copper atoms as it competes for pore space with the linker substituent groups. Water, being the smallest and most polar of the five solvent molecules, is coordinated the most closely to the copper atoms in the axial position. Hereby, it is also noticeable that in e.g. the case of hydrogen-bond donors, such as water, that hydrogen-bonding of the ether unit of the terminal methoxy groups clearly plays a role as well.

5.5.1.1: Calculation of the relative binding energies of solvent molecules for $[Cu_2(\mathbf{1})_4(sol)_2]$ and $[Cu_2(\mathbf{1^*})_4(sol)_2]$

The energy needed in order to release the solvents is given by the expression:

$$\Delta E_{RB} = E_{(\text{methoxy- coordinated complex})} + E_{(\text{solvent})} - E_{(\text{solvent-coordinated complex})}$$

Table 5-1: Energies for binding two solvent molecules to Cu(**1**)$_4$ and Cu(**1***)$_4$. **1** and **1*** relative to the binding energy of the methoxy-propoxy arms of **1** and **1*** respectively, ΔE_{RB}, in kJ/mol. sol is one of the solvent molecules: DMF, H_2O, $(CH_3)_2CO$, CH_3CN, and CH_2OH.

Copper PWs-Solvents	**ΔE_{RB} (kJ/mol)** **[$Cu_2(1)_4(sol)_2$]**	**ΔE_{RB} (kJ/mol)** **[$Cu_2(1^*)_4(sol)_2$]**
water	111.6	119.2
DMF	55.3	87.0
Ethanol	84.6	65.8
Acetone	40.4	71.5
Acetonitrile	26.4	57.7

As shown in table 5-1, the relative binding energy, ΔE_{RB}, for 2 water molecules doesn't change much between Cu(**1**)$_4$(sol)$_2$ and Cu(**1***)$_4$(sol)$_2$. The reason for that is clear from figure 5-10. The structure of the paddlewheel is the same in both the pruned and the full system. However, for DMF, and acetone, ΔE_{RB} increases. For ethanol, it decreases and ΔE_{RB} for acetonitrile doubles on changing from the pruned to the full system. In the DMF system, there is clearly extra hydrogen bonding taking place in full system while the structure is more open in the pruned system. As a consequence, ΔE_{RB} for DMF decreases from 87 kJ/mol to 55 kJ/mol. This difference might arise, because of the starting point chosen. Thus, more calculations would be required to resolve this.

Looking at the pruned acetonitrile system, one solvent molecule has a different (orthogonal) orientation. The distance for this MeCN molecule, which is oriented perpendicular to the Cu-Cu axis, is much shorter (2.2 Å) than that for the full system. For the full system, the Cu-N distance is 2.36 Å and both axial solvent molecules are in a perpendicular orientation to

the plane of the PW (more parallel to the Cu-Cu axis). As a consequence, ΔE_{RB} approximately doubles from 26 to 57 kJ/mol from the pruned to the full system because of the better overlap with the lone pair on nitrogen in MeCN. One would expect that the full system is more accurate in this case, but it is clear that the starting point of the system matters in this case.

*5.5.1.2: Infra-red spectra for [(Cu_2(**1**)(sol)$_2$], [(Cu_2(**1***)(sol)$_2$]*

The infrared spectra for the different cases of the pruned and full systems for [(Cu_2(**1**)(sol)$_2$] and [(Cu_2(**1***)(sol)$_2$] are found in figures 5-11 to 5-15. The theoretical spectra for each case, calculated for the structure, where only the methoxy-propoxy arms are coordinated and for the structure with solvent molecules coordinated in the axial position are superimposed with the experimentally observed infrared spectrum of the system, which were measured using the $\overline{\mathbf{1}}$ ligand. The extent to which the theoretical and experimental spectra correlate should indicate the extent to which the terminal methoxy groups occupy the axial positions at the copper centres of the paddlewheel structures.

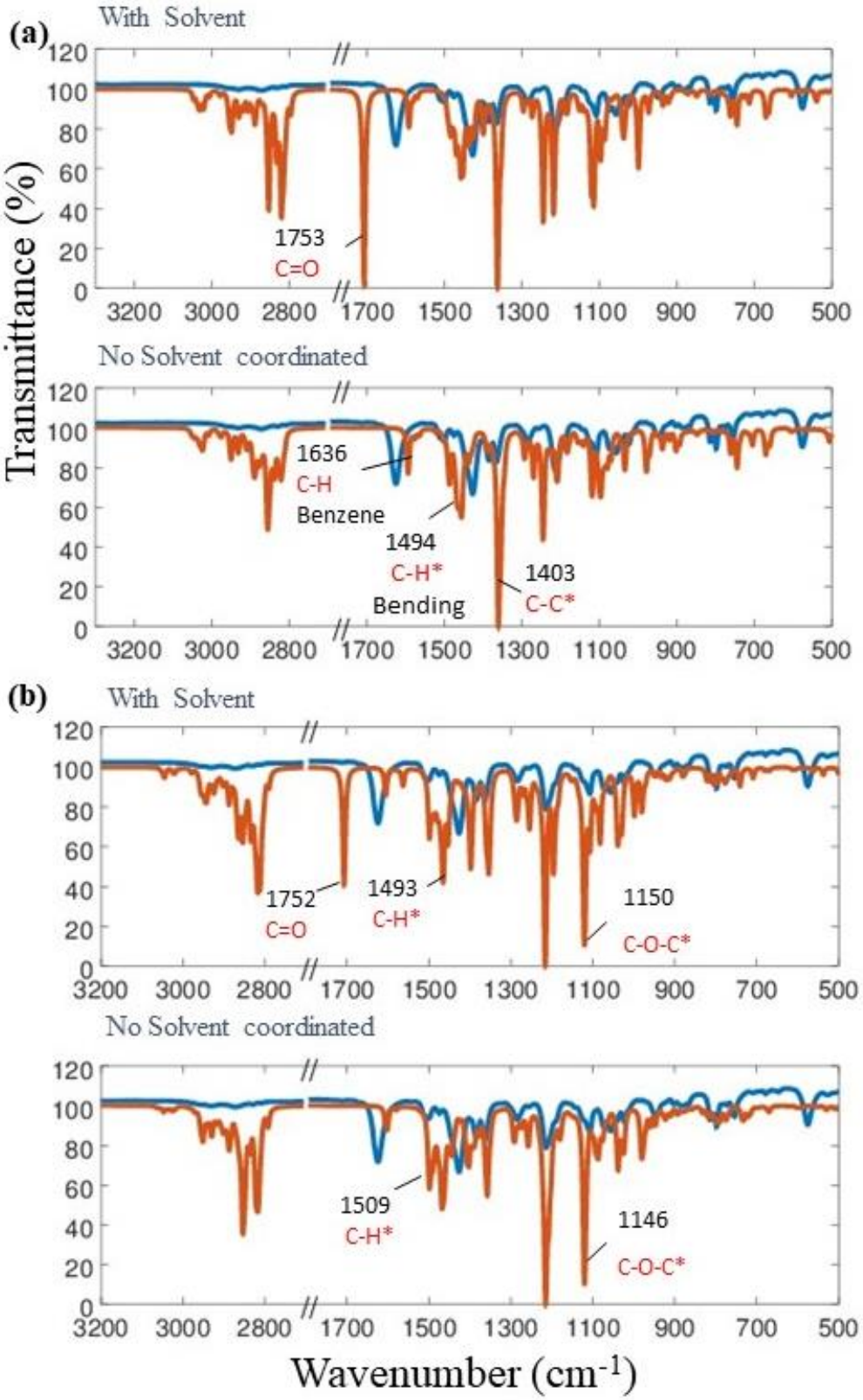

Figure 5-11: Comparison of calculated (orange) and experimental (blue) IR patterns for a) $[Cu_2(\mathbf{1})_4((Me)_2CO)_2]$, b) $[Cu(\mathbf{1^*})_4((Me)_2CO)_2]$, where **1** is 2-(3-methoxypropoxy)benzoate, **1*** is 2,5-bis(3-methoxypropoxy) benzoate, C-C* is a wagging mode of the C carboxylate group combined with the C aromatic system; C-H* is the symmetric scissor mode of the C-H alkyl ether CH_2CH_2 –O-R; C-O-C* is the wagging mode of the C-O-C alkyl ether CH_2CH_2-O-CH_3.

Figure 5.11(a) and (b) show the correlation between the calculated and experimental spectra for exfoliation in acetone for the pruned and full systems, respectively. In all four cases, a number of sharp peaks are displayed in the calculated spectrum that do not appear in the experimental spectrum. This must be due to the fact that in the experimental spectra one is sampling over a number of different conformers of the paddle-wheel. In particular, the pendant groups will be able to attain a number of different conformations, which will all have a slightly different vibrational energy, resulting in smearing of the experimental spectrum. Moreover, the presence of additional (non-coordinating) pendant groups in the full system will lead to additional smearing. However, it is clear that for both 5-11(a) and 5-11(b) the agreement between the calculated and experimental spectra for the spectra with coordinated solvent molecules is not strong as it shows a carbonyl peak of coordinated acetone at 1732 cm^{-1}. This is clearly missing in the experimental spectrum. On the other hand, the structure with coordinated methoxy groups (i.e. the one labelled no solvent coordinated) gives a spectrum, which correlates best to the experimental spectrum. It is noted that compared to the pruned system, it is clear that the overall agreement is better for the full system.

For exfoliation in acetonitrile, the situation is somewhat more complicated. For the pruned system shown in figure 5-12(a), visual inspection shows qualitative agreement between the calculated and experimental spectra for the case “with solvent”. In the case with no solvent coordinated, the correlation is good as well, as essentially all of the major peaks in the calculated and experimental spectra appear to coincide when the scaling is taken into account. For the case “with solvent”, a weak band around 2381cm^{-1} is assigned for −C≡N of acetonitrile solvent, which is missing when no solvent is coordinated. The experimental spectrum does show some broad features, probably because a number of conformations are not included in

theoretical calculations. However, the agreement for both spectra is similar, which means that one cannot categorically state whether the solvent or the methoxy groups are coordinated.

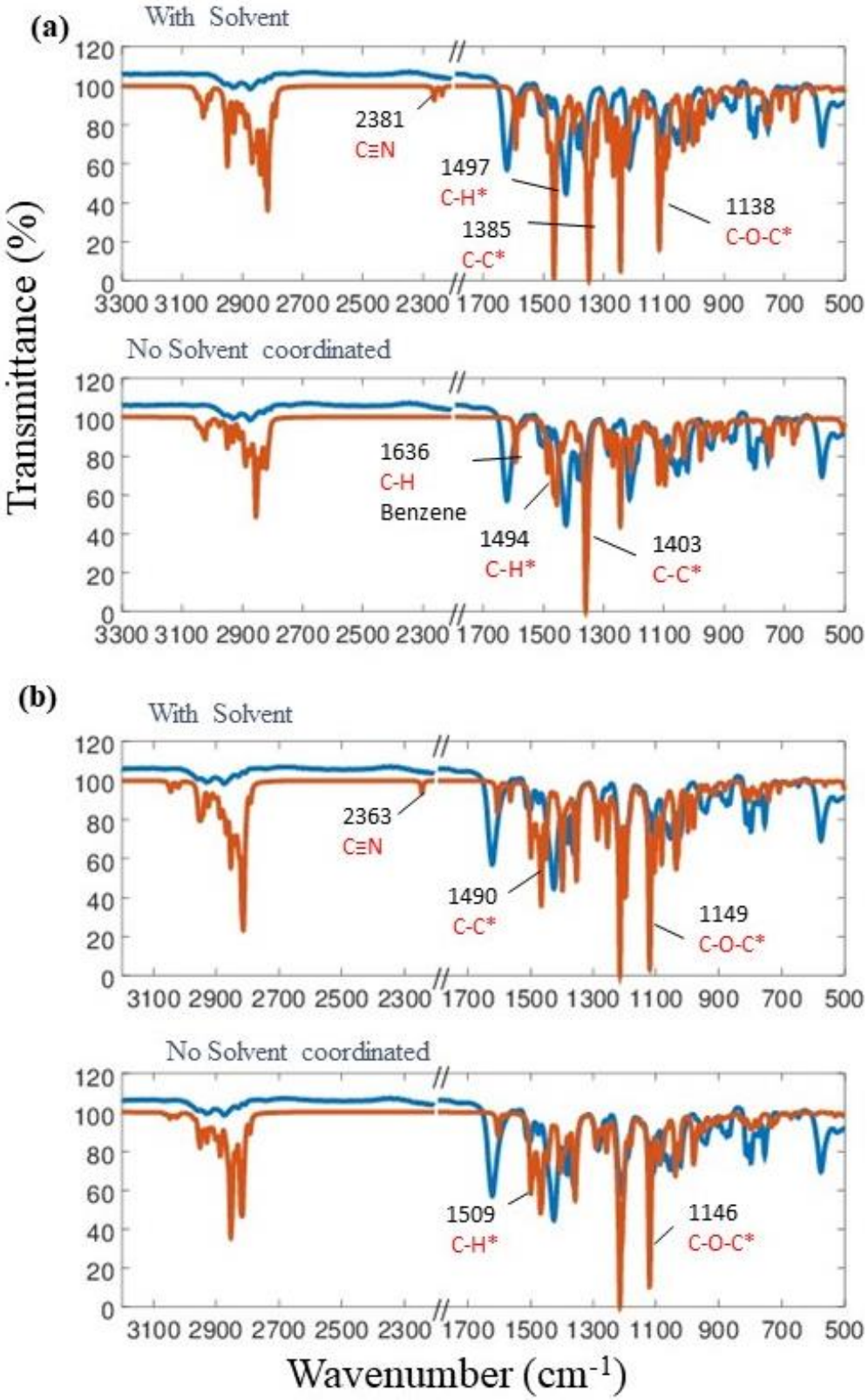

Figure 5-12: Comparison of calculated (orange) and experimental (blue) IR patterns for a) $[Cu_2(\mathbf{1})_4(MeCN)_2]$, b) $[Cu(\mathbf{1^*})_4(MeCN)_2]$ where **1** is 2-(3-methoxypropoxy)benzoate, **1*** is 2,5-bis(3-methoxypropoxy)benzoate, C-C* is a wagging mode of the C carboxylate group combined with the C aromatic system; C-H* is the symmetric scissor mode of the C-H alkyl ether CH_2CH_2 –O-R; C-O-C* is the wagging mode of the C-O-C alkyl ether CH_2CH_2-O-CH_3.

For the full system, figure 5-12(b), the correlation for the "with solvent" case is remarkably consistent between the calculated and experimental spectrum compared to the same case for the pruned system in spectra 5-12(a). A scaling factor close to one applied to the calculated spectrum appears to bring all major peaks into alignment with each other. The agreement for the lower panel of figure 5-12(b) is not dissimilar to that of the top panel. Perhaps, the agreement for the highest energy peak of the fingerprint region is slightly better for the top panel, suggesting that in this case solvent may well still be coordinated. However, experimentally there is a strong evidence that the solvent is removed in this system, whereby in particular the absence of a clear CN peak in the IR spectrum is commented upon.[270]

Figure 5-13(a) and (b) show the correlation between the calculated and experimental spectra for exfoliation in DMF for the pruned and full systems, respectively. The spectra in figure 5-13(a) show a decent correlation between theory and experiment, whereby it should be noted that the agreement for the intensity of the peaks is not as good as in the cases presented above. However, the agreement for the top panel is better than agreement for the bottom panel. In particular, in the top panel, the single sharp peak near 1706 cm^{-1} in the theoretical spectrum belongs to the carbonyl group of the coordinated DMF molecule. The presence of a similar feature in the experimental spectrum suggests that indeed DMF is coordinated axially to the copper paddle wheels in the experiment.

The spectra for the full DMF system, figure 5-13(b), exhibit an excellent correlation between the calculated and experimental spectra, particularly for the case "with solvent" a scaling factor close to one brings all major peaks into good alignment with each other. Again, it is clear that the sharp peak in theoretical spectra at 1706 cm^{-1} is due to the C=O carbonyl of DMF solvent, which is also present in the experimental spectrum, showing that in this case solvent is still coordinated.

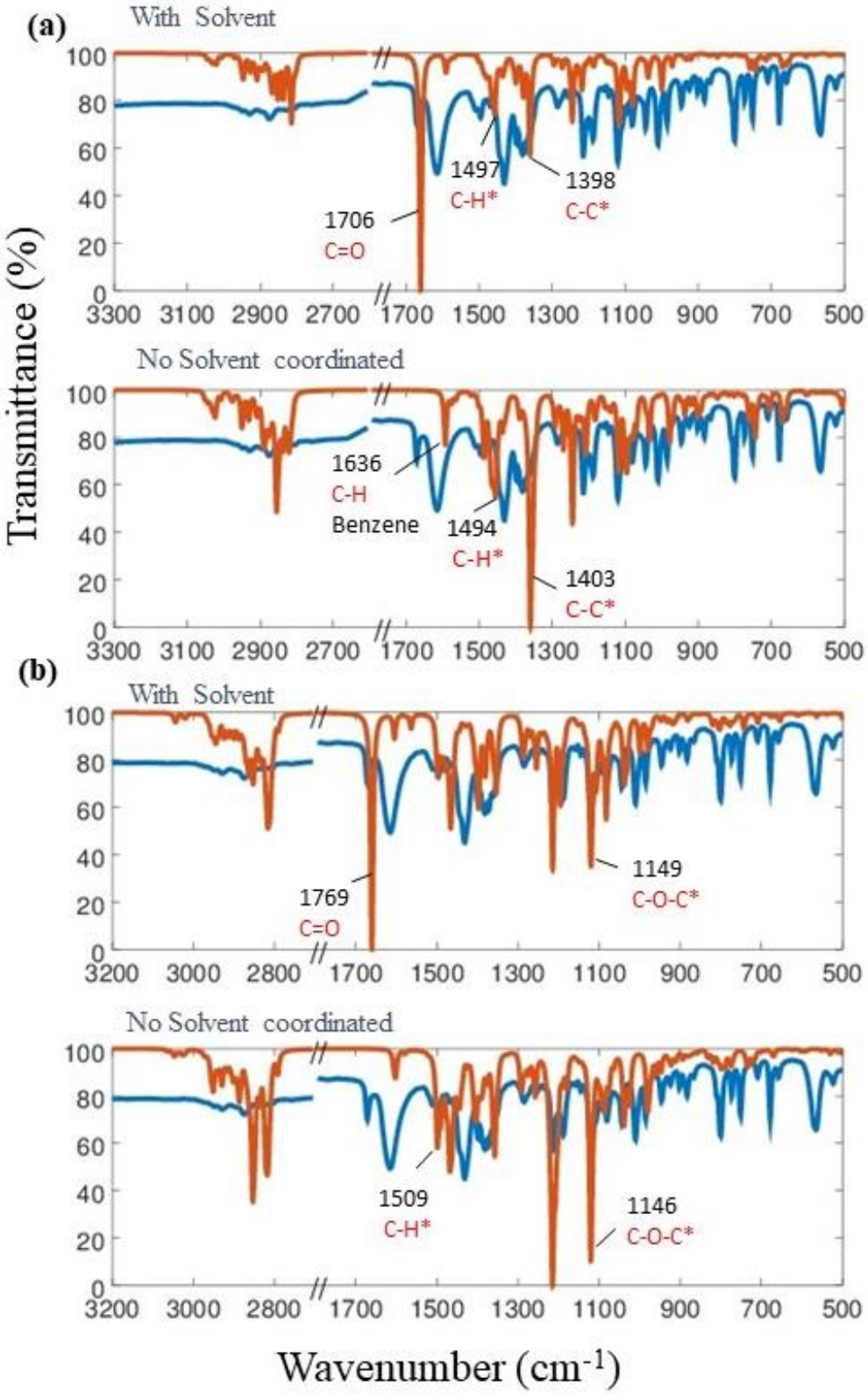

Figure 5-13: Comparison of calculated (orange) and experimental (blue) IR patterns for a) $[Cu_2(\mathbf{1})_4(DMF)_2]$, b) $[Cu(\mathbf{1^*})_4(DMF)_2]$ where **1** is 2-(3-methoxypropoxy)benzoate, **1*** is 2,5-bis(3-methoxypropoxy)benzoate, C-C* is a wagging mode of the C carboxylate group combined with the C aromatic system; C-H* is the symmetric scissor mode of the C-H alkyl ether CH_2CH_2 –O-R; C-O-C* is the wagging mode of the C-O-C alkyl ether CH_2CH_2-O-CH_3.

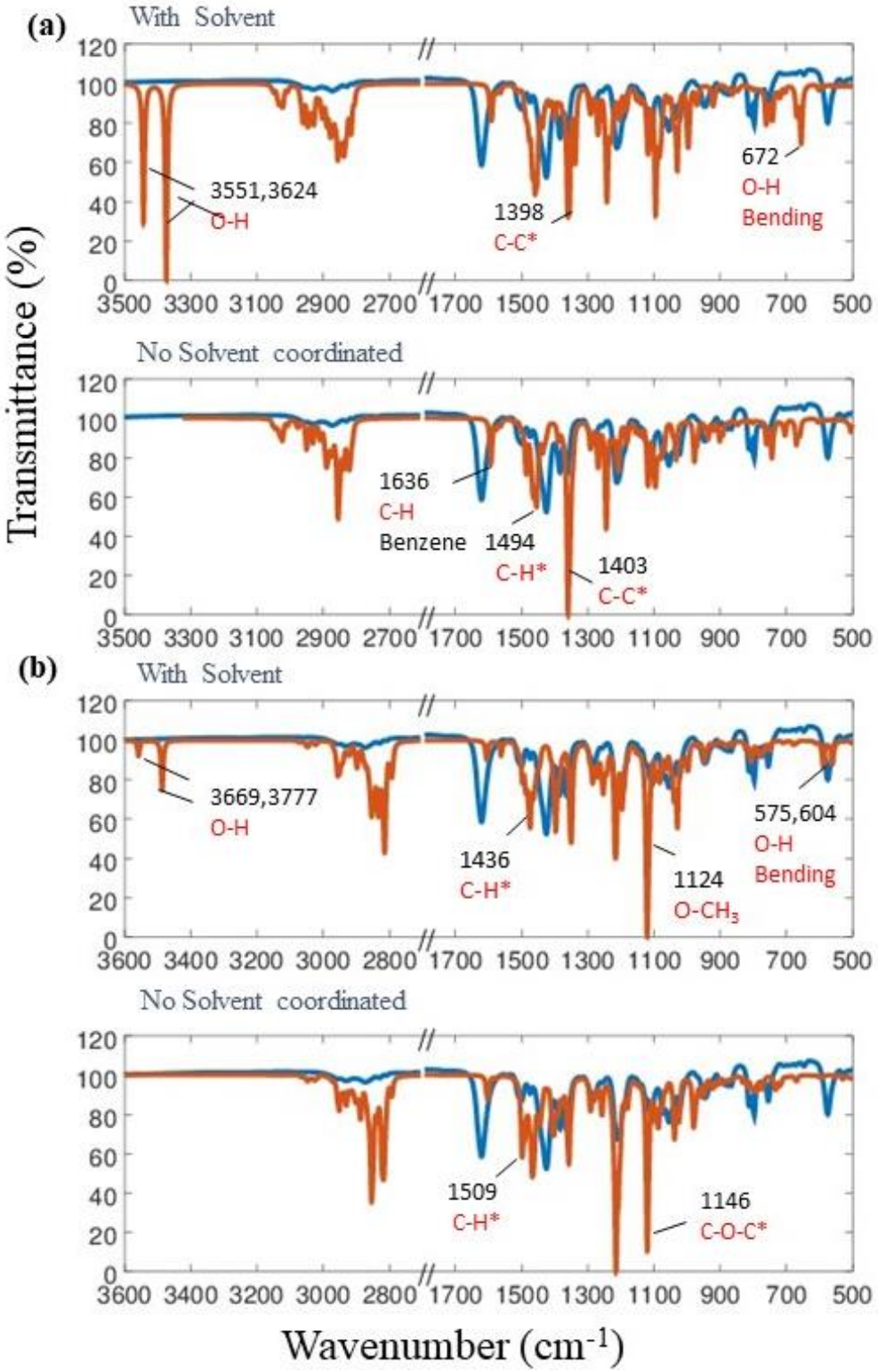

Figure 5-14: Comparison of calculated (orange) and experimental (blue) IR patterns for a) $[Cu_2(\mathbf{1})_4(EtOH)_2]$, b) $[Cu(\mathbf{1^*})_4(EtOH)_2]$ where **1** is 2-(3-methoxypropoxy)benzoate, **1*** is 2,5-bis(3-methoxypropoxy)benzoate, C-C* is a wagging mode of the C carboxylate group combined with the C aromatic system; C-H* is the symmetric scissor mode of the C-H alkyl ether CH_2CH_2 –O-R; C-O-C* is the wagging mode of the C-O-C alkyl ether CH_2CH_2-O-CH_3.

Exfoliation of ethanol is considered in figure 5-14(a) and (b) for the pruned and full systems, respectively. For the pruned system shown in figure 5-14(a), there appears to be excellent correlation between the calculated and experimental spectra for the "with solvent" case as major peaks align easily with a scaling factor close to 1. The bottom panel with the case of "no solvent coordinated" exhibits a similar good correlation between the calculated and experimental spectra for the fingerprint region. Thus, on its own, the fingerprint region of the spectrum is not able to give a definite verdict on the final structure of the copper paddlewheel. However, looking at the region above 3000 cm^{-1}, it is clear that the theoretical spectrum shows a clear −OH stretch around 3551 cm^{-1}. These peaks are clearly missing in the experimental spectrum, which indicates that in this case the axial positions are likely taken up by the methoxy groups rather than solvent molecules.

The spectra for the full system in figure 5-14(b), show a similar correlation between the calculated and experimental spectra for both cases. Although the correlation in both cases is not perfect, it is very consistent. The OH stretching peak of ethanol solvent at 3669 cm^{-1} is still an indication for the absence of solvent in the experimental spectra. However, it is noticeable that in this case these peaks are significantly less dominant than in the pruned case, probably due to the change in the structure going from the "pruned" to the "full" system. However, one would still need to conclude that in this case there are no ethanol molecules in the axial position as indeed was found experimentally.

Exfoliation in water is considered in figure 5-15(a) and (b) for the pruned and full system, respectively. The fingerprint region of the spectra in figure 5-15(a) for the pruned system again does not allow for a clear verdict on which of the two possible structures is the correct one. However, in the experimental spectrum, there is a weak water peak around 3700 cm^{-1}. This suggests that in this case as well there is water solvent bound to the axial positions.

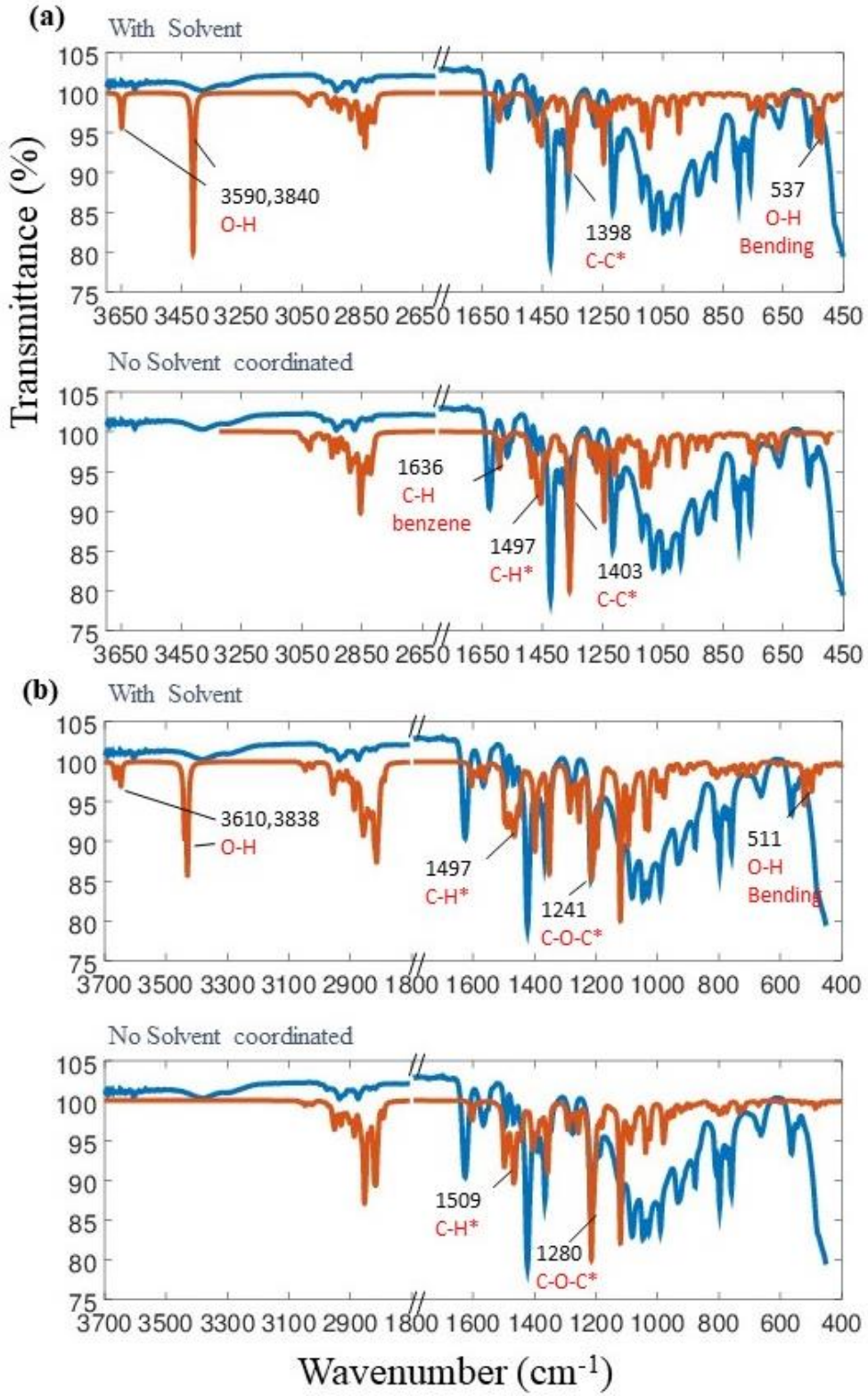

Figure 5-15: Comparison of calculated (orange) and experimental (blue) IR patterns for a) $[Cu_2(\mathbf{1})_4(H_2O)_2]$, b) $[Cu(\mathbf{1^*})_4(H_2O)_2]$ where **1** is 2-(3-methoxypropoxy)benzoate, **1*** is 2,5-bis(3-methoxypropoxy)benzoate, C-C* is a wagging mode of the C carboxylate group combined with the C aromatic system; C-H* is the symmetric scissor mode of the C-H alkyl ether CH_2CH_2-O-R; C-O-C* is the symmetric mode of the aromatic C and ether group O-$(CH_2)_3$O-CH_3.

For the spectra of the full system in figure 5.18(b), the correlation for the fingerprint region is similar to that for figure 5.15(a). The water peak at 3610 cm^{-1} is also observed in experiment around 3600 cm^{-1}, again suggesting that water solvent is present.

In comparing the calculated and experimental spectra for the different cases and the different solvents, it is notable that peak identifications in those spectra are difficult to make on a one-to-one basis. A collection of two or three sharp peaks in the calculated spectrum typically appear as a single broad peak of lower intensity in the experimental spectrum (the absolute intensities are arbitrary or rather depend on how much sample was in contact with diamond), and therefore the most useful feature is to identify the absence or presence of coordinated solvent peaks.

5.5.2: Copper methylaminopropoxy benzoate systems[$(Cu_2(2)(sol)_2$]

A series of calculations was performed on pruned systems in which the terminal methoxy groups [2-(3-methoxy propoxy) benzoate], ligand **1**, have been replaced by terminal methylamino groups, [2(3-methylaminopropoxy) benzoate], ligand **2**. The optimized structures for these are shown in figures 5-16 to 5-21.

Figure 5-16 shows the optimized structure of the pruned system with methylamino groups occupying the axial coordination positions about the copper centres of the paddlewheel structure. As can be seen, the amine nitrogen atom is tilted significantly towards the copper-copper axis of the paddlewheel. Nitrogen is expected to coordinate more strongly to copper than oxygen. Indeed, comparison with figure 5-5 shows a shorter distance between N and Cu than Cu-O in the methoxy case.

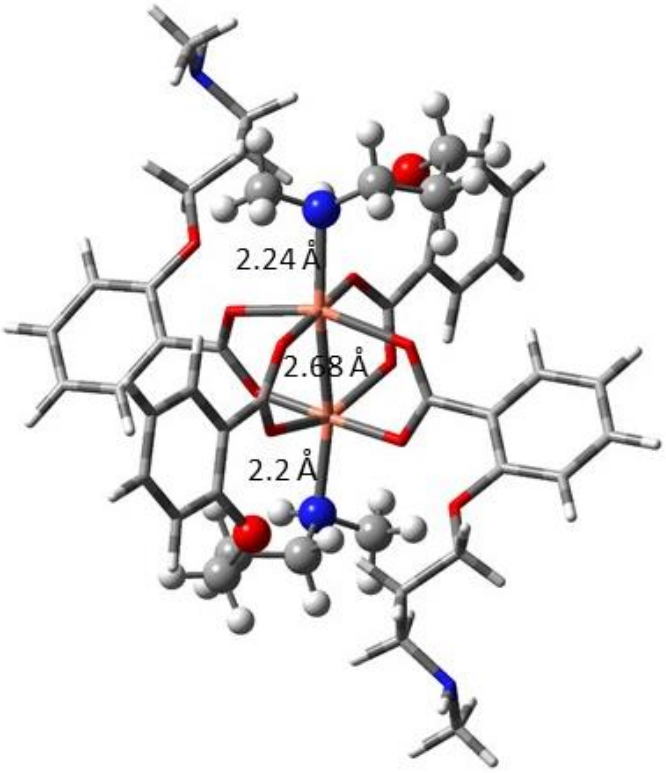

Figure 5-16: Optimized structure with no solvent coordinated using ligand **2**.

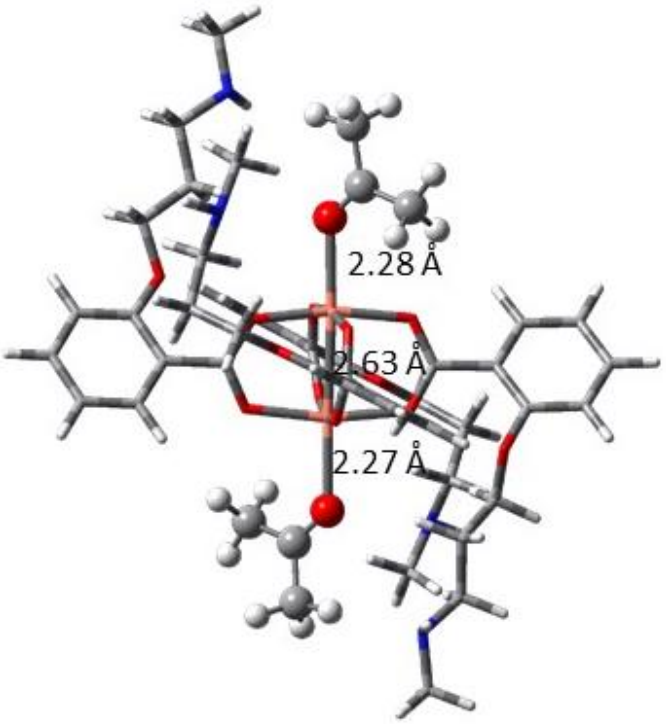

Figure 5-17: Optimized structure for ligand **2** with coordinated acetone.

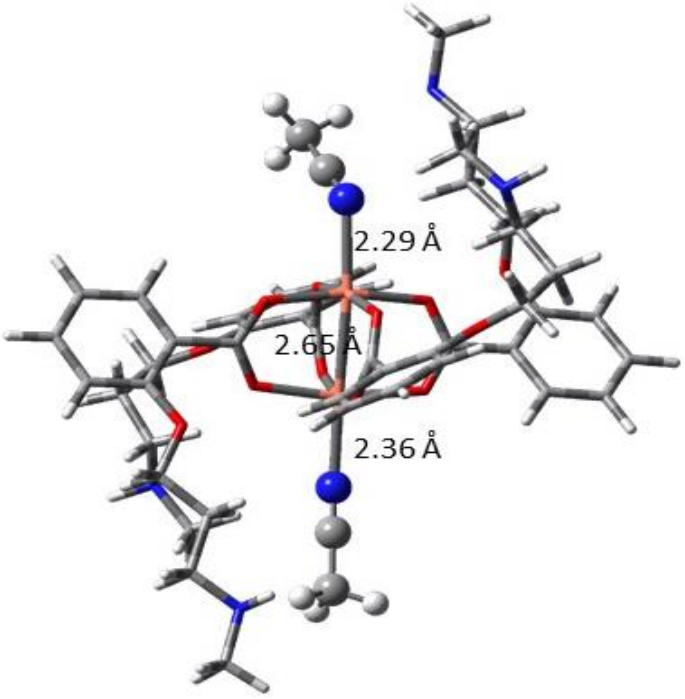

Figure 5-18: Optimized structure for ligand **2** with coordinated acetonitrile.

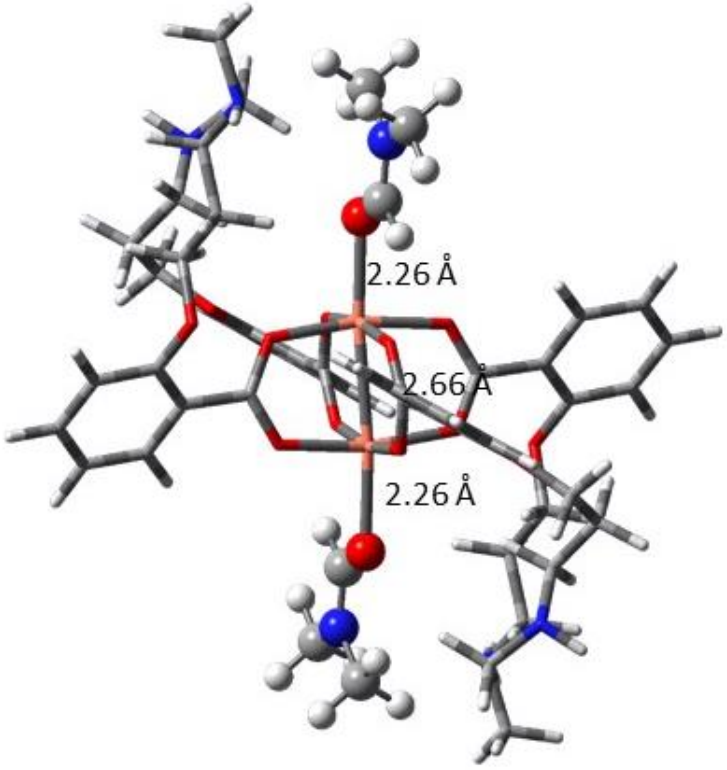

Figure 5-19: Optimized structure for ligand **2** with coordinated dimethylformamide.

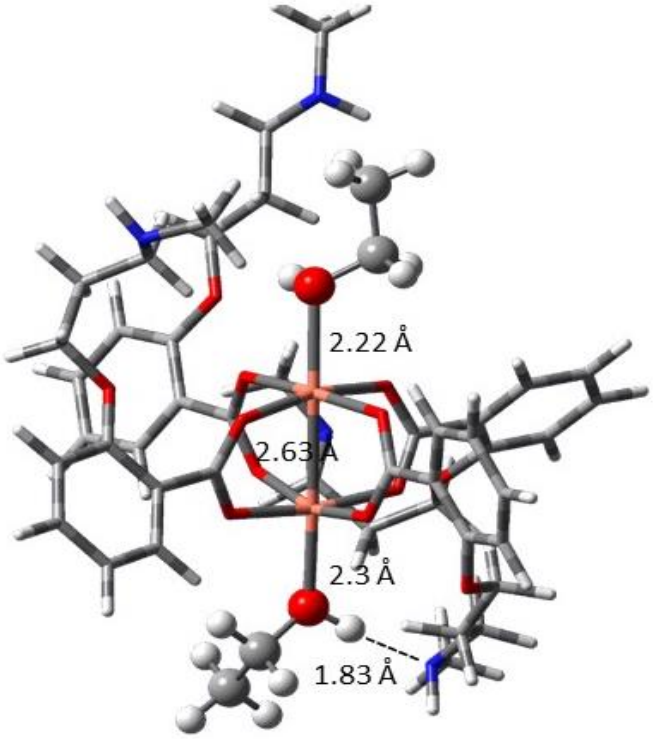

Figure 5-20: Optimized structure for ligand **2** with coordinated ethanol.

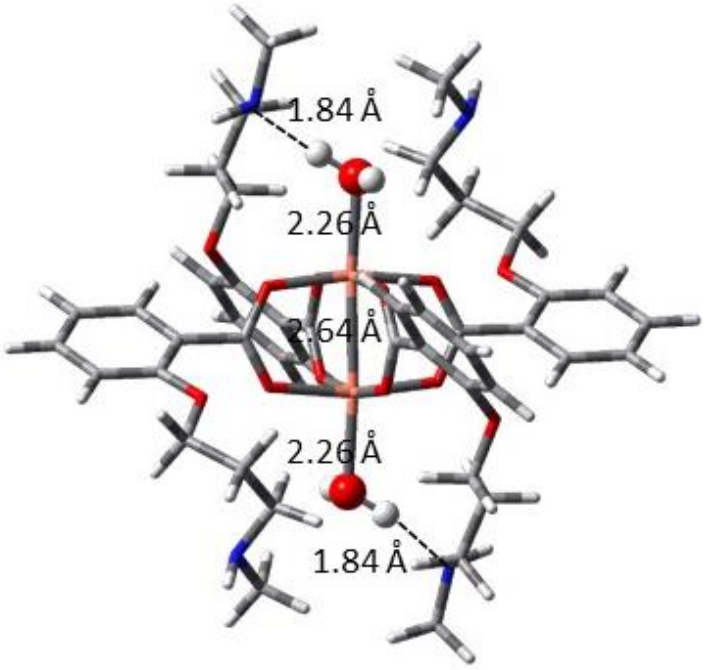

Figure 5-21: Optimized structure for ligand **2** with coordinated water.

In figure 5-17 it can be seen that the optimized position of the coordinated acetone molecules is truly axial, on the copper-copper axis of the paddlewheel structure. There appears little difference in the binding energy of acetone with the methoxy case shown in figure 5-6, as evidenced by the similarity in Cu-O distance. In figure 5-18, however, the coordinated acetonitrile solvent molecules are tilted away from the axial position, although the nitrogen atoms of the cyano group do occupy the axial positions. Again, there are only minor differences with the methoxy case shown in figure 5-7. However, changes in the orientation of the MeCN ligand do reinforce our conclusion that it moves in a flat PES as a function of orientation with respect to the Cu-Cu axis. Similarly, in figure 5-19, the dimethylformamide molecules are tilted almost completely away from the axial position, with the carbonyl oxygen atoms directed away from the copper-copper axis to about the same extent as the nitrogen atoms of acetonitrile. Again, structural differences with the methoxy case depicted in figure 5-8 are minor.

Figure 5-20 shows the optimised position of ethanol solvent molecules, with the hydroxyl oxygen atoms occupying the axial positions directly. Figure 5-21 is interesting in that even though the coordinated water molecule is so small that it occupied the axial positions very closely in the methoxy analogue, it is tilted somewhat away from the axial positions in the methylamine-substituted analogue. This can be rationalized as being due to hydrogen bonding between the water molecule and the nitrogen atom of the methylamine group. In both cases, the structural differences with the corresponding cases for ligand **1** are minor.

*5.5.2.1: Infra-red calculations for [(Cu_2(**2**)(sol)$_2$]*

The infrared spectra for the methylamine analogues are shown in figures 5-22 to 5-26. In this case there are no experimental spectra to compare to. Thus, the spectra with coordinated solvent molecules are superimposed onto the spectrum obtained from the structure where the methylamino arms are coordinated in the axial position on the paddlewheel.

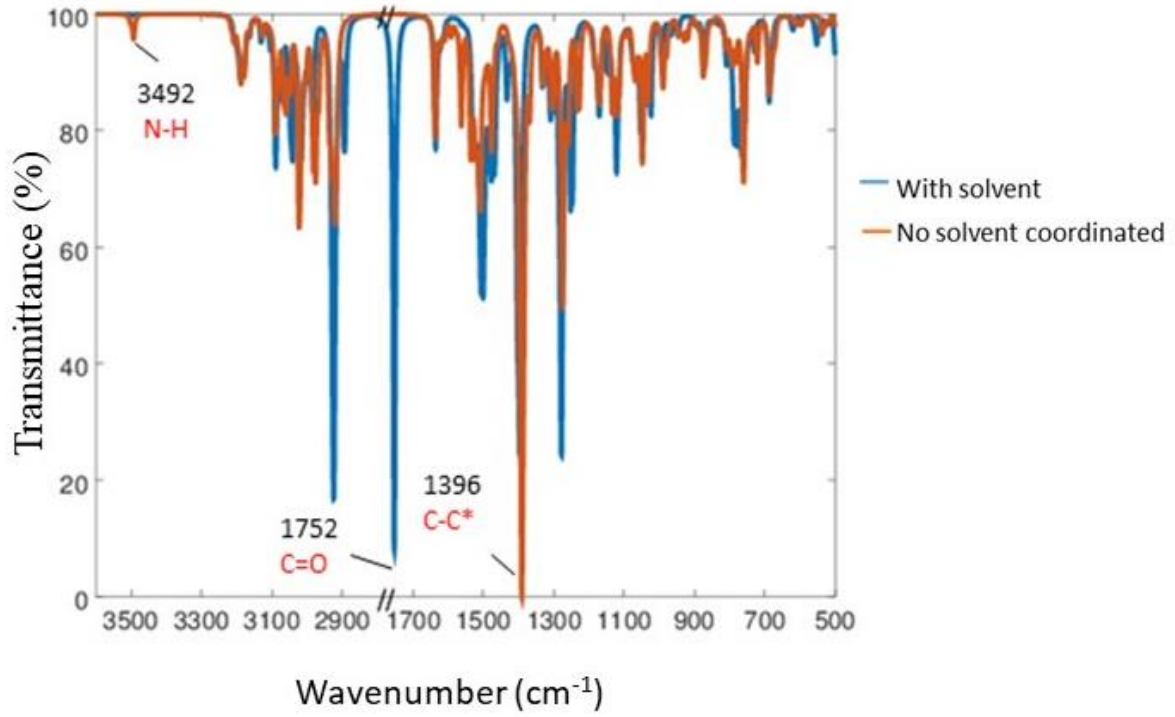

Figure 5-22: Comparison of "no solvent coordinated" (orange) and "with solvent" (blue) IR patterns for $[Cu_2(\mathbf{2})_4(Me)_2CO)_2]$ where **2** is 2-(3-methylaminopropoxy)benzoate, C-C* is a wagging mode of C carboxylate group combined with C aromatic system.

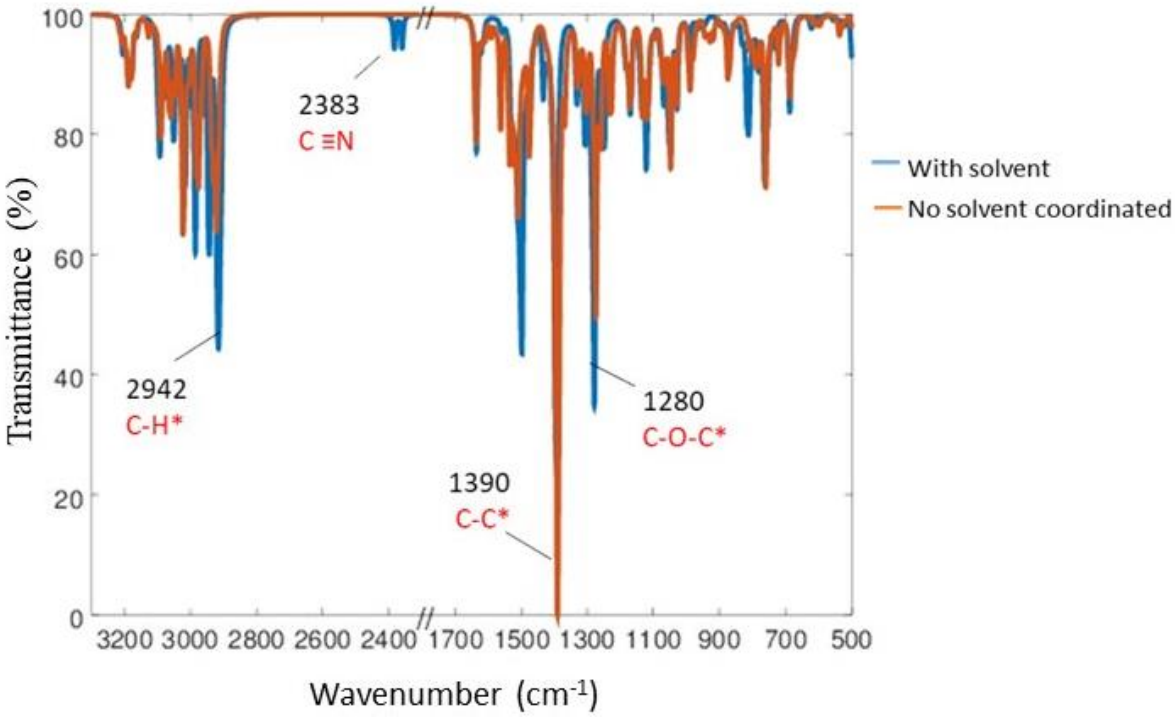

Figure 5-23: Comparison of "no solvent coordinated" (orange) and "with solvent" (blue) IR patterns for $[Cu_2(\mathbf{2})_4(MeCN)_2]$ where **2** is 2-(3-methylaminopropoxy)benzoate. C-C* is a wagging mode of C carboxylate group combined with C aromatic system; C-H* is the stretching mode of C-H MeCN; C-O-C* is the wagging mode of C-O-C alkyl ether CH_2CH_2-O-Ph.

In figure 5-22, for the case of acetone the calculated spectra with axial solvent and no solvent coordinated are very similar, as was the case with the spectra of the corresponding methoxy analogues. The stretching mode of C=O carbonyl of acetone is observed at 1752 cm^{-1} and should be good diagnostic for any experimental structure as for the case of the methoxy analogues. For spectra in figure 5-23, the similarity between the calculated spectra with solvent and no solvent coordinated is clear. The major difference between the two spectra is the cyano peak at 2383 cm^{-1}. However, these peaks are very small and therefore it may be difficult to assign the experimental spectrum solely based on features like these.

As before, the spectra in figure 5-24 show the similarity between the calculated spectra for the cases with axial solvent and with solvent exchanged. A sharp peak at 1707cm^{-1} in "with solvent" spectrum is due the C=O stretching of the coordinated DMF molecule and should again be a clear diagnostic for the presence of axially coordinated solvent molecules as was the case for the methoxy analogue described in figure 5-13.

In the spectra of figure 5-25, similarly, the fingerprint region does not show a clear distinction between the two cases. Interestingly, in this case the OH stretch is shifted to a lower frequency compared to ligand **1** in figure 5-14 (3263 cm^{-1}). This appears to be caused by the fact that in this case the optimization ended up with a hydrogen bond between solvent and pendant groups. The presence or absence of such interactions could lead to significant smearing, which may make the presence of solvent for this case less clear. The discussion for the water case (figure 5-26) is similar to that for ethanol. Again in this case, a hydrogen bond between solvent and pendant groups shifts the OH stretch to a lower frequency (3279 cm^{-1}) compared to the methoxy case. However, as in the methoxy case the water OH stretch is very strong and as such should probably survive in the experimental spectrum, if there is coordinated solvent.

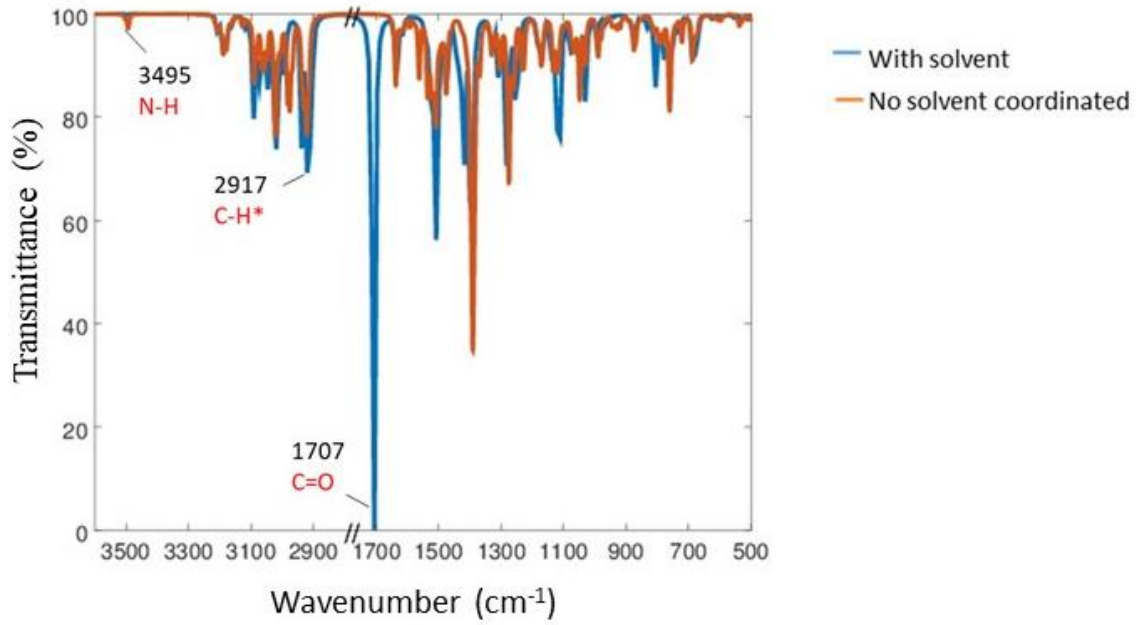

Figure 5-24: Comparison of "no solvent coordinated" (orange) and "with solvent" (blue) IR patterns for $[Cu_2(\mathbf{2})_4(DMF)_2]$ where **2** is 2-(3-methylaminopropoxy)benzoate, C-H* is the stretching mode of C-H DMF.

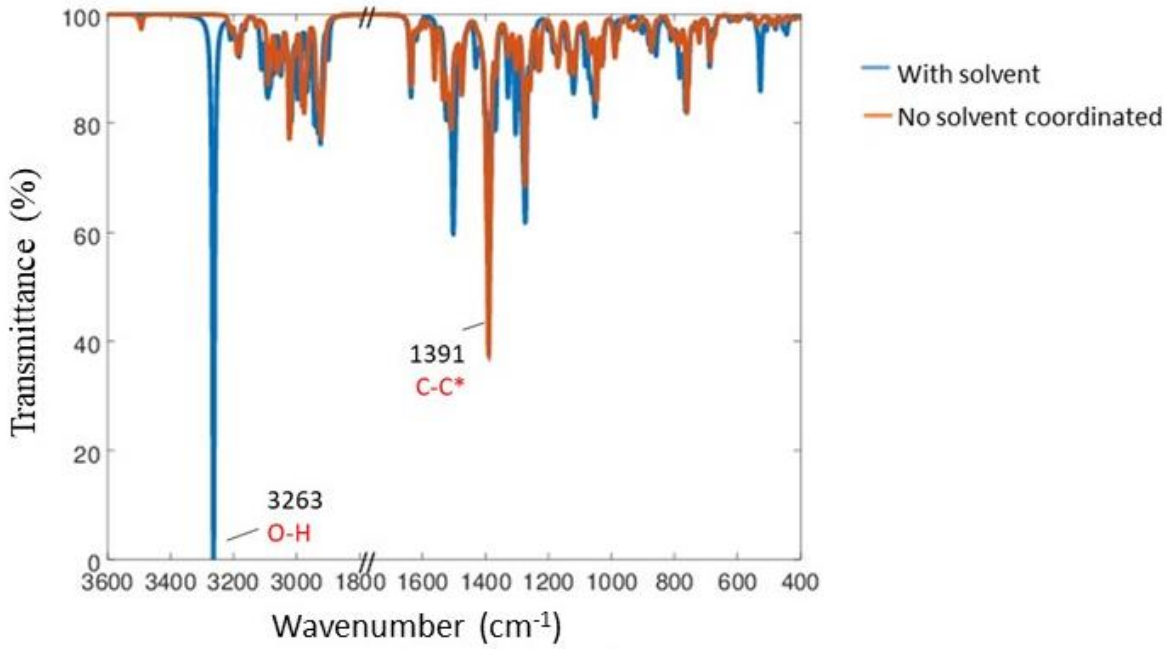

Figure 5-25: Comparison of "no solvent coordinated" (orange) and "with solvent" (blue) IR patterns for $[Cu_2(\mathbf{2})_4(EtOH)_2]$ where **2** is 2-(3-methylaminopropoxy)benzoate. C-C* is a wagging mode of C carboxylate group combined with C aromatic system.

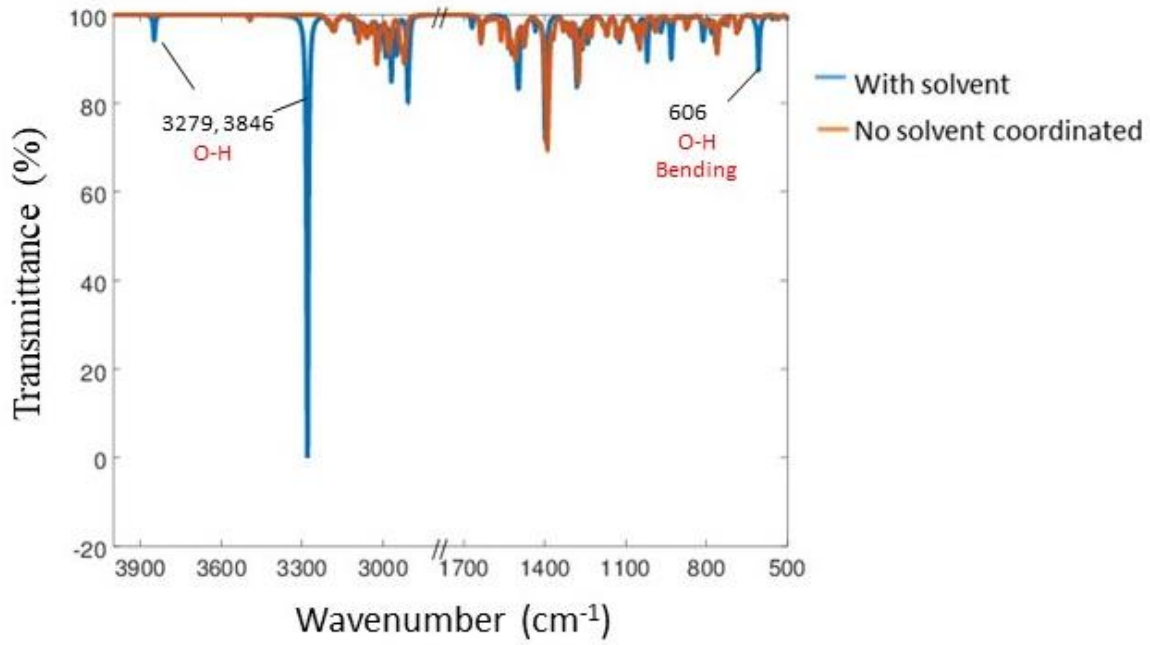

Figure 5-26: Comparison of "no solvent coordinated" (orange) and "with solvent" (blue) IR patterns for $[Cu_2(\mathbf{2})_4(H_2O)_2]$ where **2** is 2-(3-methylaminopropoxy)benzoate.

5.5.3: Copper methylmercaptopropoxy benzoate systems $[(Cu_2(3)(sol)_2]$

The optimized structures for pruned analogues with terminal methylmercapto groups [2(3-methylmercapto) propoxy benzoate], ligand **3,** are shown in figures 5-27 to 5-32.

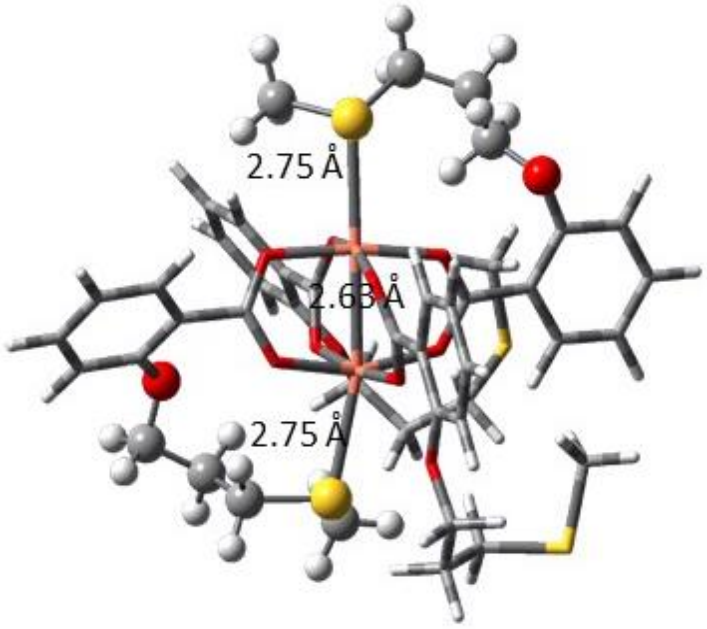

Figure 5-27: DFT calculated structures of the Cu-PW motif show the structure with no solvent coordinated using ligand **3**.

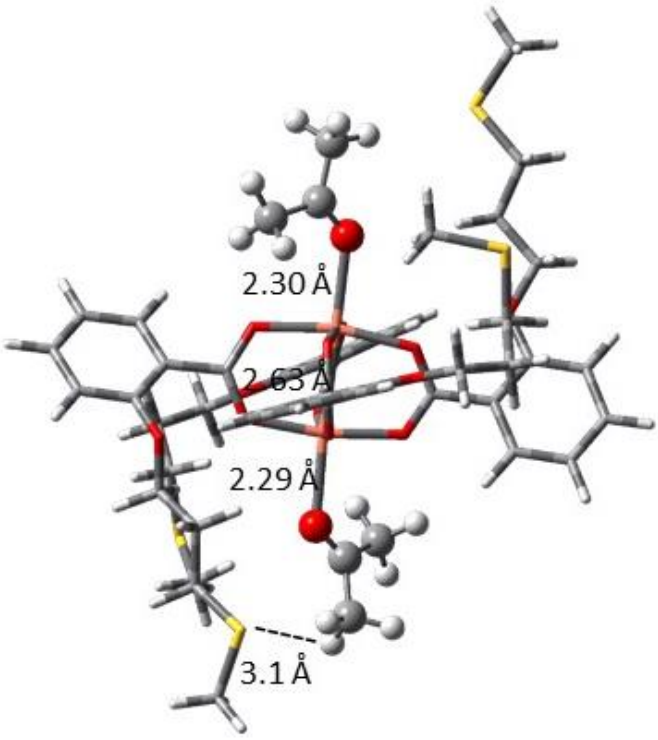

Figure 5-28: DFT calculated structures of the Cu-PW motif show the structure with coordinated acetone using ligand **3**.

Figure 5-27 shows the case in which the sulfur atom of the methylmercapto group occupies the axial positions of the copper centres of the paddlewheel structure in the pruned system. Being a significantly larger atom than either oxygen or nitrogen, the sulphur atom does not appear to occupy the axial positions of the copper atoms well. Rather, it appears to be in a position that is tilted away from the copper-copper axis. The Cu-S distances are also significantly longer than the Cu-O and Cu-N distances for ligands **1** and **2**, respectively. This was to be expected given the larger van der Waals radius for S and its more diffuse electron density.

In figure 5-28 it is readily seen that the axial positions are occupied fully by acetone molecules, while the terminal mercapto substituents extend away from the copper paddlewheel structures. The carbonyl oxygen atoms of the acetone molecules accordingly are able to occupy

the axial positions directly. Hydrogen-bonding in this case which would be C-H…S is clearly not strong enough to obtain a structure with the mercapto groups coordinated to the solvent molecules.

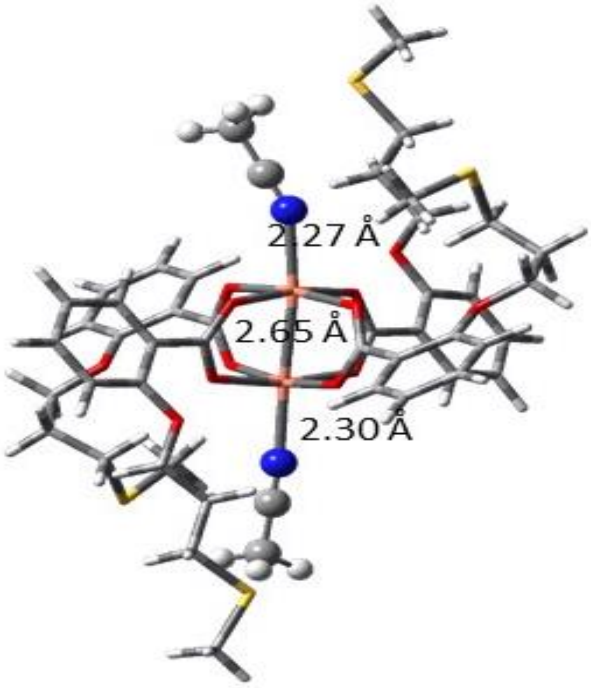

Figure 5-29: DFT calculated structures of the Cu-PW motif for the structure with coordinated acetonitrile using ligand **3**.

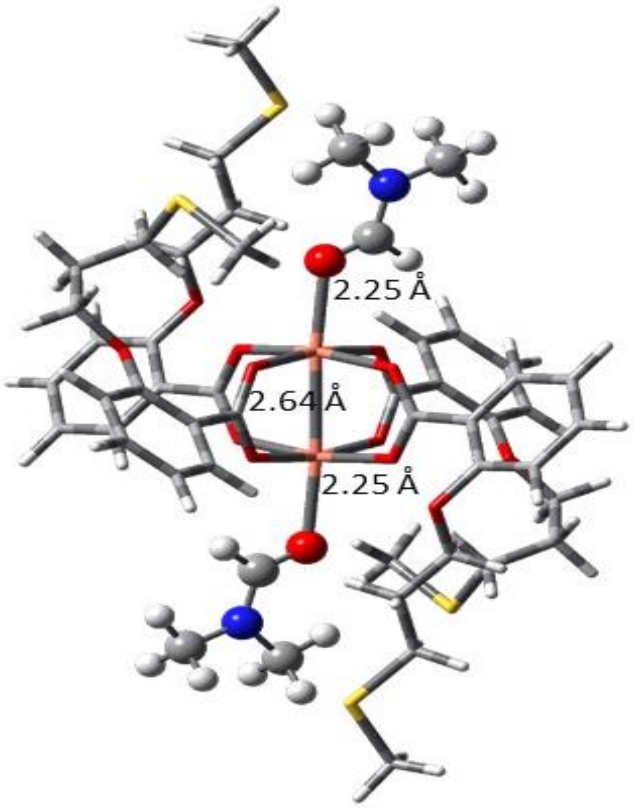

Figure 5-30: DFT calculated structures of the Cu-PW motif for the structure with coordinated DMF using ligand **3**.

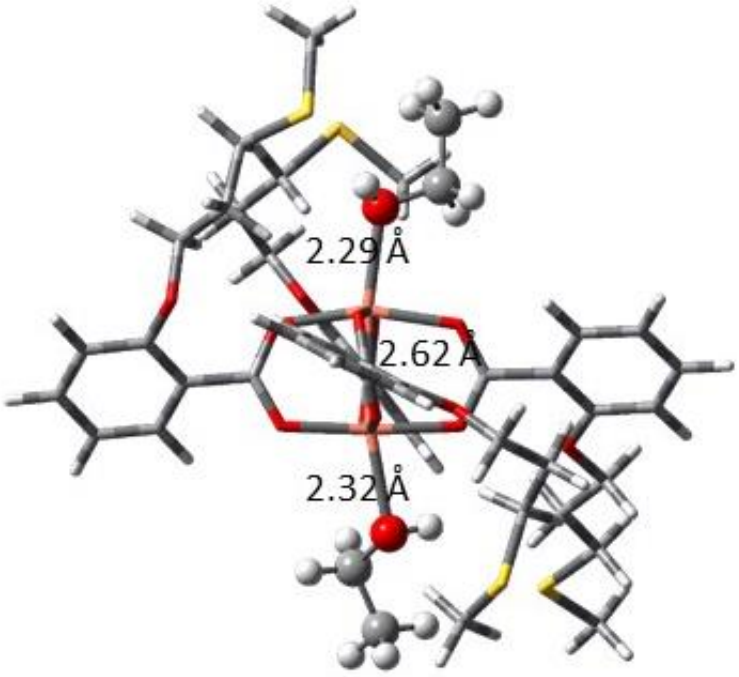

Figure 5-31: DFT calculated structures of the Cu-PW motif for the structure with coordinated ethanol using ligand **3**.

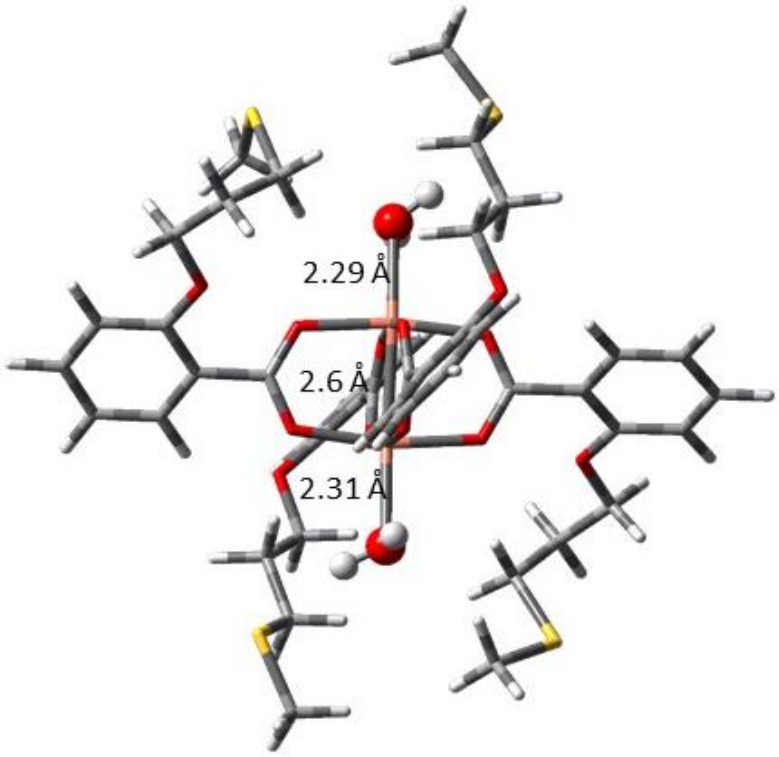

Figure 5-32: DFT calculated structures of the Cu-PW motif for the structure with coordinated water using ligand **3**.

In figure 5-29 the same relative positioning is found with the nitrile nitrogen atoms occupying the axial positions directly and the terminal mercapto substituents extending outward and away from the copper paddlewheel structures. The acetonitrile molecules themselves are also positioned more directly in line with the copper-copper axis than was the case in the methylamine analogue. This is evidenced by the fact that the Cu-N-Cu angles are 154° and 175° in this case, compared to 126° and 165° in the amine case. In all cases, the Cu-Cu-N angle is larger than 171°. In this case, there is more obvious coordination of the mercapto groups with the solvent, although the distances are clearly longer than for the amino and methoxy cases.

Similarly, in figure 5-30, the carbonyl oxygen of the dimethylformamide molecules occupy the axial positions directly while the mercapto substituents extend away from the

copper centres. In figure 5-31, it is the oxygen atoms of the ethanol molecules that occupy the axial positions directly, and in figure 5-32 it is the water molecules that are axially coordinated. As with the methylamine analogue, the water molecules appear to hydrogen bond with the sulfur atoms, resulting in their displacement slightly away from the copper-copper axis in the optimized structure. In all cases with coordinated solvent molecules, the distances of the ligand the Cu-atoms is similar to the methoxy and amino cases.

*5.5.3.1: Infra-red calculations for [(Cu_2(**3**)($sol)_2$]*

The infrared spectra of the terminal methylmercapto analogues are found in figures 5-33 to 5-37. Again as in the case for ligand **2**, there are no experimental spectra to compare to. Instead, as for ligand **2**, the spectra with coordinated solvent molecules are superimposed onto the spectrum obtained from the structure where the methylmercapto arms are coordinated in the axial position on the paddlewheel.

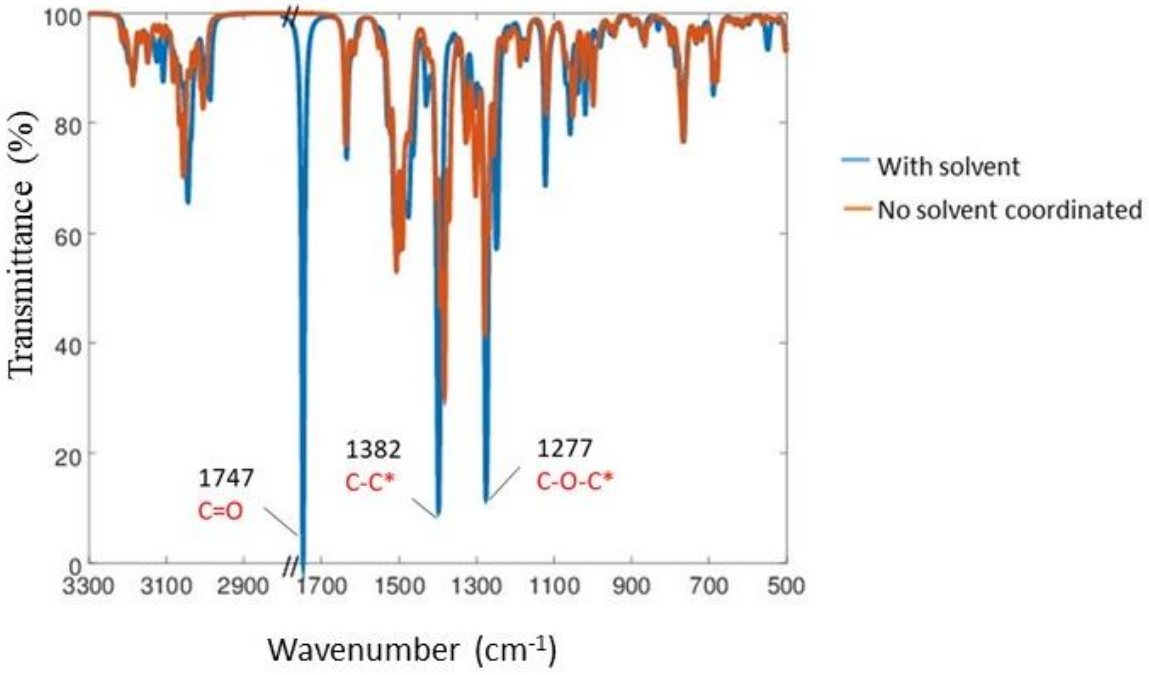

Figure 5-33: Comparison of "no solvent coordinated" (orange) and "with solvent" (blue) IR patterns for $[Cu_2(\mathbf{3})_4(Me)_2CO)_2]$ where **3** is 2-(3-methylmercaptopropoxy)benzoate, C-C* is a wagging mode of C carboxylate group combined with C aromatic system; C-O-C* is the wagging mode of C-O-C alkyl ether CH_2CH_2-O-Ph.

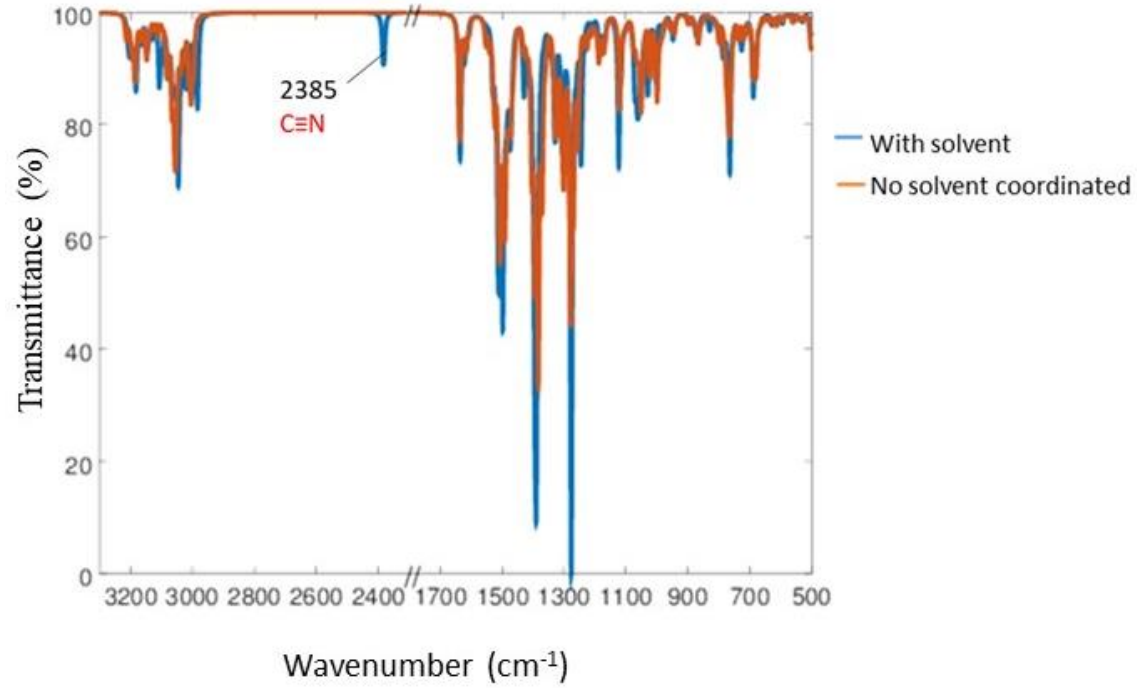

Figure 5-34: Comparison of "no solvent coordinated" (orange) and "with solvent" (blue) IR patterns for $[Cu_2(\mathbf{3})_4(MeCN)_2]$ where **3** is 2-(3-methylmercaptopropoxy)benzoate.

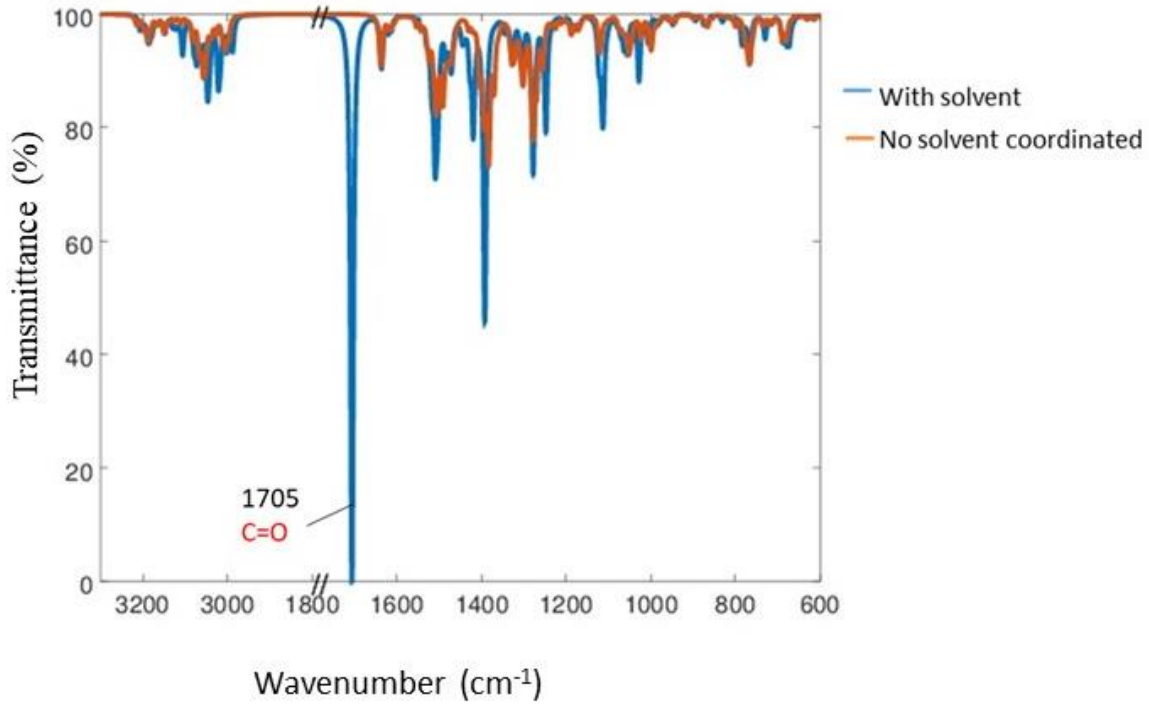

Figure 5-35: Comparison of "no solvent coordinated" (orange) and "with solvent" (blue) IR patterns for $[Cu_2(\mathbf{3})_4(DMF)_2]$ where **3** is 2-(3-methylmercaptopropoxy)benzoate.

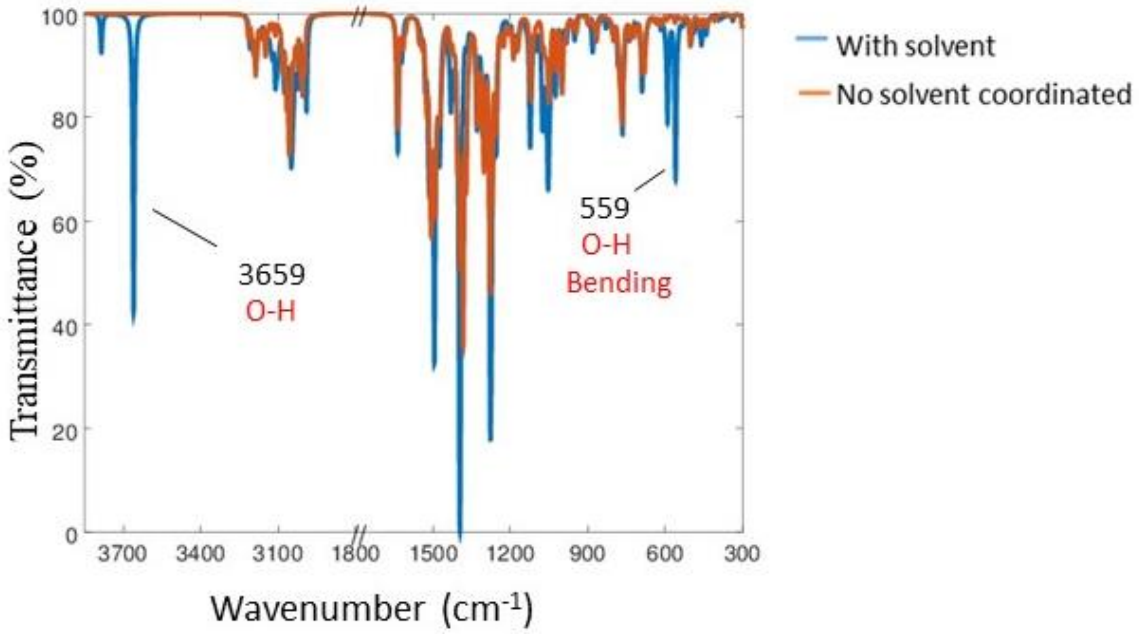

Figure 5-36: Comparison of "no solvent coordinated" (orange) and "with solvent" (blue) IR patterns for $[Cu_2(\mathbf{3})_4(EtOH)_2]$ where **3** is 2-(3-methylmercaptopropoxy)benzoate.

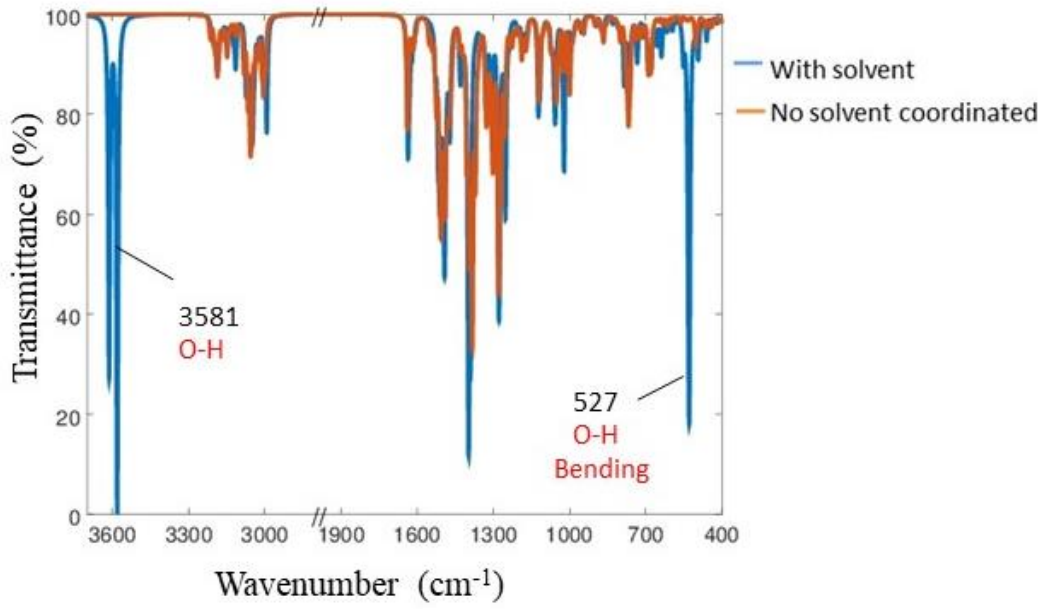

Figure 5-37: Comparison of "no solvent coordinated" (orange) and "with solvent" (blue) IR patterns for $[Cu_2(\mathbf{3})_4(H_2O)_2]$ where **3** is 2-(3-methylmercaptopropoxy)benzoate.

The spectra 5-33 and 5-34 show little difference between the case with solvent coordinated and the case in which the pendant groups are coordinated. However, in both cases there are clear solvent peaks, which could provide a diagnostic, whereby it is noted that there is only a single CN stretch in the acetonitrile case (because of symmetry), which is stronger than for the methylamine case depicted in figure 5-23.

In figures 5-36 and 5-37, the calculated and experimental spectra are similar for both the case with solvent and solvent exchanged. The lack of hydrogen-bonding clearly shows in figure 5-36 in the higher energy of the OH stretch (3659 cm^{-1}) compared to figure 5-25. Similarly, for figure 5-37, absence of hydrogen bonding leads to an increasing the OH frequency compared to figure 5-26.

5.5.4: Comparison of binding energies in the three different ligands of copper systems $[Cu_2(L)_4X_2]$

Given that the optimized structures indicate a decided lack of interest on the part of the sulfur atom in the terminal mercapto groups to coordinate or to be in close proximity to the copper centres of the paddlewheel structure in the pruned system, it is also highly unlikely that their behaviour in the analogous full system would be any different. Therefore, no such calculations were attempted. For methylamine analogues there could be a difference between the full and pruned system. However, to ensure an honest comparison between the three systems, in the table below, the relative binding energies for the three different ligands for the pruned systems are shown.

Table 5-2: Binding energy of 2 solvent molecules to $[Cu(\mathbf{1})_4(sol)_2]$, $[Cu(\mathbf{2})_4(sol)_2]$ and $[Cu(\mathbf{3})_4(sol)_2]$. Relative to $Cu(\mathbf{1})_4$, $Cu(\mathbf{2})_4$, and $Cu(\mathbf{3})_4$ respectively with **1**, **2**, or **3** coordinated respectively, ΔE_{RB} in kJ/mol.

Copper-Coordinated Solvents	ΔE_{RB} (kJ/mol) $[Cu_2(\mathbf{1})_4(sol)_2]$	ΔE_{RB} (kJ/mol) $[Cu_2(\mathbf{2})_4(sol)_2]$	ΔE_{RB} (kJ/mol) $[Cu_2(\mathbf{3})_4(sol)_2]$
water	111.6	55.3	69.2
DMF	55.3	–9.4	47.8
Ethanol	84.6	53.8	68.5
Acetone	40.4	–9.4	25.3
Acetonitrile	26.4	–25.8	21.2

Table 5-2 shows that the process for displacing the solvent molecules and coordinating the pendant arms is endothermic for both oxygen and sulphur, whereby the endothermicity is less for sulphur. This is likely due to the fact that oxygen is a better hydrogen bond acceptor. This stabilizes the structure in which solvent is coordinated in the axial position. The case for

nitrogen is different. Here, replacing the solvent molecules with the pendant arms is an exothermic process in a number of cases. Coupled with the increasing entropy for this process, this suggest that for ligand **2** fewer structures with coordinated solvent will exist. The difference between oxygen and sulfur suggest that some more detailed fine-tuning of the final structure is possible as well.

5.6: Conclusions

In investigating the behaviour of liquid phase exfoliation, Foster *et al*[270] hypothesized that the exfoliation of alkyl-ether functionalized layered metal-organic frameworks might proceed through the axial coordination of a terminal methoxy substituent on the copper centres of the corresponding paddlewheel structure. This would depend on which solvent was used for sonication of the layered MOF. This would require the methoxy group to attain the proper orientation to approach that position within the pore space of the framework structure, it would also and have need to bind strongly enough to displace any solvent molecules that have occupied the axial position and coordinated to the copper atoms. In this computational study, it has been shown that the terminal methoxy groups appears to fully occupy the axial positions of the copper atom coordination sphere in case of acetone, acetonitrile, and ethanol but not for water and DMF, pages 184,187, and 190. There are a number of possible reasons for this. Firstly, the relatively positive copper atom would naturally attract the electron-rich ether oxygen atom. Secondly, as was alluded to above, that the oxygen atom would have to line up with the copper atom within the pore space of the metal-organic framework. This is possible, because alkyl chains are highly flexible. Hereby, it should be noted that the range and type of motion that an alkyl side chain is capable of undertaking in response to external influences such as dipolar attractions between the etheric oxygen atom and the positive copper atom is restricted. Lastly, the coordinative bonding energy between the etheric oxygen atom and the

copper atom has to compete with the coordinative bonding energy of the solvent molecules that may be present in the pore space and that are intrinsically much more labile (easily lost) than the methoxy-terminated side chains on the linker molecules. In examining analogous structures having terminal methylamino and methylmercapto groups in place of the terminal methoxy groups on the linker molecule substituents, we have shown that changing the structure does not appear to influence the binding of molecules structurally. However, binding energies do change, as would be expected.

Chapter 6: Conclusion and Future work

Building on the work presented in this thesis, there is essentially unlimited potential for future studies and applications of computational chemistry in the area discussed. The literature review in Chapter one clearly shows that there has been an exponential grow in the MOFs field in the last 20 years with no clear indication that this is abating. In particular, it is clear that the number of metal atoms that are suitable for construction of metal-organic frameworks is limited by their elemental identities and usable oxidation states. However, the number of organic linker molecules that could be used is essentially limitless, allowing the design and construction of metal-organic frameworks having an equally unlimited range of pores and pore characteristics.

In chapter three, we examined the minimum energy conformations of the complexes $[Zr_6(\mu_3\text{-}O)_4(\mu_3\text{-}OH)_4(O_2CH)_9(O_2CC_6H_5)_3]$, $[Zr_6(\mu_3\text{-}O)_4(\mu_3\text{-}OH)_4(O_2CH)_9(O_2CC_6H_4X)(O_2CC_6H_5)_2]$, $[Zr_6(\mu_3\text{-}O)_4(\mu_3\text{-}OH)_4(O_2CH)_9(O_2CC_6H_3X)_2(O_2CC_6H_5)]$, $[Zr_6(\mu_3\text{-}O)_4(\mu_3\text{-}OH)_4(O_2CH)_9(O_2CC_6H_2X)_3]$ where X represents a series of *ortho* substituents on bidentate benzoate ligands.

As such, these structures model the basic building blocks of a larger metal-organic framework structure. Our studies focussed on the interior voids of the metal-organic framework structure, since the binding energy of adsorbed molecules in such locations is a significant determining factor in regard to the adsorption of various molecules onto metal-organic frameworks. It is clear from our calculations that in particular, amines and alcohols appear to have potential in the separation of gases, in particular CO_2 versus N_2 whereby additional gases in the gas stream, such as water can have a large effect on the final efficiency of such methods. This is entirely in line with the literature, where the relative humidity of a gas stream has been used to either adsorb or release CO_2 from porous systems.[2] The effect of the presence of water in the system is an important factor in comprehending the functioning and design of new materials. In

particular, the optimal operating concentration of water would be crucial to obtain. However, such calculations are beyond the scope of this thesis. However, it is clear from our calculations, that CO_2 sequestration could be quite effective.

Unsurprisingly, the exact method for studying these systems turns out to be very important as well. In particular, the inclusion of dispersion has a significant effect on the value of the binding energy calculated, in particular for the adsorption of hydrogen. It is clear from our calculations that additional work is needed to ascertain the accuracy and precision of the present DFT methods to come to a more precise understanding of how strongly certain gases bind, in particular, our system will need to be re-investigated using *ab initio* methods or potentially accurately parametrised force field methods to ascertain the relative accuracy of our calculations. Similarly, metal-organic frameworks that are formed on a physical support of some kind could find many useful applications such as filtration devices for the desalination of water, or even the capture of water from atmospheric moisture. However, how such a support would affect the structure of the MOF and therefore the binding energies of the gases of interest is something that should be investigated in future work.

In chapter four, we investigated the predictive capability of computation in regard to electronic and spectral properties of atoms and molecules adsorbed in MOFs. Our results here are clearly mixed. It is clear that our calculations could be improved upon further. Our work of the X-ray photoelectron spectra shows that, whilst qualitative agreement between theory and experiment is clearly achieved, the precision with which the spectra are generated demands improvement of the methodology. Our work on the calculation of NMR spectra shows that neglect of core electrons is clearly not a reasonable approximation, since qualitative agreement turned out to be unachievable. Inclusion of core electrons, therefore, seems the most logical next step in this project. However, we only investigated a single computational method, based

on literature data. It is clear that other methods will need to be tested as well to obtain a clearer idea of the pros and cons of the different approximations made. Similarly, it should be possible to draw on results from the literature and investigate the effect of altering the MOF on e.g. the ^{13}C and ^{1}H spectra. The advantage of tackling the problem in this way would be that we would be able to draw on a much large body of work in the literature to compare our calculations to. In general, we need to conclude that more research is needed to determine the minimum bases set size/combinations needed to reproduce the experimental results as quantitatively and consistently as possible. In particular, we note that all-electron calculations should be attempted for these systems to fully explore the effect of the neglect of the core electrons.

As the last chapter demonstrated, the generation of infrared spectra shows more promise in obtaining clear correlations between experiment and theory. It was noted that conformational sampling would be needed to obtain a better agreement between theory and experiment. In particular, while the computed spectra in chapter 5 exhibit clear, sharp peaks, in most cases they could not be matched fully to the experimentally observed spectra. However, our calculations make it very clear that the pendant arms on the benzoate linkers will be capable of coordinating to empty axial sites of the paddlewheels. In examining analogous structures having terminal methylamino and methylmercapto groups in place of the terminal methoxy groups on the linker molecule substituents, we have shown that changing the structure mainly influences binding energies, as would be expected. Our results strongly suggest that the hypothesis of Foster *et al*. that the pendant groups play an important role in the exfoliation of the 3D MOF into a 2D MON is a sensible one. To investigate this further, we need to do investigate more hydrophobic systems by replacing the –O methoxy atom with $–CH_2$ and compare that with the hydrophilic version (methoxy, aminomethyl, and mercapto methyl systems) that have been done. In that hydrophobic case, binding to the axial sites is no longer

possible. Thus, we will be able to ascertain the influence of the potential binding of pendant arms on the final structure of the MONs as well as on the exfoliation process.

It is clear to us that our calculations are the first step towards further understanding of the issues involved in the adsorption of gases in MOFs. However, it is also clear that we have had to make a number of approximations to make our calculations tractable. For some approximations, it was made clear by our calculations that these approximations have to be dropped in future work. For other approximations, this is less clear. Thus, more work is needed to elucidate further. In particular, it has been assumed throughout that single paddlewheels or Zr-oxo clusters can be used to describe the full MOF system accurately. To investigate this further, we need to extend our investigation to periodic DFT calculations. This will allow us to ascertain whether structurally our approach describes the bulk system accurately enough. However, this will largely get us a handle on structural information. To get a better idea of the accuracy of the relative binding energies calculated, particularly in view of the large contribution of dispersion for the binding of some molecules, the use of *ab initio* methods will need to be investigated to get a better agreement between theory and experiment. This will then also allow us to develop scaling factors or correlation curves, which will allow the use of lower accuracy methods to get higher accuracy results. It is clear to us as well, that the more experimental data is available, the easier this task becomes. Therefore, close cooperation with experimentalists is crucial to make this come to fruition.

For the modelling of MONs it is clear that conformational freedom plays an important role in determining the IR spectra of the final nanosheets. Therefore, an approach, which includes conformational sampling, most probably through a periodic molecular dynamics (MD) approach, potentially in combination with a periodic DFT approach for calculating the IR spectra is something, which should be investigated, since this potentially could lead to a

significant improvement in the agreement between theory and experiment. It should also be investigated, whether other forms of spectroscopy could be amenable to a combined experimental/theoretical approach. In particular, if the use of NMR on second row elements (O, C, N) is practicable experimentally, then it would be something which could be investigated theoretically as well. Core electrons are less of an issue in this case and there is a large body of literature, which would allow us to define the appropriate methods to use much more clearly. Again here, a combined MD/DFT approach may be the most appropriate way forward.

Finally, it is clear from our work that only the surface of this important area of materials research has been scratched by us. There are many more avenues that should be explored. A combined theory/experimental approach will be crucial to make the advances necessary to make these materials as efficient as possible and of the largest possible benefit to mankind.

References

1 S. Kitagawa, R. Kitaura and S. Noro, Angew. Chem Int. Ed., 2004, **43**, 2334–2375.

2 X. S. Zhao and G. Q. Lu, Nanoporous Materials: Science and Engineering Imperial College Press, London, 2004.

3 K. Ishizaki, S. Komarneni and M. Nanko, Porous Materials: process technology and applications, Springer Science+Business Media Dordrecht, 1998.

4 N. Z. Logar and V. Kaučič, Acta Chim. Slov., 2006, **53**, 117–135.

5 J. Rouquerolt, D. Avnir, C. W. Fairbridge, D. H. Everett, J. H. Haynes, N. Pernicone, J. D. F. Ramsay, K. S. W. Sing and K. K. Unger, Pure Appl. Chem., 1994, **66**, 1739–1758.

6 K. Maex, M. R. Baklanov, D. Shamiryan, F. Iacopi, S. H. Brongersma and Z. S. Yanovitskaya, J. Appl. Phys., 2003, **93**, 8793–8841.

7 S. N. Azizi, A. R. Samadi-Maybodi, M. Yarmohammadi, Open J. Inorg. Chem., 2012, **2**, 1–5.

8 J. E. Kogel, N. C. Trivedi and J. M. Barker, Industrial minerals & Rock: Commodities, Markets, and Uses, Society for Mining, Metallurgy, and Exploration, 2006, 1039–1065.

9 B. F. Sels and L. M. Kustov, Zeolites and Zeolite-like Materials, Elsevier B.V. 2016.

10 Y. Tian and J. Wu, Langmuir, 2017, **33**, 996–1003.

11 S. Sircar and A. Myers, Handbook of Zeolite Science and Technology, Marcel Dekker, Inc., 2003.

12 B. Jha and D. N. Singh, Fly Ash Zeolites: Innovations, Applications, and Directions, Springer Science+Business Media Singapore, 2016.

13 N. Kosinov, J. Gascon, F. Kapteijn and E. J. M. Hensen, J. Memb. Sci., 2016, **499**, 65–79.

14 K. C. Khulbe, T. Matsuura, C. Y. Feng and A. F. Ismail, RSC Adv., 2016, **6**, 42943–42961.

15 F. Rouquerol, J. Rouquerol, K. S. W. Sing, P. Llewellyn and G. Maurin, Adsorption by powders and porous solids, Elsevier Ltd., UK, 2nd Edition, 2014.

16 R. Xu, W. Pang, J. Yu, Q. Huo, J. Chen, Chemistry of zeolites and related porous materials: synthesis and structure, John Wiley & Sons, 2007.

17 R. Xu, W. Pang and Q. Huo, Modern Inorganic Synthetic Chemistry, Elsevier B.V., Amsterdam, 2011.

18 H. Furukawa, K. E. Cordova, M. O'Keeffe and O. M. Yaghi, Science, 2013, **341**, 1230444.

19 S. Chong, G. Thiele and J. Kim, Nat. Commun., 2017, **8**, 1-9

20 A. D. Covington, Chem. Soc. Rev., 1997, 111–126.

21 M. Robin, Inorganic Chemistry, 1962, **1**, 337-342.

22 M. Bosch, S. Yuan, W. Rutledge and H. C. Zhou, Acc. Chem. Res., 2017, **50**, 857–865.

23 K. A. Hofmann and F. Küspert, Z. Anorg. Chem., 1897, **15**, 204–207.

24 J. Rayner and H. Powell, J. Chem. Soc., 1952, 319-328.

25 B. F. Hoskins and R. Robson, J. Am. Chem. Soc., 1990, **112**, 1546–1554.

26 B. F. Hoskins and R. Robson, J. Am. Chem. Soc., 1989, **111**, 5962–5964.

27 B. F. Abrahams, B. F. Hoskins, J. Liu and R. Robson, J. Am. Chem. Soc., 1991, **113**, 3045–3051.

28 O. M. Yaghi, G. Li and H. Li, Nature, 1995, **378**, 703–706.

29 S. R. Batten, S. M. Neville and D. R. Turner, Coordination polymers - Design, Analysis and Application, Royal Society of Chemistry, 2009.

30 J. W. McBain, Lond.Edinb.Dubl.Phil.Mag., 1909, **18**, 916–935.

31 I. Langmuir, J. Am. Chem. Soc., 1916, **38**, 2221–2295.

32 S. Brunauer, P. H. Emmett and E. Teller, J. Am. Chem. Soc., 1938, **60**, 309–319.

33 D. P. Broom and K. M. Thomas, MRS Bulletin, 2013, 38, 412–421.

34 X. Zhao, B. Xiao, A. J. Fletcher, K. M. Thomas, D. Bradshaw and M. J. Rosseinsky, Science, 2004, **306**, 1012–1015.

35 J. R. Li, J. Sculley and H. C. Zhou, Chem. Rev., 2012, **112**, 869–932.

36 Y. He, W. Zhou, R. Krishna and B. Chen, Chem. Commun., 2012, **48**, 11813.

37 S. C. Xiang, Z. Zhang, C. G. Zhao, K. Hong, X. Zhao, D. R. Ding, M. H. Xie, C. De Wu, M. C. Das, R. Gill, K. M. Thomas and B. Chen, Nat. Commun., 2011, **2**, 204–207.

38 E. D. Bloch, W. L. Queen, R. Krishna, J. M. Zadrozny, C. M. Brown, J. R. Long, Science, 2012, **335**, 1606–1609.

39 K. A. Cychosz, R. Ahmad and A. J. Matzger, Chem. Sci., 2010, **1**, 293.

40 M. Kuhn and F. Umbach, Eucers, 2011, **1**, 1-52.

41 K. S. W. Sing, Pure Appl. Chem., 1985, **57**, 603–619.

42 A. N. Khlobystov, A. J. Blake, N. R. Champness, D. A. Lemenovskii, A. G. Majouga, N. V. Zyk and M. Schröder, Coord. Chem. Rev., 2001, 222, 155–192.

43 B. Rather, B. Moulton, R. D. B. Walsh and M. J. Zaworotko, Chem. Commun., 2002, **2**, 694–5.

44 W. Li, S. Henke and A. K. Cheetham, APL Mater., 2014, **2**, 123902.

45 T. D. Bennett and A. K. Cheetham, Acc. Chem. Res., 2014, **47**, 1555–1562.

46 E. C. Spencer, M. S. R. N. Kiran, W. Li, U. Ramamurty, N. L. Ross and A. K. Cheetham, Angew. Chemie - Int. Ed., 2014, **53**, 5583–5586.

47 E. C. Spencer, R. J. Angel, N. L. Ross, B. E. Hanson and J. A. K. Howard, J. Am. Chem. Soc., 2009, **131**, 4022–4026.

48 R. Kumar, D. Raut, I. Ahmad, U. Ramamurty, T. K. Maji and C. N. R. Rao, Mater. Horiz., 2014, **1**, 513–517.

49 N. Khosrovani and A. W. Sleight, J. Solid State Chem., 1996, **11**, 2–11.

50 A. Schneemann, V. Bon, I. Schwedler, I. Senkovska, S. Kaskel and R. A. Fischer, Chem. Soc. Rev., 2014, **43**, 6062–6096.

51 X.-H. Miao and L.-G. Zhu, Z. Anorg. Allg. Chem, 2008, **634**, 335–338.

52 N. Stock and S. Biswas, Chem. Rev., 2012, **112**, 933–969.

53 J. H. Cavka, S. Jakobsen, U. Olsbye, N. Guillou, C. Lamberti, S. Bordiga and K. P. Lillerud, J. Am. Chem. Soc., 2008, **130**, 13850–13851.

54 L. Valenzano, B. Civalleri, S. Chavan, S. Bordiga, M. H. Nilsen, S. Jakobsen, K. P. Lillerud and C. Lamberti, Chem. Mater., 2011, **23**, 1700–1718.

55 H. Li, M. Eddaoudi, M. OKeeffe and O. M. Yaghi, Nature, 1999, **402**, 276–279.

56 T. T. T. Huong, P. N. Thanh, N. T. X. Huynh and D. N. Son, VNU J. Sci. Math. – Phys., 2016, **32**, 67–85.

57 S. S. Y. Chui, S. M. F. Lo, J. P. H. Charmant, A. G. Orpen and I. D. Williams, Science, 1999, **283**, 1148–1150.

58 Basolite™ C300 produced by BASF, https://www.sigmaaldrich.com/catalog/product/aldrich/688614?lang=en&region=GB, Access date 13th February 2018.

59 H. K. Chae, D. Y. Siberio-Perez, J. Kim, Y. Co, M. Eddoudi, A. J. Matzger, M. Okeeffe, and O. M. Yaghi, Nature, 2004, **427**, 523–527.

60 A. G. Wong-Foy, A. J. Matzger and O. M. Yaghi, J. Am. Chem. Soc., 2006, **128**, 3494–3495.

61 B. Chen, N. W. Ockwig, A. R. Millward, D. S. Contreras and O. M. Yaghi, Angew. Chem - Int. Ed., 2005, **44**, 4745–4749.

62 X. Lin, J. Jia, X. Zhao, K. M. Thomas, A. J. Blake, G. S. Walker, N. R. Champness, P. Hubberstey and M. Schröder, Angew. Chem - Int. Ed., 2006, **45**, 7358–7364.

63 A. G. Wong-Foy, O. Lebel and A. J. Matzger, J. Am. Chem. Soc., 2007, **129**, 15740–15741.

64 P. Horcajada, C. Serre, M. Vallet-Regí, M. Sebban, F. Taulelle and G. Férey, Angew. Chem - Int. Ed., 2006, **45**, 5974–5978.

65 G. Férey, C. Serre, C. Mellot-Draznieks, F. Millange, S. Surblé, J. Dutour and I. Margiolaki, Angew. Chem - Int. Ed., 2004, **43**, 6296–6301.

66 L. Hamon, C. Serre, T. Devic, T. Loiseau, F. Millange, G. Ferey and G. D. Weireld, J. Am. Chem. Soc., 2009, **131**, 8775–8777.

67 M. Latroche, S. Surblé, C. Serre, C. Mellot-Draznieks, P. L. Llewellyn, J. H. Lee, J. S. Chang, H. J. Sung and G. Férey, Angew. Chem - Int. Ed., 2006, **45**, 8227–8231.

68 J. S. Lee, S. H. Jhung, J. W. Yoon, Y. K. Hwang and J. S. Chang, J. Ind. Eng. Chem., 2009, **15**, 674–676.

69 P. L. Llewellyn, S. Bourrelly, C. Serre, A. Vimont, M. Daturi, L. Hamon, G. De Weireld, J. Chang, D. Hong, Y. K. Hwang and S. H. Jhung, Langmuir, 2008, **24**, 7245–7250.

70 G. Férey, C. Mellot-Draznieks, C. Serre, F. Millange, J. Dutour, S. Surblé and I. Margiolaki, Science, 2005, **309**, 2040–2042.

71 N. Klein, I. Senkovska, K. Gedrich, U. Stoeck, A. Henschel, U. Mueller and S. Kaskel, Angew. Chem - Int. Ed., 2009, **48**, 9954–9957.

72 B. Mu, P. M. Schoenecker and K. S. Walton, J. Phys. Chem. C, 2010, **114**, 6464–6471.

73 K. Koh, A. G. Wong-Foy and A. J. Matzger, J. Am. Chem. Soc., 2009, **131**, 4184–4185.

74 Y. S. Bae, D. Dubbeldam, A. Nelson, K. S. Walton, J. T. Hupp and R. Q. Snurr, Chem. Mater., 2009, **21**, 4768–4777.

75 M. Eddaoudi, J. Kim, N. Rosi, D. Vodak, J. Wachter, M. O. Keeffe, O. M. Yaghi, Science, 2002, **295**, 469–472.

76 S. Ma, Pure Appl. Chem., 2009, **81**, 2235–2251.

77 J. L. C. Rowsell, J. Eckert and O. M. Yaghi, J. Am. Chem. Soc., 2005, **127**, 14904–14910.

78 S. Ma, D. Sun, M. Ambrogio, J. A. Fillinger, S. Parkin and H. C. Zhou, J. Am. Chem. Soc., 2007, **129**, 1858–1859.

79 S. Ma, J. Eckert, P. M. Forster, J. W. Yoon, Y. K. Hwang, J.-S. Chang, C. D. Collier, J. B. Parise and H.-C. Zhou, J. Am. Chem. Soc., 2008, **130**, 15896–15902.

80 R. T. Yang, Gas Separation by Adsorption Processes, Butterworth Publishers, United states of America, 1987.

81 C. Mao-Chun Hong Ling, Design and construction of coordination polymers, John Wiley & Sons, Canada, 2009.

82 M. Dincă and J. R. Long, J. Am. Chem. Soc., 2005, **127**, 9376–9377.

83 T. E. Kaiser, H. Wang, V. Stepanenko and F. Würthner, Angew. Chem - Int. Ed., 2007, **46**, 5541–5544.

84 R. Birkhoff and M. Nurminen, Alkylation and Polymerization NExOCTANE™ Technology for Isooctane Production, McGraw-Hill, New York, 2004.

85 K. Li, D. H. Oslon, J. Seidel, T. J. Emge, H. Gong, H. Zeng, and J. Li, J. Am. Chem. Soc., 2009, **131**, 10368–10369.

86 D. Britt, D. Tranchemontagne and O. M. Yaghi, Proc. Natl. Acad. Sci., 2008, **105**, 11623–11627.

87 A. Dąbrowski, Adv. Colloid Interface Sci., 2001, **93**, 135–224.

88 L. E. Kreno, K. Leong, O. K. Farha, M. Allendorf, D. Van Richard P. and J. T. Hupp, Chem. Rev., 2012, **112**, 1105–1125.

89 Y. B. Zhang, W. X. Zhang, F. Y. Feng, J. P. Zhang and X. M. Chen, Angew. Chem - Int. Ed., 2009, **48**, 5287–5290.

90 A. R. Millward and O. M. Yaghi, J. Am. Chem. Soc., 2005, **127**, 17998–17999.

91 H. Furukawa, N. Ko, Y. B. Go, N. Aratani, S. B. Choi, J. Kim and O. M. Yaghi, Science, 2010, **329**, 424–429.

92 J. A. Botas, G. Calleja, M. Sánchez-Sánchez and M. G. Orcajo, Langmuir, 2010, **26**, 5300–5303.

93 R. Vaidhyanathan, S. S. Iremonger, G. K. H. Shimizu, P. G. Boyd, S. Alavi and T. K. Woo, Science, 2010, **330**, 650–653.

94 L. Hamon, P. L. Llewellyn, T. Devic, A. Ghoufi, G. Clet, V. Guillerm, G. D. Pirngruber, G. Maurin, C. Serre, G. Driver, W. Van Beek, E. Jolimaître, A. Vimont, M. Daturi and G. Férey, J. Am. Chem. Soc., 2009, **131**, 17490–17499.

95 O. Talu, Adv. Colloid Interface Sci., 1998, **76**–**77**, 227–269.

96 M. Murthi and R. Q. Snurr, Langmuir, 2004, **20**, 2489–2497.

97 Y.-S. Bae, O. K. Farha, J. T. Hupp and R. Q. Snurr, J. Mater. Chem., 2009, **19**, 2131.

98 D. P. Broom, Hydrogen Storage Materials: The Characterisation of Their Storage Properties, Springer-Verlag London, 2011.

99 K. J. Gross and K. R. Carrington, S. Barcelo, A. Karkamkar, J. Purewal, S. Ma, H. Zhau, P. Dantzer, K. Ott, T. Burcel, T. Semeslberger, Y. Pivak, B. Dam, D. Chandra, Adsorpt. J. Int. Adsorpt. Soc., 2010, 1–301.

100 M. Felderhoff, C. Weidenthaler, R. von Helmolt and U. Eberle, Phys. Chem. Chem. Phys., 2007, **9**, 2643-2653.

101 D. Zhao, D. Yuan and H.-C. Zhou, Energy Environ. Sci., 2008, **1**, 222.

102 D. W. Bruce, D. O'Hare and R. I. Walton, Energy Materials, John Wiley & Sons, UK, 2011.

103 B. Xiao, P. S. Wheatley, X. Zhao, A. J. Fletcher, S. Fox, A. G. Rossi, I. L. Megson, S. Bordiga, L. Regli, K. M. Thomas and R. E. Morris, J. Am. Chem. Soc., 2007, **129**, 1203–1209.

104 R. C. Lochan and M. Head-Gordon, Phys. Chem., 2006, **8**, 1357-1370.

105 C. E. Wilmer, M. Leaf, C. Y. Lee, O. K. Farha, B. G. Hauser, J. T. Hupp and R. Q. Snurr, Nat. Chem., 2012, **4**, 83–89.

106 E. Bichoutskaia, M. Suyetin, M. Bound, Y. Yan and M. Schröder, J. Phys. Chem. C, 2014, **118**, 15573–15580.

107 J. B. DeCoste, M. H. Weston, P. E. Fuller, T. M. Tovar, G. W. Peterson, M. D. LeVan and O. K. Farha, Angew. Chemie - Int. Ed., 2014, **53**, 14092–14095.

108 Seminar on Adsorption | MicrotracBEL Corp.Microtrac-bel.com, Access date 10th January 2018.

109 J. Yang, C. Li, Z. Cheng, X. Zhang, Z. Quan, C. Zhang and J. Lin, J. Phys. Chem. C, 2007, **111**, 18148–18154.

110 J. Klafter and M. F. Shlesinger, Proc. Natl. Acad. Sci., 1986, **83**, 848–851.

111 X. Zhao, S. Villar-Rodil, A. J. Fletcher and K. M. Thomas, J. Phys. Chem. B, 2006, **110**, 9947–9955.

112 C. R. Reid and K. M. Thomas, J. Phys. Chem. B, 2001, **105**, 10619–10629.

113 A. J. Fletcher, E. J. Cussen, D. Bradshaw, M. J. Rosseinsky and K. M. Thomas, J. Am. Chem. Soc., 2004, **126**, 9750–9759.

114 S. Lowell, J. E. Shields, M. A. Thomas and M. Thommes, Characterization of Porous Solids and Powders: Surface Area, Pore Size and Density, Springer Science+Business Media New York, USA, 2004.

115 P. Pendleton and A. Badalyan, J. Springer Science + Business Media, Inc., 2005, **11**, 61–66.

116 K. S. W. Sing, D. H. Everett, R. A. W. Haul, L. Moscou, R. A. Pierotti, J. Rouquerol, T. Siemieniewska, Pure Appl. Chem., 1985, **57**, 603–619.

117 A. Badalyan, P. Pendleton and H. Wu, Rev. Sci. Instrum., 2001, **72**, 3038–3045.

118 D. Farrusseng, Metal-Organic Frameworks: Applications from Catalysis to Gas Storage, Wiley-VCH Verlag & Co., Germany, 2011.

119 K. Tan, N. Nijem, Y. Gao, S. Zuluaga, J. Li, T. Thonhauser and Y. J. Chabal, CrystEngComm, 2015, **17**, 247–260.

120 F. Jensen, Introduction to Computational Chemistry, John Wiley & Sons, England, 2nd Edition, 2007.

121 J. C. A. Boeyens and J. F. Ogilvie, Models, Mysteries and Magic of Molecules, Springer, Dordrecht, Netherlands, 2008.

122 D. C. Young, Computational Chemistry: A Practical Guide for Applying Techniques to Real-World Problems, John Wiley and Sons, New York, 2001.

123 F. L. Pilar, Elementary Quantum Chemistry, McGraw-Hill Publishing Company, New York, 2nd Edition, 1990.

124 P. A. M. Dirac, The Principles Of Quantum Mechanics, Oxford University Press, London, 3rd Edition, 1948.

125 G. C. Schatz and M. A. Ratner, Quantum Mechanics In Chemistry, Dover Publications, Inc., New York, 2002.

126 M. Born and R. Oppenheimer, Ann. Phys., 1927, **84**, 457–484.

127 D. M. Burland and G. W. Robinson, Proc. Natl. Acad. Sci, 1970, **66**, 257-264.

128 J. A. Pople and D. L. Beveridge, Approximate Molecular Orbital Theory, McGraw-Hill Book Company, USA, 1970.

129 B. Viswanathan, The Development of Non-Born-Oppenheimer Self-Consistent Field Method and Computational Cluster Studies on the Solvation of Cations and Anions, PhD Thesis, Dalhousie University, 2005.

130 C. E. Dykstra, Ab initio Calculation of the Structures and Properties of Molecules, Elsevier Science Publishers B.V., Amsterdam, 1988.

131 P. Pechukas, Ber. Bunsenges. Phys. Chem., 1982, **86**, 372–378.

132 D. G. Truhlar, B. C. Garrett and S. J. Klippenstein, J. Phys. Chem., 1996, **100**, 12771–12800.

133 R. A. Marcus, J. Chem. Phys., 1986, **85**, 5035–5040.

134 R. A. Marcus, J. Chem. Phys., 1964, **41**, 2614–2623.

135 R. A. Marcus, J. Chem. Phys., 1964, **41**, 2624–2633.

136 R. A. Marcus, J. Chem. Phys., 1965, **43**, 1598–1605.

137 S. J. Klippenstein and R. A. Marcus, J. Chem. Phys., 1990, **93**, 2418–2424.

138 S. J. Klippenstein and R. A. Marcus, J. Chem. Phys., 1989, **91**, 2280–2292.

139 D. M. Wardlaw and R. A. Marcus, Chem. Phys. Lett., 1984, **110**, 230–234.

140 C. Møller and M. S. Plesset, Phys. Rev., 1934, **46**, 618–622.

141 A. H. Nayfeh, Linear and Nonlinear Structural Mechanics: Perturbation Methods,

Wiley-VCH, Weinheim, Federal Republic of Germany, 2nd Edition, 2004.

142 D. R. Hartree, Proc. Cambridge Phil. Soc., 1928, **24**, 89–110.

143 V. Fock, Z. Phys., 1930, **61**, 126-148.

144 J. C. Slater, Phys. Rev., 1930, **35**, 210–211.

145 G. A. Gallup, Valence Bond Methods Theory and applications, Cambridge University Press, USA, 2003.

146 T. Koopmans, Physica, 1933, **1**, 104–113.

147 C. C. J. Roothaan, Revs. Mod. Phys., 1951, **23**, 69–89.

148 C. C. J. Roothaan, Revs. Mod. Phys., 1960, **31**, 179–185.

149 G. G. Hall, Proc. R. Soc. Lond., 1951, **205**, 541-552.

150 J. C. Slater, Phys. Rev., 1929, **34**, 1293–1322.

151 M. W. Schmidt and M. S. Gordon, Annu. Rev. Phys. Chem., 1998, **49**, 233-266.

152 R. J. Bartlett, J. Phys. Chem., 1989, **93**, 1697–1708.

153 W. Koch and M. C. Holthausen, A Chemist's Guide to Density Functional Theory, Wiley-VCH Verlag, Germany, 2nd Edition, 2001.

154 J. C. Slater, Phys. Rev., 1951, **81**, 385–390.

155 E. Wigner and F. Seitz, Phys. Rev., 1933, **43**, 804–810.

156 E. Wigner and F. Seitz, Phys. Rev., 1934, **46**, 509–524.

157 P. Hohenberg and W. Kohn, Phys. Rev., 1964, **136**, B 864-B 871.

158 B. B. Laird, R. B. Ross and T. Ziegler, Am. Chem. Soc, 1996, 1–19.

159 W. Kohn and I. J. Sham, Phys. Rev., 1965, **140**, 1133-1138.

160 E. J. Baerends, O. V Gritsenko and R. van Leeuwen, Am. Chem. Soc., 1995, **629**, 20–41.

161 A. Szabo and N. S. Ostlund, Modern Quantum Chemisrty: Introduction to Advanced Electronic Structure Theory, Macmillan Publishing Co., Inc., New York,

1982.

162 J. A. Pople and R. K. Nesbet, J. Chem. Phys., 1954, **22**, 571–572.

163 F. Weinhold and C. R. Landis, Chem. Educ. Res. Pr., 2001, **2**, 91–104.

164 A. E. Reed and F. Weinhold, J. Chem. Phys., 1983, **78**, 4066–4073.

165 A. E. Reed and F. Weinhold, Isr. J. Chem., 1991, **31**, 277–285.

166 J. K. Badenhoop and F. Weinhold, J. Chem. Phys., 1997, **107**, 5406–5421.

167 D. Sajan, L. Joseph, N. Vijayan and M. Karabacak, Elsevier B.V., 2011, **81**, 85–98.

168 B. D. Dunnington and J. R. Schmidt, J. Chem. Theory Comput., 2012, **8**, 1902–1911.

169 P. St. Petkov, G. N. Vayssilov, J. Liu, O. Shekhah, Y. Wang, C. Wöll and T. Heine, ChemPhysChem, 2012, **13**, 2025–2029.

170 H. Furukawa, K. E. Cordova, M. O. Keeffe and O. M. Yaghi, Science, 2013, **341**, 1230444 (1)- (12).

171 J. L. C. Rowsell and O. M. Yaghi, Microporous Mesoporous Mater., 2004, 73, 3–14.

172 S. R. Batten, N. R. Champness, X.-M. Chen, J. Garcia-Martinez, S. Kitagawa, L. Öhrström, M. O'Keeffe, M. Paik Suh and J. Reedijk, Pure Appl. Chem., 2013, 85, 1715–1724.

173 M. Eddaoudi, J. Kim, D. Vodak, A. Sudik, J. Wachter, M. O'Keeffe and O. M. Yaghi, PNAS, 2002, **99**, 4900–4904.

174 H. M. Chase, B. Rudshteyn, B. T. Psciuk, M. A. Upshur, B. F. Strick, R. J. Thomson, V. S. Batista and F. M. Geiger, J. Phys. Chem. B, 2016, **120**, 1919–1927.

175 Y. H. Kim, J. Kang and S. H. Wei, Phys. Rev. Lett., 2010, **105**, 1–4.

176 K. A. H. Alzahrani and R. J. Deeth, J. Mol. Model, 2016, **80**, 1-13.

177 F. X. Coudert and A. H. Fuchs, Coord. Chem. Rev., 2015, **307**, 211–236.

178 M. E. Braun, C. D. Steffek, J. Kim, P. G. Rasmussen and O. M. Yaghi, Chem. Commun., 2001, **2**, 2532–2533.

179 J. T. Hughes and A. Navrotsky, J. Am. Chem. Soc., 2011, **133**, 9184–9187.

180 J. D. Howe, Y. Liu, L. Flores, D. A. Dixon and D. S. Sholl, J. Chem. Theory Comput., 2017, **13**, 1341–1350.

181 A. D. Becke, J. Chem. Phys., 1993, **98**, 5648–5652.

182 K. Raghavachari and G. W. Trucks, J. Chem. Phys., 1989, **91**, 1062–1065.

183 J.-P. Blaudeau and M. P. McGrath, J. Chem. Phys., 1997, **107**, 5016-5021.

184 D. Andrae, U. Haussermann, M. Dolg, H. Stoll, H. Preuss, Theor. Chim. Acta 1990, **77**, 123-141.

185 M. J. Frisch, G. W. Trucks, H. B. Schlegel, G. E. Scuseria, M. A. Robb, J. R. Cheeseman, G. Scalmani, V. Barone, B. Mennucci, G. A. Petersson, H. Nakatsuji, M. Caricato, X. Li, H. P. Hratchian, A. F. Izmaylov, J. Bloino, G. Zheng, J. L. Sonnenberg, M. Hada, M. Ehara, K. Toyota, R. Fukuda, J. Hasegawa, M. Ishida, T. Nakajima, Y. Honda, O. Kitao, H. Nakai, T. Vreven, J. A. Montgomery, Jr., J. E. Peralta, F. Ogliaro, M. Bearpark, J. J. Heyd, E. Brothers, K. N. Kudin, V. N. Staroverov, R. Kobayashi, J. Normand, K. Raghavachari, A. Rendell, J. C. Burant, S. S. Iyengar, J. Tomasi, M. Cossi, N. Rega, J. M. Millam, M. Klene, J. E. Knox, J. B. Cross, V. Bakken, C. Adamo, J. Jaramillo, R. Gomperts, R. E. Stratmann, O. Yazyev, A. J. Austin, R. Cammi, C. Pomelli, J. W. Ochterski, R. L. Martin, K. Morokuma, V. G. Zakrzewski, G. A. Voth, P. Salvador, J. J. Dannenberg, S. Dapprich, A. D. Daniels, Ö. Farkas, J. B. Foresman, J. V. Ortiz, J. Cioslowski, and D. J. Fox, Gaussian 09 (Gaussian, Inc., Wallingford CT, 2009).

186 V. V Butova, M. A. Soldatov, A. A. Guda, K. A. Lomachenko and C. Lamberti,

Russ. Chem. Rev., 2016, **85**, 280–307.

187 G. González Miera, A. Bermejo Gómez, P. J. Chupas, B. Martín-Matute, K. W. Chapman and A. E. Platero-Prats, Inorg. Chem., 2017, **56**, 4576–4583.

188 O. M. Yaghi, M. O'Keeffe, N. W. Ockwig, H. K. Chae, M. Eddaoudi and J. Kim, Nature, 2003, **423**, 705–714.

189 J. J. Perry IV, J. A. Perman and M. J. Zaworotko, Chem. Soc. Rev., 2009, **38**, 1400-1417.

190 D. J. Tranchemontagne, J. L. Mendoza-Cortés, M. O'Keeffe and O. M. Yaghi, Chem. Soc. Rev., 2009, **38**, 1257–1283.

191 A. Otero, J. Fernández-Baeza, A. Antiñolo, J. Tejeda, A. Lara-Sánchez, L. Sánchez-Barba, M. Fernández-López and I. López-Solera, Inorg. Chem., 2004, **43**, 1350–1358.

192 S. Gross, J. Mater. Chem., 2011, **21**, 15853–15861.

193 G. Kickelbick, D. Holzinger, C. Brick, G. Trimmel and E. Moons, Chem. Mater., 2002, **14**, 4382–4389.

194 S. O. Baumann, M. Puchberger and U. Schubert, Dalton. Trans., 2011, **40**, 1401–1406.

195 D. Feng, H.-L. Jiang, Y.-P. Chen, Z.-Y. Gu, Z. Wei and H.-C. Zhou, Inorg. Chem., 2013, **52**, 12661–12667.

196 V. Bon, I. Senkovska, I. A. Baburin and S. Kaskel, Cryst. Growth Des., 2013, **13**, 1231–1237.

197 D. Feng, K. Wang, J. Su, T. F. Liu, J. Park, Z. Wei, M. Bosch, A. Yakovenko, X. Zou and H. C. Zhou, Angew. Chem - Int. Ed., 2015, **54**, 149–154.

198 D. Feng, W. C. Chung, Z. Wei, Z. Y. Gu, H. L. Jiang, Y. P. Chen, D. J. Darensbourg and H. C. Zhou, J. Am. Chem. Soc., 2013, **135**, 17105–17110.

199 D. Feng, Z. Y. Gu, J. R. Li, H. L. Jiang, Z. Wei and H. C. Zhou, Angew. Chem - Int. Ed., 2012, **51**, 10307–10310.

200 D. Feng, Z. Y. Gu, Y. P. Chen, J. Park, Z. Wei, Y. Sun, M. Bosch, S. Yuan and H. C. Zhou, J. Am. Chem. Soc., 2014, **136**, 17714–17717.

201 H. L. Jiang, D. Feng, K. Wang, Z. Y. Gu, Z. Wei, Y. P. Chen and H. C. Zhou, J. Am. Chem. Soc., 2013, **135**, 13934–13938.

202 M. Ganesh, P. Hemalatha, M. M. Peng, W. S. Cha and H. T. Jang, Aerosol Air Qual. Res., 2014, **14**, 1605–1612.

203 Y. R. Lee, J. Kim and W. S. Ahn, Korean J. Chem. Eng., 2013, **30**, 1667–1680.

204 M. Bosch, M. Zhang and H.-C. Zhou, Adv. Chem., 2014, 1–8.

205 M. L. Kelty, W. Morris, A. T. Gallagher, J. S. Anderson, K. A. Brown, C. A. Mirkin and T. D. Harris, Chem. Commun., 2016, **52**, 7854–7857.

206 H. Reinsch, B. Bueken, F. Vermoortele, I. Stassen, A. Lieb, K. P. Lillerud and D. De Vos, CrystEngComm, 2015, **17**, 4070–4074.

207 P. Á. Szilágyi, P. Serra-Crespo, J. Gascon, H. Geerlings and B. Dam, Front. Energy Res., 2016, **4**, 2012–2017.

208 S. J. Lee, C. Doussot, A. Baux, L. Liu, G. B. Jameson, C. Richardson, J. J. Pak, F. Trousselet, F. X. Coudert and S. G. Telfer, Chem. Mater., 2016, **28**, 368–375.

209 L. Sarkisov, Dalton. Trans., 2016, **45**, 4203–4212.

210 C. Zhang, C. Han, D. S. Sholl and J. R. Schmidt, J. Phys. Chem. Lett., 2016, **7**, 459–464.

211 M. Vandichel, J. Hajek, A. Ghysels, A. De Vos, M. Waroquier and V. Van Speybroeck, CrystEngComm, 2016, **18**, 7056–7069.

212 K. D. Vogiatzis, E. Haldoupis, D. J. Xiao, J. R. Long, J. I. Siepmann and L. Gagliardi, J. Phys. Chem. C, 2016, **120**, 18707–18712.

213 Hu, S. Faucher, Y. Zhuo, Y. Sun, S. Wang and D. Zhao, J. Chem. Eur., 2015, **21**, 17246–17255.

214 H. Wu, Y. S. Chua, V. Krungleviciute, M. Tyagi, P. Chen, T. Yildirim and W. Zhou, J. Am. Chem. Soc., 2013, **135**, 10525–10532.

215 V. Gutov, M. G. Hevia, E. C. Escudero-Adán and A. Shafir, Inorg. Chem., 2015, **54**, 8396–8400.

216 B. Li, X. Zhu, K. Hu, Y. Li, J. Feng, J. Shi and J. Gu, J. Hazard. Mater., 2016, **302**, 57–64.

217 H. Wu, T. Yildirim and W. Zhou, J. Phys. Chem. Lett., 2013, **4**, 925–930.

218 B. Van De Voorde, I. Stassen, B. Bueken, F. Vermoortele, D. De Vos, R. Ameloot, J. C. Tan and T. D. Bennett, J. Mater. Chem. A, 2015, **3**, 1737–1742.

219 O. V. Gutov, M. G. Hevia, E. C. Escudero-Adán and A. Shafir, Inorg. Chem., 2015, **54**, 8396–8400.

220 S. Øien, D. Wragg, H. Reinsch, S. Svelle, S. Bordiga, C. Lamberti and K. P. Lillerud, Cryst. Growth Des., 2014, **14**, 5370–5372.

221 M. Vandichel, J. Hajek, F. Vermoortele, M. Waroquier, D. E. De Vos and V. Van Speybroeck, CrystEngComm, 2015, **17**, 395–406.

222 W. Liang, C. J. Coghlan, F. Ragon, M. Rubio-Martinez, D. M. D'Alessandro and R. Babarao, Dalton. Trans., 2016, **45**, 4496–4500.

223 A. W. Thornton, R. Babarao, A. Jain, F. Trousselet and F. X. Coudert, Dalton. Trans., 2016, **45**, 4352–4359.

224 P. Ghosh, Y. J. Colón and R. Q. Snurr, Chem. Commun., 2014, **50**, 11329–11331.

225 S. Dissegna, R. Hardian, K. Epp, G. Kieslich, M. V. Coulet, P. Llewellyn and R. A. Fischer, CrystEngComm, 2017, **19**, 4137–4141.

226 L. M. Geever, D. M. Devine, M. J. D. Nugent, J. E. Kennedy, J. G. Lyons, A. Hanley and C. L. Higginbotham, Eur. Polym. J., 2006, **42**, 2540–2548.

227 Q. Chai, Y. Jiao and X. Yu, Gels, 2017, **3**, 6, 1-15.

228 The Cambridge Structural Database, C. R. Groom, I. J. Bruno, M. P. Lightfoot and S. C. Ward, Acta Cryst. (2016). B72, 171-179

229 S. Grimme, J. Antony, S. Ehrlich and H. Krieg, J. Chem. Phys., 2010,**132**, 154104.

230 A. Austin, G. Petersson, M. Frisch, F. Dobek, G. Scalmani and K. Throssell, J. Chem. Theory Comput., 2012, **8**, 4989-5007.

231 S. Grimme, J. Comput. Chem, 2006, **27**, 1787-1799.

232 Y. Zhao and D. Truhlar, Theor. Chem. Acc., 2007, **120**, 215-241.

233 J. Chai and M. Head-Gordon, Phys. Chem. Chem. Phys, 2008, **10**, 6615-6620.

234 K. S. Thanthiriwatte, E. G. Hohenstein, L. A. Burns and C. D. Sherrill, J. Chem. Theory Comput., 2011, **7**, 88–96.

235 A. D. Buckingham, D. A. Dunmur and R. L. Disch, J. Am. Chem. Soc., 1968, **90**, 3104–3107

236 Gouzman, M. Dubey, M. D. Carolus, J. Schwartz and S. L. Bernasek, Surf. Sci., 2006, **600**, 773–781.

237 K. C. Popat, E. E. L. Swan and T. A. Desai, Langmuir, 2005, **21**, 7061–7065.

238 M. Giesbers, A. T. M. Marcelis and H. Zuilhof, Langmuir, 2013, **29**, 4782–4788.

239 Z. Kang, S. Wang, L. Fan, M. Zhang, W. Kang, J. Pang, X. Du, H. Guo, R. Wang and D. Sun, Commun. Chem., 2018, 1-8.

240 K. Kim, Y. Zhang, P. B. Kreider, X. Chong, A. X. Wang, P. R. Ohodnicki and J. P. Baltrus, Thin Solid Films, 2018, **659**, 24-35.

241 S. Tardio and P. J. Cumpson, Surface and Interface Analysis, 2018, **50**, 5–12.

242 R. Smith, PhD Thesis, Investigating the Growth, Flexibility and Catalytic Activity of Metal-Organic Frameworks, University of Sheffield, 2017.

243 W. Gao and L. Reven, Langmuir, 1995, **11**, 1860–1863.

244 J. T. Woodward, A. Ulman and D. K. Schwartz, Langmuir, 1996, **12**, 3626–3629.

245 E. S. Gawalt, G. Lu, S. L. Bernasek and J. Schwartz, Langmuir, 1999, **15**, 8929–8933.

246 E. L. Hanson, J. Schwartz, B. Nickel, N. Koch and M. F. Danisman, J. Am. Chem. Soc., 2003, **125**, 16074–16080.

247 E. D. Glendening, A. E. Reed, J. E. Carpenter, and F. Weinhold, NBO version 3.1, (TCI, University of Wisconsin, Madison), 1998.

248 I. Alkorta and J. Elguero, Magn. Reson. Chem., 2004, **42**, 955–961.

249 N. Grimblat and A. M. Sarotti, Chem. Eur. J., 2016, **22**, 12246–12261.

250 E. Pankratyev, A. Tulyabaev and L. Khalilov, J. Comput. Chem., 2011, **32**, 1993-1997.

251 A. M. Sarotti and S. C. Pellegrinet, J. Org. Chem., 2009, **74**, 7254–7260.

252 K. K. Baldridge and J. S. Siegel, J. Phys. Chem. A, 1999, **103**, 4038–4042.

253 H. Lampert, W. Mikenda, A. Karpfen and H. Kählig, J. Phys. Chem. A, 1997, **101**, 9610–9617.

254 M. Bühl and T. van Mourik, Wiley Interdiscip. Rev. Comput. Mol. Sci., 2011, **1**, 634–647.

255 E. W. Della, I. J. Lochert, J. E. Peralta, R. H. Contreras, Magn. Reson. Chem., 2000, **38**, 395–402.

256 K. S. Novoselov, A. K. Geim, S. V. Morozov, S. V. Dubonos, Y. Zhang and D. Jiang, Nature, 2005, **72**, 201401.

257 V. Nicolosi, M. Chhowalla, M. G. Kanatzidis, M. S. Strano and J. N. Coleman, Science , 2013, **340**, 1226419.

258 J. C. Tan, P. J. Saines, E. G. Bithell and A. K. Cheetham, ACS Nano, 2012, **6**, 615–621.

259 Y. Li and R. Yang, AIChE J., 2007, 54, 269-279.

260 Y. Li and W. Yang, Chinese J. Catal., 2015, **36**, 692–697.

261 Z. Zheng, R. Grünker and X. Feng, Adv. Mater., 2016, **28**, 6529–6545.

262 H. Zhang, ACS Nano, 2015, **9**, 9451–9469.

263 Y. Ding, Y. P. Chen, X. Zhang, L. Chen, Z. Dong, H. L. Jiang, H. Xu and H. C. Zhou, J. Am. Chem. Soc., 2017, **139**, 9136–9139.

264 S. Hillier, E. M. M. Marwa and C. M. Rice, Clay Miner., 2013, **48**, 563–582.

265 M. Valaškova and G. S. Martynkova, Clay Minerals in Nature - Their Characterization, Modification and Application, InTech, Croatia, 2012.

266 L. Li, C. Nan, J. Lu, Q. Peng and Y. Li, Chem. Commun., 2012, **48**, 6945.

267 A. Gallego, C. Hermosa, O. Castillo, I. Berlanga, C. J. Gõmez-García, E. Mateo-Martí, J. I. Martínez, F. Flores, C. Gõmez-Navarro, J. Gõmez-Herrero, S. Delgado and F. Zamora, Adv. Mater., 2013, **25**, 2141–2146.

268 J. N. Coleman, M. Lotya, A. O. ' Neill, S. D. Bergin, P. J. King, U. Khan, K. Young, A. Gaucher, S. De, R. J. Smith, I. V Shvets, S. K. Arora, G. Stanton, H.-Y. Kim, K. Lee, G. T. Kim, G. S. Duesberg, T. Hallam, J. J. Boland, J. J. Wang, J. F. Donegan, J. C. Grunlan, G. Moriarty, A. Shmeliov, R. J. Nicholls, J. M. Perkins, E. M. Grieveson, K. Theuwissen, D. W. Mccomb, P. D. Nellist and V. Nicolosi, Science, 2011, **331**, 568–571.

269 K. He, Z. Cao, R. Liu, Y. Miao, H. Ma and Y. Ding, Nano Res., 2016, **9**, 1856–1865.

270 J. A. Foster, S. Henke, A. Schneemann, R. A. Fischer and A. K. Cheetham, Chem. Commun., 2016, **52**, 10474–10477.

271 S. Henke, R. Schmid, J. D. Grunwaldt and R. A. Fischer, Chem. Eur. J., 2010, **16**, 14296–14306.

272 J. R. Loader, PhD Thesis, Computational Studies & Assisted Structural Characterisation of Metal-Organic Frameworks University of Sheffield, 2013.

273 P. Smart, C. A. Mason, J. R. Loader, A. J. H. M. Meijer, A. J. Florence, K. Shankland, A. J. Fletcher, S. P. Thompson, M. Brunelli, A. H. Hill and L. Brammer, Chem. - A Eur. J., 2013, 19, 3552–3557.

274 John W. Eaton, David Bateman, Søren Hauberg, Rik Wehbring (2016). GNU Octave version 4.2.0 manual: a high-level interactive language for numerical computations. URL http://www.octave.org.

Appendix

Chapter 3

We also performed some calculations on the OH defect, loss of OH, in which the coordination site normally occupied by the oxygen atom of a hydroxyl group is vacant. This defect is characterized by spin changes relatives to the other three defect sites, see figures below

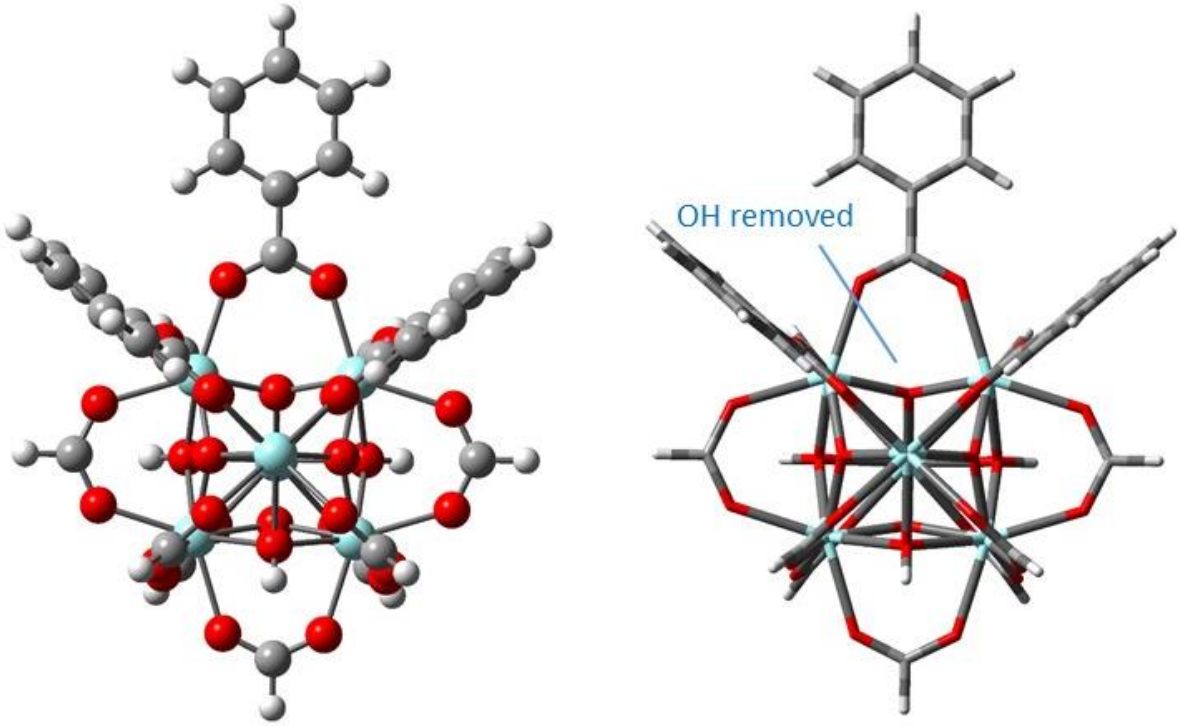

Figure A 3-1: Structure of $[Zr_6(\mu_3\text{-}O)_4(\mu_3\text{-}OH)_3(O_2CH)_9(O_2CPh)_3]$ with OH Defect, (left: ball), (right: stick), where OH is removed from an OH-site.

Table A 3-1: Computed Binding Energies for CO_2, CH_4, N_2 and H_2 using B3LYP//6-311G(d, p)+ SDD(Zr) in kJ/mol. (R is the unsubstituted benzoate ligand).

Linker	OH Defect							
	E CO_2		E CH_4		E N_2		E H_2	
	DFT	DFT-D	DFT	DFT-D	DFT	DFT-D	DFT	DFT-D
3R	-6.9	-40.5	-0.06	-26.2	-5	-28.4	-0.33	-11.1
2R+R-NH_2	-10.3	-45.6	-0.69	-28.4	-5.6	-29.3	-0.62	-11.3
R+2R-NH_2	-12.2	-52.6	-3.6	-36.3	-8.2	-38.8	-3.2	-21.4
R+2R-NH_2(iso)	-9.48	-44.7	-2.29	-29.5	-5	-38.9	-0.08	-12
3R-NH_2	-9.4	-40.2	-0.9	-27.8	-5.5	-24.3	-2	-12.7
2R+R-CH_2NH_2	-9.8	-45.4	-0.68	-28.9	-5.1	-31.3	-0.47	-12.8
2R+R-CH_2OH	-9.3	-44.3	-0.2	-29.1	-5.1	-31.5	-0.33	-12.5
2R+RCH_2CONH_2	-8.7	-42	-3.2	-35.6	-2.3	-34.9	-0.72	-18.5

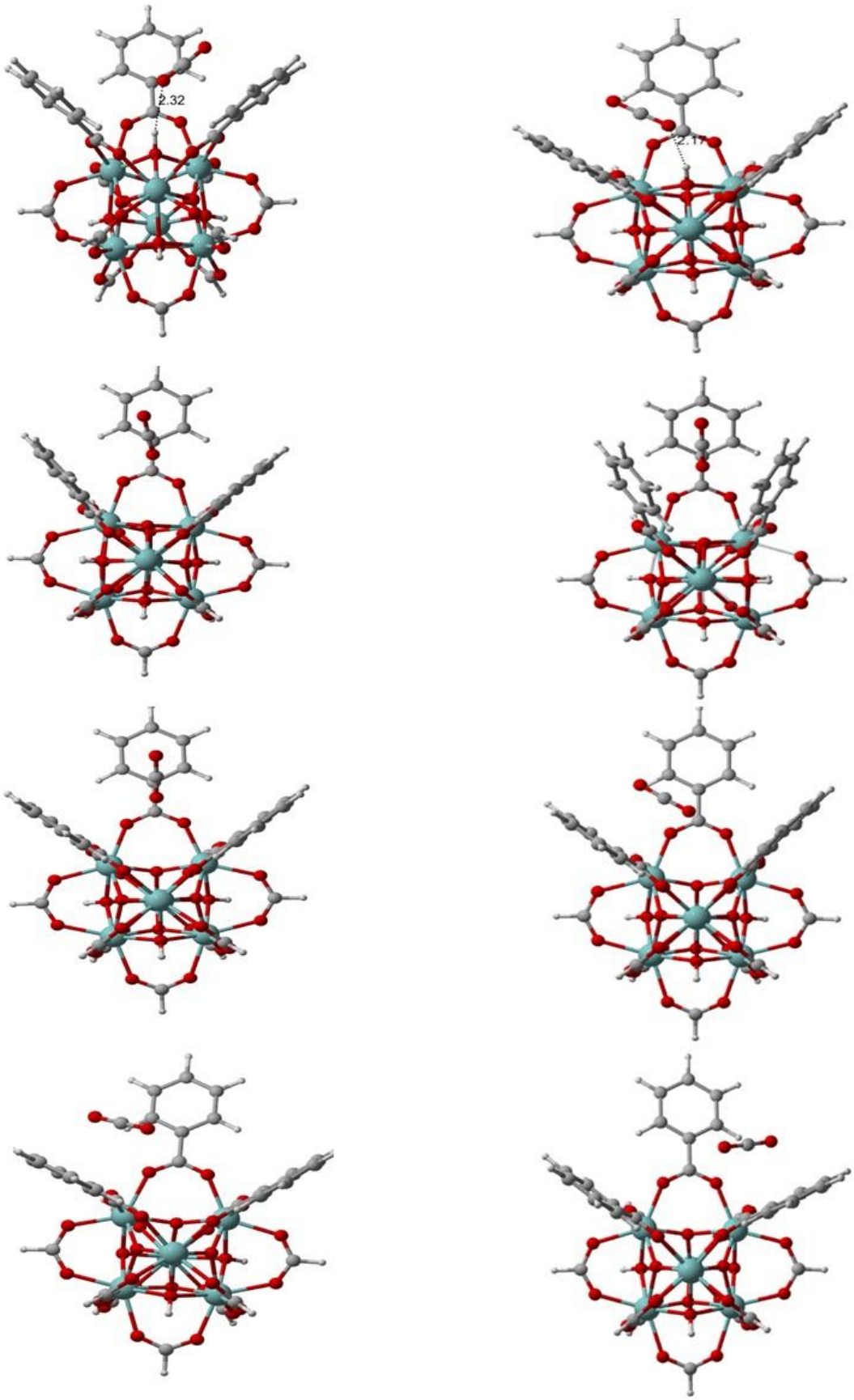

A 3-1-1: DFT(left) and DFT-D(right) Minimum Energy Structure for Adsorbed **CO_2** in 'No Defect, O, OH, H_2O Defects' (top to bottom) Configuration with **Unsubstituted**.

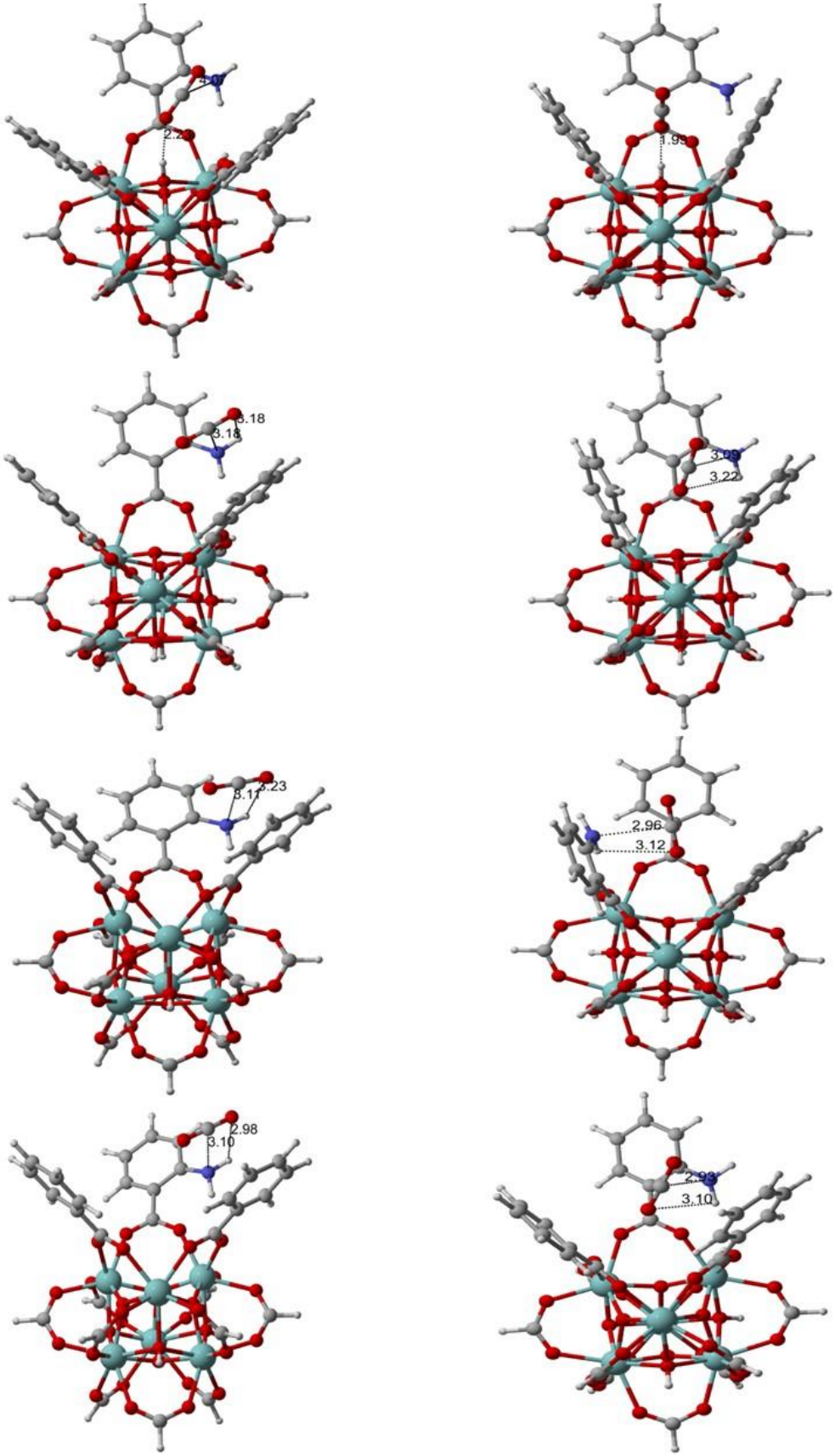

A 3-1-2: DFT(left) and DFT-D(right) Minimum Energy Structure for Adsorbed **CO_2** in 'No Defect, O, OH, H_2O Defects' (top to bottom) Configuration with **NH_2** Substituent.

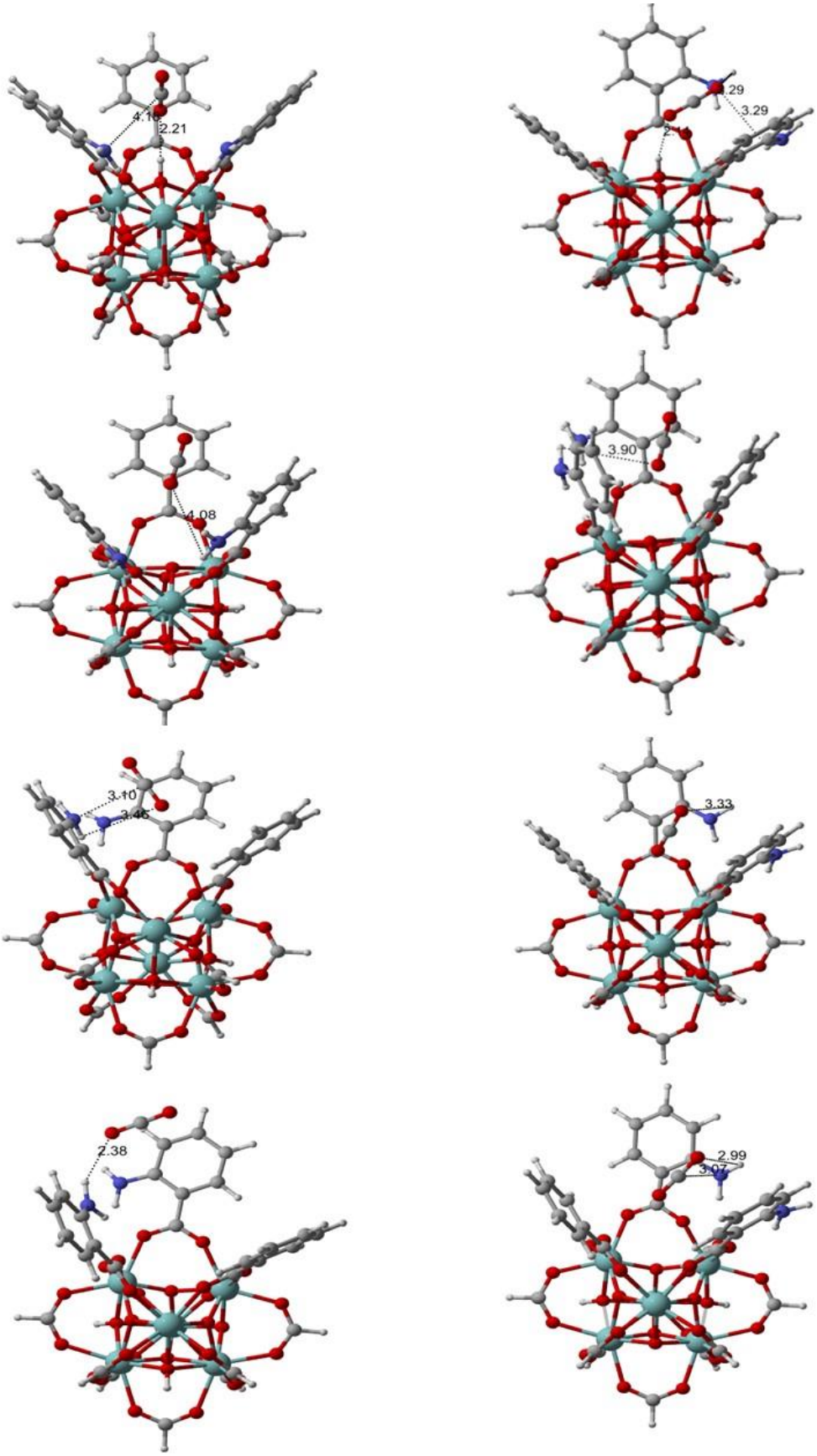

A 3-1-3: DFT(left) and DFT-D(right) Minimum Energy Structure for Adsorbed **CO_2** in 'No Defect, O, OH, H_2O Defects' (top to bottom) Configuration with **$2NH_2$** Substituent.

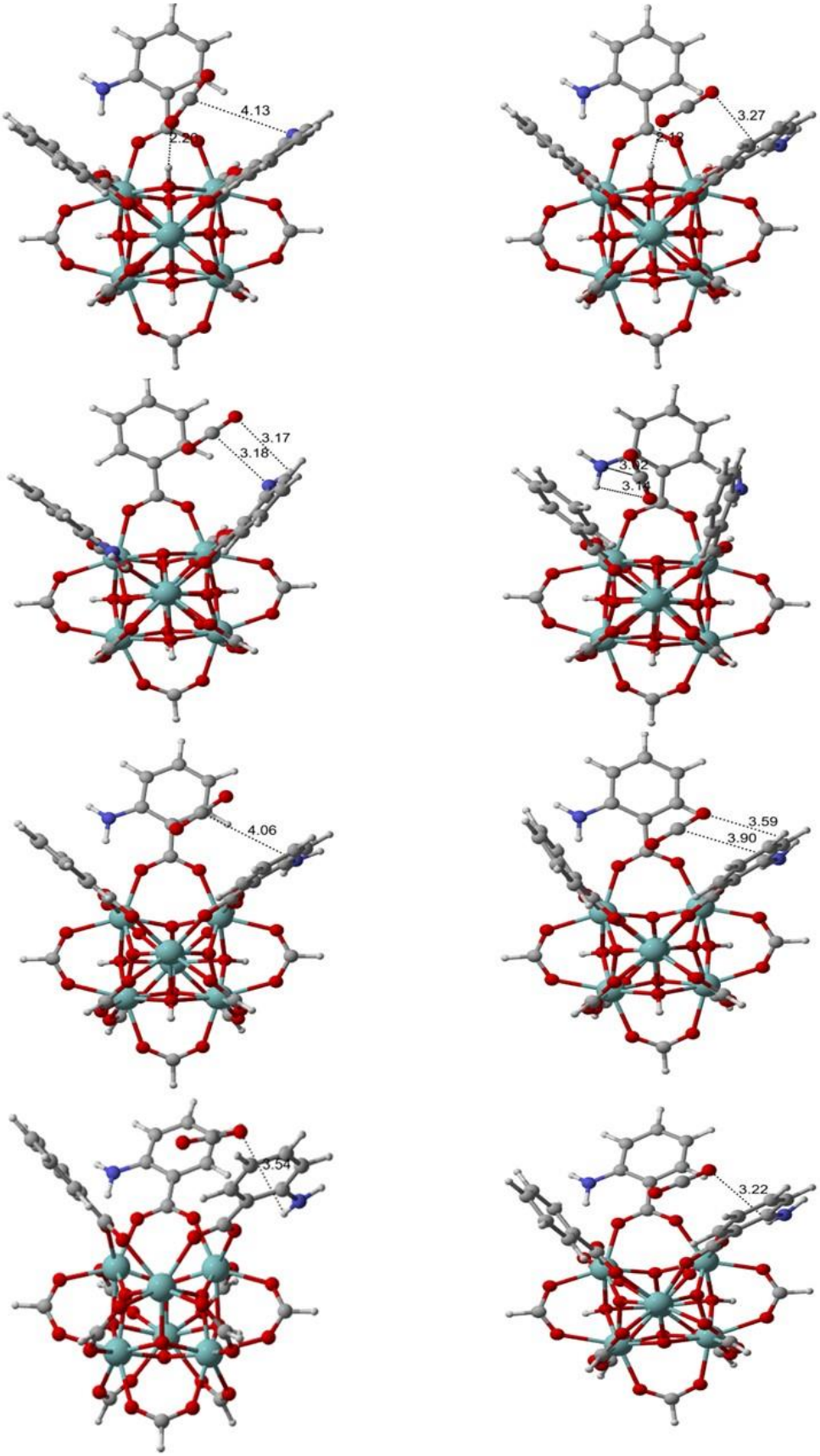

A 3-1-4: DFT(left) and DFT-D(right) Minimum Energy Structure for Adsorbed **CO_2** in 'No Defect, O, OH, H_2O Defects' (top to bottom) Configuration with **$2NH_2$-iso** Substituent.

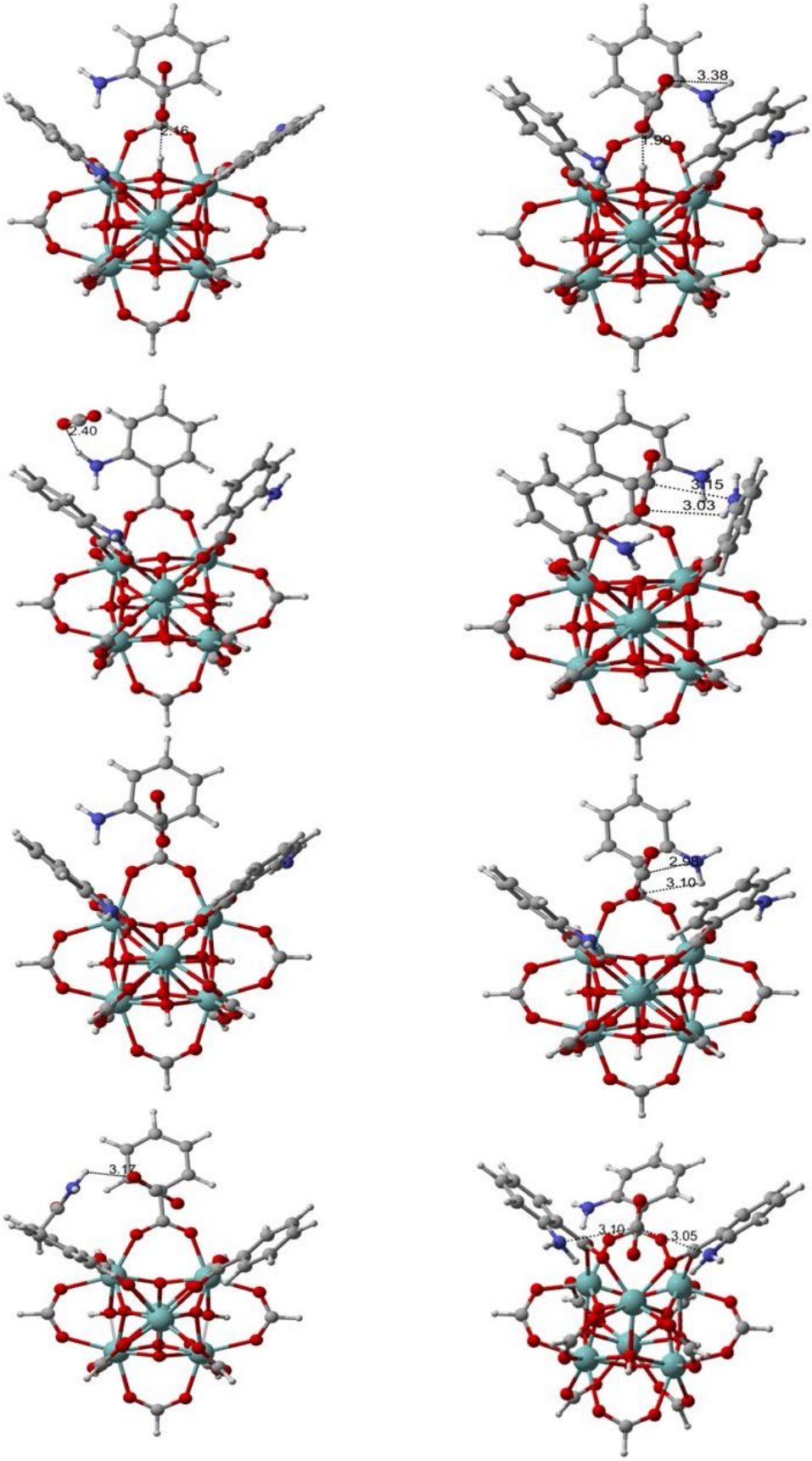

A 3-1-5: DFT(left) and DFT-D(right) Minimum Energy Structure for Adsorbed $\mathbf{CO_2}$ in 'No Defect, O, OH, H_2O Defects' (top to bottom) Configuration with $\mathbf{3NH_2}$ Substituent.

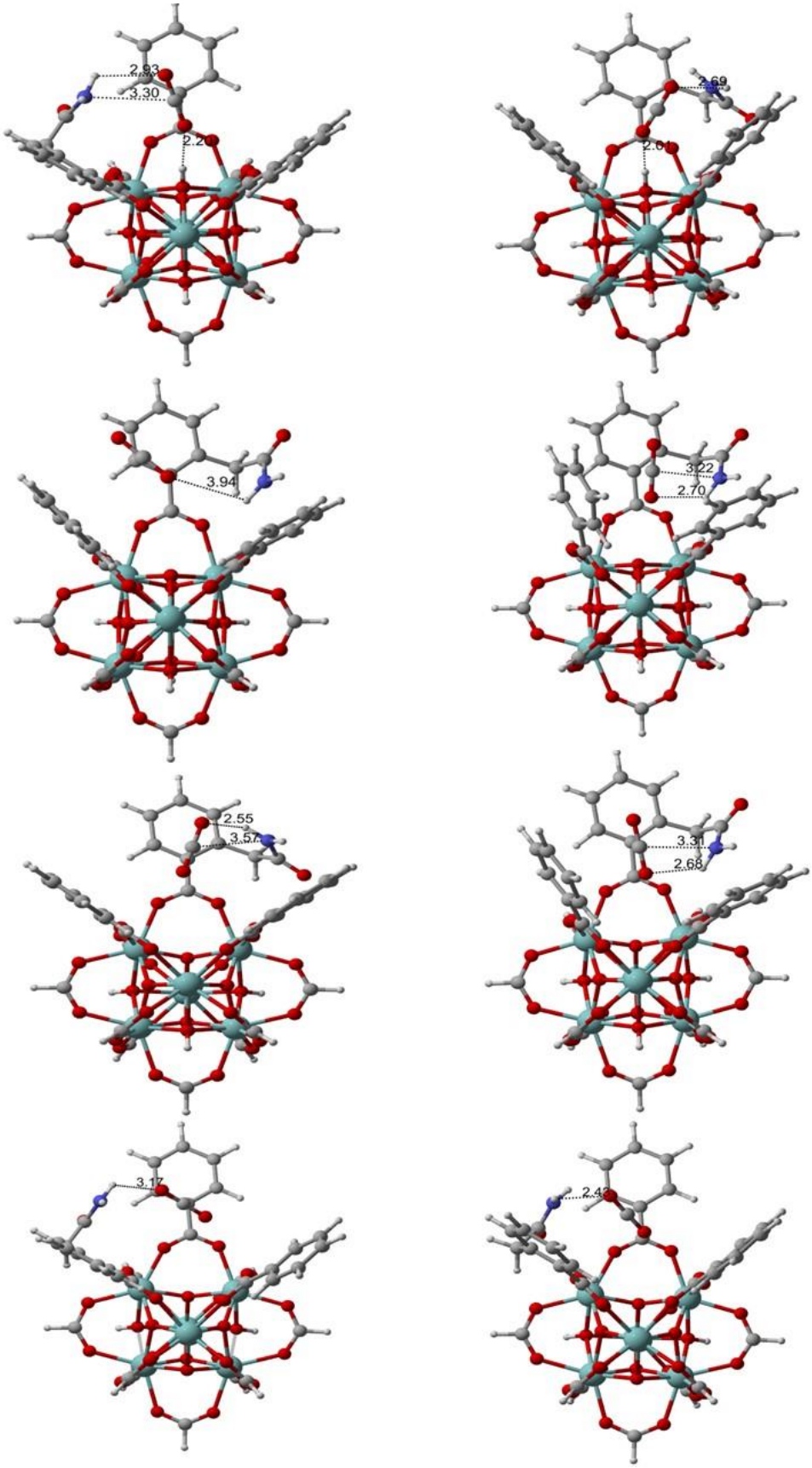

A 3-1-6: DFT(left) and DFT-D(right) Minimum Energy Structure for Adsorbed **CO_2** in 'No Defect, O, OH, H_2O Defects' (top to bottom) Configuration with **CH_2CONH_2** Substituent.

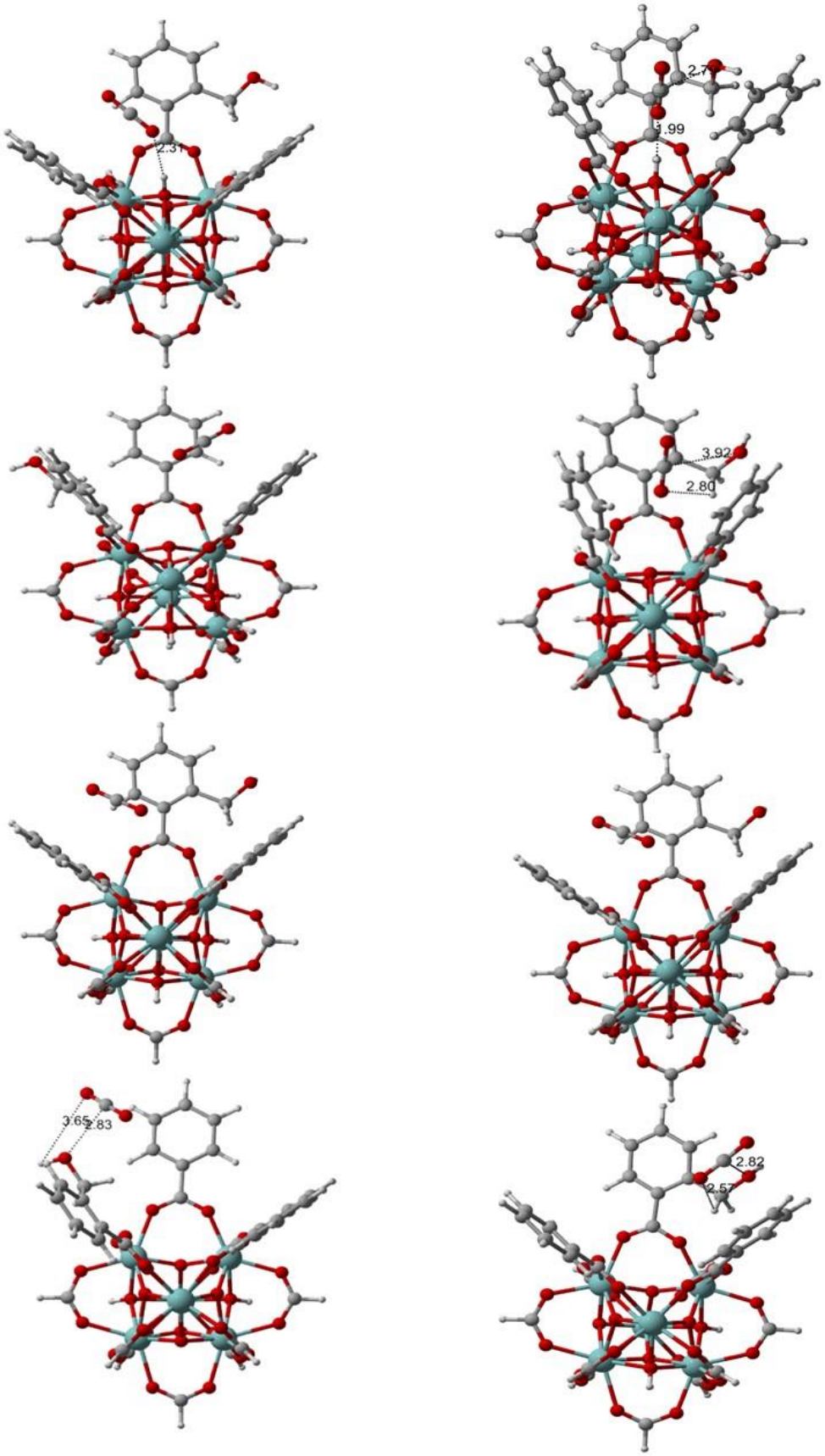

A 3-1-7: DFT(left) and DFT-D(right) Minimum Energy Structure for Adsorbed **CO_2** in 'No Defect, O, OH, H_2O Defects' (top to bottom) Configuration with **CH_2OH** Substituent.

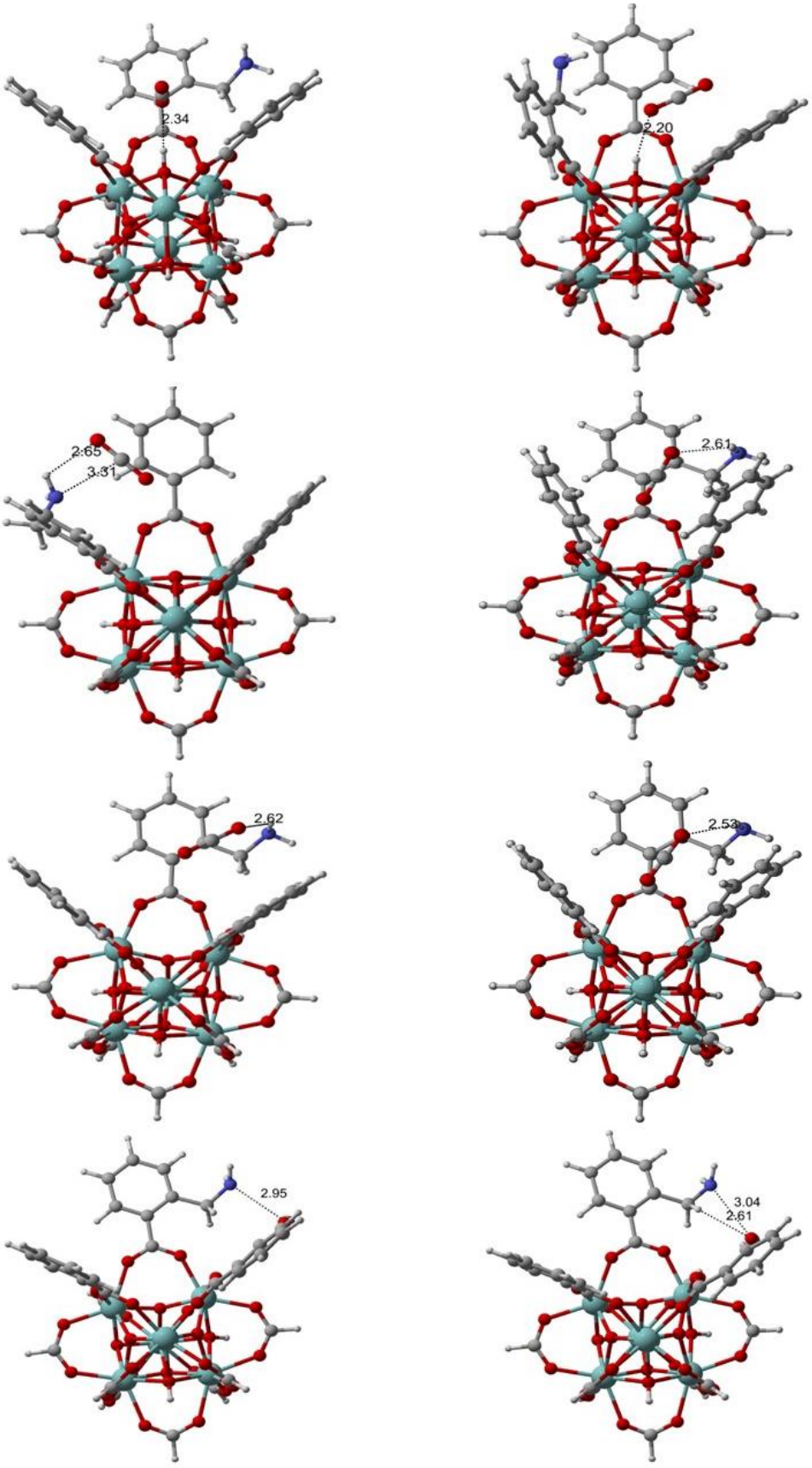

A 3-1-8: DFT(left) and DFT-D(right) Minimum Energy Structure for Adsorbed $\mathbf{CO_2}$ in 'No Defect, O, OH, H_2O Defects' (top to bottom) Configuration with $\mathbf{CH_2NH_2}$ Substituent.

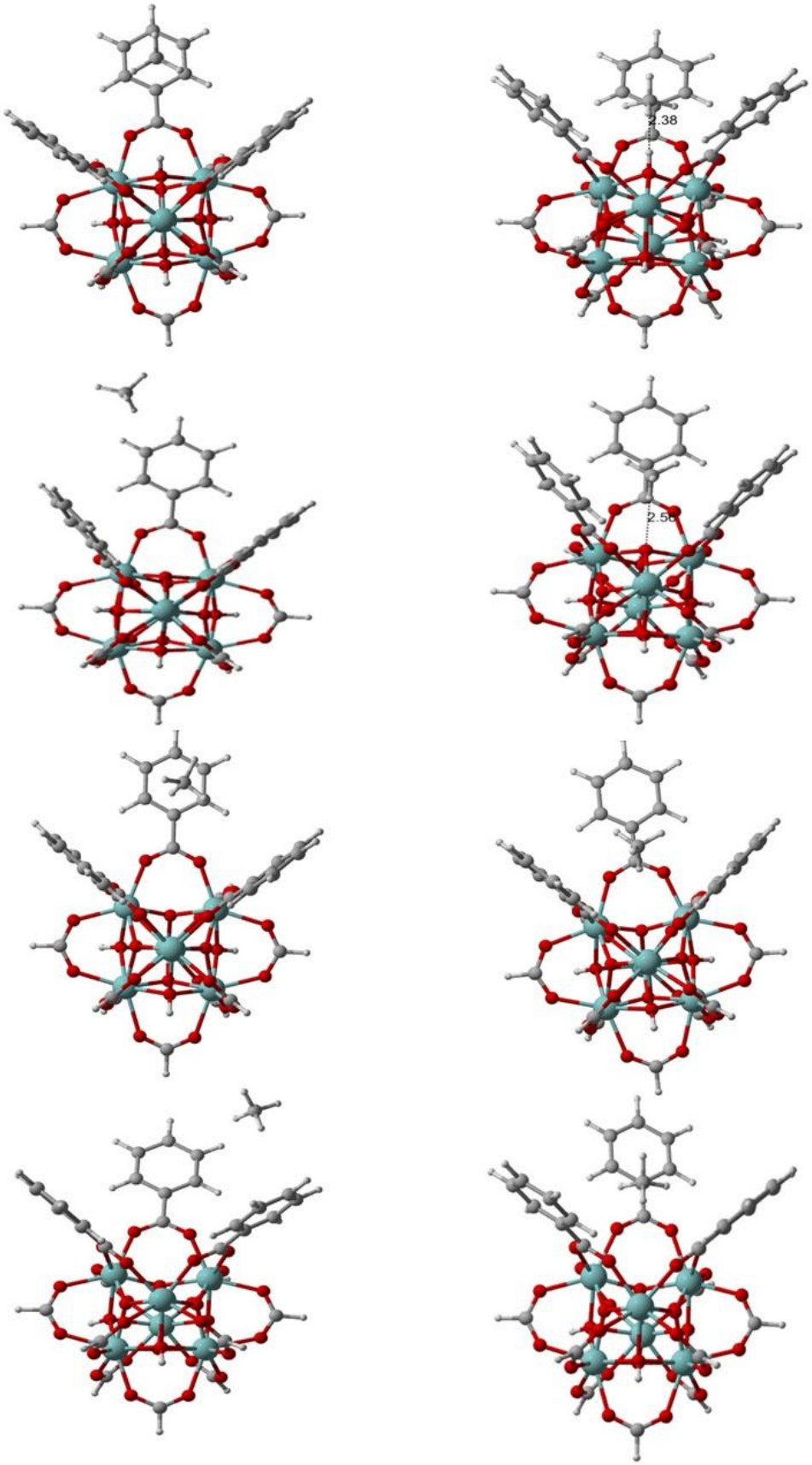

A 3-2-1: DFT(left) and DFT-D(right) Minimum Energy Structure for Adsorbed **CH_4** in 'No Defect, O, OH, H_2O Defects' (top to bottom) Configuration with **Unsubstituted**.

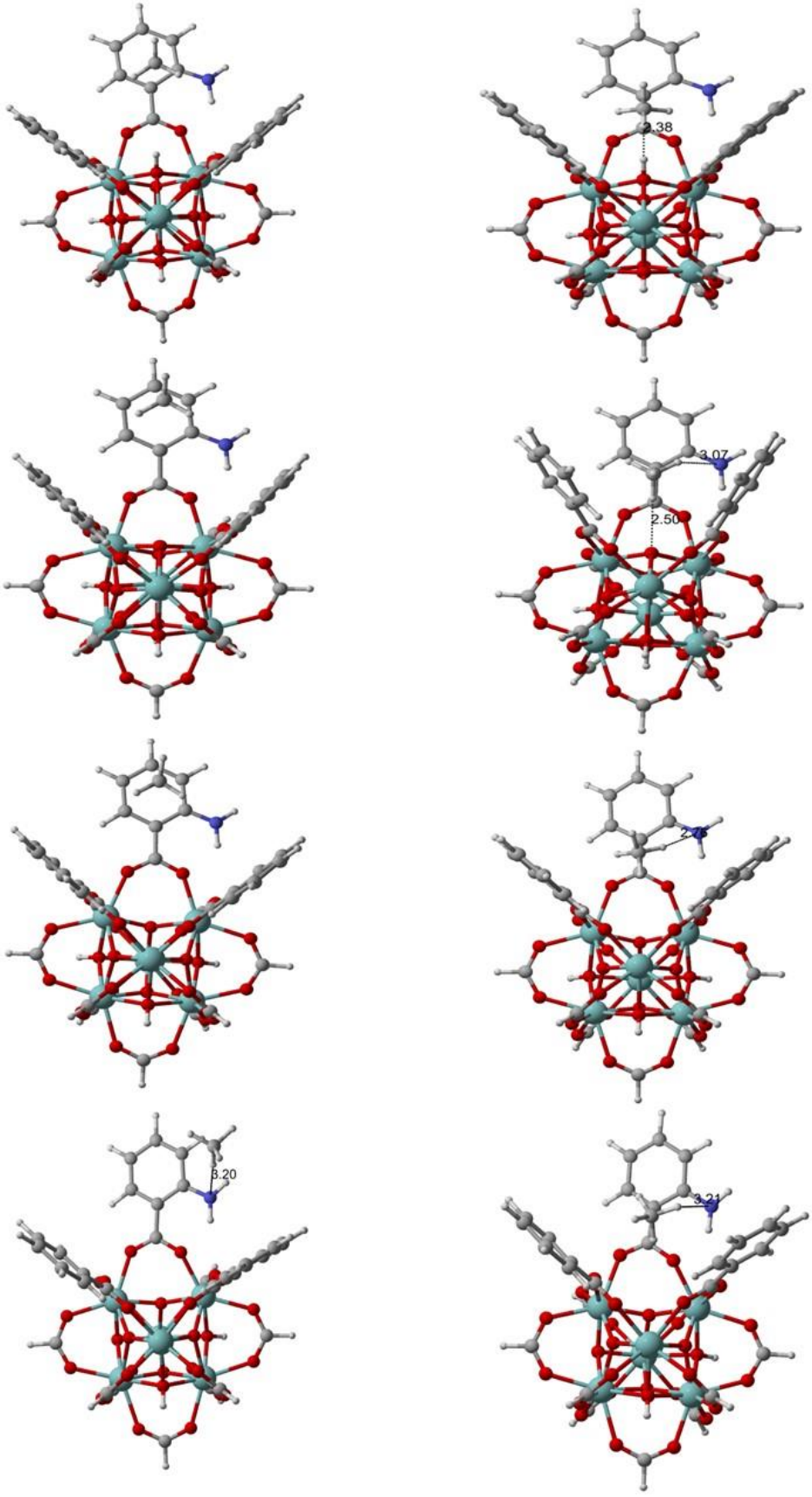

A 3-2-2: DFT(left) and DFT-D(right) Minimum Energy Structure for Adsorbed **CH_4** in 'No Defect, O, OH, H_2O Defects' (top to bottom) Configuration with **NH_2 Substituent**.

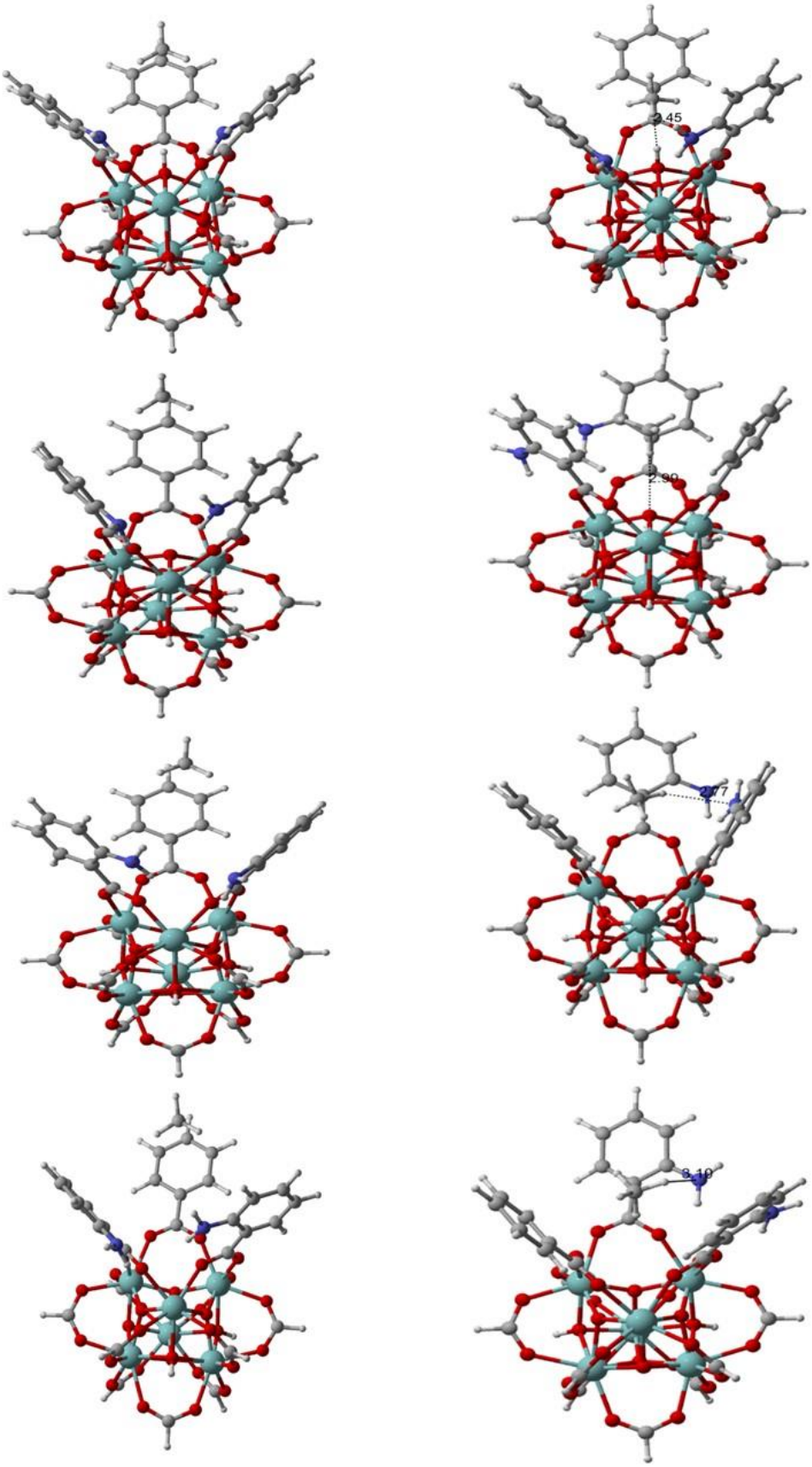

A 3-2-3: DFT(left) and DFT-D(right) Minimum Energy Structure for Adsorbed **CH_4** in 'No Defect, O, OH, H_2O Defects' (top to bottom) Configuration with **$2NH_2$ Substituent**.

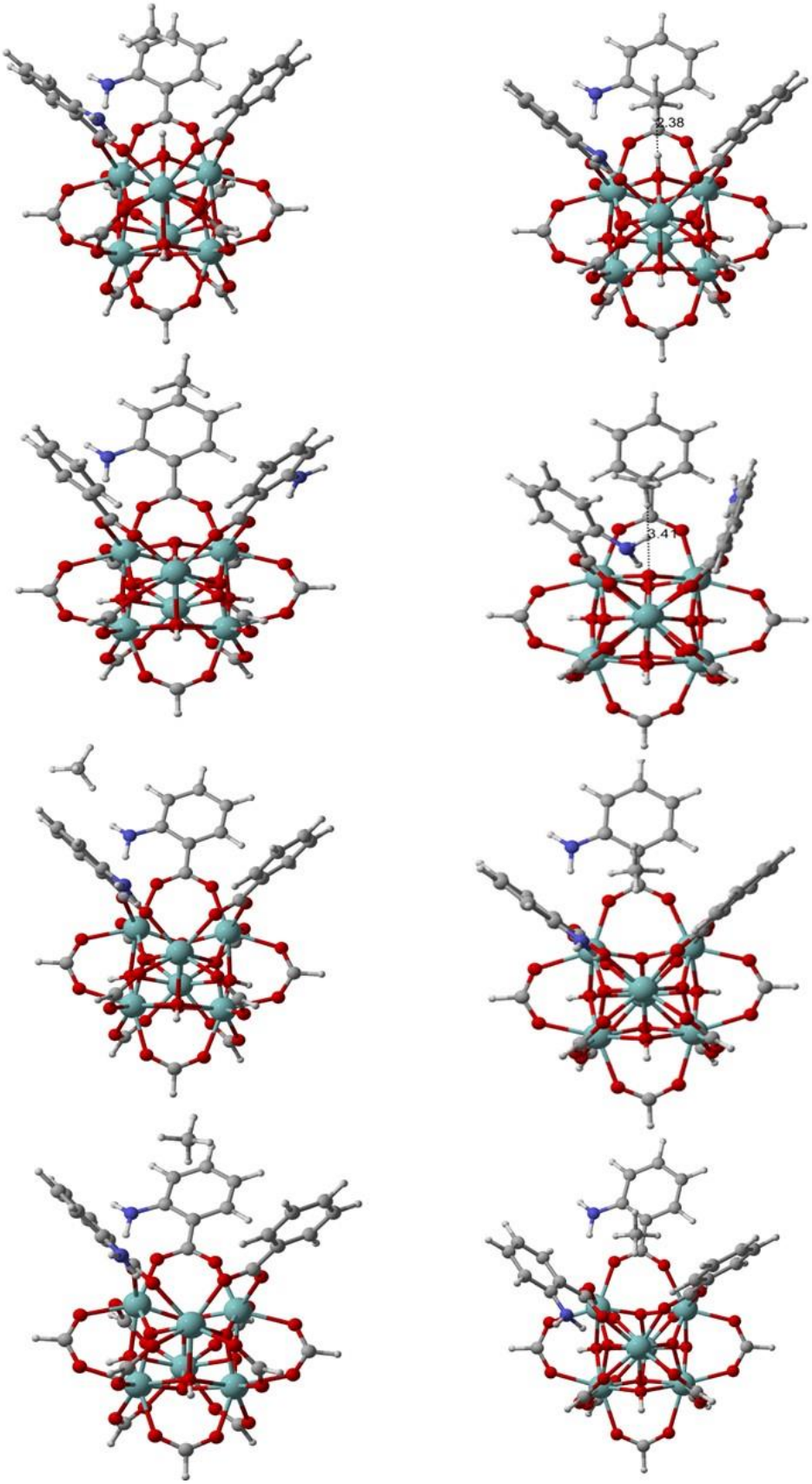

A 3-2-4: DFT(left) and DFT-D(right) Minimum Energy Structure for Adsorbed **CH_4** in 'No Defect, O, OH, H_2O Defects' (top to bottom) Configuration with **$2NH_2$iso Substituent**.

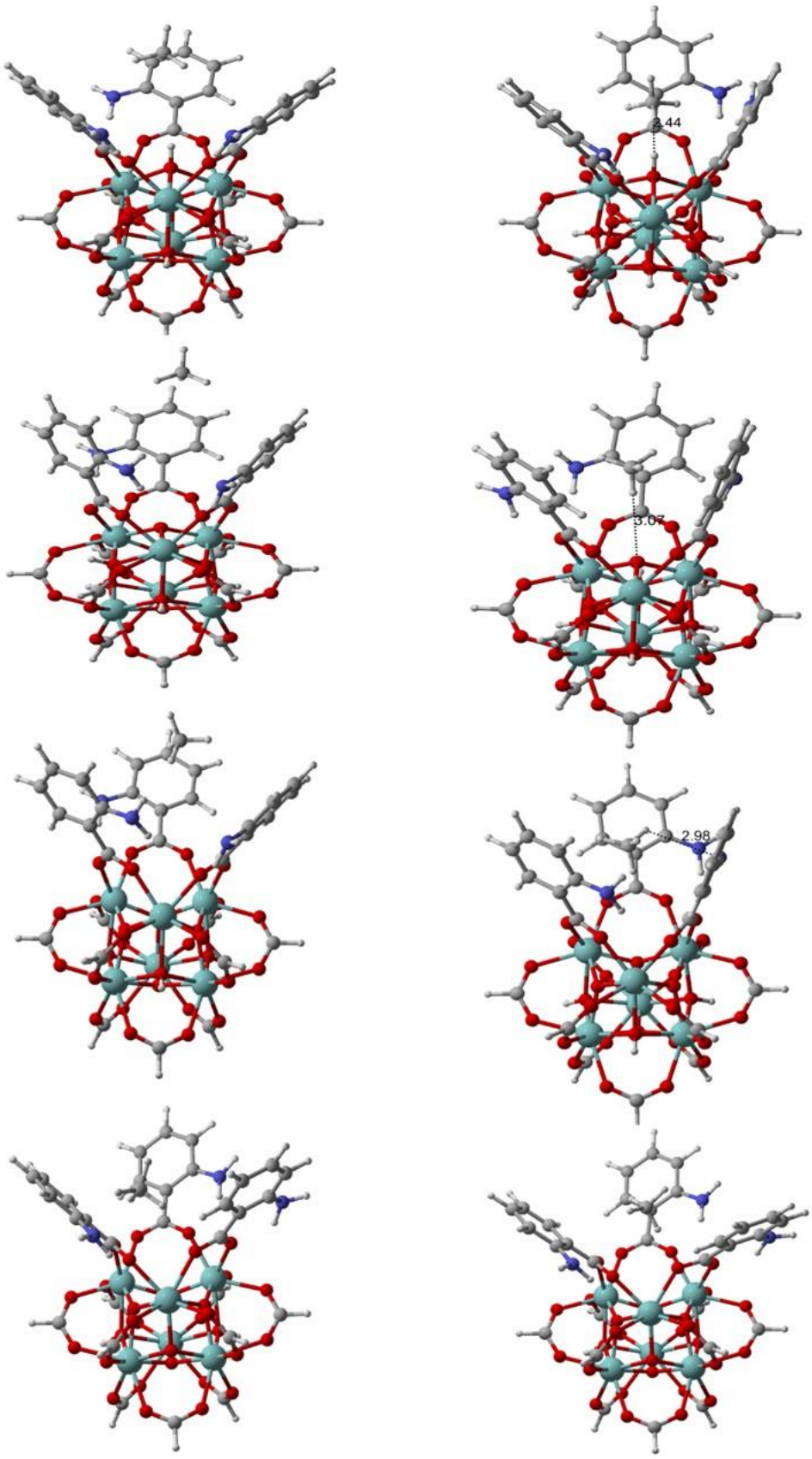

A 3-2-5: DFT(left) and DFT-D(right) Minimum Energy Structure for Adsorbed **CH_4** in 'No Defect, O, OH, H_2O Defects' (top to bottom) Configuration with **$3NH_2$ Substituent**.

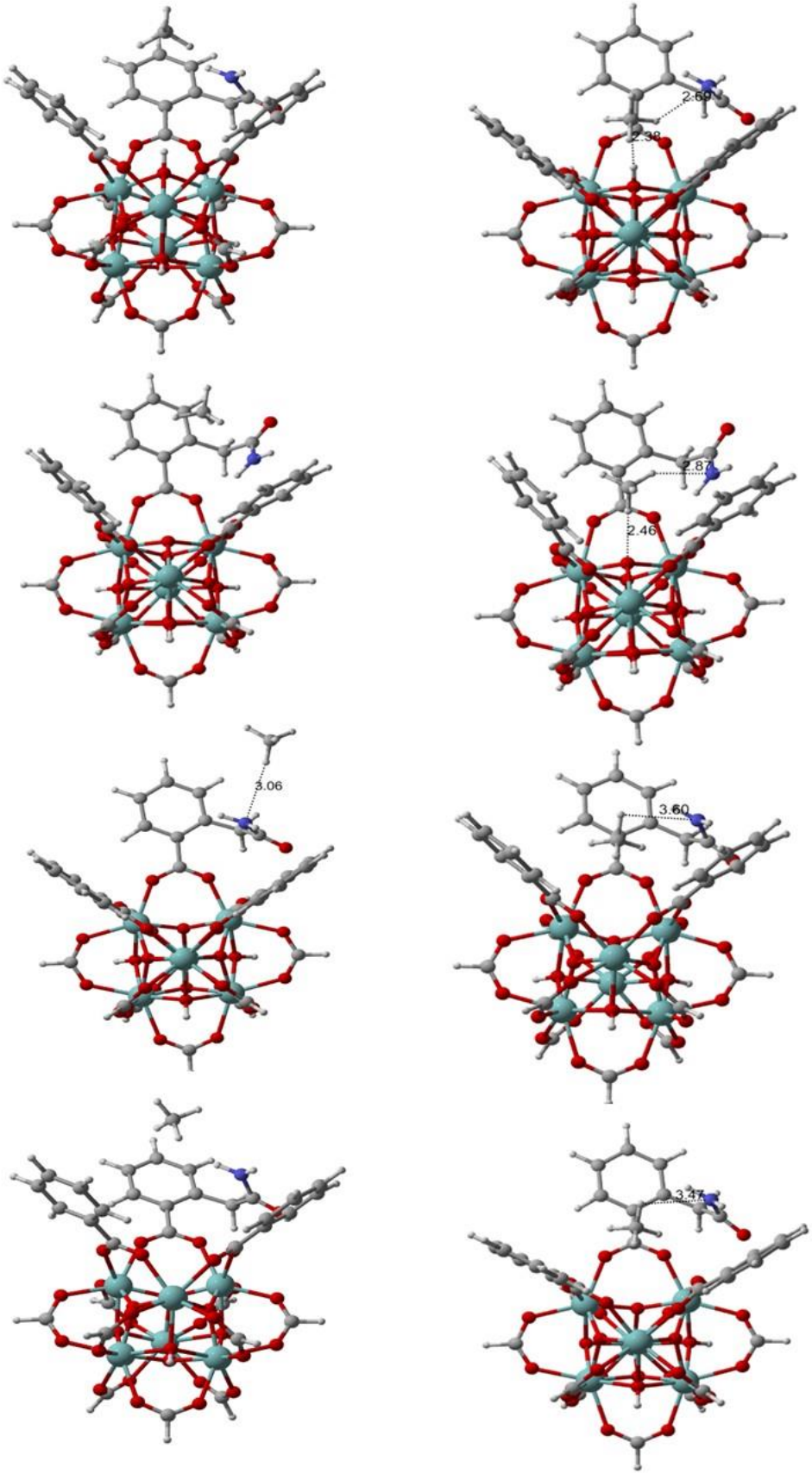

A 3-2-6: DFT(left) and DFT-D(right) Minimum Energy Structure for Adsorbed **CH_4** in 'No Defect, O, OH, H_2O Defects' (top to bottom) Configuration with **CH_2CONH_2 Substituent**.

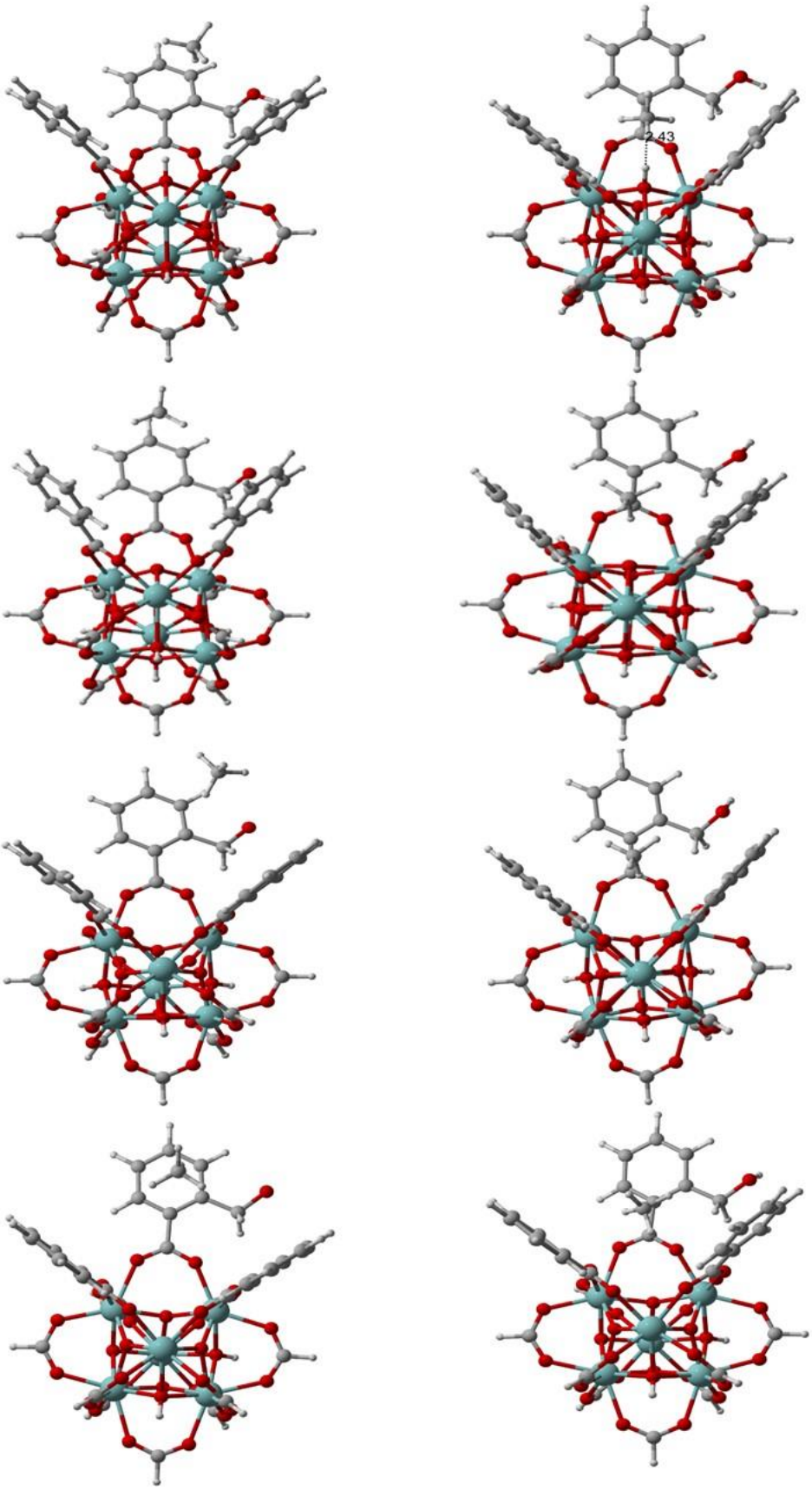

A 3-2-7: DFT(left) and DFT-D(right) Minimum Energy Structure for Adsorbed **CH_4** in 'No Defect, O, OH, H_2O Defects' (top to bottom) Configuration with **CH_2OH Substituent**.

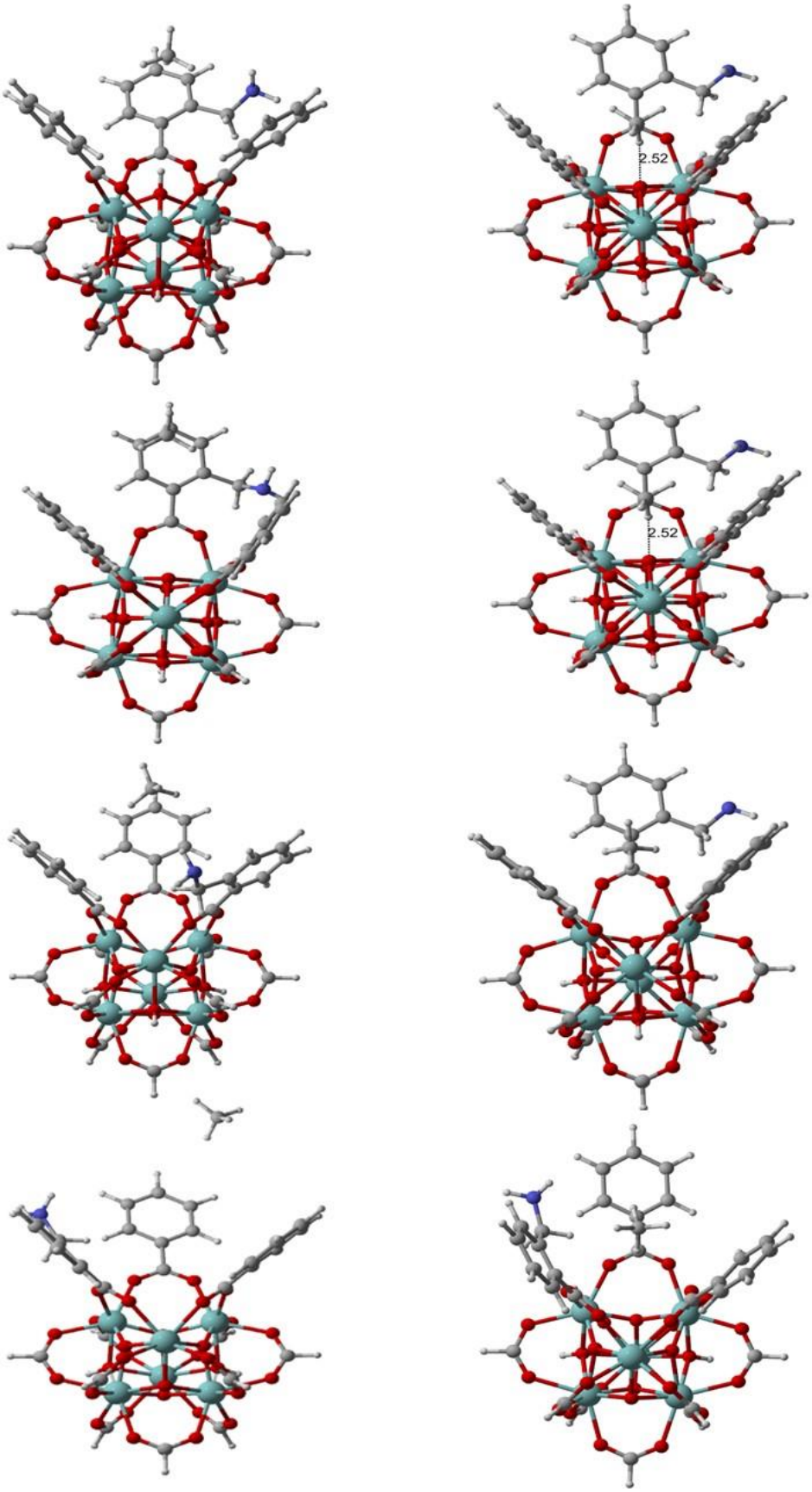

A 3-2-8: DFT(left) and DFT-D(right) Minimum Energy Structure for Adsorbed **CH_4** in 'No Defect, O, OH, H_2O Defects' (top to bottom) Configuration with **CH_2NH_2 Substituent**.

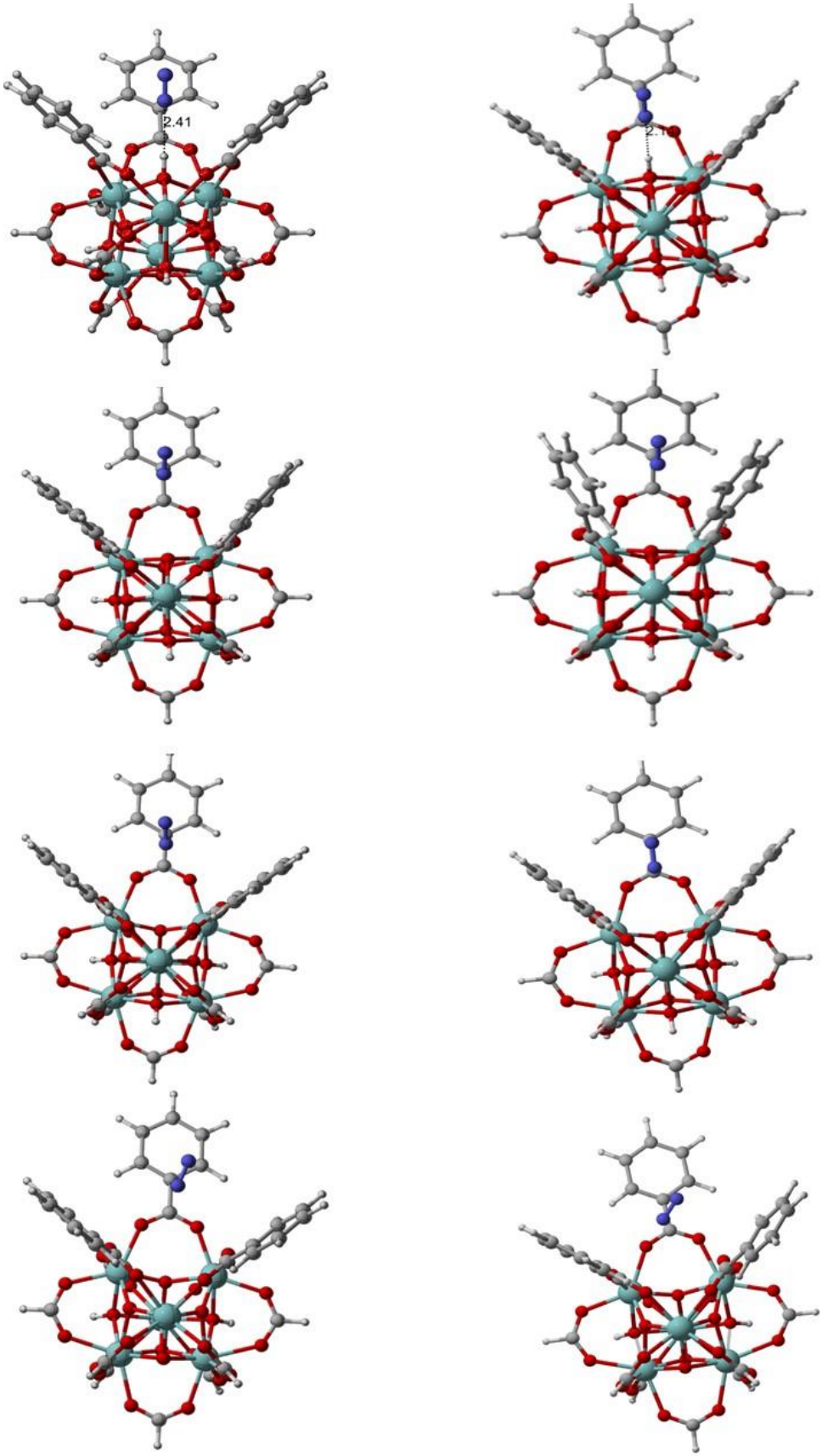

A 3-3-1: DFT(left) and DFT-D(right) Minimum Energy Structure for Adsorbed N_2 in 'No Defect, O, OH, H_2O Defects' (top to bottom) Configuration with **Unsubstituted**.

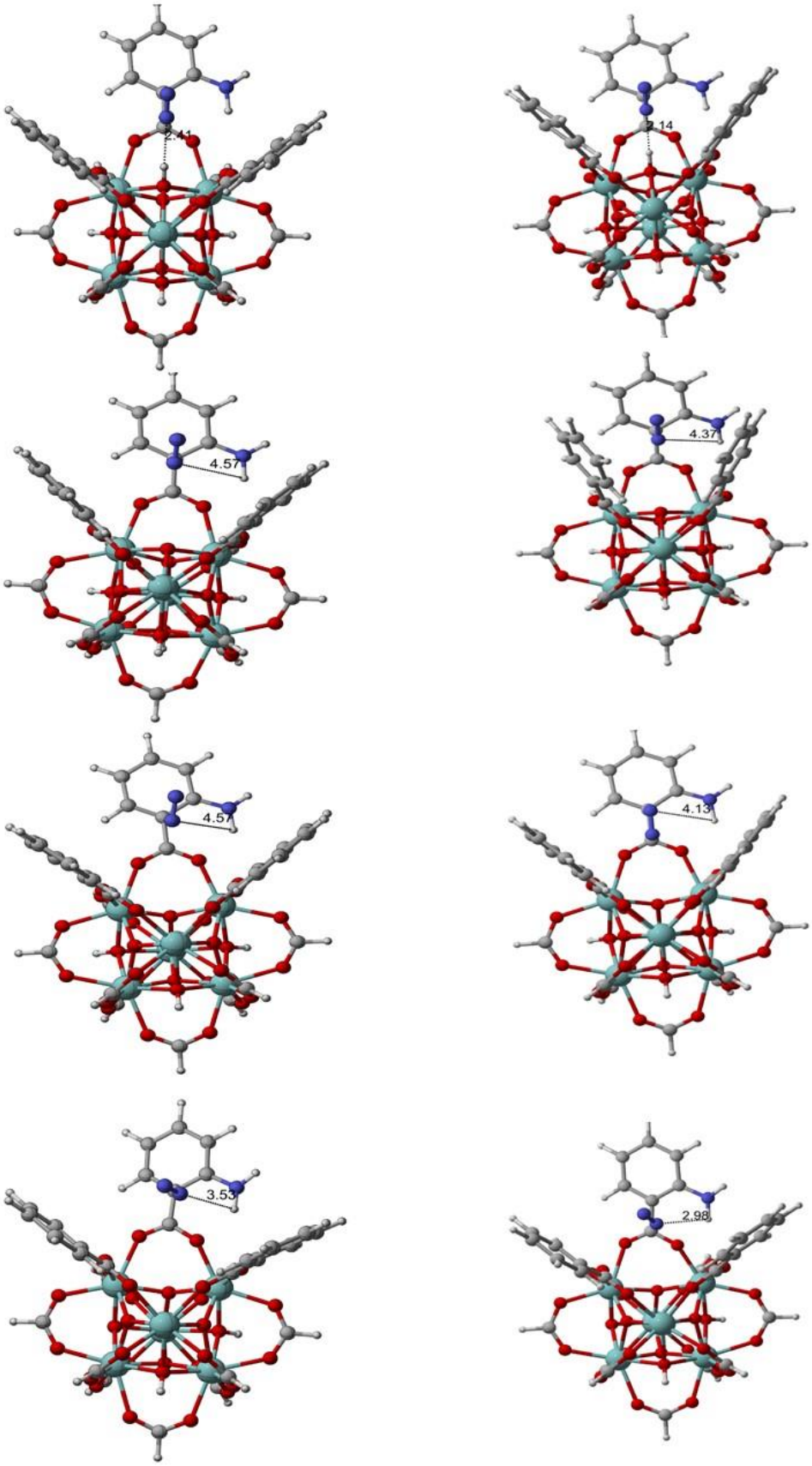

A 3-3-2: DFT(left) and DFT-D(right) Minimum Energy Structure for Adsorbed N_2 in 'No Defect, O, OH, H_2O Defects' (top to bottom) Configuration with **NH_2 Substituent**.

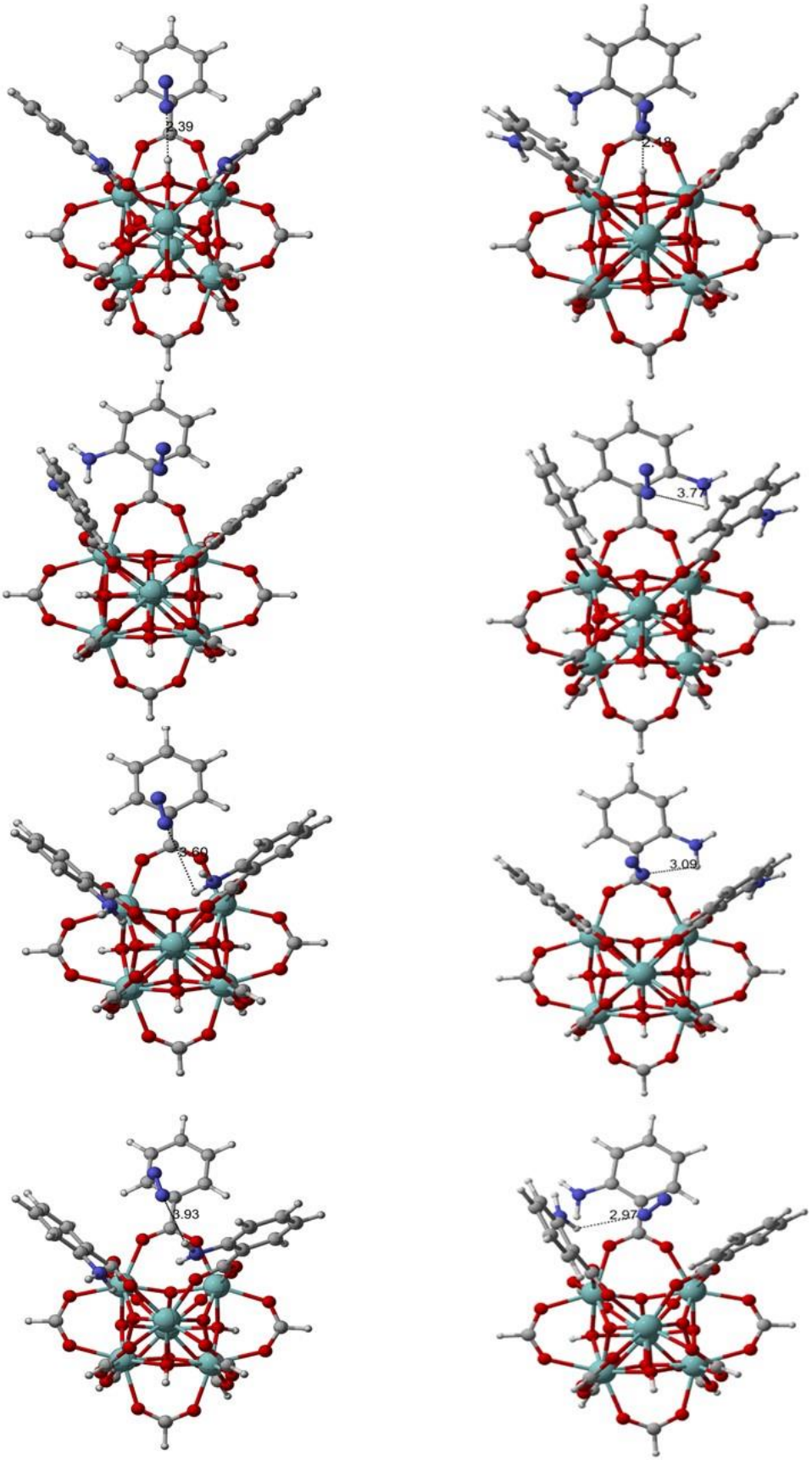

A 3-3-3: DFT(left) and DFT-D(right) Minimum Energy Structure for Adsorbed $\mathbf{N_2}$ in 'No Defect, O, OH, H_2O Defects' (top to bottom) Configuration with $\mathbf{2NH_2}$ **Substituent**.

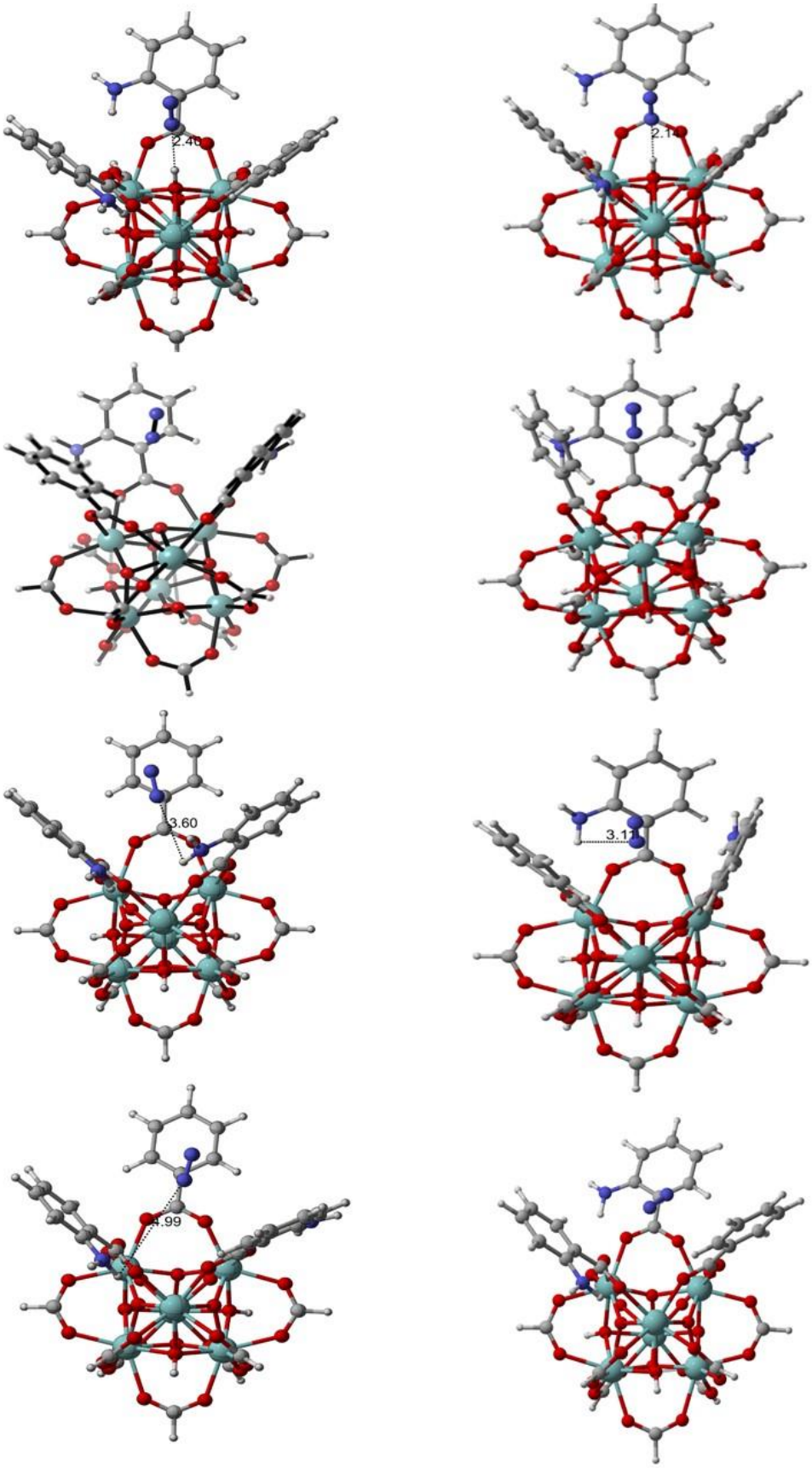

A 3-3-4: DFT(left) and DFT-D(right) Minimum Energy Structure for Adsorbed **CH_4** in 'No Defect, O, OH, H_2O Defects' (top to bottom) Configuration with **$2NH_2$-iso Substituent**.

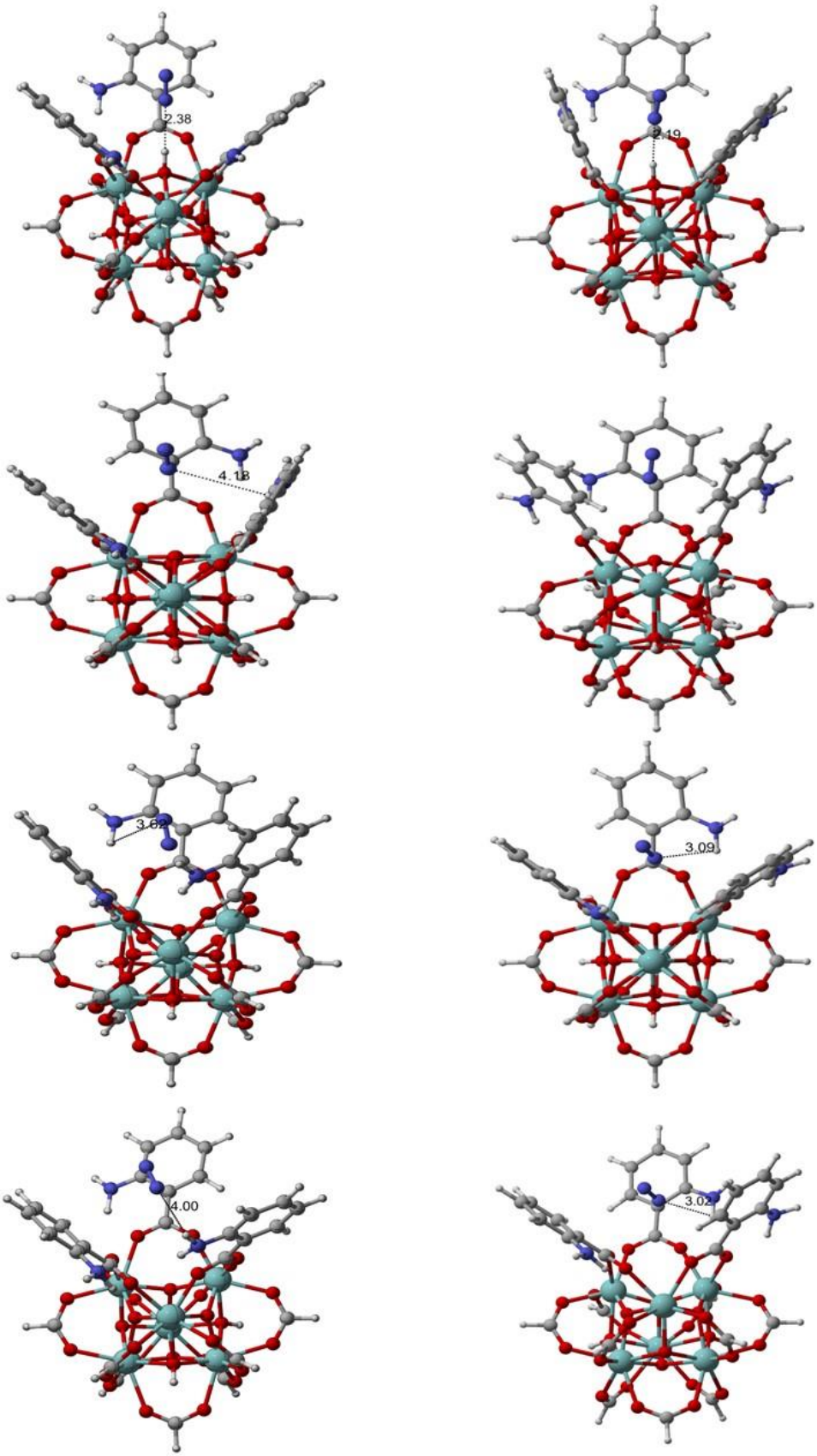

A 3-3-5: DFT(left) and DFT-D(right) Minimum Energy Structure for Adsorbed N_2 in 'No Defect, O, OH, H_2O Defects' (top to bottom) Configuration with **3NH_2 Substituent**.

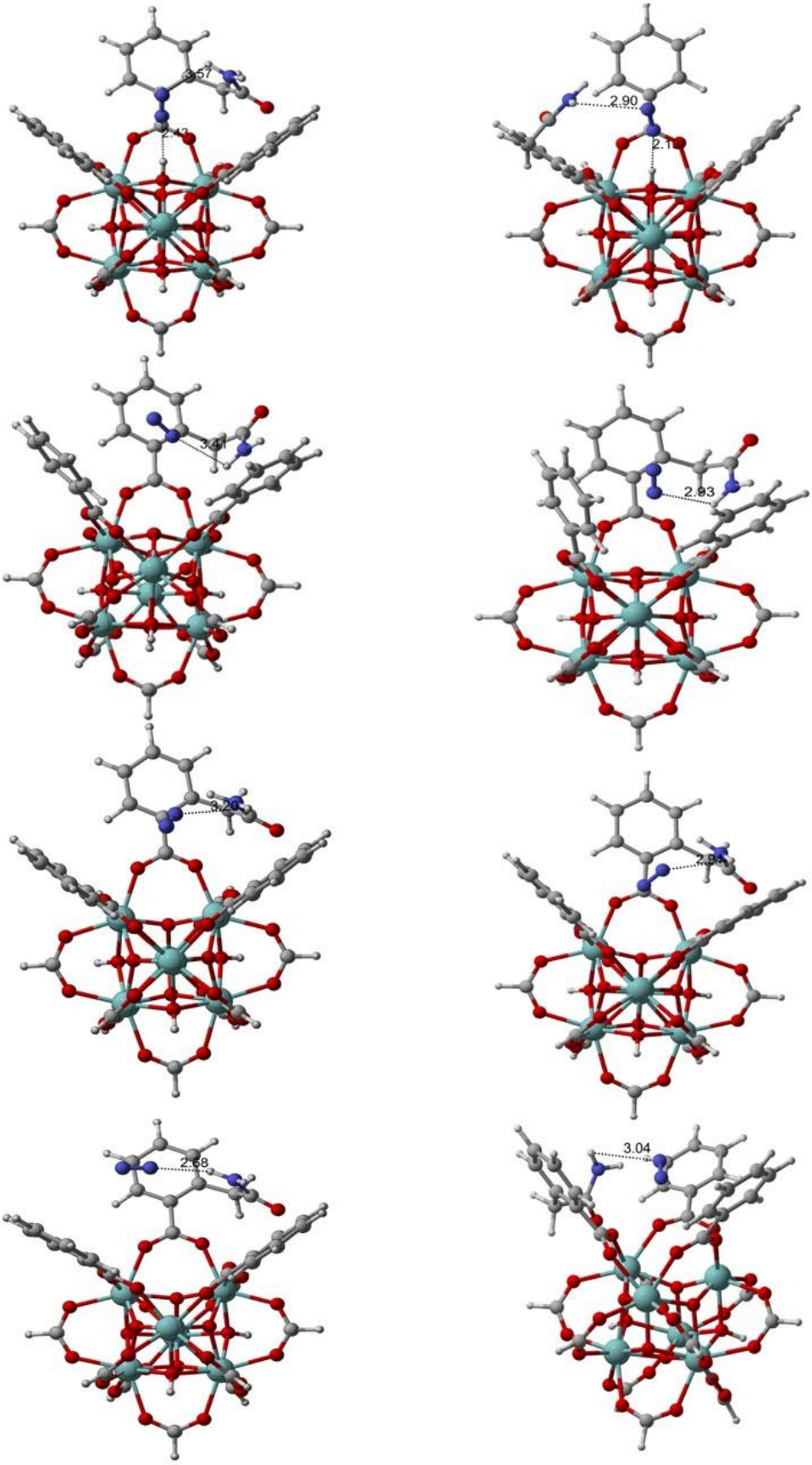

A 3-3-6: DFT(left) and DFT-D(right) Minimum Energy Structure for Adsorbed N_2 in 'No Defect, O, OH, H_2O Defects' (top to bottom) Configuration with **CH_2CONH_2 Substituent**.

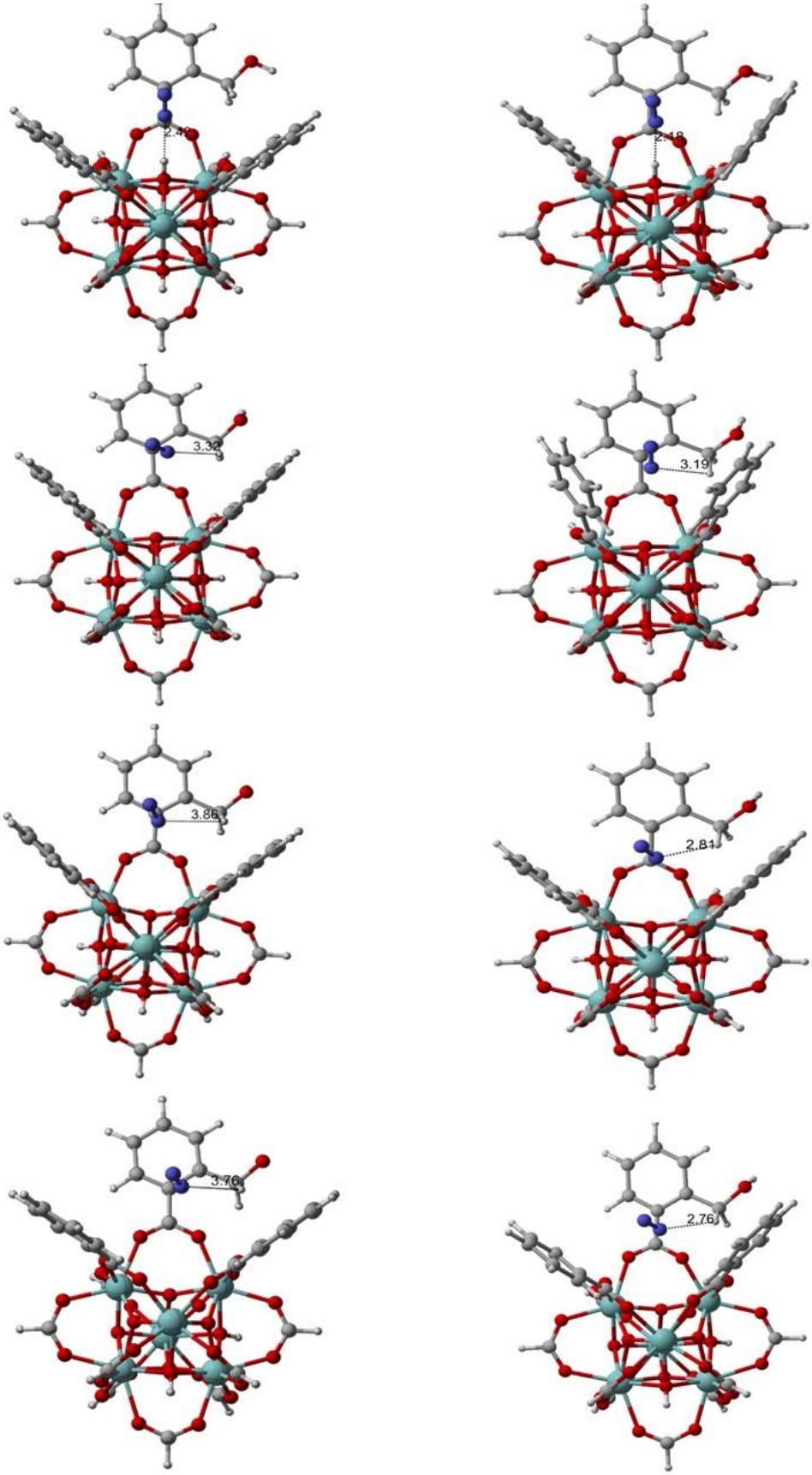

A 3-3-7: DFT(left) and DFT-D(right) Minimum Energy Structure for Adsorbed N_2 in 'No Defect, O, OH, H_2O Defects' (top to bottom) Configuration with **CH_2OH Substituent**.

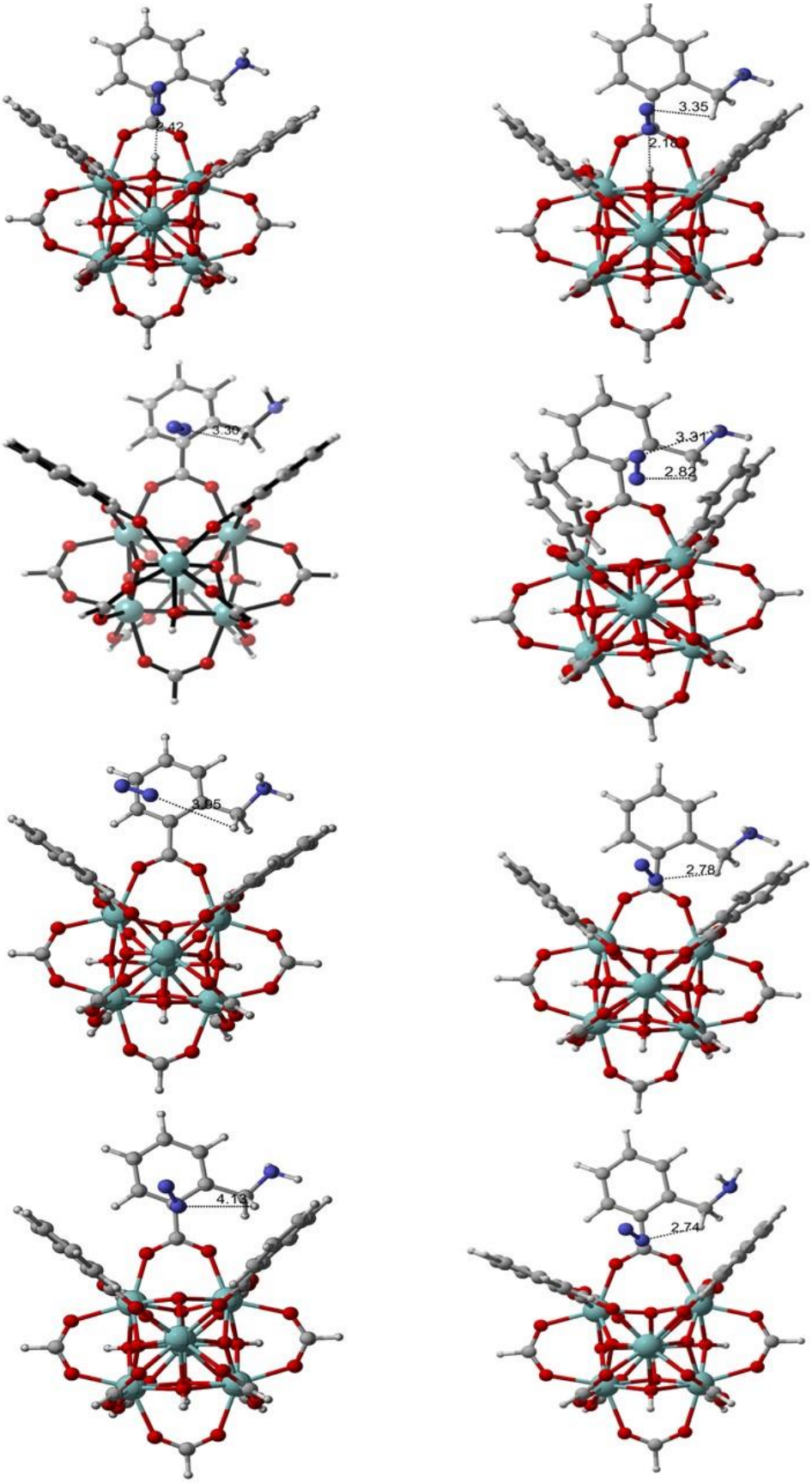

A 3-3-8: DFT(left) and DFT-D(right) Minimum Energy Structure for Adsorbed N_2 in 'No Defect, O, OH, H_2O Defects' (top to bottom) Configuration with **CH_2NH_2 Substituent**.

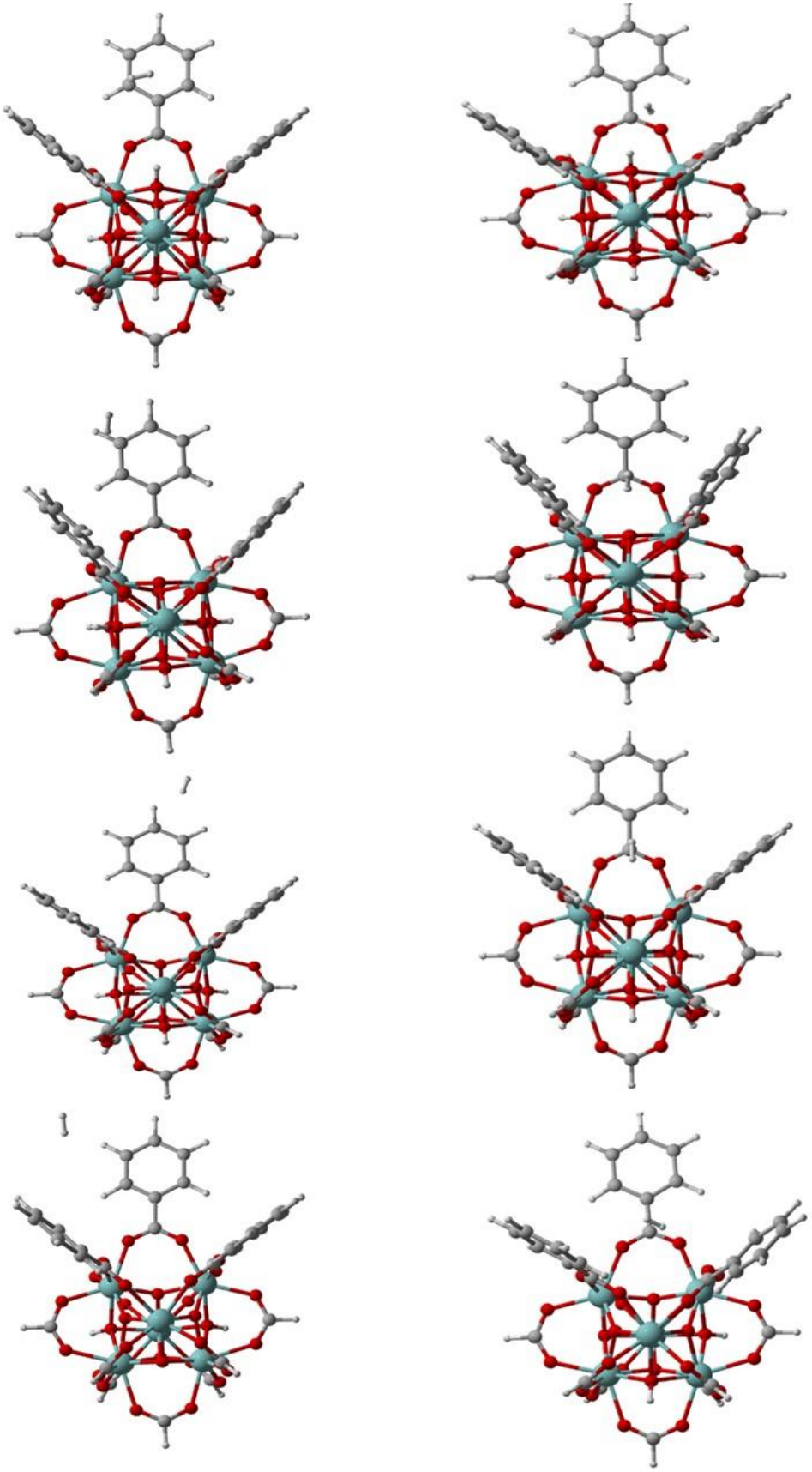

A 3-4-1: DFT(left) and DFT-D(right) Minimum Energy Structure for Adsorbed **H_2** in 'No Defect, O, OH, H_2O Defects' (top to bottom) Configuration with **Unsubstituted**.

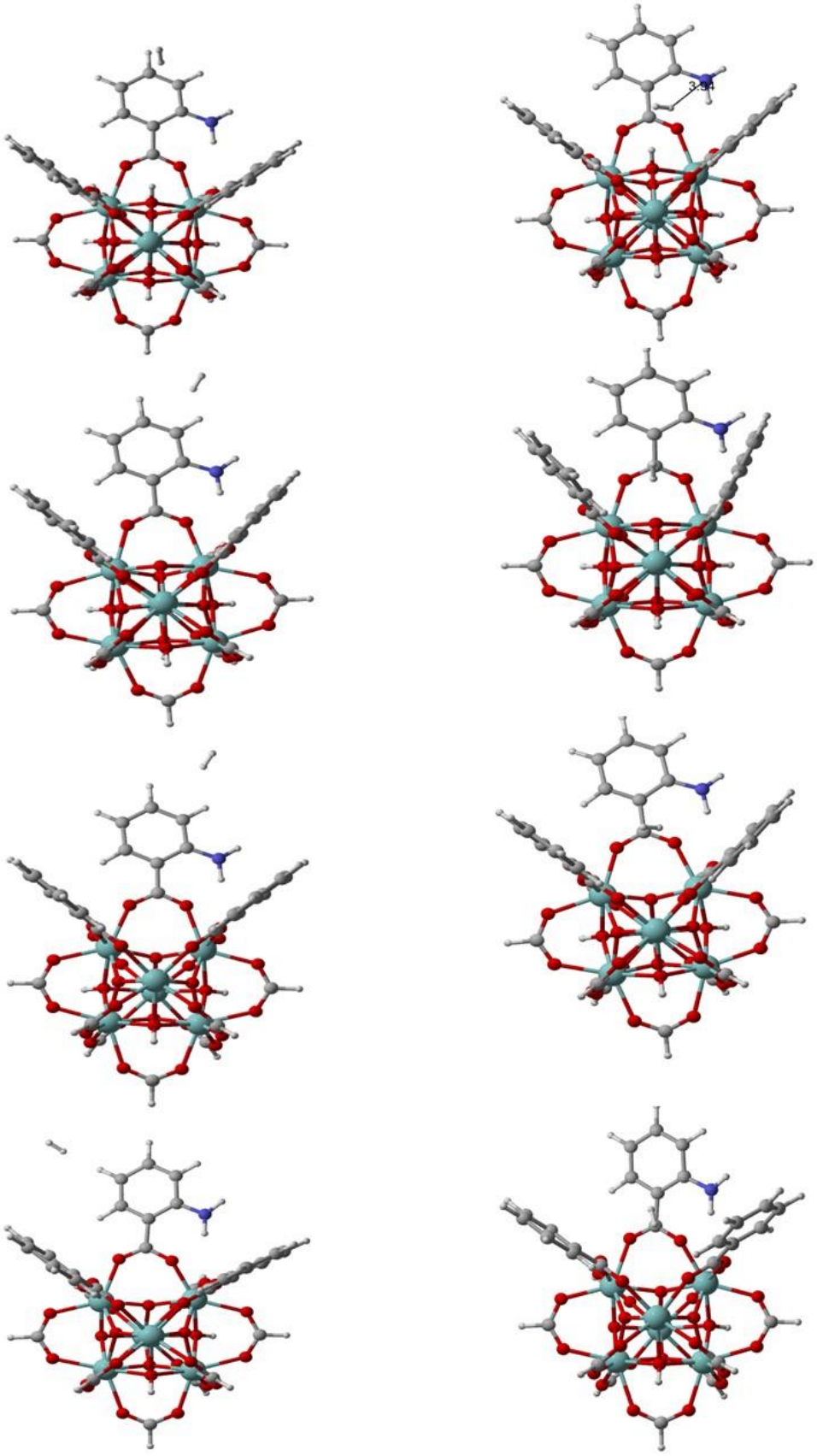

A 3-4-2: DFT(left) and DFT-D(right) Minimum Energy Structure for Adsorbed **H_2** in 'No Defect, O, OH, H_2O Defects' (top to bottom) Configuration with **NH_2 Substituent**.

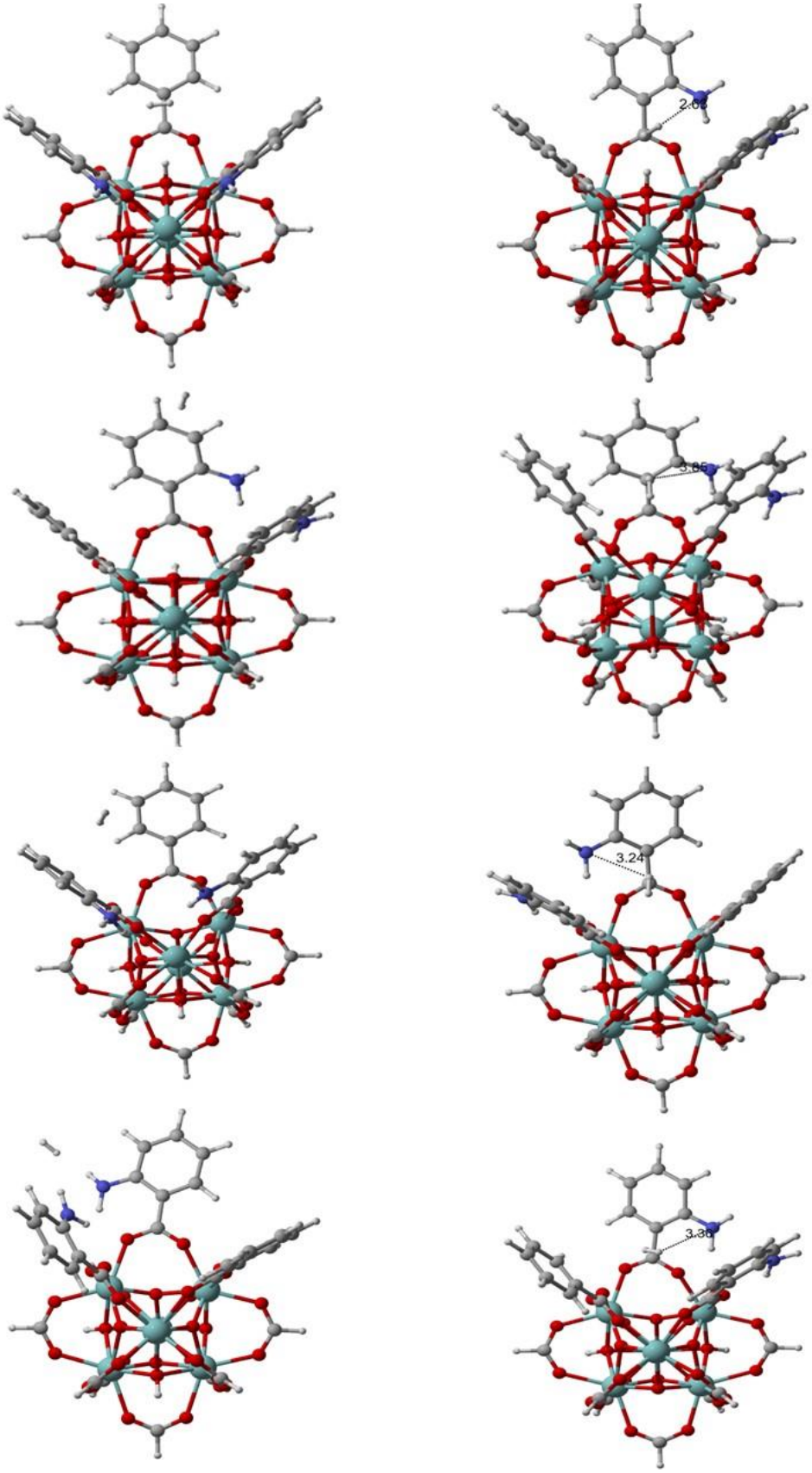

A 3-4-3: DFT(left) and DFT-D(right) Minimum Energy Structure for Adsorbed **H_2** in 'No Defect, O, OH, H_2O Defects' (top to bottom) Configuration with **$2NH_2$ Substituent**.

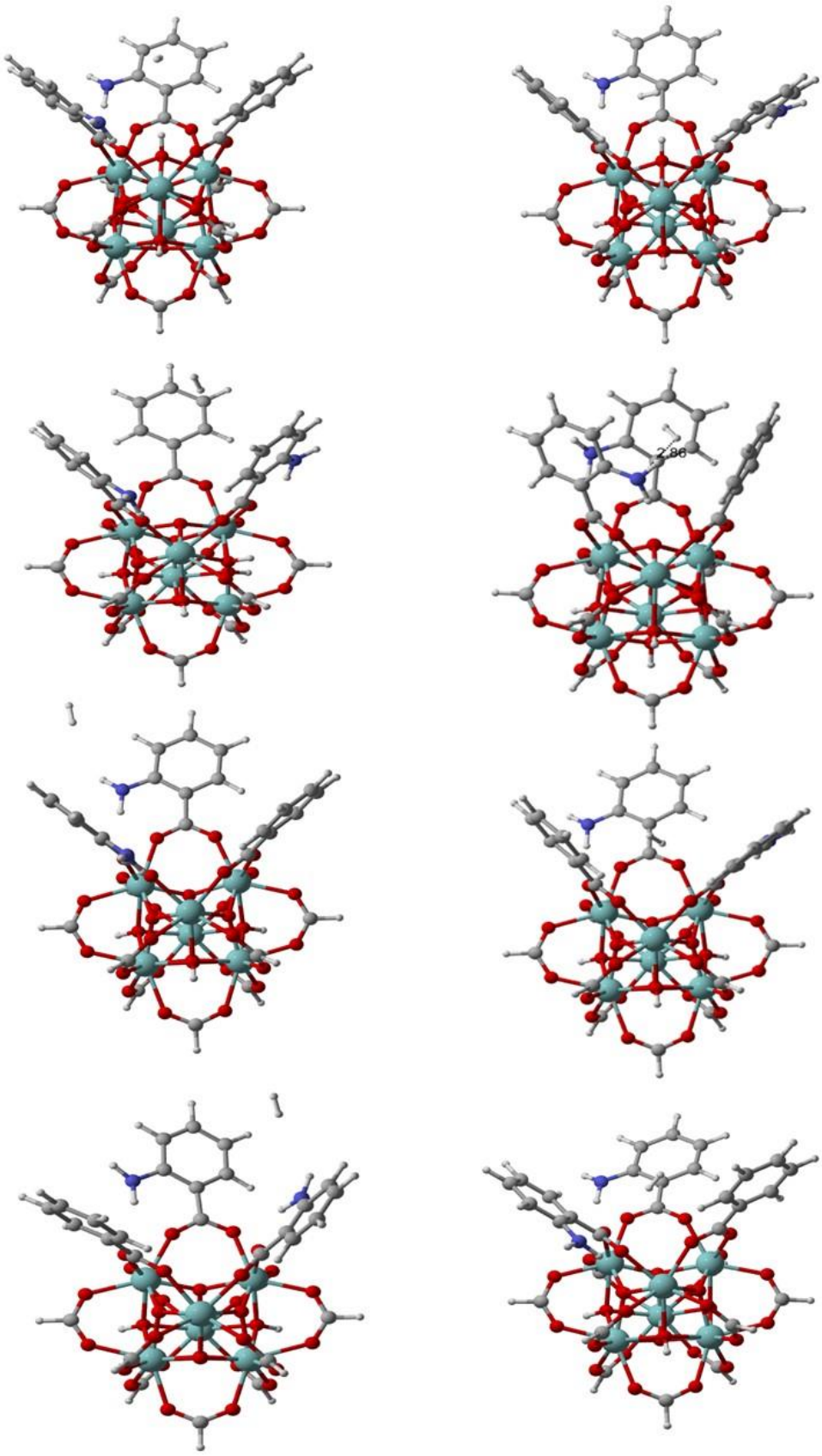

A 3-4-4: DFT(left) and DFT-D(right) Minimum Energy Structure for Adsorbed **CH_4** in 'No Defect, O, OH, H_2O Defects' (top to bottom) Configuration with **$2NH_2$-iso Substituent**.

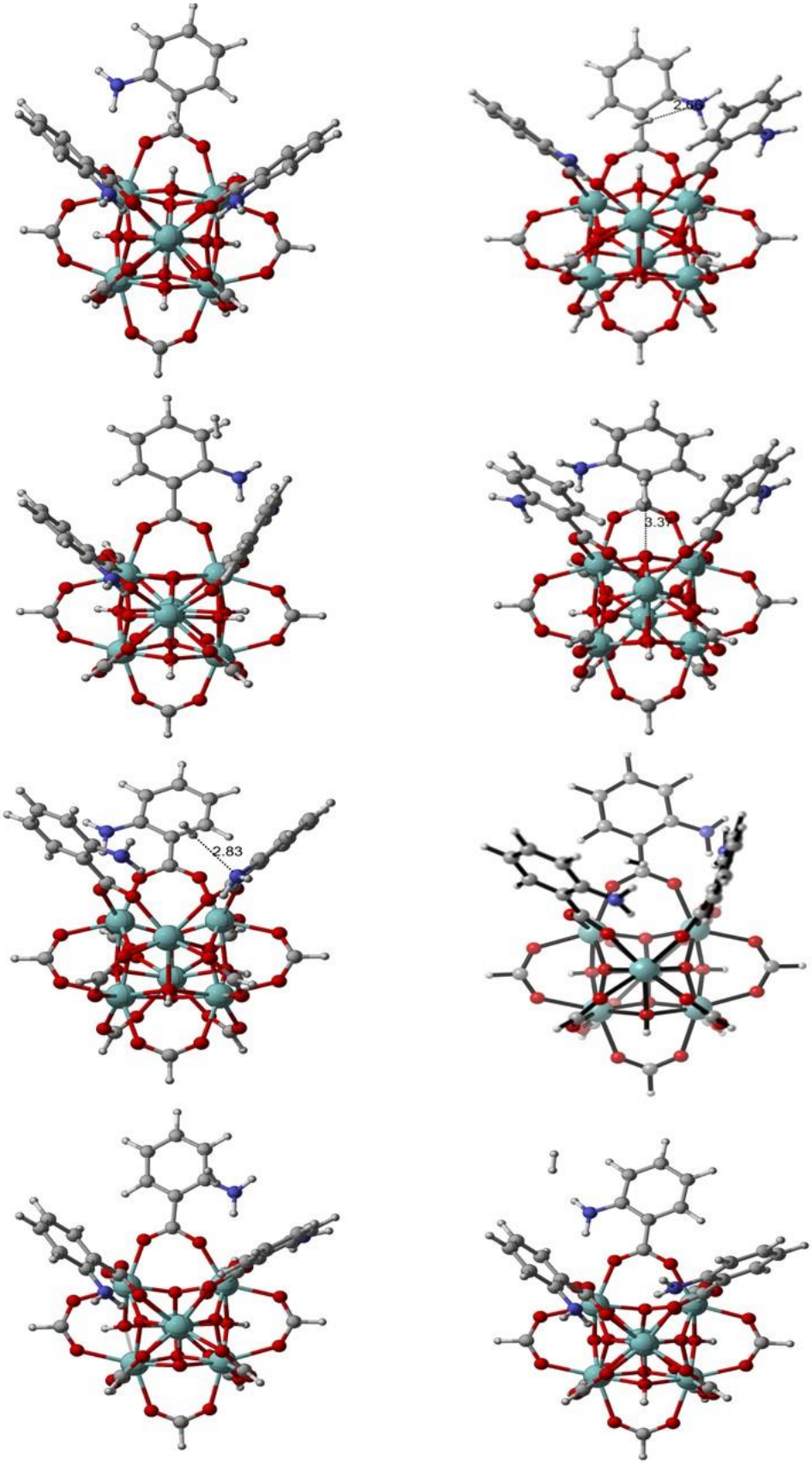

A 3-4-5: DFT(left) and DFT-D(right) Minimum Energy Structure for Adsorbed $\mathbf{H_2}$ in 'No Defect, O, OH, H_2O Defects' (top to bottom) Configuration with **3NH_2 Substituent**.

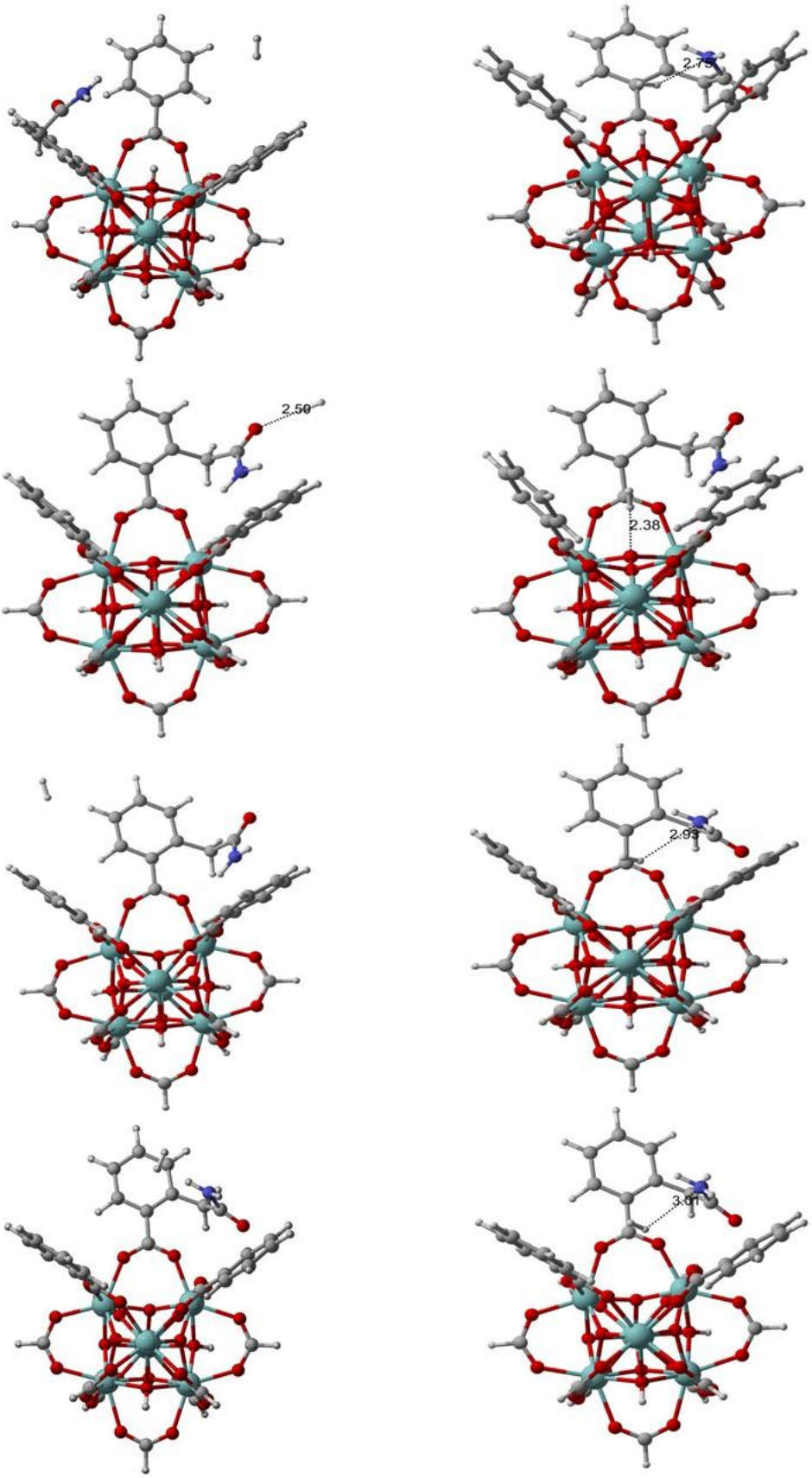

A 3-4-6: DFT(left) and DFT-D(right) Minimum Energy Structure for Adsorbed **H_2** in 'No Defect, O, OH, H_2O Defects' (top to bottom) Configuration with **CH_2CONH_2 Substituent**.

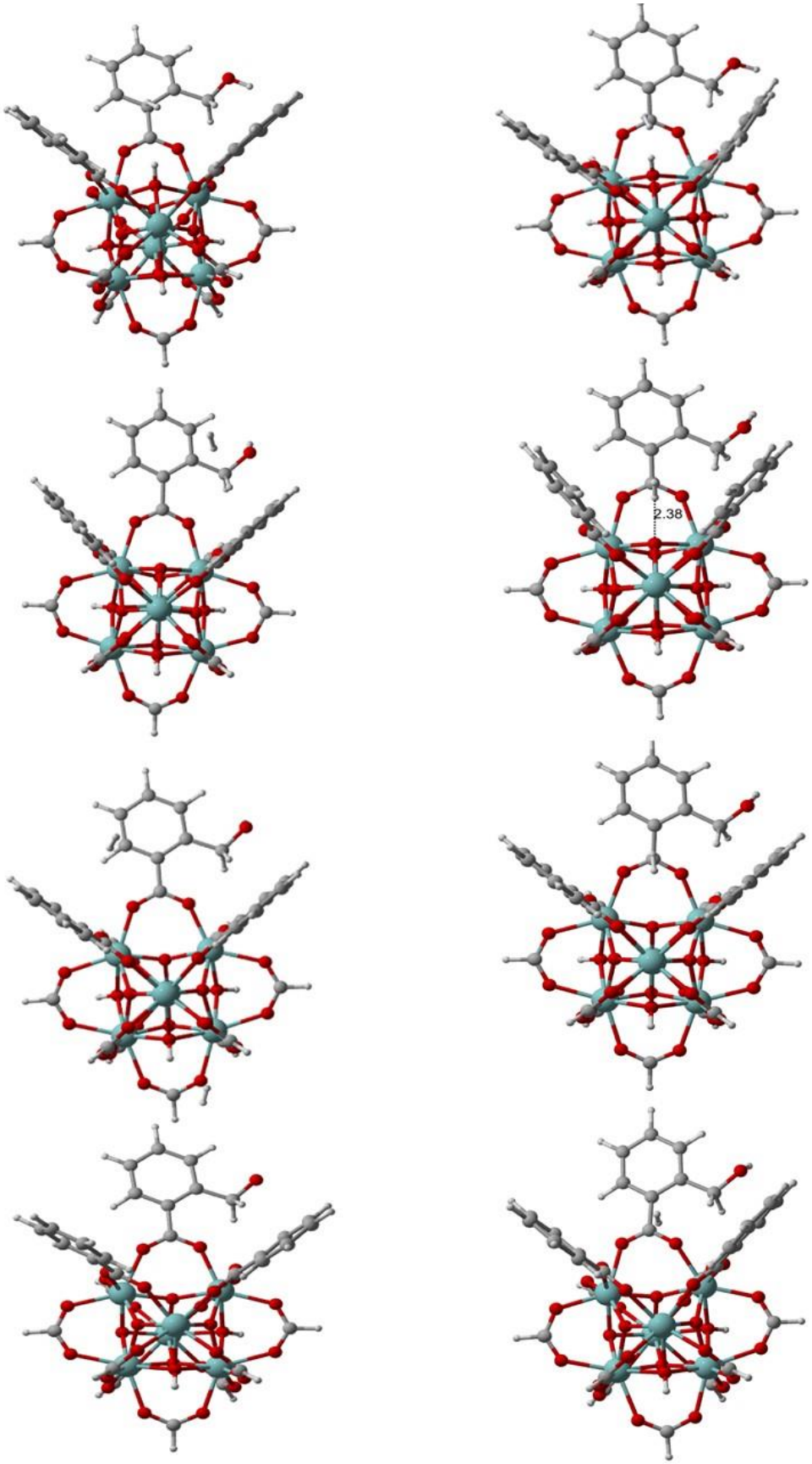

A 3-4-7: DFT(left) and DFT-D(right) Minimum Energy Structure for Adsorbed **H_2** in 'No Defect, O, OH, H_2O Defects' (top to bottom) Configuration with **CH_2OH Substituent**.

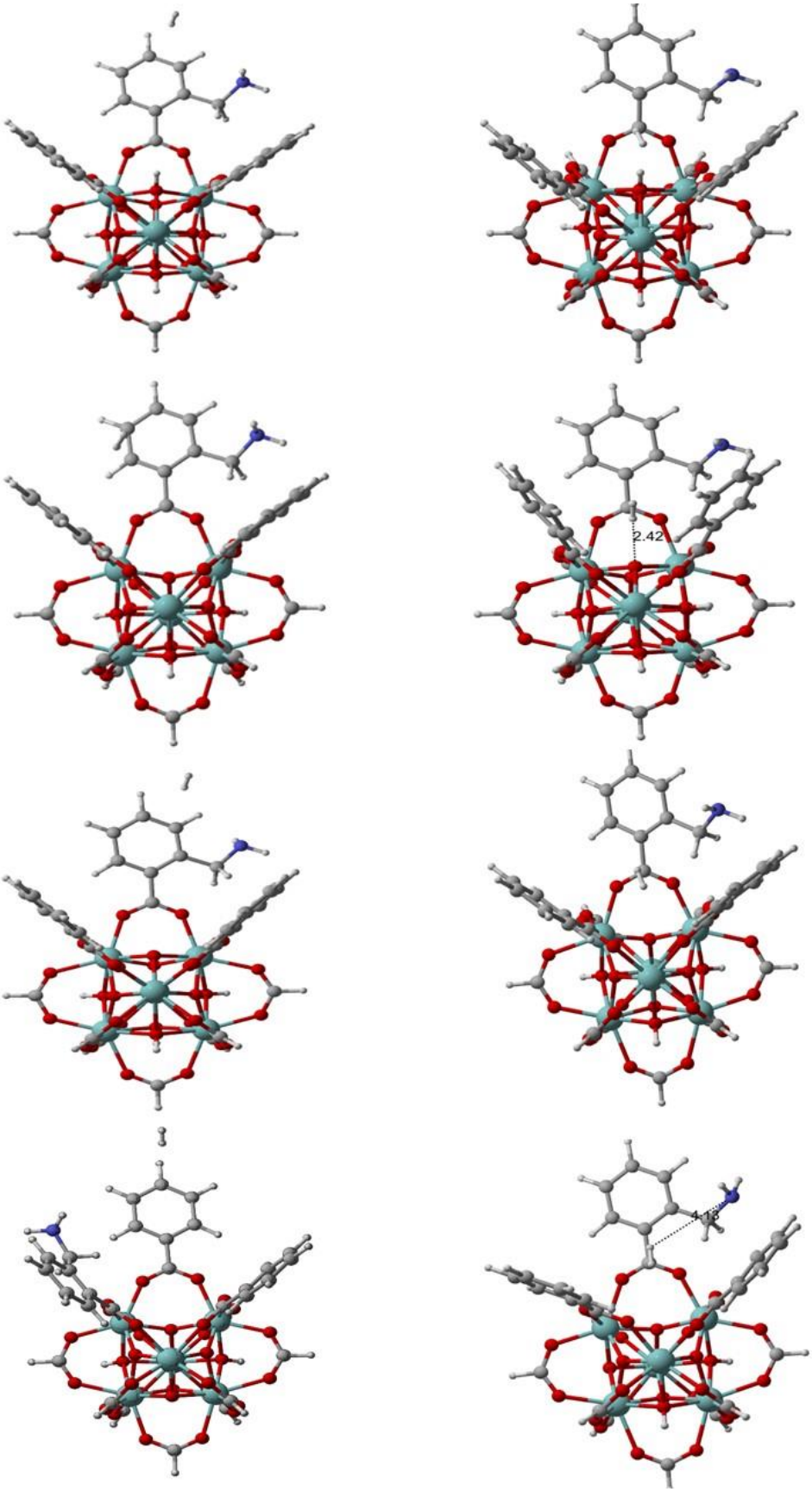

A 3-4-8: DFT(left) and DFT-D(right) Minimum Energy Structure for Adsorbed **H_2** in 'No Defect, O, OH, H_2O Defects' (top to bottom) Configuration with **CH_2NH_2 Substituent**.

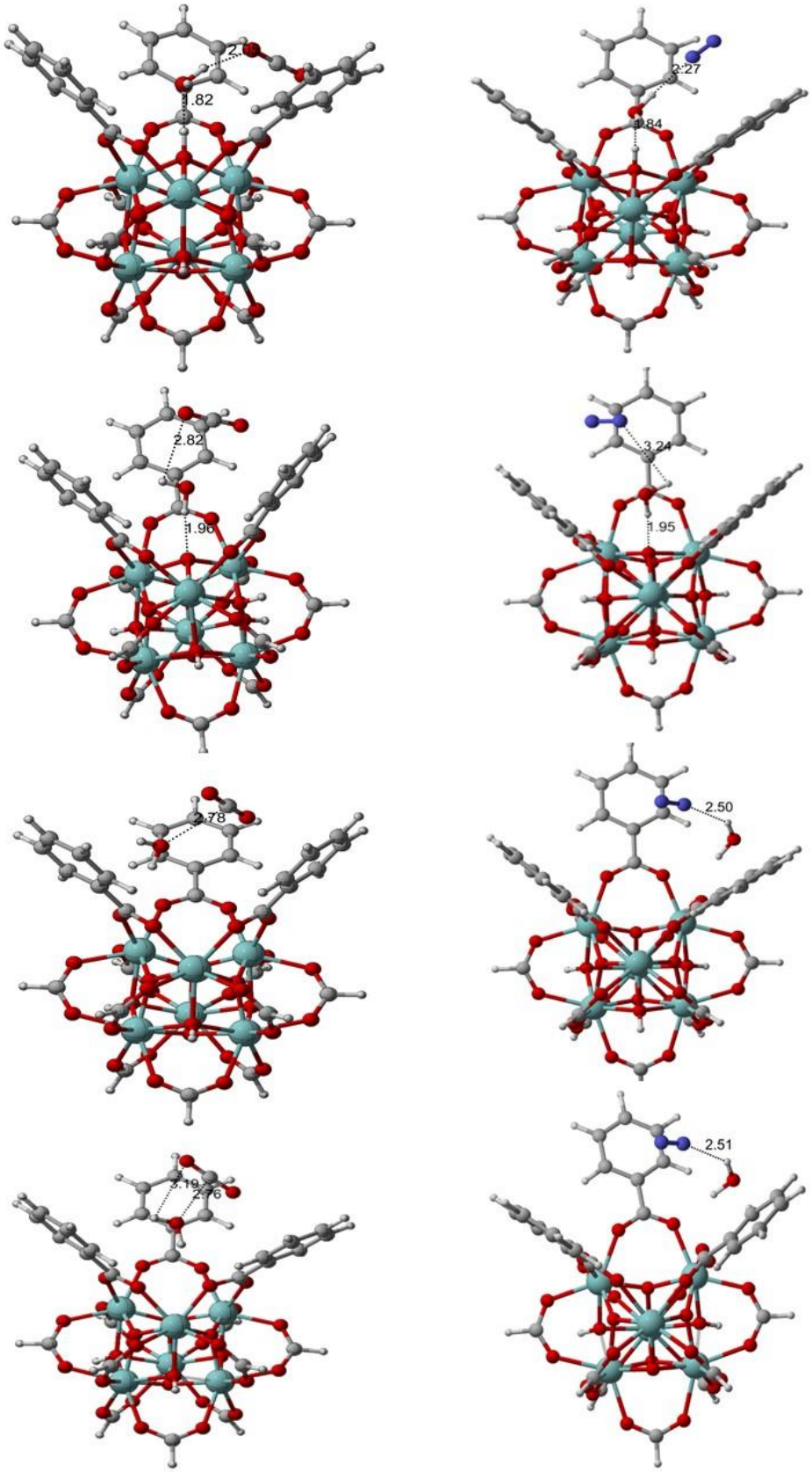

A 3-5-1: DFT(left) and DFT-D(right) Minimum Energy Structure for Adsorbed **CO_2**, **N_2** in 'No Defect, O, OH, H_2O Defects' (top to bottom) Configuration with **Unsubstituted** in presence of water.

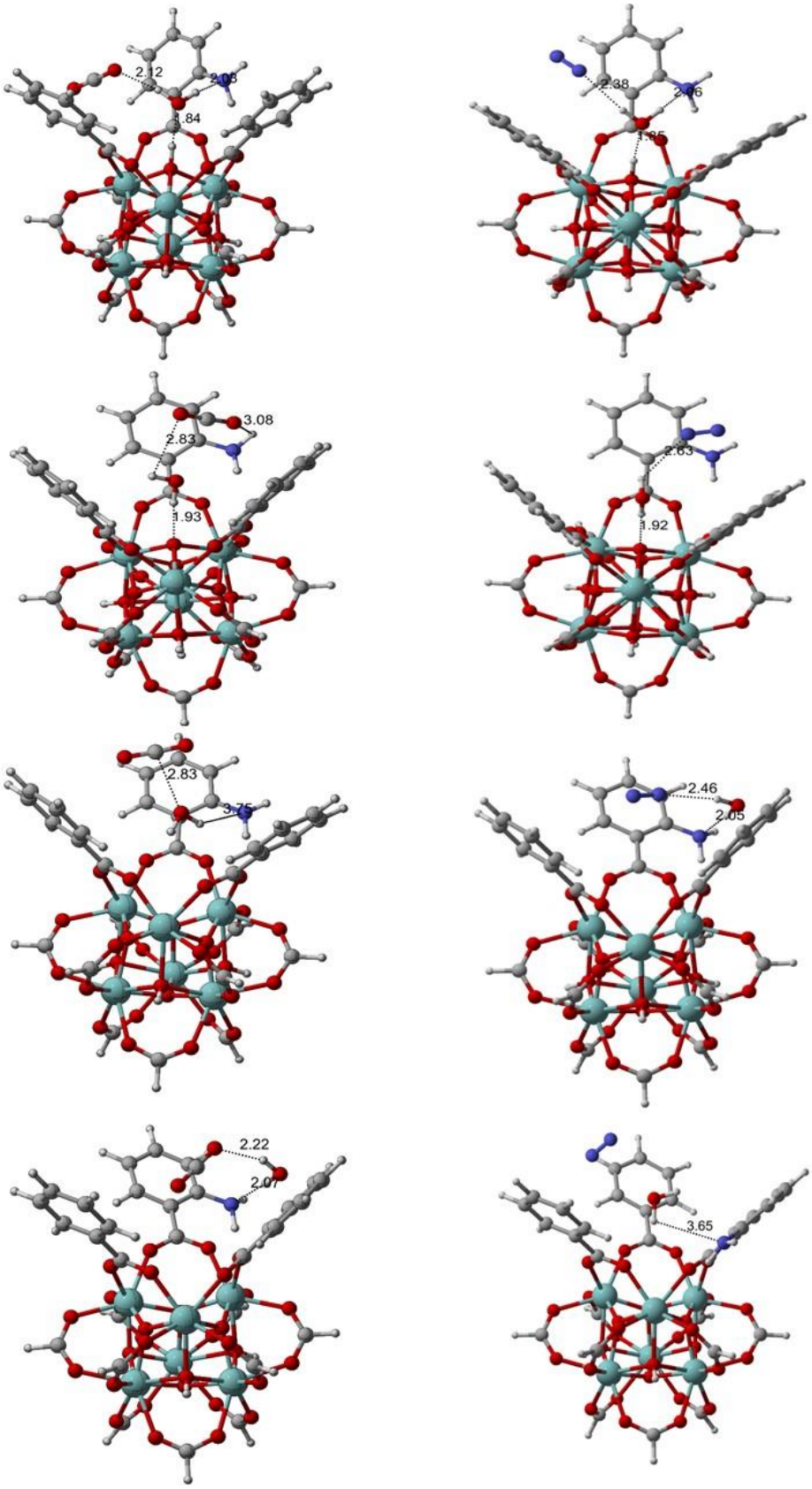

A 3-5-2: DFT(left) and DFT-D(right) Minimum Energy Structure for Adsorbed **CO_2**, **N_2** in 'No Defect, O, OH, H_2O Defects' (top to bottom) Configuration with **NH_2 Substituent** in presence of water.

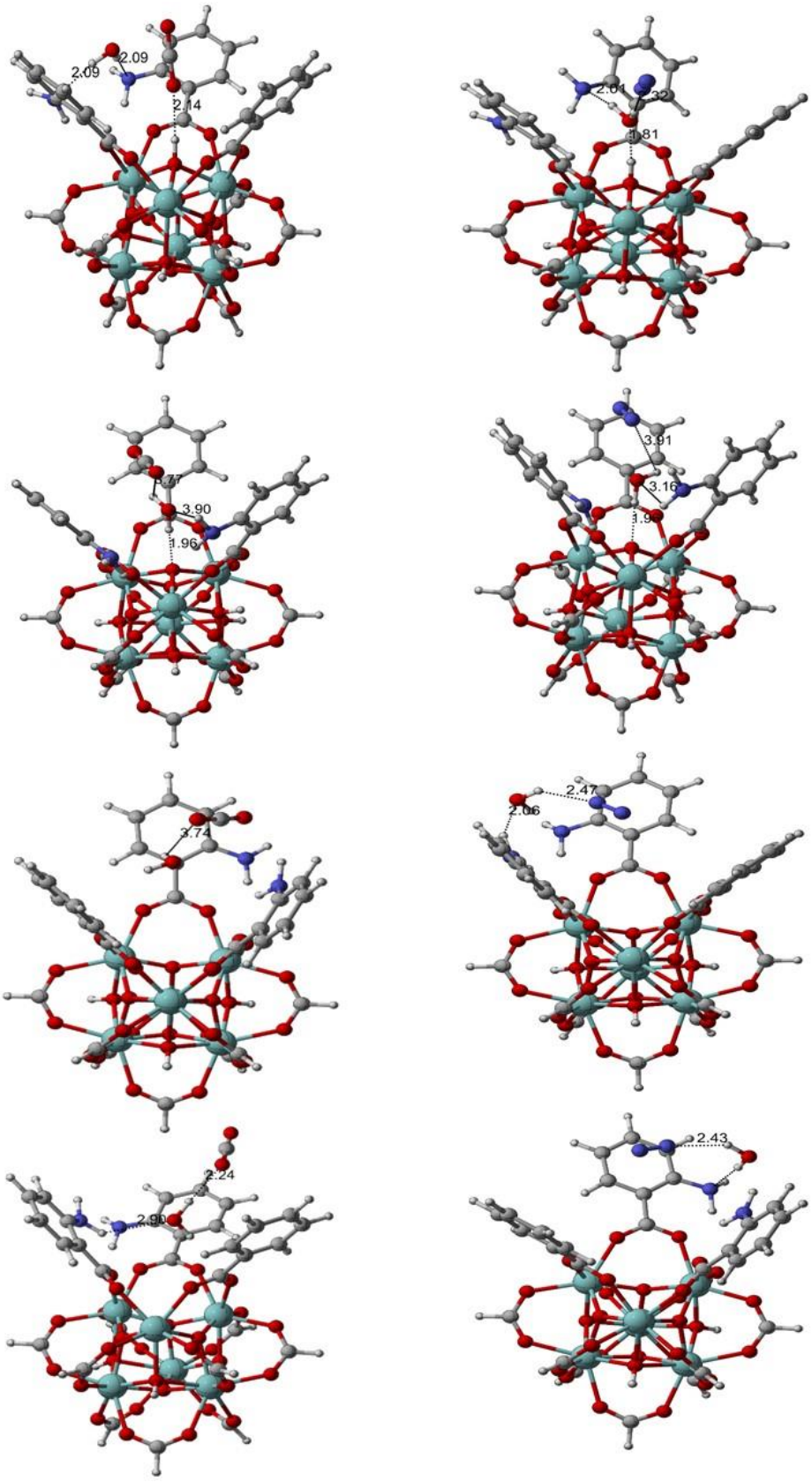

A 3-5-3: DFT(left) and DFT-D(right) Minimum Energy Structure for Adsorbed **CO_2, N_2** in 'No Defect, O, OH, H_2O Defects' (top to bottom) Configuration with **$2NH_2$ Substituent** in presence of water.

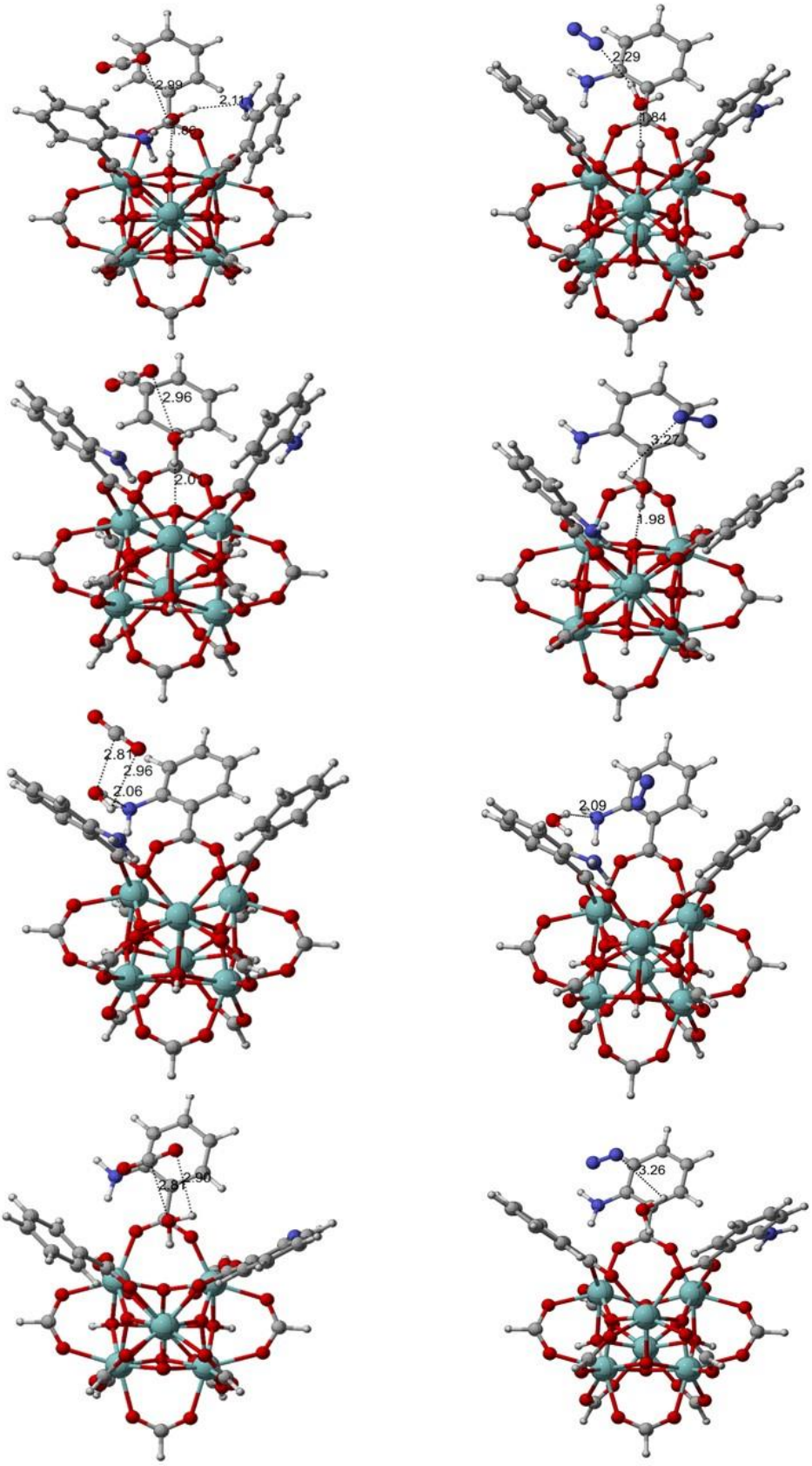

A 3-5-4: DFT(left) and DFT-D(right) Minimum Energy Structure for Adsorbed **CO_2, N_2** in 'No Defect, O, OH, H_2O Defects' (top to bottom) Configuration with **$2NH_2$-iso Substituent** in presence of water.

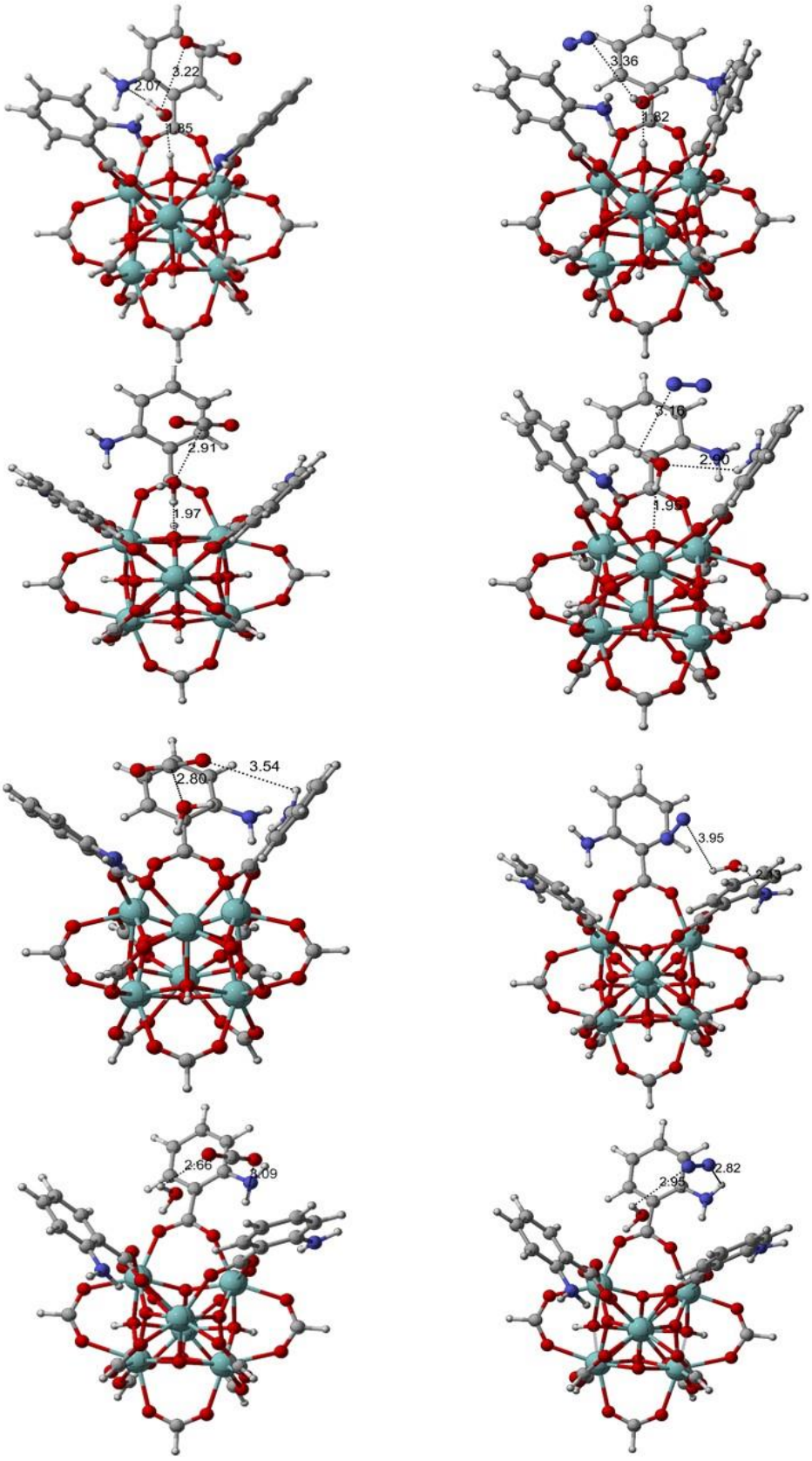

A 3-5-5: DFT(left) and DFT-D(right) Minimum Energy Structure for Adsorbed **CO_2, N_2** in 'No Defect, O, OH, H_2O Defects' (top to bottom) Configuration with **$3NH_2$ Substituent** in presence of water.

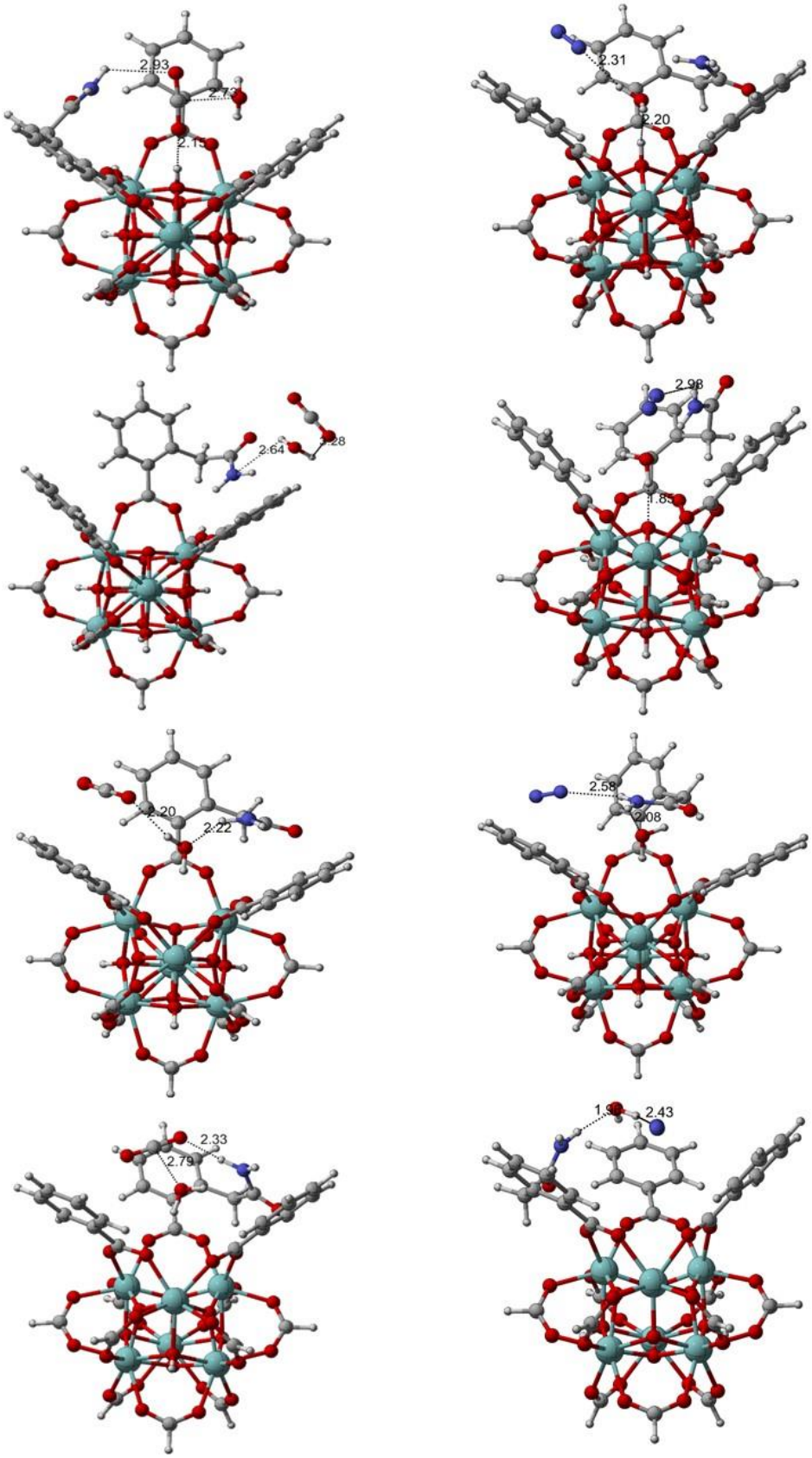

A 3-5-6: DFT(left) and DFT-D(right) Minimum Energy Structure for Adsorbed **CO_2, N_2** in 'No Defect, O, OH, H_2O Defects' (top to bottom) Configuration with **CH_2CONH_2 Substituent** in presence of water.

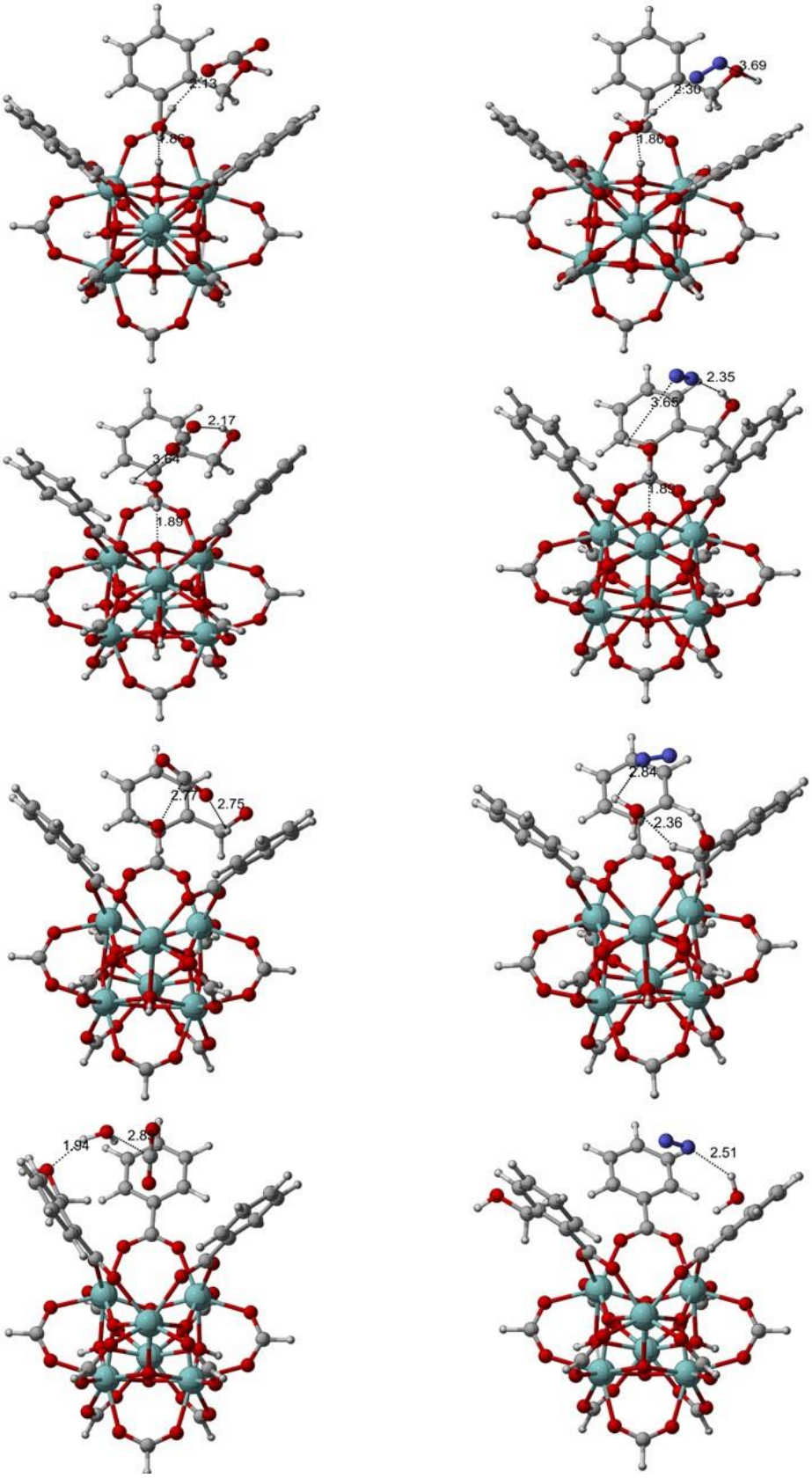

A 3-5-7: DFT(left) and DFT-D(right) Minimum Energy Structure for Adsorbed **CO_2, N_2** in 'No Defect, O, OH, H_2O Defects' (top to bottom) Configuration with **CH_2OH Substituent** in presence of water.

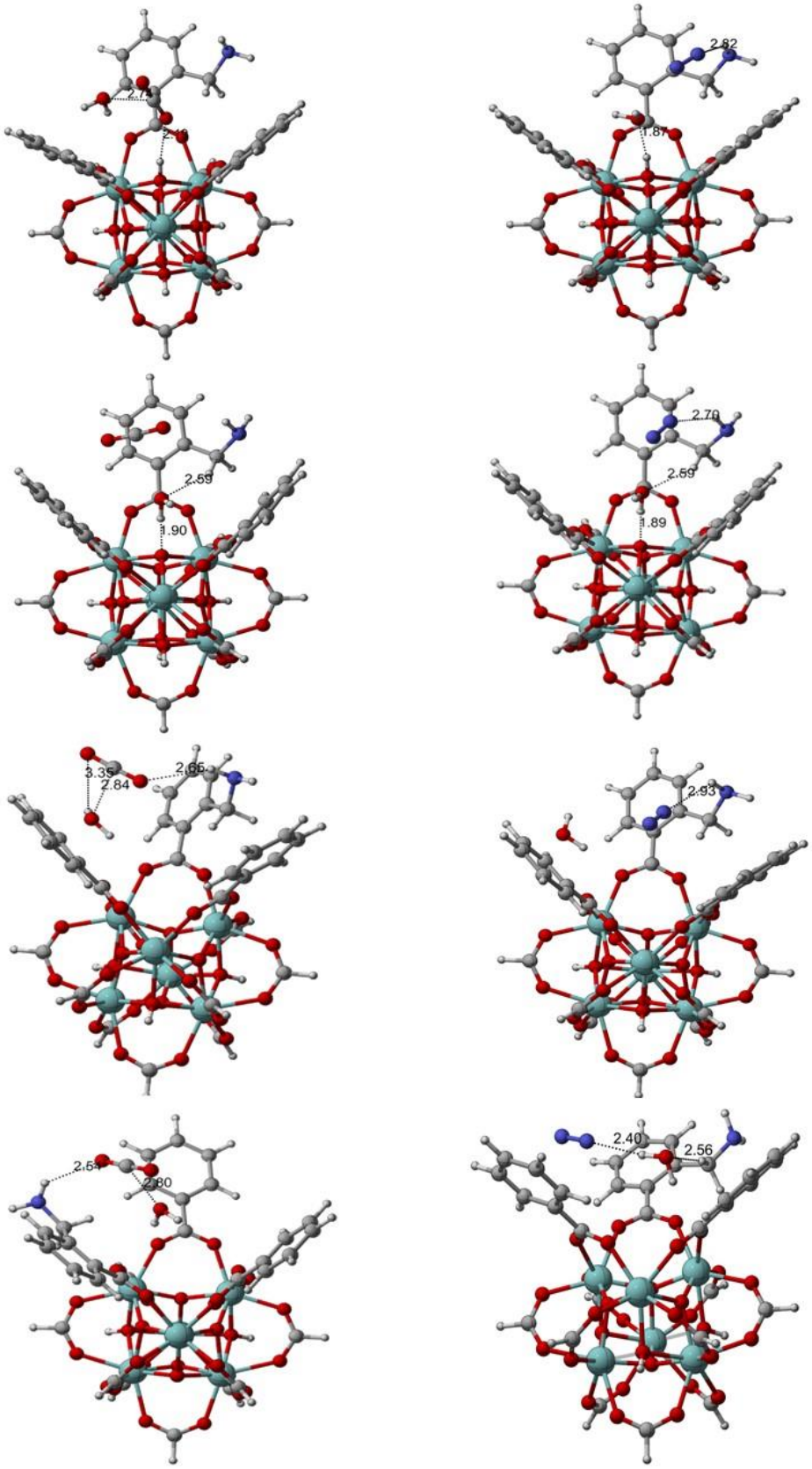

A 3-5-8: DFT(left) and DFT-D(right) Minimum Energy Structure for Adsorbed CO_2, N_2 in 'No Defect, O, OH, H_2O Defects' (top to bottom) Configuration with CH_2NH_2 **Substituent** in presence of water.